School of Electrical Engineering, Computing and
Mathematical Sciences

Curtin Institute of Radio Astronomy

Black Holes and Neutron Stars in Galactic Globular Clusters

Alessandro Paduano

This thesis is presented for the Degree of
Doctor of Philosophy
of
Curtin University

January 2023

To the best of my knowledge and belief this thesis contains no material previously published by any other person except where due acknowledgement has been made. This thesis contains no material which has been accepted for the award of any other degree or diploma in any university.

Alessandro Paduano

24 January 2023

"This is where the fun begins."

— Anakin Skywalker

We acknowledge that Curtin University works across hundreds of traditional lands and custodial groups in Australia, and with First Nations people around the globe. We wish to pay our deepest respects to their ancestors and members of their communities, past, present, and to their emerging leaders. Our passion and commitment to work with all Australians and peoples from across the world, including our First Nations peoples are at the core of the work we do, reflective of our institutions' values and commitment to our role as leaders in the Reconciliation space in Australia.

ACKNOWLEDGEMENTS

There are a multitude of people I need to thank here for making this thesis possible, and I would not have been able to complete my PhD if it weren't for the professional and personal help from everyone.

Right at the top of this section, I need thank my supervisors: Arash, James, and Adela. None of what I've achieved would have been remotely possible without your guidance, help, and continuous encouragement, even when we had to spend hours on end observing 47 Tuc. Adela, thank you for staying on as a supervisor even when you had moved on from CIRA, and for the sense of calm you'd bring to my supervisor meetings. It was always amusing to sit on the sidelines with you as James and Arash would argue with each other. Arash, thank you for always being willing to help and talk about my work, whether it was at 8 in the morning right as you arrived or 5 in the evening when you wanted to go home. Thank you for all the continuous encouragement, checking in on me, and just all the other conversations we've had over the past few years. And to James, I don't know what you saw in me as a naive and ignorant first-year student back in the summer of 2017, but it was this opportunity that piqued my interest in accretion physics and inspired me to see where my research journey would take me. I'm very grateful for all the support you've given me throughout my undergrad degree

and PhD, and I definitely wouldn't have arrived at the place I am now without your guidance.

To the rest of the accretion physics group, thanks for being continuously amused as week after week I would produce a deeper image of 47 Tuc, and for putting up with my endless paper reviews on weird black hole papers I would find on arXiv.

In addition to my supervisors and the accretion group members, there are several other CIRA staff members who I need to thank. Cath, thanks for all the good chats over lunch, all the quick chats about the weekend's footy and our mutual dislike of Collingwood (although the Eagles are still the superior team over Carlton), and for all the wonderful places you've taken me during all the hikes we've. I also want to thank you for all the support you've given me while I was applying for the BoM position, for putting up with my frantic stressing for weeks on end, and continually checking up on me. Thank you for always being someone to talk to, and for making the institute a much better place. I'd also like to thank my panel members, Ramesh, Sam, Christene, and Anshu, for all their support during my PhD; Tim for helping me make the deepest ATCA image; and Jack and Marcin for putting up with my power-trips while running journal club.

I am very fortunate to have been surrounded by an amazing group of fellow PhD students who have made each and every day a fun and different experience, and have had to continuously put up with me sticking magnetic dust filters to the ceiling, stealing the side panels from PCs, and all the various other pranks and shenanigans I've gotten up to over the years. The first mention has to go to Mawson, Danica, and Freya, as the group of us have made it all the way from naive first-year students to PhD students together.; there's no one else I'd rather have done my degree with. And I suppose Jaiden can also slot in here, although I will maintain that I am the more senior PhD student. But on a serious note, thanks for our regular lunch walks, always being willing to chat, and for everything else. Susmita, thank you for all the tea, and always being willing to

annoy me or let me annoy you during the day. I'm sure we could've finished much sooner if we didn't end up distracting each other so much. Angie and Garvit, it's been very nice to watch you go from undergrads to PhD students during my time here. Garvit, thanks for letting me always mess with your PC in some way. Angie, thanks for all the good chats and rants we've had over the past year, I've really appreciated it all. And I also have to mention Ferry, Ben, Steve, Mike, Silvia and Lieke here too for all the fun times we've had.

The last, but certainly not least, students I have to thank are my deskmates, Tyrone and Callan; we were absolute menaces in the our little back corner. Thanks for all the procrastinating chats and walks to the kitchen we've had. The memes have been top tier.

There are also several people outside of CIRA that I need to also thank. I think the first group I need to thank is the Mens 1s team from the Kalamunda Hockey Club. I've really enjoyed being among this group during my PhD and I don't think I would have been able to finish it in a sane state if not for being with this group over the last seven years. The hockey has been great, the banter even better, and I'll miss being able to play for Kala until I get back to Perth. Save me a spot in the dugout for when I come and visit.

Matt, Chris, Arni, Corey, Grace, and Rachel. Thanks for being the original Physics gang. I'm glad we've still been able to catch up and hang out. Matt, Chris, Arni, thanks for all the memes we've had in the many video games we've played together. From Chris and I camping at the back of Nuketown, to my rampages throughout the galaxy in Stellaris, I've enjoyed every bit of it.

I would never have made it this far without all the support my brothers, Giacomo and Cristiano, have given me. Thank you for all the fights, weird conversations, banter, and all the other brotherly things you've done all the time. And to my parents, Tony and Peta, thank you for everything. I would never have been able to achieve the things I have without you providing the basis for me to flourish.

ABSTRACT

Globular clusters are large, spherical clusters of stars that orbit the centre of the galaxy in which they reside. Because of their ages, their most massive stars have already reached the end of their evolutionary pathways and formed compact stellar remnants such as black holes and neutron stars. The remaining stars consist of very old main sequence and giant stars.

Globular clusters contain up to a few million stars within a volume of about a cubic parsec. A consequence of these high stellar densities is that the population of compact objects in the cluster frequently undergoes interactions with the stars in the cluster, leading to the formation of exotic binary systems. These exotic binary systems include X-ray binaries (binary systems which consist of a black hole or neutron star and a companion star) and millisecond pulsars (old pulsars that have been recycled and spun up to have a spin period of a few milliseconds). The higher formation rate of these exotic systems in globular clusters relative to the Galactic field makes these clusters a fantastic environment in which to undertake detailed studies of X-ray binaries, which provide a way to study the universal process of accretion physics over short (human) timescales and the exotic nature of compact stellar remnants.

A powerful way to study X-ray binaries in globular clusters is through multi-

wavelength radio and X-ray observations. Optical studies of globular clusters can be challenging due to the crowded nature of the core of the cluster. Radio and X-ray observations are therefore used as they can target the emission from the outflowing jets and infalling accreted material respectively in an X-ray binary. These observations can then be combined with other data, such as optical spectroscopic data, to identify X-ray binaries and other exotic systems in globular clusters and flag them for future study. In this thesis, we target a variety of black holes and neutron stars in globular clusters to ascertain their properties, and use deep radio observations to search for the population of black holes in globular clusters that have remained invisible.

One such interesting X-ray binary that has been identified in a globular cluster is the source NGC 6652B in the globular cluster NGC 6652. We obtained simultaneous radio and X-ray observations to investigate the relationship between the radio and X-ray emission from this source. These data indicate that the source displays persistent X-ray flaring and moderately variable radio emission, including occasional radio flares. Optical spectra of this source also indicate variable Hα emission switching between emission and absorption over a timescale of a few hours. These properties suggest that NGC 6652B is best explained as a transitional millisecond pulsar candidate, the suspected progenitor systems to millisecond pulsars. This indicates that globular clusters could host an overabundance of transitional millisecond pulsars, meaning they are ideal environments to probe millisecond pulsar formation.

We then targeted another cluster for follow-up study; the cluster NGC 3201, which is the first globular cluster confirmed to contain black holes. We use radio and X-ray observations of the cluster to search for multiwavelength emission from these black holes, of which we find no evidence. This indicates that the black holes are not accreting, or that any accretion is extremely inefficient. The non-detection of these black holes indicate that the current available radio and X-ray data on globular clusters are simply not sensitive enough to detect very faintly

accreting black holes, where the accretion rates are extremely low due to the suspected detached natures of these systems.

To overcome this limitation, we conducted an ultra-deep radio survey of the globular cluster 47 Tucanae to search for these very faintly accreting black holes. The image of 47 Tucanae that we produced during this process is the deepest radio image ever made using the Australia Telescope Compact Array, reaching sensitivities that are the goals of the next generation of radio facilities. We use these data to identify a faint radio source at the centre of 47 Tucanae which we conclude, after analysis of further multiwavelength data, is best explained as either an undiscovered pulsar or an intermediate-mass black hole candidate. The latter case would represent the first direct detection of an intermediate-mass black hole through radio observations. We use these ultra-deep radio data to produce a radio source catalogue of 47 Tucanae, detecting 81 sources within the half-light radius of the cluster. Through the detection of a radio counterpart to the X-ray source 47 Tucanae W41 for the first time, we suggest that this source is actually a redback pulsar rather than a W Ursae Majoris variable, as had been previously hypothesised.

This thesis indicates the value of multiwavelength observations of globular clusters for further studies of the X-ray binaries they contain, and in particular the value of deep radio observations of these sources. The deep radio survey of 47 Tucanae has offered an indication of the sensitivities that will be achieved with the next generation of radio facilities, and how these facilities can be used to probe extremely faint sources in globular clusters.

STATEMENT OF CONTRIBUTION BY CO-AUTHORS

Chapter 3 of this thesis, "The MAVERIC Survey: Simultaneous *Chandra* and VLA observations of the transitional millisecond pulsar candidate NGC 6652B", is a reproduction of an already published work by Paduano et al. (2021) ("The MAVERIC Survey: Simultaneous *Chandra* and VLA observations of the transitional millisecond pulsar candidate NGC 6652B", Monthly Notices of the Royal Astronomical Society, Volume 506, Issue 3, pp. 4107-4120, DOI: https://doi.org/10.1093/mnras/stab1928). This is my own work except for the following. V. Tudor proposed for and acquired the radio and X-ray data, performed initial data reduction and calibration, originally identified the radio source, and calculated the radio spectral index. Optical spectroscopic data from the SOAR telescope were collected and calibrated by J. Strader, who also provided the text regarding the collection and calibration of this data. A. W. Shaw collected and performed initial calibration of the optical photometric data from the Gemini Acquisition camera. Discussions on the data reduction and implications of the results were contributed by my supervisory panel – A. Bahramian, J. C. A. Miller-Jones, and A. Kawka. Further discussions were also contributed by J. Strader,

L. Chomiuk, C. O. Heinke, T. J. Maccarone, C. T. Britt, R. M. Plotkin, A. W. Shaw, L. Shishkovsky, E. Tremou, V. Tudor, and G. R. Sivakoff. I drafted the manuscript and distributed it to all co-authors for proofreading. All co-authors provided input and feedback on the manuscript until the final version was produced.

Chapter 4 of this thesis, "The MAVERIC Survey: The first radio and X-ray limits on the detached black holes in NGC 3201", is adapted from an already published work by Paduano et al. (2022) ("The MAVERIC Survey: The first radio and X-ray limits on the detached black holes in NGC 3201", Monthly Notices of the Royal Astronomical Society, Volume 510, Issue 3, pp. 3658-3673, DOI: https://doi.org/10.1093/mnras/stab3743). This is my own work except for the following. Radio data acquisition was conducted by J. C. A Miller-Jones. Radio data were calibrated and images produced by V. Tudor. F. Göttgens provided the rotational velocities and the stellar radii for the stellar companions to the BHs in the cluster. S. Kamann assisted with the calculations of the rotation rates of some stellar companions to the BHs. J. C. A. Miller-Jones assisted with the calculations of the BH mass accretion rates. Discussions regarding the interpretation of the results were contributed by my supervisory panel – A. Bahramian, J. C. A. Miller-Jones, and A. Kawka. Further discussions were also contributed by F. Göttgens, J. Strader, L. Chomiuk, S. Kamann, S. Dreizler, C. O. Heinke, T. Husser, T. J. Maccarone, E. Tremou, and Y. Zhao. I drafted the manuscript and distributed it to all co-authors for proofreading. All co-authors provided input and feedback on the manuscript until the final version was produced.

Chapter 5 of this thesis, "Ultra-deep ATCA imaging of 47 Tucanae reveals a central compact radio source", is a reproduction of a submitted manuscript by Paduano et al. ("Ultra-deep ATCA imaging of 47 Tucanae reveals a central compact radio source", The Astrophysical Journal). This is my own work except for the following. The radio data were acquired by me, A. Bahramian, J. C. A. Miller-Jones, and T. J. Galvin. T. J. Galvin assisted with the imaging of the data.

The optical HST data, text describing the calibration of these data, and cluster CMDs were provided by L. Rivera Sandoval. A. Kawka performed HST/STIS UV data analysis, and provided text describing this. S. Kamann provided the MUSE spectra of the central stars in the cluster, the Hα flux image and residuals map of this region, and text outlining the collection and calibration of these data. J. Strader assisted with the astrometric alignment of the multiwavelength data and provided text outlining this process. The analysis of BY Dra stars from ZTF and VLASS was done by A. Bahramian, who also provided text outlining this process. Discussions regarding the interpretation of the results were contributed by my supervisory panel – A. Bahramian, J. C. A. Miller-Jones, and A. Kawka. Further discussions were also contributed by T. J. Galvin, L. Rivera Sandoval, S. Kamann, L. Chomiuk, C. O. Heinke, T. J. Maccarone, and S. Dreizler. I drafted the manuscript and distributed it to all co-authors for proofreading. All co-authors provided input and feedback on the manuscript until the final version was produced.

Chapter 6 of this thesis, "A radio source catalogue of 47 Tucanae", is as yet unpublished. This is my own work except for the following. The analysis of 47 Tuc W41 was the result of discussions with T. J. Maccarone and will be published in a manuscript in preparation by Maccarone et al.. This discussion has been synthesised into this chapter. Discussions regarding the interpretation of the results were contributed by my supervisory panel – A. Bahramian, J. C. A. Miller-Jones, and A. Kawka. Further discussions were also contributed by T. J. Maccarone, and J. Strader.

(Signature of candidate)

(Signature of supervisor)

ACRONYMS AND ABBREVIATIONS

AB Active binary.

ACIS Advanced CCD Imaging Spectrometer.

ACS Advanced Camera for Surveys.

AGN Active galactic nucleus.

APEC Astrophysical Plasma Emission Code.

ARF Ancillary response file.

ATCA Australia Telescope Compact Array.

BH Black hole.

BHXB Black hole X-ray binary.

BI Back-illuminated.

BY Dra BY Draconis.

CABB Compact Array Broadband Backend.

CASA Comman Astronomy Software Application.

CC Continuous clocking.

CCD Charge-coupled device.

CIAO Chandra Interactive Analysis of Operations.

CV Cataclysmic variable.

ESA European Space Agency.

FI Front-illuminated.

FUV Far ultraviolet.

FWHM Full-width at half maximum.

GC Globular cluster.

HETG High energy transmission grating.

HMXB High-mass X-ray binary.

HRC High Resolution Camera.

HRMA High Resolution Mirror Assembly.

HST Hubble Space Telescope.

HUGS HST UV Globular Cluster Survey.

ICRS International celestial reference system.

IMBH Intermediate-mass black hole.

INTEGRAL INTErnational Gamma-Ray Astrophysics Laboratory.

IR Infrared.

JD Julian Date.

LETG Low energy transmission grating.

LIGO Laser Interferometer Gravitational-Wave Observatory.

LMXB Low-mass X-ray binary.

LTAO Laser tomographic adaptive optics.

MAVERIC Milky-way ATCA and VLA Exploration of Radio-sources in Clusters.

MJD Modified Julian Date.

MSP Millisecond pulsar.

MUSE Multi Unit Spectroscopic Explorer.

NFM Narrow-field mode.

NGC New General Catalogue.

ngVLA Next Generation Very Large Array.

NS Neutron star.

NSXB Neutron star X-ray binary.

NuSTAR Nuclear Spectroscopic Telescope Array.

NUV Near ultraviolet.

PSF Point spread function.

PSR pulsar.

RFI Radio frequency interference.

RLOF Roche-lobe overflow.

RMF Response matrix file.

RMS Root-mean square.

ROSAT Röntgensatellit.

SKA Square Kilometre Array.

STIS Space Telescope Imaging Spectrograph.

TE Timed exposure.

tMSP Transitional millisecond pulsar.

TOPCAT Tools for OPerations on Catalogues And Tables.

ULX Ultraluminous X-ray source.

UTC Coordinated Universal Time.

UV Ultraviolet.

VLA Very Large Array.

VLT Very Large Telescope.

W UMa W Ursae Majoris.

WCS World coordinate system.

WD White dwarf.

XMM-Newton X-ray Multi-Mirror Mission.

XRB X-ray binary.

XRT X-ray Telescope.

XSPEC X-ray Spectral Fitting Package.

CONTENTS

LIST OF FIGURES

LIST OF TABLES

CHAPTER 1

INTRODUCTION

1.1   Formation of compact objects

Black holes (BHs) and neutron stars (NSs) are compact objects representing the end of stellar evolution in massive stars. Only the largest stars in the Universe will form NSs and BHs, with the most massive O and B spectral type stars with masses $> 8M_\odot$ going on to form BHs. These most massive stars have short lifetimes, on the timescale of tens of millions of years. Most main sequence stars will end their lives after billions of years as white dwarfs (WDs).

These massive stars have temperatures and internal pressures in their cores sufficient for elements heavier than hydrogen and helium to undergo nuclear fusion. This fusion occurs until Fe is formed in the core of the star. Due the high binding energy in Fe nuclei, fusing elements beyond Fe is endothermic rather than exothermic, thus preventing further fusion in the star's core. Fe continues to build up in the core of the star until the inward gravitational force due to the mass of the core exceeds the outward force provided by internal radiation pressure causing the beginning of a collapse. Nuclear photodisintegration and neutronisation further weaken the pressure support of the core which continues

to collapse until the threshold for neutron degeneracy pressure is reached. The Pauli Exclusion Principle prevents the neutrons from occupying the same quantum state, and this neutron degeneracy halts the collapse of the star resulting in a proto-neutron star. This process is known as core-collapse, leading to a type II supernova where the outer envelope of the star is blasted outward. The most recent supernova in the Milky Way is thought to be Cassiopeia A, which occurred in the 17th century (Krause et al., 2008). SN 1987A is another notable recent supernova, that occurred in the Large Magellanic Cloud in 1987.

NSs that are formed after a core-collapse supernova have typical masses of $\sim 1.4 M_\odot$ and typical radii of $\sim 10\,\mathrm{km}$, and are the densest objects to exist in the Universe. Many other astrophysical objects are different types of NSs, such as pulsars, which are rapidly rotating NSs formed due to the conservation of angular momentum during the supernova and emit beams of radiation from their poles. The maximum possible mass for a NS is yet to be quantified, although it is speculated to be in the realm of $2.5 - 3 M_\odot$. The heaviest known NS is the "black widow" pulsar PSR J0952-0607 which has a mass of $2.35 \pm 0.17 M_\odot$ (Romani et al., 2022). PSR J2215+5135, a "redback" binary millisecond pulsar, is another of the heaviest known NSs with a mass of $2.27^{+0.17}_{-0.15} M_\odot$ (Linares et al., 2018).

If the core mass of a collapsing star is large enough, then neutron degeneracy pressure will fail to prevent further collapse and the core will continue to collapse inside its Schwarzschild radius. This will result in the formation of a BH, which is governed by the metrics of general relativity. The transition mass between a BH and a NS is typically assumed to be around $3 M_\odot$. Some of the lightest known BHs are 2MASS J05215658+4359220 ($3.3^{+2.8}_{-0.7} M_\odot$, Thompson et al., 2019) and NGC 3201 BH1 ($4.36 \pm 0.41 M_\odot$, Giesers et al., 2018).

Theory predicts an upper mass gap for BHs in the mass range of $40 - 120 M_\odot$. This is due to the pair instability in large stars suppressing the formation of large BHs. The pair instability occurs when pair production of electrons and positrons

2

in the star's core reduces the radiation pressure needed to maintain hydrostatic equilibrium (Woosley et al., 2007). This causes the internal temperature to rise to a level sufficient enough to cause the ignition of O and Si. What follows is a cycle of the core collapsing and ejecting portions of its envelope, significantly reducing its mass, until a stable configuration is reached, before eventually undergoing a core-collapse supernova or direct collapse to leave a substantially less massive compact object (Woosley, 2017, 2019). Pair instability supernovae typically occur when the He core of the star is greater than $32M_\odot$, and has the effect of reducing a star's mass before it can form a large BH. For core masses $\gtrsim 60M_\odot$, the star will either be completely disrupted or undergo direct collapse into a BH (Fowler & Hoyle, 1964; Ober et al., 1983; Bond et al., 1984; Heger et al., 2003). The theoretical prediction of an upper mass gap has been challenged recently with detections of BHs by the Laser Interferometer Gravitational-Wave Observatory (LIGO) with masses within this mass gap (Abbott et al., 2020; Abbott et al., 2020). However, further theoretical studies have shown that the bounds of the predicted upper mass gap are not yet rigidly defined, and are sensitive to many factors including the nuclear reaction rate within stars (Farmer et al., 2020; Costa et al., 2021), the rotation of the stars (Marchant & Moriya, 2020), super-Eddington accretion onto the source (van Son et al., 2020), or a combination of these (Woosley & Heger, 2021).

1.2 X-ray binaries

X-ray binaries (XRBs) are binary star systems containing a compact object, either a BH or a NS, and a companion star, in a close enough orbit for accretion to occur. The classification XRB broadly applies to any object that fits this description, and there are a number of XRB sub-types depending on the behaviour of the compact object and the type of companion star. XRBs are split by companion mass into high-mass X-ray binaries (HMXBs) and low-mass X-ray binaries (LMXBs), with the differences between these classifications shown in Figure 1.1. Approximately

a third of all known XRBs contain a BH as the compact object (Liu et al., 2007; Corral-Santana et al., 2016; Tetarenko et al., 2016). This section presents an overview of XRBs based on the review by Tauris & van den Heuvel (2006).

HMXBs are XRBs where the companion star has a mass $> 10 M_\odot$ and are generally very luminous, early-type O and B stars. Due to the requirement for the companion star to be of early-type, HMXBs are young systems, with typical ages of $< 10^7$ years. The companion star almost fills its Roche-lobe (Hirai & Mandel, 2021) and the accretion in these systems is mainly through the capture of stellar winds or atmospheric Roche-lobe overflow.

LMXBs are XRBs where the companion star has a mass $< 1 M_\odot$, with companions of later spectral types. LMXBs are much older than HMXBs, with typical ages of $> 10^9$ years due to their less massive companion stars. The accretion in these systems is due to the companion star filling its Roche lobe. The evolution of LMXBs to eventually form millisecond pulsars (MSPs) is shown in Figure 1.2. The initial mass transfer of the primary star is driven by either the nuclear evolution of the primary ($P_{orb} > 2$ days) or by the loss of angular momentum via magnetic braking and gravitational wave radiation. The primary follows its evolutionary pathway and eventually undergoes a supernova, leaving behind a compact remnant object. Provided the binary is not disrupted by this initial supernova and the orbital separation is sufficiently close, the system left behind is a LMXB. The mass transfer begins once the secondary evolves and fills its Roche-lobe.

XRBs with companions with masses between 1 and $10 M_\odot$ are called intermediate-mass X-ray binaries, however in practice these systems are not observed for a few reasons as outlined in van den Heuvel (1975) and Tauris & van den Heuvel (2006). The large mass ratio with the central compact object implies that the Roche-lobe overflow phase (see Chapter 1.2.2.1) for these systems is short-lived, only on the timescale of 10^3 years, when compared to LMXBs with much more stable and long-lived mass transfer phases. These high mass transfer rates could cause the dense gas close to the NS to absorb the X-ray emission, meaning there is a se-
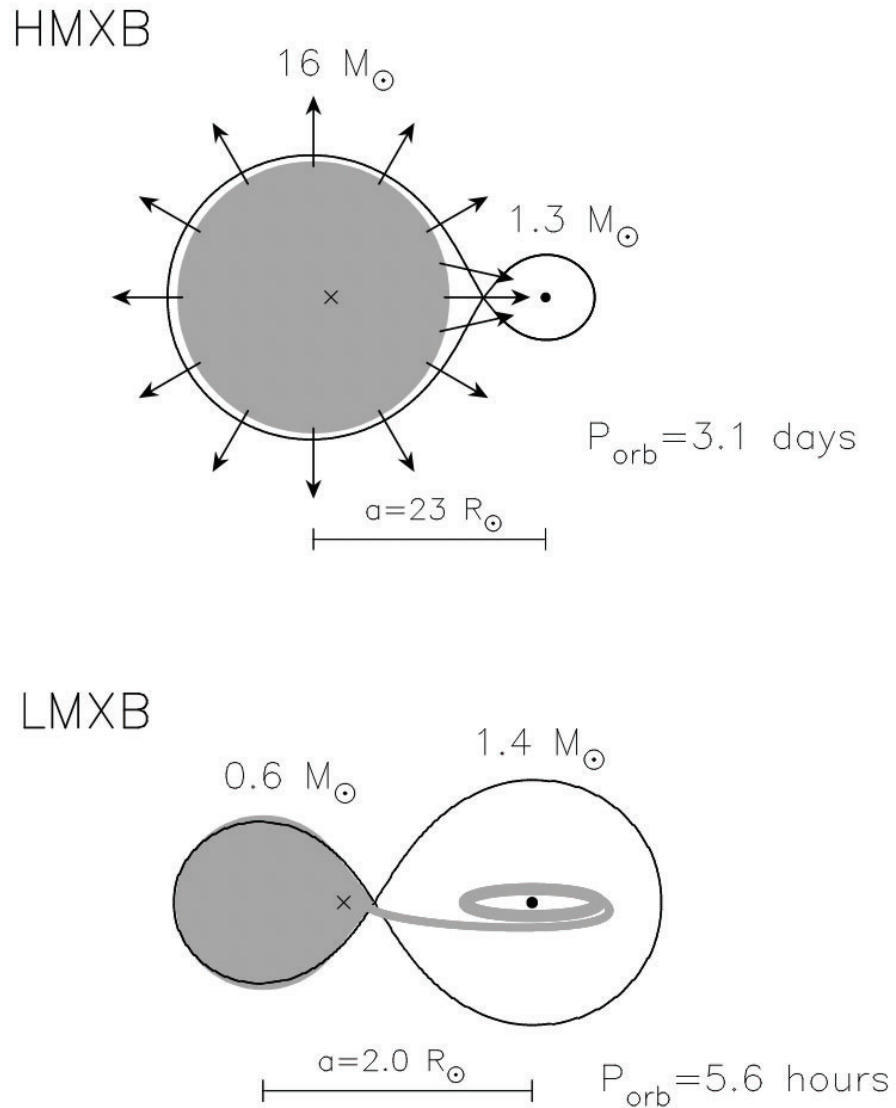
Figure 1.1: The differences between high-mass and low-mass X-ray binaries. HMXBs contain a high-mass companion star, meaning the orbital separation is larger and the orbital period is longer to accommodate this. The accretion in HMXBs is through wind accretion. This is in contrast to LMXBs which contain low-mass stars in binaries with much shorter orbital periods, where the accretion is driven by RLOF. Figure from Tauris & van den Heuvel (2006).
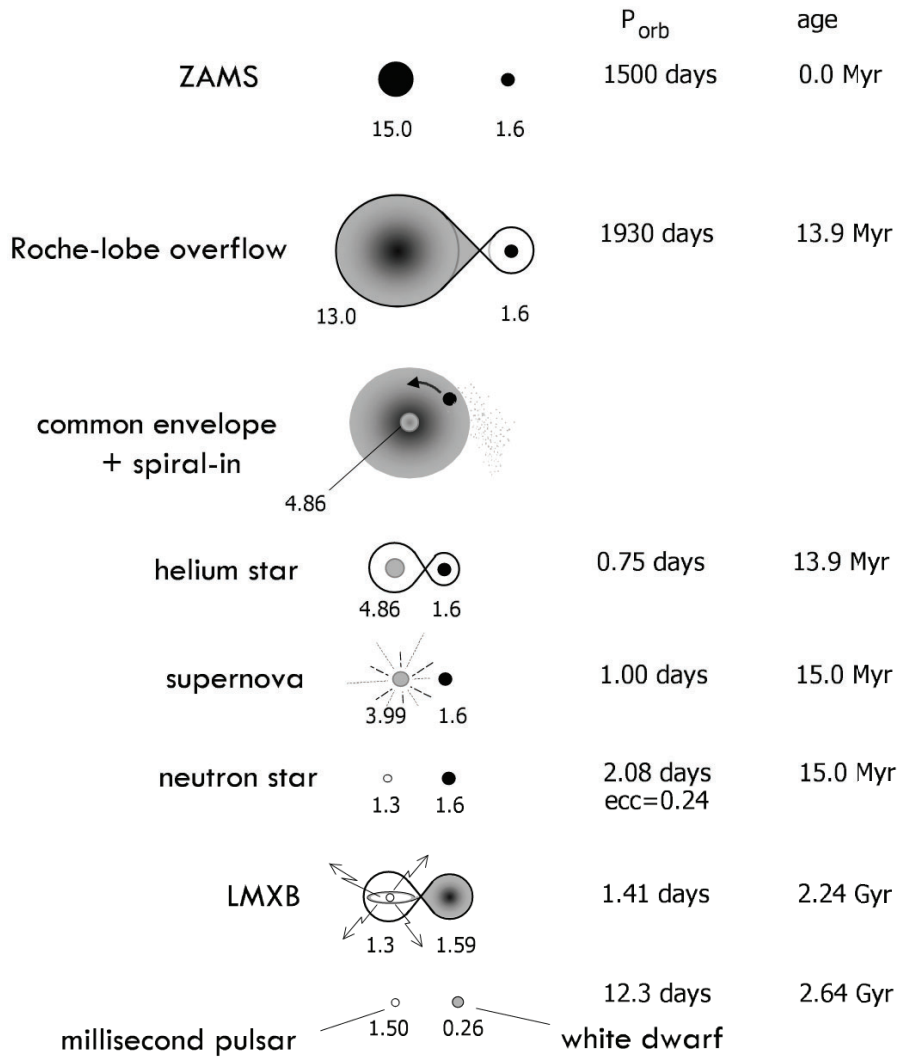
Figure 1.2: The evolutionary pathway of LMXBs to eventually form MSPs. Figure from Tauris & van den Heuvel (2006).

lection effect against observing these systems. Furthermore, intermediate-mass X-ray binaries do not have strong stellar winds like HMXBs do, meaning this wind cannot be easily detected further adding to the selection effects against observing these systems.

1.2.1 Black hole X-ray binaries and millisecond pulsars

This thesis primarily focuses on BH X-ray binary (BHXB) and MSP systems. BHXBs are XRBs where the compact object is a BH and about one third of all known XRBs are thought to be BHXBs (Liu et al., 2007; Corral-Santana et al., 2016; Tetarenko et al., 2016). BHXBs typically go through periods of quiescence, where the system is faint and there is very little accretion onto the compact object, and outburst, where rapid mass transfer occurs and the system brightens.

As pulsars age, they radiate energy through magnetic dipole radiation and radio pulsations. This loss of energy causes the pulsar to start spinning slower until no detectable emission is observed from the system. If this 'dead' pulsar is in a binary system with a companion star, it can accrete matter and angular momentum and be spun up to have a period of a few milliseconds (Alpar et al., 1982). These systems are MSPs and represent the end of this recycling process. LMXBs containing NSs were thought to be the progenitor systems to MSPs, and this link was confirmed through the detection of millisecond pulsations from the LMXB SAX J1808.4-3624 (Wijnands & van der Klis, 1998), demonstrating that there is an evolutionary link between LMXBs and MSPs.

The final piece of the evolutionary link between LMXBs and MSPs has been confirmed in recent years with the discovery of transitional millisecond pulsars (tMSPs; Archibald et al. 2009). tMSPs are MSPs that switch between a rotation-powered radio pulsar state and a sub-luminous accretion-powered LMXB state on a timescale of months to years. To date, there have only been three confirmed tMSPs: PSR J1023+0038 (Archibald et al., 2009; Stappers et al., 2014), IGR J18245-2452 (Papitto et al., 2013), and XSS J12270-4859 (Bassa et al., 2014).

Of these, PSR J1023+0038 (J1023) is the most well studied source due to its proximity to Earth (1.4 kpc; Deller et al. 2012), and IGR J18245-2452 (M28I) is notable for being located in the globular cluster M28 making it the only tMSP to be located in a cluster. It is also worth noting that all three confirmed tMSPs are redback pulsar systems, MSPs where the companion stars, with typical masses of $0.2 - 0.5 M_\odot$, are being ablated by the pulsar wind (Roberts, 2013; Strader et al., 2019a). There are also a handful of tMSP candidates located both in globular clusters (e.g., Bahramian et al., 2018b; Paduano et al., 2021) and in the Galactic field (e.g., Bogdanov & Halpern, 2015; Rea et al., 2017; Coti Zelati et al., 2019; Li et al., 2018; Miller et al., 2020; Strader et al., 2021). These systems display observed properties similar to tMSPs, but have not yet been observed to display a state change.

tMSPs display different observational characteristics depending on their current state. In the rotation-powered MSP state, tMSPs display properties typical of redback pulsars and radio pulsations can be detected (Archibald et al., 2009; Papitto et al., 2013), but are also occasionally eclipsed by either the secondary or the ionised material present in the system. The eclipses in J1023 were found to have different durations depending on the observed frequency (Archibald et al., 2009, 2013). The X-ray emission in this state is also faint, with typical X-ray luminosities of $L_X < 10^{32} \, \mathrm{erg \, s^{-1}}$ (Linares, 2014).

In the sub-luminous LMXB state, the radio pulsations from the pulsar become undetectable, and are instead replaced with bright, flat-spectrum continuum radio emission (Hill et al., 2011; Stappers et al., 2014; Deller et al., 2015) which is thought to be produced by the self-absorbed synchrotron emission from outflowing jets. It is not known whether the accretion flow quenches the radio pulsations, or whether they are absorbed by the intrabinary material. The X-ray emission from tMSPs in the accreting state brightens to typical luminosities of $L_X \sim 10^{33} \, \mathrm{erg \, s^{-1}}$ (Bogdanov & Halpern, 2015). While MSPs are gamma-ray sources there is a distinct brightening of the gamma-ray flux of a tMSP in the accreting state,

increasing by a factor of at least five compared to the pulsar state (Stappers et al., 2014; Johnson et al., 2015). tMSPs also seem to display optical and UV pulsations, although these have only been observed in J1023 and are thought to be produced by shocks between the pulsar wind and the accretion flow (Ambrosino et al., 2017; Illiano et al., 2022)

Perhaps the most striking property of a tMSP in the LMXB state is the bimodal distribution of the X-ray flux, which alternates between an X-ray low and an X-ray high mode on a sub-hour timescale. In the X-ray high mode, X-ray flares up to $L_X \sim 10^{34}\,\mathrm{erg\,s^{-1}}$ are also observed (de Martino et al., 2013; Bogdanov & Halpern, 2015). This bimodal distribution of X-ray flux has been observed to be anticorrelated with the continuum radio emission, where an X-ray low mode corresponds to a radio high mode and vice versa (Bogdanov et al., 2018). This observed property is thought to be caused by active accretion onto the NS being interrupted by ejected material driven by the pulsar. This behaviour is one of the best ways to identify new tMSP candidates.

Due to the small number of confirmed tMSPs and limited number of good, convincing candidates, there are still numerous questions about these systems and the final stages of the pulsar recycling process as the accretion phase is starting to switch off. It is still unknown how the population of tMSPs compares to that of normal pulsars. Given that one tMSP and some candidates are located in globular clusters, it is also unknown if this population differs from the population of tMSPs in the Galactic field. Identifying new tMSPs will help with these population studies, and also provide further information for how the presence of a strong magnetic field affects accretion.

1.2.2 Accretion in X-ray binaries

The process of accretion is fundamental in XRBs, and is the process by which external matter, whether it be from a companion star or the ambient surroundings, falls onto a compact object. This process releases large amounts of energy from

the liberated gravitational potential energy of the matter falling deeper into the potential well of the compact object. The accretion luminosity can be expressed as:

$$L_{acc} = \frac{GM\dot{M}}{R},\tag{1.1}$$

where M is the mass of the compact object, R is the radius of the compact object, and $\dot{M}$ is the mass accretion rate, usually expressed in $M_{\odot}\text{yr}^{-1}$. This equation holds if all the gravitational potential energy of the infalling matter were released at the surface of the compact object, as is typical for NSs. For BHs, the Schwarzschild radius would need to be used instead.

1.2.2.1 Roche lobes

As mentioned previously, a XRB consists of a compact object and a companion star. For this thesis, we define the compact object as the primary with mass M_1, and the companion star as the secondary with mass M_2, giving a mass ratio of $q = M_2/M_1$. LMXBs have $q < 1$ and HMXBs typically have $q > 1$. Accretion in XRBs will generally involve the Roche lobes of the two components. The geometry of the Roche lobes for a binary system is shown in Figure 1.3. As can be seen, the Roche lobes for the two objects form a figure-eight shape, and are connected through the L_1 Lagrange point for the binary system, meaning matter can move through the L_1 Lagrange point from one Roche lobe to the other.

As the companion star in an XRB evolves, it will expand to fill its Roche lobe, causing material to spill into the Roche lobe of the compact object. This is called Roche lobe overflow (RLOF), and is one of the main mechanisms for accretion in an XRB. If there is no mass transfer through RLOF, then the only way that matter can be transferred to the compact object is through stellar winds. These binaries are called detached binaries. The size of the Roche lobe can be calculated analytically using the equations from Eggleton (1983), where the Roche lobe of
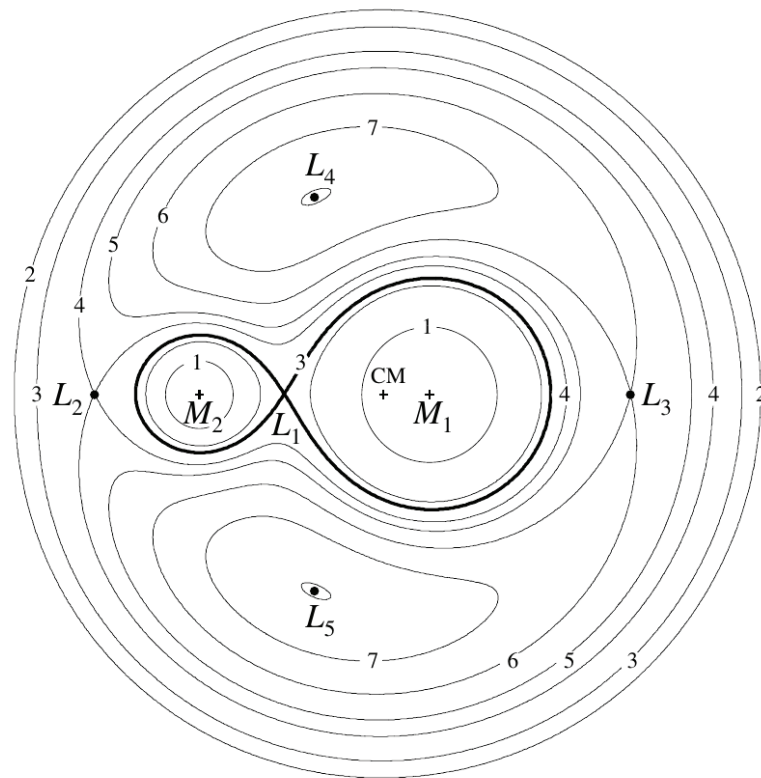
Figure 1.3: The Roche lobes and Lagrange points of two objects M_1 and M_2 in a binary system. The Roche lobes for the two objects are joined at the L_1 Lagrange point. Figure from Frank et al. (2002).

the secondary R_2 as a fraction of the orbital separation a is expressed as:

$$\frac{R_2}{a} = \frac{0.49q^{2/3}}{0.6q^{2/3} + \ln(1 + q^{2/3})}.$$ (1.2)

1.2.2.2 Accretion disks

Gas transferred through RLOF cannot fall straight onto a compact object due to the conservation of angular momentum. As the gas moves into the Roche lobe of the primary, it adopts a minimum energy orbit for its given angular momentum, resulting in a circular orbit. The circularisation radius R_{circ} is the initial orbit where the gas has the same angular momentum as gas passing through the L_1 Lagrange point, and can be expressed as (Frank et al., 2002)

$$\frac{R_{circ}}{a} = \frac{4\pi^2 a^3}{GM_1 P^2}\left(\frac{b_1}{a}\right)^4.$$ (1.3)

R_{circ} is always smaller than the Roche lobe of the primary.

The gas in this orbiting ring at R_{circ} eventually loses energy and sinks further into the gravitational potential well of the primary. As the gas loses angular momentum, it spirals inwards through a series of approximately circular orbits. The result of this series of circular orbits is the formation of an accretion disk. The mechanism for angular momentum loss in the disk is through viscosity. The viscosity of the disk causes the energy of the gas to be dissipated through heating the gas, which produces observable X-ray emission. Given the extremely complex nature of viscosity ν in an accretion disk, it is usually parameterised using the alpha prescription based on Shakura & Sunyaev (1973) and expressed as:

$$\nu = \alpha c_s t.$$ (1.4)

Here, c_s is the sound speed in the disk, t is the disk thickness, and α parameterises all our ignorance about viscosity.
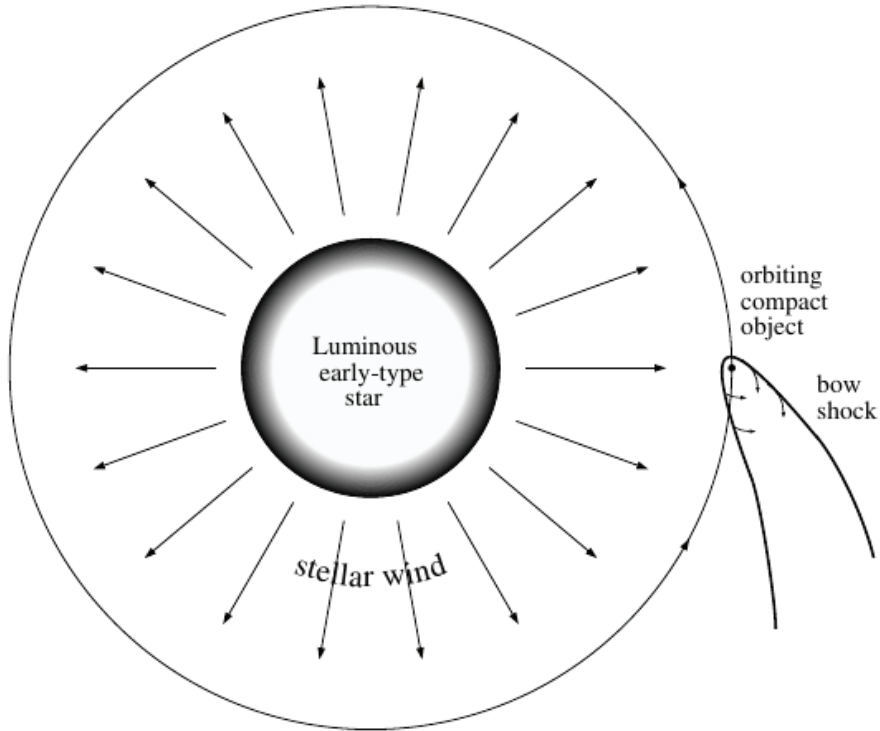
Figure 1.4: A compact object accreting from the stellar winds of the companion star. The compact object moves through the companion's stellar winds, resulting in a bow shock being formed. Figure from Frank et al. (2002).

1.2.2.3 Stellar wind accretion

There are also some binary systems where the accretion occurs through the capture of stellar winds rather than RLOF. This is common in the case of HMXBs, where you have a luminous early-type star with very strong stellar winds, and also in the case of detached LMXBs where the binary separation is large enough to prevent the secondary from filling its Roche lobe. In both of these cases, the compact object will move through the emitted stellar winds of the companion, accreting a portion of it. The geometry of these scenarios is shown in Figure 1.4.

As in the RLOF case, an accretion disk can form around the compact object if the circularisation radius R_{circ} is larger than the surface of the compact object.

In a stellar wind regime the circularisation radius is (Frank et al., 2002)

$$\frac{R_{circ}}{a} = \frac{M_1^3(M_1 + M_2)}{16\lambda^4(a)M_2^4}\left(\frac{R_2}{a}\right)^4,$$ (1.5)

where M_1 and M_2 are the masses of the primary and secondary respectively, R_2 is the radius of the secondary, a is the binary separation, and $\lambda(a)$ is the wind law describing the stellar winds of the companion. The amount of stellar wind captured by the compact object $\dot{M}$ is given as a fraction of the total wind mass loss rate of the companion $-\dot{M}_w$ (Frank et al., 2002)

$$\frac{\dot{M}}{-\dot{M}_w} \cong \frac{1}{4}\left(\frac{M_1}{M_2}\right)^2\left(\frac{R_2}{a}\right)^2.$$ (1.6)

Accretion due to stellar wind capture is much more inefficient than RLOF, and observable emission is only produced due to the large wind mass loss rate of the companion star

1.2.3 Radiative emission from X-ray binaries

A LMXB is composed of different components as shown in Figure 1.5. As previously mentioned, the two objects in a LMXB are a compact object and a low-mass companion star. If the orbit is sufficiently small, the star fills its Roche lobe, creating a stream of material into the Roche lobe of the compact object which eventually forms an accretion disk as discussed in Section 1.2.2.2. The accretion disk represents inflow in the system, where matter is falling onto the compact object. There is also outflowing matter moving away from the compact object in the form of collimated jets. Each component of a LMXB contributes observable emission at different parts of the electromagnetic spectrum through different emission mechanisms. The focus of this thesis are the optical, radio, and X-ray emission from these objects.
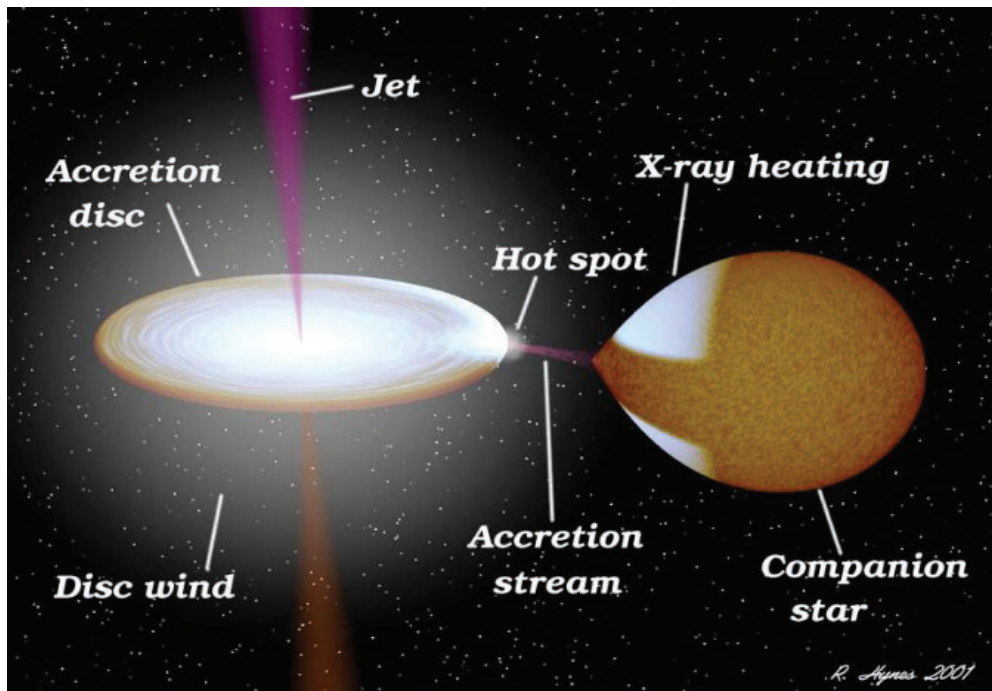
Figure 1.5: The different components of a LMXB system. The companion star is filling its Roche lobe, causing material to spill into the gravitational potential well of the compact object and resulting in the formation of an accretion disk. Material is also outflowing from the system in the form of jets. Image credit: NASA/R. Hynes.

1.2.3.1 Optical emission

The optical emission in a LMXB can originate from either the star or the accretion disk, depending on whether the system is in outburst or quiescence. The star is approximated as a blackbody, and primarily emits radiation through blackbody emission. Blackbody radiation is thermal radiation emitted by an object that is at a temperature above absolute zero. The spectral radiance emitted by a blackbody in units of $\mathrm{W\,m^{-2}\,sr^{-1}\,Hz^{-1}}$ is described by Planck's law of blackbody radiation:

$$B_\nu(T) = \frac{2h\nu^3}{c^2} \frac{1}{\exp\left(\frac{h\nu}{k_\mathrm{B}T}\right) - 1}, \tag{1.7}$$

where h is Planck's constant, c is the speed of light, k_B is the Boltzmann constant, ν is frequency, and T is the temperature of the blackbody. Figure 1.6 shows the spectral radiance for blackbodies of varying temperatures. Measuring the blackbody spectrum of a star in a LMXB allows us to estimate its temperature and size.

Spectral lines will also be observable in the spectrum of the companion star. Each element has a unique energy level configuration, meaning that elements can be identified based on observing the radiation that is emitted from electrons transitioning between energy levels. In astrophysical objects, we view these unique signatures as spectral lines, produced either by emission or absorption. Spontaneous emission is caused by excited electrons emitting energy to return to a lower, more stable energy level. This process produces an emission spectrum; bright lines at specific frequencies among a dark continuum. Absorption is caused by a cold gas absorbing photons with specific energies from a source of radiation causing the excitation of some electrons, and an absorption spectrum appears as dark lines among a continuous spectrum of light. Absorption spectra, in particular, can be used to identify the elemental composition of different stars in the Universe if the spectra are of high quality and have a high signal-to-noise ratio. An example of the Sun's absorption spectrum is shown in Figure 1.7. Using
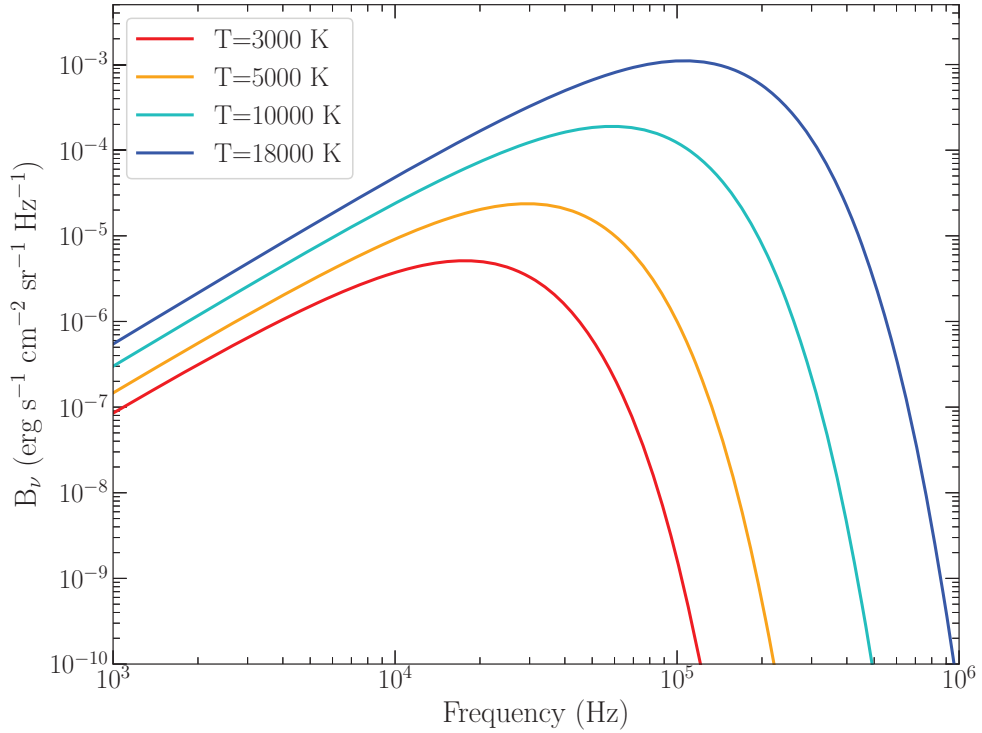
Figure 1.6: The blackbody spectrum for objects at different temperatures.

spectroscopy to measure the optical spectrum of the companion star in a LMXB allows for the class of star to be identified, in addition to identifying any features that may originate from the accretion disk instead.

The accretion disk also contributes some optical emission from the system, and dominates the optical emission when the system is in outburst. For example, in the X-ray transient A0620-00, at least 10% of the total light in the near-infrared is modelled to come from the accretion disk (Cantrell et al., 2010); and in the candidate BHXB 47 Tucanae X9, there is a substantial blue component to the optical flux of the system originating from the accretion disk (Knigge et al., 2008).

1.2.3.2 Radio emission

The radio emission from LMXBs comes from outflowing jets. Jets are the outflow of matter and energy from accreting compact objects, and will usually be aligned along the spin axis of the compact object. The primary emission mechanism
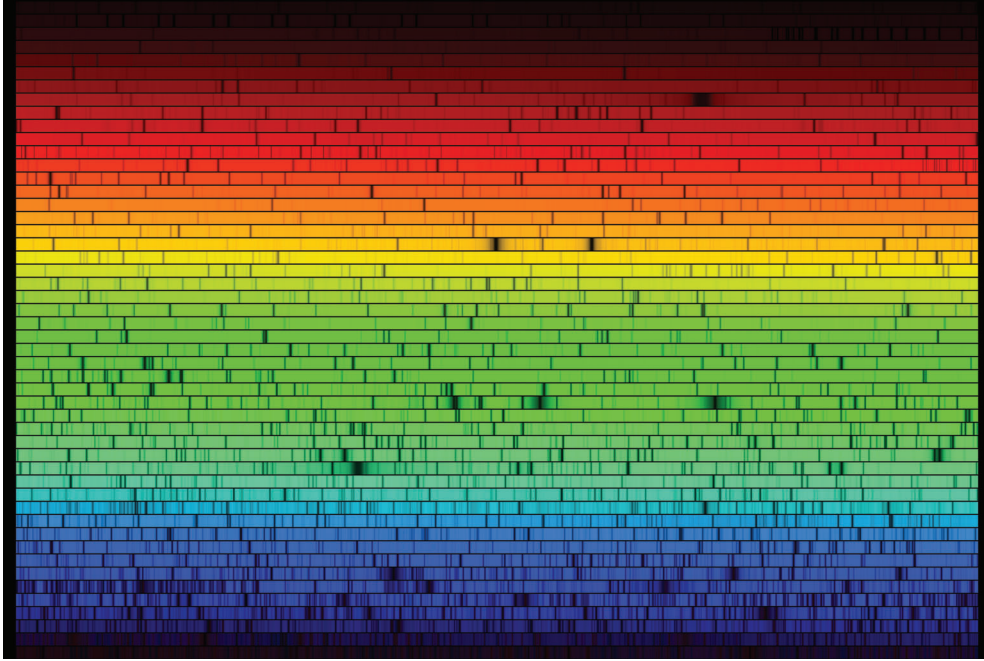
Figure 1.7: The absorption spectrum of the Sun across a wavelength range from 4000 to 7000 Å. Figure source: N. A. Sharp, NOAO/NSO/Kitt Peak FTS/AU-RA/NSF.

responsible for this radio emission is synchrotron radiation, which is produced by charged particles being accelerated by an external magnetic field. The observed synchrotron spectrum from a source will be the sum of the spectra from the individual synchrotron emitting particles, and can often be approximated as a power-law $S_\nu \propto \nu^\alpha$ where α is the spectral index. We can write that the distribution of particle energies in the source is:

$$N(E)dE \propto E^{-\delta}dE, \tag{1.8}$$

where δ is the particle distribution index and is related to the spectral index by:

$$\alpha = -\frac{\delta - 1}{2}, \tag{1.9}$$

meaning the spectral index of the power-law spectrum is directly related to the distribution of particle energies in the source.
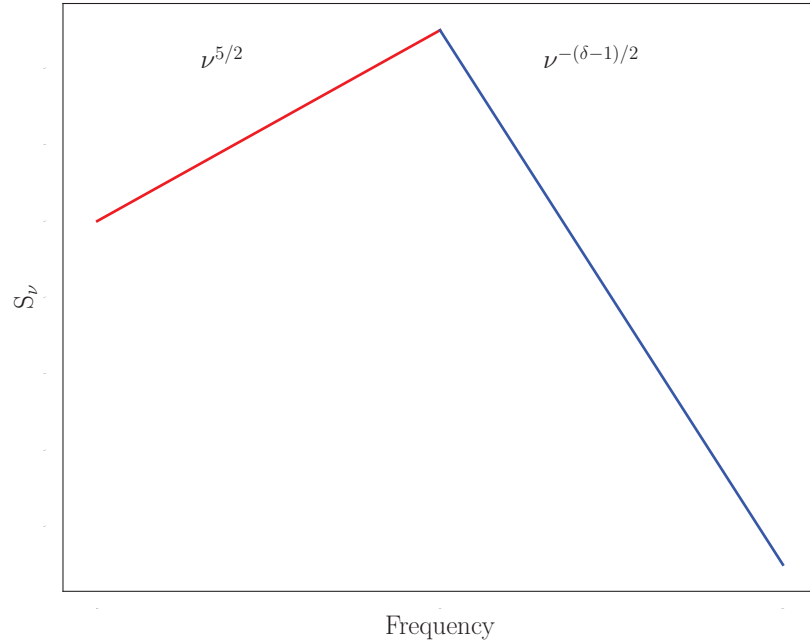
Figure 1.8: An example synchrotron spectrum from a source. In the regime where the source is optically thick (red), the emission spectrum follows a power-law with a spectral index of $5/2$. In the regime where the source is optically thin (blue), the spectral index of the power law is $-(\delta - 1)/2$.

This process of synchrotron emission also has an associated absorption process, where a charged particle in a magnetic field absorbs a photon. The process by which synchrotron emitting particles absorb the synchrotron radiation they emit is called synchrotron self-absorption. At low frequencies in the regime where the source is optically thick, the spectrum of a synchrotron self-absorbed source follows a power-law $S_\nu \propto \nu^{5/2}$. The synchrotron spectrum from a source is shown in Figure 1.8. From this figure, it is clear to see that the spectrum is composed of the self-absorbing portion in the optically thick regime following a spectral index $\alpha = 5/2$, and the synchrotron emitting portion in the optically thin regime following a spectral index $\alpha = -(\delta - 1)/2$.

Outflowing jets in a LMXB have been observed in two types: steady jets and transient jets. Steady jets are thought to have bulk Lorentz factors $\Gamma < 2$ and display flat radio spectra (Fender et al., 2004). The radio emission from a steady jet is in the form of partially self-absorbed synchrotron emission from

the jet. Transient jets are thought to have much higher bulk Lorentz factors ($\Gamma > 2$) and display turned-over synchrotron spectra that are self-absorbed at lower frequencies, where the emission originates from discrete ejection events.

Some of the proposed jet-launching mechanisms include the Blandford-Znajek process (Blandford & Znajek, 1977) and the Blandford-Payne mechanism (Blandford & Payne, 1982). In the Blandford-Znajek process, which requires a BH, the magnetic field lines from the magnetised accreted material thread through the event horizon of the BH. The frame-dragging effect of the BH causes the magnetic field lines to move inducing an electromagnetic force, accelerating charged particles along the axis of rotation and creating jets dominated by Poynting flux. The Blandford-Payne mechanism does not require a BH and can be used in NS systems to launch jets. The accretion disk is threaded by magnetic field lines which co-rotate with the disk and this differential rotation in the disk causes the magnetic field lines to shear and be reconnected. The magnetic field forces matter to be driven outwards, and this outflow is then collimated into a jet due to the creation of a toroidal magnetic field.

1.2.3.3   X-ray emission

The X-ray emission from LMXBs originates from the accretion flow, including the accretion disk and the corona around the inner regions of the disk. The accretion disk has a top and bottom face, both of which will radiate as a blackbody. The temperature of these blackbodies is expressed as a function of radius from the centre of the disk, as shown in Frank et al. (2002), and has the following expression:

$$T(r) = \left\{ \frac{3GM\dot{M}}{8\pi r^3 \sigma} \left[1 - \left(\frac{r_\star}{r} \right)^{1/2} \right] \right\}^{1/4}, \tag{1.10}$$

where $r_\star$ is the radius of the primary. The total flux from an accretion disk observed at an inclination angle i and distance d can be calculated as:

$$F_\nu = \frac{2\pi \cos i}{d^2} \int_{r_\star}^{r_{out}} B_\nu r dr, \qquad (1.11)$$

where the integral is taken between the surface of the primary and the outer radius of the accretion disk. By substituting in Planck's radiation law (Equation 1.7), the received flux from the accretion disk reduces to:

$$F_\nu = \frac{4\pi h \cos i \nu^3}{c^2 d^2} \int_{r_\star}^{r_{out}} \frac{r dr}{\exp\left(\frac{h\nu}{k_{\mathrm{B}} T(r)}\right) - 1}. \qquad (1.12)$$

The emitted spectrum of an accretion disk is shown in Figure 1.9. From this figure, it can be seen that the disk spectrum has three different regimes. At low frequencies, we have the Rayleigh-Jeans tail where $F_\nu \propto \nu^2$, and at high frequencies, we have the Wien tail were $F_\nu \propto \nu^3 \exp(-h\nu/k_{\mathrm{B}}T)$. In the intermediate frequencies between these two regimes, we have the case where $F_\nu \propto \nu^{1/3}$. However, this intermediate regime is only noticeable when the outer radius of the disk is much larger than the inner radius. Because of the extreme viscosity in the accretion disk, typical disk temperatures are $\sim 10^7\,\mathrm{K}$, meaning the resulting spectral energy distribution resembles a blackbody curve peaking in the X-rays.

1.3 Globular clusters

Globular clusters (GCs) are large, spherical, gravitationally bound clusters of stars that orbit the centres of their host galaxies. The stellar densities at the cores of GCs can reach values of $10^6\,\mathrm{stars\,pc^{-3}}$ (Harris, 1996), which is orders of magnitude greater than typical values in the Galactic field. The size of a GC can be described by three parameters: the core radius (r_c), the half-light radius (r_h), and the tidal radius (r_t). For this thesis, the first two measurements of physical size are the most important. The core radius is the radius at which the surface
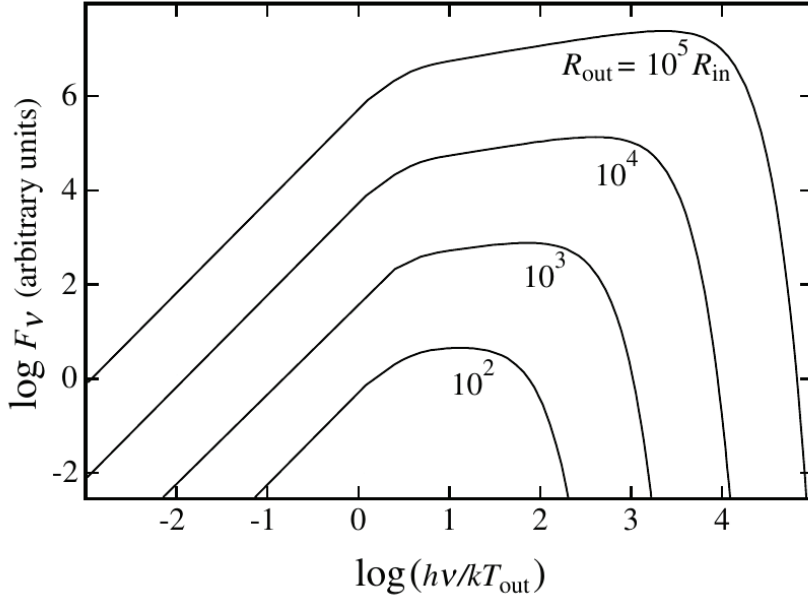
Figure 1.9: The emitted spectrum of an accretion disk as a function of frequency. The different curves indicate the emitted flux for different outer accretion disk radii. Figure from Frank et al. (2002).

brightness of the cluster reduces by a factor of a half, and the half-light radius is the radius within which half of the cluster light is contained. The tidal radius can be considered as the edge of the cluster, where the gravitational pull from the rest of the galaxy is greater than the gravitational pull of the cluster.

1.3.1 Globular clusters in the Milky Way

The Milky Way contains 158 known GCs (Baumgardt et al., 2019). The GCs that are relevant to this thesis are discussed below, and their relative positions in the sky are shown in Figure 1.10.

1.3.1.1 NGC 6652

NGC 6652 is a GC located in the Sagittarius constellation just south of the celestial equator. It is located at a distance of 9.46 ± 0.14 kpc (Baumgardt & Vasiliev, 2021), and has a mass of $5.2 \times 10^4 M_\odot$. X-ray observations of the cluster
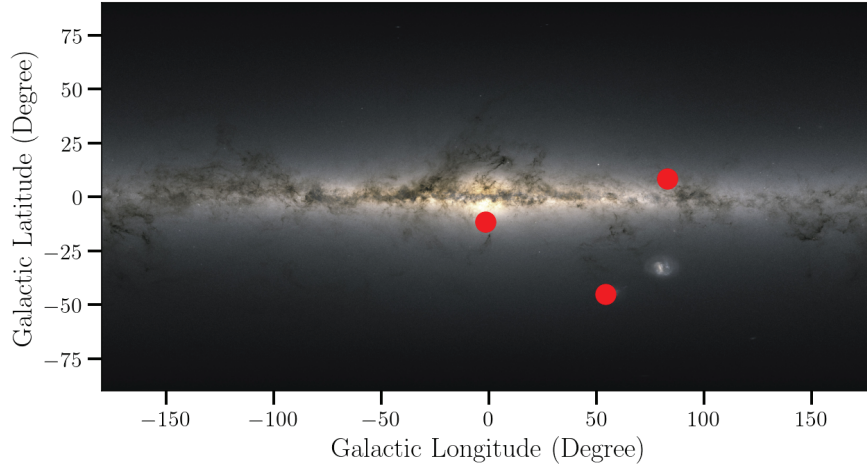
Figure 1.10: The locations of NGC 6652, NGC 3201, and 47 Tuc in the Milky Way. NGC 6652 and NGC 3201 are located close to the Galactic plane while 47 Tuc is located near the Small Magellanic Cloud.

have identified one bright LMXB in addition to several other XRBs with lower X-ray luminosities (Heinke et al., 2001; Stacey et al., 2012).

1.3.1.2   NGC 3201

NGC 3201 is a GC located just above the Galactic plane in the constellation of Vela. The cluster is located at a distance of 4.74 ± 0.04 kpc (Baumgardt & Vasiliev, 2021) and has a mass of $1.41 \times 10^5 M_\odot$, lighter than that of 47 Tuc. NGC 3201 has a large radial velocity of > 400 km s^{-1}, and has a high binary fraction in its core (0.128 ± 0.008, Milone et al., 2012).

NGC 3201 stands out as the first Galactic GC for which stellar-mass BHs have been confidently identified. Two BHs and one candidate have been identified through radial velocity studies using the Multi Unit Spectroscopic Explorer (MUSE) instrument on the Very Large Telescope (Giesers et al., 2018, 2019). These recent discoveries have had huge implications for the study of stellar populations within GCs, as it indicated that BHs were not ejected from the cluster as once thought and can survive in the core (see Section 1.3.3). All three of these systems are detached binaries, meaning there is very little to no mass transfer occurring.

23

Figure 1.11: An image of the globular cluster 47 Tucanae taken using the Hubble Space Telescope. Image credit: J. Mack and G. Piotto.

1.3.1.3 47 Tucanae

47 Tucanae (47 Tuc, NGC 104) is the second-brightest GC to the naked eye. 47 Tuc is located at a distance of 4.52 ± 0.03 kpc (Baumgardt et al., 2019) and has a mass of $8.95 \times 10^5 M_\odot$. The extinction of 47 Tuc is very low ($E(B-V) = 0.04 \pm 0.02$, Salaris et al., 2007), and the declination of the cluster ($\sim -72°$) means that it is located far from the Galactic plane. An image of 47 Tuc taken with the Hubble Space Telescope is shown in Figure 1.11.

Due to the location of 47 Tuc, it is an easy target for multiwavelength studies. The cluster has been observed extensively in both X-rays by the *Chandra* X-ray Telescope (> 1 Ms total exposure), and from UV to IR wavelengths by the Hubble Space Telescope (> 2 Ms total exposure). Over 300 X-ray sources have been identified in 47 Tuc (Heinke et al., 2005; Bhattacharya et al., 2017). These X-ray sources are split across many source classes including LMXBs, MSPs, accreting WDs, and chromospherically active binaries. 47 Tuc also contains a candidate BH in an ultracompact binary system, the X-ray source 47 Tuc X9, that may be the first ultracompact BHXB identified in the Milky Way (Miller-Jones et al., 2015; Bahramian et al., 2017).

47 Tuc also contains the second largest population of pulsars in a GC after Terzan 5. 47 Tuc currently contains 29 known pulsars, including 19 in binary systems and 23 with phase-coherent timing solutions. Nine new pulsars have been discovered since 2003, including the recent discoveries of 47 Tuc ac and 47 Tuc ad using the MeerKAT radio telescope (Ridolfi et al., 2021). Modelling of the cluster indicates that 47 Tuc may contain around 50 MSPs (Ye et al., 2021) hinting at a sizeable undiscovered population, indicating the potential for a large number of these sources to be detected in the upcoming MeerKAT GC pulsar survey.

1.3.2 X-ray binaries in globular clusters

The large stellar densities in GCs make them factories for producing binary systems. GCs have an overabundance of XRBs by approximately two orders of magnitude per unit mass than the Galactic field (Clark, 1975). The formation channels available to XRBs in GCs are what drives this overabundance. In a GC, XRBs will primarily form through dynamical channels, rather than through primordial binary evolution. These dynamical channels include collisions between compact objects and giant stars (Sutantyo, 1975), tidal captures (Fabian et al., 1975), and exchange interactions into primordial binary systems (Hills, 1976).

The first X-ray sources detected in GCs were variable X-ray sources, thought to be XRBs (Clark, 1975), detected using *OSO-7* and *Uhuru*. This spurred X-ray campaigns of GCs, which discovered a large number of faint X-ray sources ($L_X < 10^{35} \, \mathrm{erg \, s^{-1}}$) in 71 GCs using the *Einstein* satellite (Hertz & Grindlay, 1983). A further survey of 80 GCs was conducted by Verbunt et al. (1995) as part of the *ROSAT* All Sky Survey. To explain the number of XRBs detected in GCs, the encounter rate of a GC was formulated by Verbunt & Hut (1987). The encounter rate of a GC is parameterised by the cluster density and the inverse velocity dispersion of the cluster ($\Gamma \propto \int \rho^2/\sigma$), as higher cluster densities will lead to more encounters, while stars that have a higher velocity are less likely to

be trapped in a binary. Most modern X-ray surveys of GCs (e.g., Grindlay et al., 2001; Heinke et al., 2003a,b, 2005, 2006; Guillot et al., 2009; Zhao et al., 2019; Bahramian et al., 2020) have been conducted using the *Chandra* X-ray Telescope due to its angular resolution being sufficient to resolve different sources in the dense cluster cores.

The dynamical formation channels in clusters result in a large number of X-ray emitting binaries and sources being present in GCs. Various classes of accreting white dwarfs make up a large fraction of these X-ray emitting binaries in GCs (Grindlay et al., 2001; Pooley et al., 2002). 47 Tucanae has the largest cataclysmic variable (CV) population of any GC, with 43 identified CVs (Rivera Sandoval et al., 2018). The majority of sources below X-ray luminosities of $10^{31}\,\mathrm{erg\,s^{-1}}$ are active binaries (ABs); chromospherically active, tidally-locked binary stars that produce X-rays (Güdel, 2002). Most bright XRBs ($L_X > 10^{34}\,\mathrm{erg\,s^{-1}}$ in GCs have been identified as NSXBs (Bahramian et al., 2014). GCs also contain large populations of MSPs, with more than 150 MSPs detected in the Milky Way GC system[1]. The GCs Terzan 5 and 47 Tucanae have the largest known populations of pulsars in GCs. There are also a handful of candidate and confirmed tMSPs in GCs. The confirmed tMSP M28I resides in the cluster M28 (Papitto et al., 2013), and two candidate tMSPs have been identified in Terzan 5 and NGC 6652 (Bahramian et al., 2018b; Paduano et al., 2021).

Following on from the first X-ray surveys of GCs, the first radio surveys of GCs began to be conducted in 1975 using a variety of different radio facilities. These included the NRAO interferometer (Johnson, 1976; Johnson et al., 1977; Rood et al., 1978), the Arecibo 305-m telescope (Terzian & Conklin, 1977), and the Effelsberg radio telescope. These initial surveys were only sensitive to sources with a radio flux density $> 1\,\mathrm{mJy}$, and covered S to X bands in frequency (2-11 GHz). After the discovery of MSPs (Alpar et al., 1982), several timing surveys of GCs were conducted with the aim of detecting pulsars at lower frequencies

---

[1] http://www.naic.edu/~pfreire/GCpsr.html

(Hamilton et al., 1985; Fruchter & Goss, 1990, 2000). It is now known that GCs host a large population of pulsars, with Bayesian estimates indicating a population of more than 2000 pulsars within the Galactic GC system (Turk & Lorimer, 2013). The most recent comprehensive radio continuum survey of several Galactic GCs is the MAVERIC (Milky-way ATCA VLA Exploration of Radio Sources in Clusters) Survey (Shishkovsky et al., 2020; Tudor et al., 2022), which is the first radio continuum survey to reach median noise levels $< 10\,\mu\mathrm{Jy\,beam^{-1}}$. This survey used the ATCA and the VLA to cover 50 Galactic GCs with a distance $< 9\,\mathrm{kpc}$ and a mass $> 10^5 M_\odot$.

1.3.3 Black holes in globular clusters

While many binary systems containing NSs and white dwarfs have been identified in GCs, the same cannot be said about BHs. GCs are expected to host a population of BHs due to their age, but this population has remained undetected until recently. These non-detections initially agreed with early theories about how BHs should interact in a GC environment. The BHs will be the heaviest objects in the cluster, and will sink to the centre of the cluster through mass segregation. A separate sub-cluster of BHs will then be formed due to the Spitzer mass instability (Spitzer, 1969), with this sub-cluster being dynamically decoupled from the rest of the cluster. This BH population will eventually be ejected from the cluster through mutual gravitational interactions. This was supported by early analytical estimates and simulations of BHs in GCs indicating that a very small or non-existent population would remain (Kulkarni et al., 1993; Sigurdsson & Hernquist, 1993; Heggie & Giersz, 2008).

New observational studies after the turn of the millennium began to cast doubt over this hypothesis. In 2007, Maccarone et al. (2007) identified a BHXB candidate within the galaxy NGC 4472, with several more extra-galactic BH candidates being identified in the years following (Shih et al., 2010; Brassington et al., 2010; Irwin et al., 2010; Barnard et al., 2011; Maccarone et al., 2011).

These sources were identified as ultra-luminous X-ray sources (ULXs) thought to be associated with stellar-mass BHs. In 2012, the first candidate BHs in Galactic GCs were identified, with the discovery of two candidates in the cluster M22 through radio continuum imaging (Strader et al., 2012a). Following this, four further BH candidates were discovered in various other clusters (Chomiuk et al., 2013; Miller-Jones et al., 2015; Shishkovsky et al., 2018; Zhao et al., 2020b). Further advancements in the simulation of GCs began to suggest that only the most massive BHs will sink to the centre of the cluster, leaving the remaining light BHs well mixed within the surrounding medium (Mackey et al., 2008; Moody & Sigurdsson, 2009; Breen & Heggie, 2013; Morscher et al., 2013, 2015). This reduction in the ejection rate of BHs from the cluster also helps to heat the cluster through exchanges with stars.

The first dynamically-confirmed BH in a Galactic GC was identified in 2018, when a BH of mass 4.53 ± 0.21 $M_\odot$ was detected in the cluster NGC 3201 (Giesers et al., 2018). This was achieved through radial velocity studies with MUSE. Another two BHs with masses of 7.68 ± 0.50 $M_\odot$ and 4.4 ± 2.8 $M_\odot$ were also identified in NGC 3201 (Giesers et al., 2019). This indicates that a population of BHs can remain in GCs without being ejected. These BH systems are detached systems, meaning there is very little mass transfer from the companion star onto the compact object, resulting in little multi-wavelength emission (Paduano et al., 2022). Further modelling of GCs now suggests that a large population of BHs should be contained in GCs, with ~ 200 stellar-mass BHs predicted in the clusters NGC 3201 and 47 Tucanae (Kremer et al., 2018; Ye et al., 2021). While the BHs in NGC 3201 are detached and most likely not accreting, it is unknown if this extends to all BHs in other GCs. This raises challenges for the prospect of detecting these faintly accreting sources as they will most likely be very faint radio and/or X-ray sources, requiring long telescope integration times to produce a significant detection.

1.4 Intermediate-mass black holes

Intermediate-mass BHs (IMBHs) are BHs with a mass falling in the range of $10^2 M_\odot \lesssim M_{\mathrm{BH}} \lesssim 10^5 M_\odot$, and bridge the gap between stellar-mass BHs formed in the deaths of massive stars and supermassive BHs found at the centres of galaxies. Several candidate IMBHs have been reported previously in the literature, however very few of these candidates have stood up to robust scrutiny. The clearest detection of an IMBH to date is the gravitational wave event GW190521, where the merger of two BHs with masses of $85 M_\odot$ and $66 M_\odot$ resulted in the formation of a $142 M_\odot$ BH (Abbott et al., 2020). This section provides a brief overview of IMBH formation and IMBH searches, with a focus on GCs. A recent review by Greene et al. (2020) provides a more comprehensive overview of this topic.

1.4.1 IMBH formation

There are three main seeding models considered for the formation of IMBHs. These consist of the direct collapse of gas clouds, the collapse of Population III stars, and gravitational runaway events. The first two models are not relevant to star clusters and are generally limited to redshifts $z > 10$ due to the need for molecular hydrogen.

In star clusters, IMBHs are suspected to form through gravitational runaways. This method is believed to form BHs with masses $10^{3-4} M_\odot$, and the formation scenarios are split into the slow and fast formation models depending on the time taken for the IMBH to form in the cluster. The slow formation scenario (Miller & Hamilton, 2002) begins with a single massive BH ($M > 50 M_\odot$) that then grows through sequential mergers of the BHs that have mass segregated to the centre of the GC, resulting in an IMBH with mass of order $10^3 M_\odot$. This result was verified through further simulations by Gültekin et al. (2004). These simulations also indicated that reducing the mass of initial seed BH to $\sim 10 M_\odot$ would limit the growth of an IMBH to a source of mass $\sim 240 M_\odot$, with a low probability of this source remaining bound to the cluster. Heavier initial BHs are needed for the

eventual IMBH to remain bound to the cluster. Gültekin et al. (2006) showed in later simulations that including gravitational radiation in these simulations speeds up the formation of an eventual IMBH, and also increases the probability that the IMBH is retained in the cluster. The fast formation scenario involves the collisional runaway of massive stars, eventually leading to the formation of an IMBH (Portegies Zwart & McMillan, 2002).

Despite these gravitational runaway formation channels being available, there is a lack of theoretical support for the IMBH formation in GCs. With regards to the slow formation channel, the dynamical interactions between the initial sub-cluster of BHs can cause the IMBH seed to be ejected from the cluster. Holley-Bockelmann et al. (2008) shows that it is difficult to retain IMBHs with masses $\lesssim 10^3 M_\odot$ in this environment with several sequential mergers, as only a handful of GCs have sufficiently high densities and masses to be able to retain these BH merger products (Antonini et al., 2019). The fast formation scenario is suspected to be limited to clusters with short initial relaxation times, excluding most GCs (Portegies Zwart & McMillan, 2002). Nonetheless, it is suspected that these merger events will eventually produce an IMBH that is detectable with the current generation of gravitational wave observatories (Gültekin et al., 2004, 2006; Fragione & Bromberg, 2019; Fragione & Silk, 2020; Fragione et al., 2022). In particular, Fragione et al. (2022) find that the merger rate of the events that produce IMBHs to be in the range of $0.01 - 10 \; \mathrm{Gpc}^{-3} \, \mathrm{yr}^{-1}$, with the current gravitational wave observatories such as LISA and LIGO able to detect a few merger events a year of IMBHs with masses $\lesssim 1000 M_\odot$.

1.4.2   IMBHs in GCs

A current open question in the field is whether IMBHs exist in GCs. Despite there being formation channels available in GCs, there is yet to be a robust detection of an IMBH in a cluster. Two methods that have been used to search for IMBH candidates are the modelling of pulsars in a cluster, and the measure-

ment and modelling of the stellar dynamics of the cluster, in particular velocity dispersion and stellar proper motions. Through pulsar timing, the most robust IMBH candidate in a GC has been identified in NGC 6624, where 25 years of timing observations of the pulsar PSR B1820-30A indicated that the source is most likely orbiting a central IMBH with a mass $> 7500 M_\odot$ (Perera et al., 2017). Modelling of pulsar accelerations has also been used to claim the existence of a $\sim 2300 M_\odot$ BH in 47 Tuc (Kızıltan et al., 2017), however this claim was later shown to be incorrect (Freire et al., 2017; Abbate et al., 2018).

The method of modelling the stellar dynamics of a GC has been applied to several GCs to test for a central IMBH. An IMBH has been claimed in ω-Centauri through the modelling of the radial velocity dispersion and the surface brightness profile of the cluster (Noyola et al., 2010). However, the proper motions of the stars in the cluster do not show the velocity dispersion signature needed to contain an IMBH (van der Marel & Anderson, 2010). A similar situation is seen for NGC 6388 (Lützgendorf et al., 2011, 2015; Lanzoni et al., 2013), and M54 at the centre of the Sagittarius dwarf galaxy (Ibata et al., 2009; Baumgardt, 2017).

Another method of searching for IMBHs in GCs is to use radio and X-ray observations to search for evidence of accretion from the central BH. This method is the most relevant search method for this thesis. The intracluster medium in a GC is expected to consist of ionised gas emitted from the winds of the giant stars in the cluster. This gas has been detected successfully in the cluster 47 Tuc through the timing of the pulsars in the cluster, and has a number density of $n \sim 0.2 \mathrm{cm}^{-3}$ (Abbate et al., 2018). If an IMBH is present at the cluster centre, it will accrete a portion of the gas that falls within its sphere of influence. This will result in the creation of observable radio emission in the form of an outflowing faint, flat-spectrum radio jet, and X-ray emission from the accretion flow (Maccarone, 2004). These radio jets will obey the fundamental plane of BH activity (Merloni et al., 2003; Falcke et al., 2004; Plotkin et al., 2012; Gültekin et al., 2019), which links a BH's radio luminosity L_R, X-ray luminosity L_X, and

mass M. The fundamental plane, as parameterised in Plotkin et al. (2012), is:

$$\log L_X = (1.45 \pm 0.04) \log L_R - (0.88 \pm 0.06) \log M - 6.07 \pm 1.10. \qquad (1.13)$$

Due to this relation, the radio emission from an IMBH is expected to be brighter than that of a stellar-mass BH, for a given X-ray luminosity.

This search methodology has been applied to several GCs to place mass limits on the presence of a central IMBH (e.g., Maccarone, 2005; Maccarone & Servillat, 2008; Cseh et al., 2010; Lu & Kong, 2011; Strader et al., 2012b; Tremou et al., 2018), and interpreting these limits requires making assumptions as to the accretion rate and radiative efficiency of any accretion (Pellegrini, 2005). The most recent of these studies is Tremou et al. (2018), which used the MAVERIC survey to place mass constraints on a central IMBH in 50 Galactic GCs. These clusters were observed with the ATCA and the VLA to produce deep radio images, before the fundamental plane methodology was used to estimate BH mass upper limits from the radio image noise. This study showed no evidence of accretion from a central IMBH in the clusters in the sample, further suggesting that IMBHs with masses $> 10^3 M_\odot$ are uncommon or do not exist in GCs. The mathematical derivation of the fundamental plane methodology is detailed in Appendix A for completeness.

1.5 Structure of this thesis

This thesis consists of seven chapters and three appendices, and details the study of exotic BHs and NSs in binary systems in GCs. I exploit the existing MAVERIC survey and continue to build upon its foundation by conducting targeted follow-up studies of several interesting binaries in various clusters. This work means I am able to explore the properties of unique NSs in GCs, and also search for very faintly accreting BHs.

The questions motivating this thesis that I aim to answer are:

- Do IMBHs exist in GCs?

- What population of exotic XRBs exist in GCs?

- How does the population of tMSPs compare to that of normal pulsars, and how does accretion proceed in the presence of a magnetic field?

In the current chapter (Chapter 1), I introduce and motivate this thesis, and provide an overview of GCs and XRBs that is relevant to this thesis. In Chapter 2, I explain the different telescopes and observing techniques used in this thesis. Specifically, I provide a brief overview of radio interferometry, X-ray astronomy, and optical astronomy, as these are the key observational techniques used to carry out the work presented in this. The results of this thesis are detailed in Chapters 3-6. Chapter 3 presents simultaneous multiwavelength observations of the XRB NGC 6652B to explore the relationship between the source's radio and X-ray emission, identifying the source as a new tMSP candidate. This chapter is adapted from a published paper. Chapter 4 presents the first radio and X-ray limits on the detached BHs in NGC 3201, which represent the first confirmed BHs identified in a GC. These limits show that these BHs are either not accreting or are accreting extremely inefficiently, which has implications for the detectability of similar detached systems with the current generation of radio and X-ray telescopes. This chapter is adapted from a published paper. Next, I provide an overview of the deepest radio survey ever conducted of a GC. Chapter 5 presents the discovery of the faint radio source ATCA J002405.702-720452.361, which was detected at the centre of the GC 47 Tuc through ultra-deep ATCA imaging. The survey is briefly described in this chapter, and ATCA J002405.702-720452.361 is presented as either an undiscovered pulsar or a candidate IMBH at the cluster centre. Chapter 6 provides a more comprehensive overview of this radio survey of 47 Tuc, and details the radio sources detected within the half-light radius of the cluster. The population of detected MSPs in the cluster is explored, and the source 47 Tuc W41 is presented as a new candidate redback

pulsar. Finally, Chapter 7 summarises this thesis, discusses the implications of the results presented, and provides pathways for future work, before ending with the conclusions of this thesis.

CHAPTER 2

TELESCOPES AND TECHNIQUES

2.1 Radio astronomy

Photons of light can either behave as waves or particles. For sufficiently high energies (frequencies greater than those of optical light), photons produce an electrical current via the photoelectric effect in charge-coupled devices (CCDs), usually made out of silicon. This forms the basis of modern optical and X-ray astronomy, where the incident photons are collected using a mirror or collimator and are focused onto a CCD to produce an electrical current. Other detector technologies also exist, such as pair-conversion, scintillation, and solid state detectors. However, radio waves do not have sufficient energies to cause the photoelectric effect, meaning that CCDs cannot be used. Instead, radio telescopes ranging from small conducting wires to large parabolic dishes are used to detect radio waves.

The atmosphere allows the transmission of radio waves with red/blue-shifted wavelengths between $\sim 1\,\mathrm{cm}$ and $\sim 10\,\mathrm{m}$. Therefore, radio telescopes that detect cosmic sources that emit radiation in this wavelength band can be built on Earth. Most radio telescopes consist of large, parabolic dishes with large collecting areas

that focus the incident radio emission onto a detector, the receiver, however radio telescopes can consist of other types of collecting elements. For example, the Murchison Widefield Array uses dual-polarisation dipole elements as the collector. The resolution of a telescope θ is governed by the equation

$$\theta = \frac{\lambda}{D}, \tag{2.1}$$

where λ is the wavelength of the incident radiation, and D is the diameter of the collector. A consequence of this is that large collectors are needed to provide usable resolutions at radio wavelengths. Building larger collectors has several drawbacks including expense, various engineering challenges, and limitations on where the telescope can be built and how they operate. To overcome this issue, techniques called aperture synthesis and interferometry are used, which involve combining several smaller collectors to effectively produce one single large telescope. This changes the resolution of the interferometer to

$$\theta = \frac{\lambda}{B_{max}}, \tag{2.2}$$

where B_{max} is the length of the longest baseline, or the distance between the two furthest-spaced collectors. By spreading these smaller collectors over large distances, resolutions can be reached that would be impractical to achieve by constructing a single large telescope.

2.1.1 Radio interferometry

Fundamentally, radio telescopes are dipole antennas that measure the voltages induced by the radio waves emitted by astrophysical sources. This subsection provides an overview of some basic theory for how radio interferometers work, drawing upon the works of Taylor et al. (1999), Thompson et al. (2017), and the Essential Radio Astronomy lectures provided by the National Radio Astronomy

Observatory[1].

2.1.1.1 Correlator output and complex visibilities

The simplest radio interferometer consists of two collecting elements separated by a baseline $\mathbf{b}$. Radio plane waves incident on the interferometer will reach one element prior to reaching the second element, resulting in a geometric time delay between the two elements. The geometric time delay is $\tau_g = \mathbf{b} \cdot \mathbf{s}/c$, and is dependent on the baseline between the two elements and the vector $\mathbf{s}$ which is in the direction of the radio source. The received signals from the two elements can be expressed as $V_1(t) = v_1 \cos 2\pi\nu(t - \tau_g)$ for the first element and $V_2(t) = v_2 \cos 2\pi\nu t$, where ν is the observation frequency. The output from the correlator is then $r(\tau_g) = v_1 v_2 \cos 2\pi\nu\tau_g$, where $v_1 v_2$ represents the fringe amplitude which is proportional to the total power received from the interferometer.

Up until now, the output from the correlator has been expressed in terms of voltages detected by the interferometer elements. The correlator output can also be expressed in terms of the radio brightness (in units of $\mathrm{W\,m^{-2}\,Hz^{-1}\,sr^{-1}}$) integrated over the total sky. The solid angle element $d\Omega$ receives a total power $A(\mathbf{s})I(\mathbf{s})\Delta\nu d\Omega$. This allows the total correlator output to be given as:

$$r = \Delta\nu \int_S A(\mathbf{s})I(\mathbf{s}) \cos \frac{2\pi\nu\mathbf{b} \cdot \mathbf{s}}{c} d\Omega, \tag{2.3}$$

where $\Delta\nu$ is the frequency bandwidth, $A(\mathbf{s})$ is the collecting area of the interferometer in the $\mathbf{s}$ direction, and $I(\mathbf{s})$ is the radio brightness of the source in the same direction. Two assumptions are made in expressing the correlator output in this form. The first is that the radio source is in the far field, such that the incoming radio waves can be considered planar. The second is that the source is spatially incoherent.

When radio observations of a source are taken, a phase tracking centre is usually specified. This phase-centre is expressed as $\mathbf{s}_0$, allowing us to write $\mathbf{s} =$

---

[1]https://science.nrao.edu/opportunities/courses/era
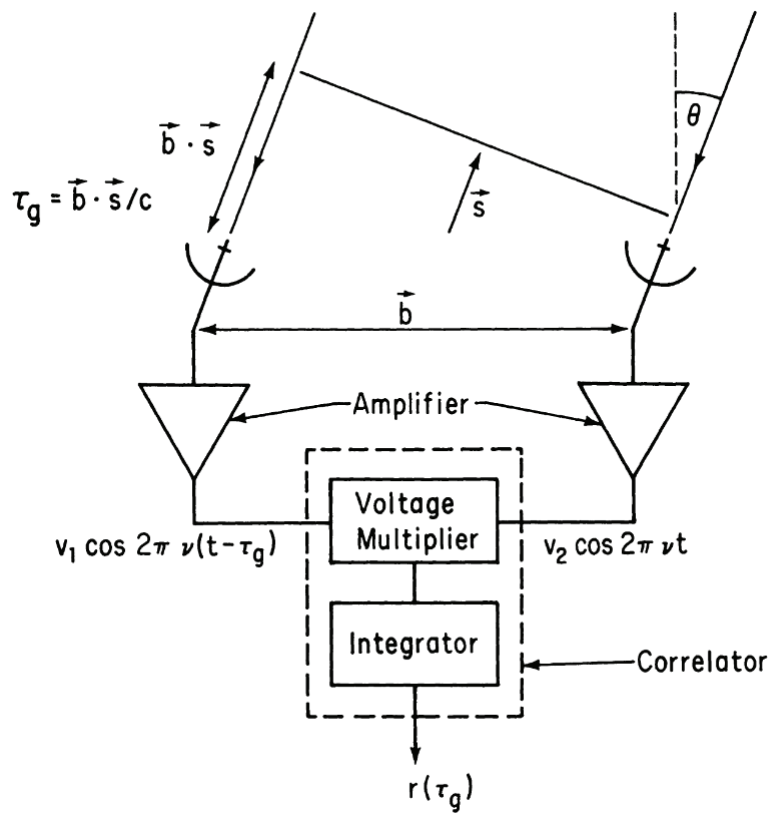
Figure 2.1: A schematic of a two element radio interferometer. The two radio dishes are separated by a baseline $\mathbf{b}$ and are pointed in the direction denoted by $\mathbf{s}$, where τ_g is the time delay between the signal reaching the two elements of the interferometer. $r(\tau_g)$ is the correlated output signal from the interferometer. Figure from Taylor et al. (1999).

$\mathbf{s}_0 + \sigma$ where σ is some offset. Equation 2.3 can then be rewritten in terms of the phase-centre to give:

$$
\begin{aligned}
r = {} & \Delta\nu \cos\left(\frac{2\pi\nu\mathbf{b}\cdot\mathbf{s}_0}{c}\right) \int_S A(\sigma)I(\sigma) \cos\frac{2\pi\nu\mathbf{b}\cdot\sigma}{c} d\Omega \\
& - \Delta\nu \sin\left(\frac{2\pi\nu\mathbf{b}\cdot\mathbf{s}_0}{c}\right) \int_S A(\sigma)I(\sigma) \sin\frac{2\pi\nu\mathbf{b}\cdot\sigma}{c} d\Omega
\end{aligned}
\tag{2.4}
$$

The complex visibility is a measurement of the coherence of a source, and the magnitude of the visibility has units of $\mathrm{W\,m^{-2}\,Hz^{-1}}$. The visibility is a Fourier transform, and is defined as:

$$
V \equiv |V|e^{i\phi_V} = \int_S \frac{A(\sigma)}{A_0} e^{-2\pi i\nu\mathbf{b}\cdot\sigma/c} d\Omega,
\tag{2.5}
$$

where in this case the term $A(\sigma)/A_0$ is the normalised antenna reception pattern as the antennas track the source, meaning that the brightness distribution of the source changes over time. Substituting the complex visibility into Equation 2.4 gives the following relation for the correlator output:

$$
r = A_0\Delta\nu|V| \cos\left(\frac{2\pi\nu\mathbf{b}\cdot\mathbf{s_0}}{c} - \phi_V\right).
\tag{2.6}
$$

Equation 2.6 contains a cosine term with an amplitude and a phase which is measured by the radio interferometer and then used to determine the amplitude and phase of the complex visibility of this baseline pair. The complex visibility is then the Fourier transform of the sky brightness, so by inverting Equation 2.5 information about the observed sky brightness can be derived. In order to improve this inverse Fourier transform, observing the source over a large range of baselines is required, meaning more collecting elements are required in the interferometer.

2.1.1.2 The (u, v, w) plane for complex visibilities

In order to practically apply the equations for the correlator output (Equation 2.3) and the complex visibility (Equation 2.5) and actually take radio observations of

the sky, a coordinate system for imaging needs to be introduced. The coordinate system used in radio astronomy is called the (u, v, w) plane, shown in Figure 2.2, which are defined with respect to the phase-centre. This coordinate system is derived such that the vector u points eastward, the vector v points northward, and the vector w is pointed towards the observed source, with all vectors measured in multiples of the central observing wavelength. The vectors u and v correspond to the l and m positions on the sky. These are direction cosines measured with respect to the (u, v) axis. The complex visibility written in terms of the (u, v, w) and the (l, m) plane is:

$$V(u, v, w) = \int_{\infty}^{\infty} \int_{\infty}^{\infty} \frac{A(l, m)}{A_0} I(l, m) e^{-2\pi i \left[ul + vm + w(\sqrt{1 - l^2 - m^2} - 1) \right]} \frac{dl\, dm}{\sqrt{1 - l^2 - m^2}}. \tag{2.7}$$

This equation can then be reduced to a 2D Fourier transform, which is more easily invertible, under the assumptions that the baselines are coplanar and that this relation is applied to a small area of sky. This inverted form is:

$$\frac{A(l, m) I(l, m)}{A_0} = \int_{\infty}^{\infty} \int_{\infty}^{\infty} V(u, v) e^{2\pi i (ul + vm)} du\, dv. \tag{2.8}$$

Each baseline of an interferometer corresponds to two points on the 2D (u, v) plane: the point (u, v) and its Hermitian inverse $(-u, -v)$. Thus, having an interferometer with more baseline pairs allows for more complete sampling of the (u, v) plane. Further sampling of the (u, v) plane can be achieved through a technique called Earth-rotation aperture synthesis. The rotation of the Earth causes the projection of the baseline vector on the (u, v) plane to move, eventually tracing out an ellipse the size of which is dependent on the declination of the source. Depending on the construction of the interferometer, full coverage of the (u, v) plane can be achieved in a number of hours. For example, east-west linear arrays, such as the Australia Telescope Compact Array, can trace out a full ellipse on the (u, v) plane in a single $12\,\mathrm{hr}$ observation. Additionally, since points on the (u, v) plane are measured in wavelengths, having a non-zero bandwidth
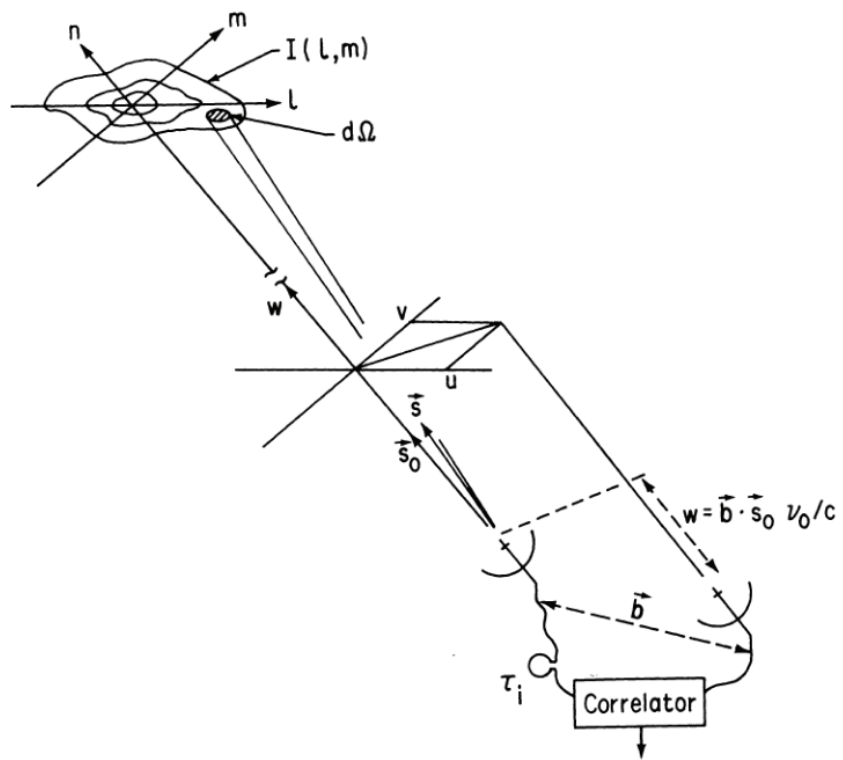
Figure 2.2: The (u, v, w) plane used in radio astronomy. Figure from Taylor et al. (1999).

Figure 2.3: An image of the Australia Telescope Compact Array showing five out of the six dishes. Image credit: John Masterson, CSIRO.

also increases the (u, v) plane coverage as each frequency channel for each baseline falls along the same angle in the (u, v) plane, but with a different magnitude.

2.1.2 Australia Telescope Compact Array

The Australia Telescope Compact Array (ATCA) is a six dish radio interferometer located in Narrabri, Australia, at an elevation of 237 m. An image of five of the dishes is shown in Figure 2.3. Each dish has a diameter of 22 m, and five of the dishes are located along a 3 km long east-west track, enabling the configuration of the telescope to be changed. The sixth dish is located 3 km west of the main track, resulting in a longest baseline of 6 km. The array can conduct observations ranging from 1.1 GHz to 105 GHz (L-band to W-band).

The array has a standard set of 17 configurations in which observations can be conducted, with the standard configurations having maximum baselines of 750 m, 1.5 km, and 6 km, in addition to several more compact configurations made with the northern spur with maximum baselines < 750 m. The configuration chosen for

observations depends on the science goal, with the extended 6 km configuration typically used for observations that require high angular resolution. Given that the array is an east-west linear interferometer, full (u, v) plane coverage can be achieved in one 12 hr observation. The latitude of the telescope site $(-32°)$ means that the array is best suited for observing objects in the southern sky. Full (u, v) plane coverage is not possible for sources north of Dec $-24°$, and sources north of Dec $48°$ cannot be observed with the array.

2.1.3 Very Large Array

The Karl G. Jansky Very Large Array (VLA) is a large radio interferometer located in New Mexico, USA. The telescope is located on the plains of San Agustin at an elevation of 2124 m. The interferometer consists of 28 dishes with a diameter of 25 m that are capable continuous frequency coverage from 1 GHz to 50 GHz. An image of the VLA in its C configuration highlighting a subset of the dishes is shown in Figure 2.4.

The dishes are arranged in a 'Y' shape, with three arms containing nine dishes each, with the dishes located on rails allowing for the telescope to be reconfigured. There are four standard configurations for the VLA. The most compact configuration is D configuration, where the array has a maximum baseline of ~ 1 km. The most extended configuration is A configuration, which has a maximum baseline length of 36.4 km. The ability to reconfigure the array between configurations with vastly different baseline lengths allows the resolution of the telescope to range between 0.2 arcsec to 0.04 arcsec. Given the shape of the array is approximately triangular, full (u, v) coverage can be obtained in about 8 hr.

Figure 2.4: An image of the Very Large Array showing a subset of the dishes in the C configuration, with a foreground radio astronomer producing radio interference through the use of a mobile phone on the site. Image credit: Alessandro Paduano, Lilia Tremou.

2.2 Calibration and imaging of radio data

2.2.1 The calibration process

In order to produce images from observed radio data, there are several calibration and flagging steps that must first be performed. It is important to identify the data that have been contaminated and are of a poorer quality when compared to the rest of an observation. These contaminated data can be due to a multitude of factors including radio frequency interference (RFI), poor weather such as heavy rain or lightning, or issues with the radio telescope itself. The removal of these contaminated data is known as flagging, and it is an essential step to ensure that the calibration solutions derived during the reduction process are accurate.

The overall aim of the calibration and data reduction process is to turn the raw radio data from the telescope into a fully calibrated dataset that can then be imaged. More fundamentally, it involves solving for the amplitudes and phases of the complex visibilities that are measured. The main calibrations that need to be performed on radio data are flux density, bandpass, amplitude, phase, and polarisation calibration. Usually at the beginning or end of an observation, a flux density and bandpass calibrator will be observed to help set the absolute flux density scale and the bandpass response of the telescope, which is the response of the instrument at different frequencies. A single, unresolved, sufficiently bright source with a stable and well-defined flux density and spectral behaviour is usually used for both flux density and bandpass calibration. For example, in the case of observations involving the ATCA, the source B1934-638 is used for this purpose as it meets all the required criteria. Resolved sources can be used if the source is suitably well modelled. Unlike the flux density and bandpass calibrator, an amplitude and phase calibrator must be located close to the source of interest and must be observed frequently over the course of the observation. This calibrator, also known as the complex gain calibrator, is used to solve for the antenna-based complex amplitude and phase gains, allowing the true visibilities to be

calculated from the measured visibilities. The complex amplitude and phase gains are solved on individual scans of the complex gain calibrator for each antenna, and are then interpolated to the time of the observation of the target source. This repeated observing ensures that the amplitude and phase calibrator is observed on timescales shorter than the variations in the atmosphere. Polarisation calibration is needed if one wishes to explore and image polarisations beyond Stokes I, such as investigating the circularly polarised (Stokes V) properties of a source.

2.2.2 The imaging process

The observed complex visibilities are the Fourier transform of the sky brightness, so by inverting this relation a radio image of the sky can be obtained. However, the (u, v) plane is undersampled given the finite number of baselines. This incomplete sampling of the (u, v) plane results in a point spread function that is the Fourier transform of the sampling function. This means that the Fourier transform of the observed complex visibilities from a radio telescope is actually a convolution between the true image and the array point spread function, also called the dirty beam. To recover the true image of the sky it needs to be deconvolved from the dirty beam.

The most common process used for deconvolution is the CLEAN algorithm, first developed by Högbom (1974). The CLEAN algorithm works by representing a radio source by a number of point sources, and interating to find the positions and flux densities of all point sources in an image. The CLEAN algorithm first computes the dirty image and the dirty beam before identifying and subtracting the brightest intensity point in the image, in addition to also subtracting the point spread function of this bright source. A delta function at the position of the subtracted component is stored, with the flux density of what was subtracted. Only a small fraction is subtracted at a time in order to avoid oversubtraction. This step repeats until all of the significant sources have been removed from the dirty image. The stopping threshold for identifying and subtracting sources is usually

set as some multiple of the RMS noise of the image in order to prevent noise spikes from incorrectly being identified as sources. The image that is left over after all the radio sources have been identified and subtracted is called the residual image. Following this, all the stored delta functions of the removed sources are convolved with an idealised point spread function (typically a Gaussian fit to the main lobe of the dirty beam) called the clean beam, before the residuals are added to this clean image to produce the final image.

One other important consideration in the imaging of radio data is the weighting applied to individual points in the (u, v) plane. There are two main weighting options called natural and uniform weighting. Natural weighting treats all points on the (u, v) plane as equal, and typically has the effect of up-weighting the data from shorter baselines given there are more shorter baselines than long ones. Natural weighting is best used for imaging faint radio sources as it gives the best signal-to-noise for the image. Uniform weighting is where all points on the (u, v) plane are adjusted by the parameter $1/N_S$, where N_S is the number of points within a set region of the (u, v) plane. Uniform weighting provides the best resolution for a radio image as this weighting scheme typically upweights the longer baselines. There also exists a third weighting scheme called Briggs weighting (Briggs, 1995), which allows one to dial between natural and uniform weighting by using a robustness parameter where $-2 \leq R \leq 2$. A robustness of 2 corresponds to natural weighting and a robustness of -2 corresponds to uniform weighting. A robustness of 0 provides a good compromise between the two weighting schemes.

2.3   X-ray astronomy

Unlike radio photons, X-ray photons have sufficient energy for CCDs, or other detectors such as solid state detectors, to be used. Given that the Earth's atmosphere is opaque to X-rays, X-ray observatories are satellites placed in orbit. Some examples of X-ray satellites are the *Chandra* X-ray Observatory, *NuSTAR*,
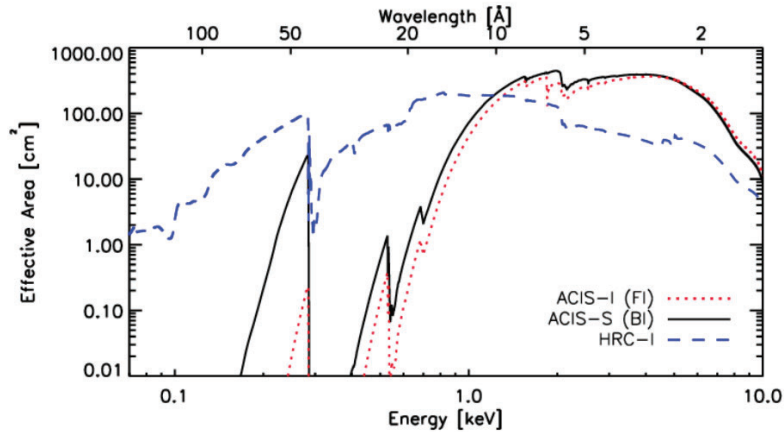
Figure 2.5: The effective area of the different science instruments on the *Chandra* X-ray Observatory plotted over the energy range 0.1-10 keV. Large variation in the effective area is seen over the plotted energy range. Figure from The *Chandra* Proposers' Observatory Guide Version 24.0.

the *INTEGRAL* satellite, the *Swift* X-ray Telescope, and the *XMM-Newton* observatory, which cover the range of low to high energy X-rays. Focusing X-ray telescopes, such as *Chandra*, *NuSTAR*, *Swift*/XRT, and *XMM-Newton*, use a complex system of cylindrical mirrors to focus incident photons onto the detector for imaging and spectroscopy.

The effective area (in units cm^2) of a X-ray telescope is the product of the geometric area of the telescope and the X-ray reflectance, which is a function of energy. There are numerous effects that impact X-ray telescopes resulting in the total geometric collecting area of the telescope being reduced to a smaller effective area, such as reflectance where the incident X-rays are reflected from the surface, and vignetting where fewer incident photons reach the focal plane due to an increase in off-axis angle. These effects must be accounted for when calculating the effective area of the telescope. Figure 2.5 shows the effective area for the two science instruments on *Chandra* over the energy range 0.1-10 keV. As can be seen, the effective area varies greatly over the plotted energy range.

2.3.1 *Chandra* X-ray Observatory

The *Chandra* X-ray Observatory is a space-based X-ray observatory successfully launched in 1999. It is one of NASA's large strategic science missions, or Flagship-class missions. *Chandra* is located in a highly elliptical, varying geocentric orbit, allowing for good observing efficiency due to spending the majority of its orbit above the Earth's radiation belts. The satellite has an apogee altitude of 1.4×10^5 km and a perigee altitude of 6×10^3 km, and currently has an orbital period of 63.5 hours[2].

Figure 2.6 contains a sketch of *Chandra* with various modules and subsystems highlighted. The satellite is composed of a spacecraft and a science instrument payload, where the spacecraft is responsible for power, communications, and orbital control. The satellite is powered by two three-panel solar arrays. The science instrument payload contains the High Resolution Mirror Assembly (HRMA); two focal plane science instruments consisting of the Advanced CCD Imaging Spectrometer (ACIS) and the High Resolution Camera (HRC); and the objective transmission gratings consisting of the High Energy Transmission Grating (HETG) and the Low Energy Transmission Grating (LETG). These instruments are briefly touched on below, with a more in-depth description of the ACIS instrument as it is the main X-ray instrument used in this thesis.

The HRMA is composed of four paraboloid-hyperboloid mirror pairs with a focal length of 10 m, and the mirror diameters range from 0.65 to 1.23 m. The unobstructed aperture of the HRMA is 1145 cm^2, but the effective area depends on the energy of the incident X-rays and ranges from 800 cm^2 at 0.25 keV to 100 cm^2 at 8.0 keV. The two focal plane instruments are the ACIS and the HRC, each having an -I and -S components. The ACIS is capable of capturing images and spectra, and the HRC is a microchannel plate instrument with high time resolution (16 µs). The layout of these two focal plane instruments is shown Figure 2.7.

---

[2]https://cxc.cfa.harvard.edu/proposer/POG/html/index.html
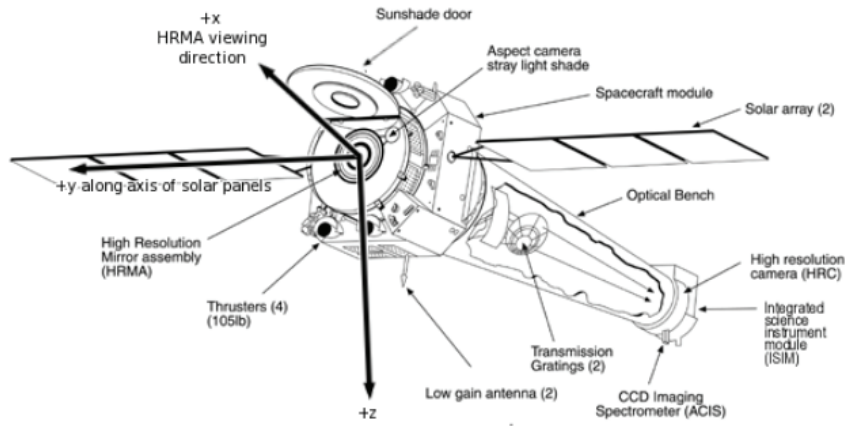
Figure 2.6: The *Chandra* X-ray Observatory, with several subsystems and modules highlighted. Figure from The *Chandra* Proposers' Observatory Guide Version 24.0.
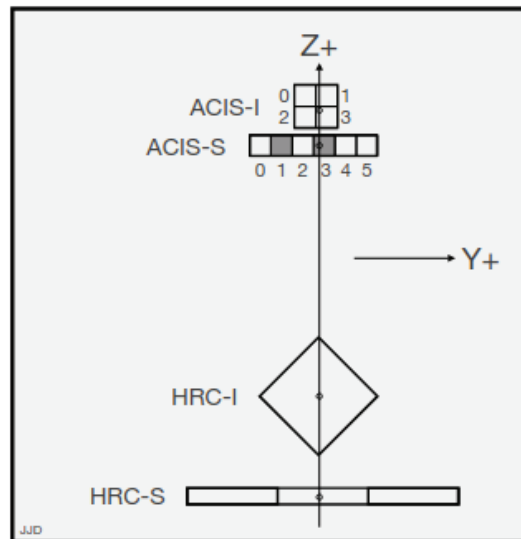
Figure 2.7: The arrangement of the ACIS and the HRC in the focal plane of *Chandra* . Figure from The *Chandra* Proposers' Observatory Guide Version 24.0.

The ACIS is able to capture images and spectra simultaneously, and can be used with the different gratings to increase the resolution of the spectra obtained. The ACIS is composed of 10 CCDs, each with 1024×1024 pixels. ACIS-I consists of four CCDs arranged in a 2×2 configuration and is primarily used for imaging. ACIS-S consists of six CCDs in a 1×6 configuration and is used for imaging or obtaining spectra. The configuration of the ACIS is shown in Figure 2.8. Additionally for ACIS-S, two of the CCDs (S1 and S3) are back-illuminated (BI) while the remaining four CCDs are front-illuminated (FI). The energy response of the BI CCDs extends to lower energies than can be reached for the FI chips. The general response of the ACIS has been changing since the launch of the observatory[3]. The BI CCD response at low-energies is degrading due to contaminant build-up, while the energy resolution of the FI CCDs has been compromised at certain positions on the CCDs due to radiation damage. When using the ACIS for on-axis imaging, the spatial resolution achievable is ~ 0.492 arcsec, which degrades as the off-axis angle increases.

When using ACIS to collect science observations, there are two choices of operating modes. In timed exposure (TE) mode, data are collected for a certain amount of time before being read out. The entire CCD can be used for this, or only a subarray of the CCD (a smaller region of the total CCD) can be used instead. Using a subarray has the advantage of reducing the read out times and reducing pileup. In continuous clocking (CC) mode, one dimension of spatial resolution is sacrificed to achieve integration times of 2.85 ms for a 1×1024 pixel image.

When observing with ACIS, *Chandra* will dither in a manner governed by a Lissajous curve with a peak-to-peak distance of 16 arcsec. This is to smooth out pixel variations, and to provide exposure in the gaps between CCDs. The effect of the dithering is corrected during calibration, however it is important to remember that this does occur during observations. Another important aspect

---

[3] https://cxc.cfa.harvard.edu/proposer/POG/html/chap1.html#tth_sEc1.10
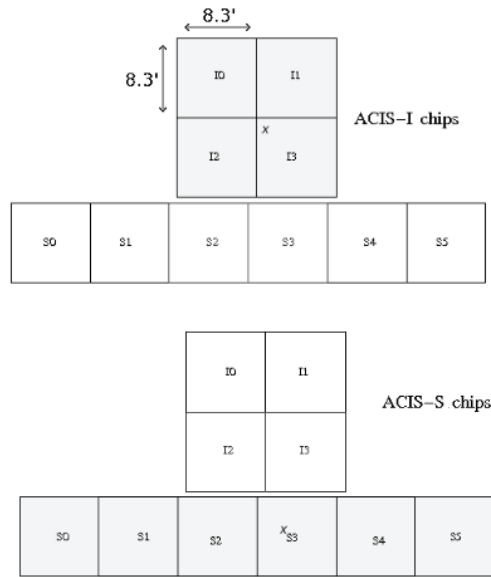
Figure 2.8: The ACIS instrument on *Chandra* . The top figure indicates the ACIS-I CCDs, while the bottom figure indicates the ACIS-S CCDs. The small cross in each figure indicates the aim point depending on which ACIS component is used. Figure from The *Chandra* Proposers' Observatory Guide Version 24.0.

to remember when observing is the effect of pileup. Pileup occurs at high count rates where two or more photons hit the detector before being read out, resulting in these photons being detected as one event. This results in the event rate being underestimated and the photon energy being overestimated. It is important to estimate if an observation will be affected by pileup, and there are several ways that pileup can be reduced or estimated. These include reducing the subarray frame time, using CC mode if 2D images are not required for the science being performed, and using one of the two transmission gratings.

2.3.2 ACIS data reduction

After data has been collected from the ACIS, primary and auxiliary data are provided in several files and directories for further analysis. Some of the files important for the analysis in this thesis are:

- Level 2 event file: A file containing the list of events from the observation,

and has been filtered so that only events within the good time intervals (GTIs) are included.

- Bad pixel file: A file containing a list of pixels on the CCDs that were considered bad during the observation.

- Sky field-of-view file: A file containing the regions describing the edges of each instrument chip.

- Orbit ephemeris file: A file containing the orbit ephemeris information for the observation which is needed if barycentric correction needs to be applied.

- Aspect solution file: A file containing the orientation information of the telescope. It is then combined with the detected position of the event on the chip to determine the celestial position of the event.

Prior to any analysis, data are always reprocessed and recalibrated. Reprocessing is done through the *Chandra* software CIAO (Fruscione et al., 2006) via tasks such as `chandra_repro`. This task performs various calibrations and corrections of the data such as updating the gain and aspect solution calibrations of the observation, verifying the accuracy of the source coordinates, and creating a new bad pixel file for the observation. Once the data are reprocessed and recalibrated, further analysis such as lightcurve extraction and spectral analysis can be performed. Extracting lightcurves involves using the `dmextract` task to bin the data to analyse the variability of the science target and the background field. For spectral analysis of a point source, the task `specextract` is used to extract source and background spectra of the science target. A source region, containing the events believed to be associated with the science target, and a background region, sampling the background event rate in a region close to the source, are defined within which spectra will be extracted. During this process, the ancillary response file (ARF) and redistribution matrix file (RMF) are created. These two files are important for describing the instrumental effects of the telescope. The

ARF contains the product of the effective area and the quantum efficiency (fraction of incident photons registered) in units of cm^2 counts photon^{-1}. The RMF is matrix multiplication that describes how the observed counts are spread by the resolution of the detector.

2.3.3 X-ray spectral modelling

As mentioned above, the ACIS can capture X-ray images and spectra simultaneously. This means that the X-ray spectrum of the source can be modelled. Generally, X-ray spectra need to have defined source and background regions, where the source region contains all the events expected to be associated with an X-ray source, and the background file contains an estimate of the background events near the source region. The ARF and RMF are used here to ensure that the instrumental effects are properly accounted for.

When the ACIS collects a spectrum of an X-ray source, it obtains the number of photon counts within discrete instrument channels. The observed spectrum is related to the true spectrum $f(I, E)$ of the source by the following equation:

$$C(I) = \int f(I, E) R(I, E) dE \tag{2.9}$$

where $C(I)$ is the number of photon counts, and $R(I, E)$ is the instrument response. Since this equation is not easily invertible, the observed spectrum is usually fit with a model spectrum to try and determine which spectral model best describes the data. Through this process, a fit statistic will be calculated which can be used to determine if the model is a good fit for the data, or if another model must be chosen. Usually, the observed data will have a contribution from the source and the background near the source. The background spectrum can either be accounted for in the model, or addressed separately.

In the regime where there are a large number of observed X-ray counts, the data can be assumed to be drawn from a Gaussian distribution and thus χ^2

statistics are used to fit the data, with a fit statistic of:

$$S^2 = \sum_{i=1}^{N} \frac{(y_i - m_i)^2}{\sigma_i^2} \tag{2.10}$$

where the sum is over the number of data points N, y_i are the observed data rates with errors σ_i, and m_i are the predicted data rates from the chosen spectral model. In this regime, the background spectrum is easily accounted for as the difference of two Gaussian distributions is another Gaussian distribution.

In the regime where we have few observed counts, Gaussian-based statistics such as χ^2 are inappropriate for modelling the data, and instead Poisson statistics should be used. Here, the fit statistic used is the C statistic as given by Cash (1979):

$$C = 2 \sum_{i=1}^{N} (tm_i) - S_i \ln(tm_i) + \ln(S_i!) \tag{2.11}$$

where S_i are the observed counts, t is the exposure time, and m_i are again the predicted count rates from the chosen spectral model. The C statistic will asymptote to S^2 in the Gaussian regime when the observed counts become large. However, accounting for the background spectrum is more difficult in this regime, as the difference between two Poisson distributions is not another Poisson distribution. To properly consider the background spectrum an extension of the C statistic called the W statistic[4] which is expressed as:

$$W/2 = \sum_{i=1}^{N} t_s m_i + (t_s + t_b) f_i - S_i \ln(t_s m_i + t_s f_i) - B_i \ln(t_b f_i) - S_i (1 - \ln S_i) - B_i (1 - \ln B_i),$$
$$\tag{2.12}$$

where t_s and t_b are the exposure times for the source and background spectra respectively, f_i is the background model, and B_i are the background data, with the other parameters the same as defined above.

There are a large number of X-ray spectral models that one can use to model X-ray data. The main software used in this thesis to perform X-ray spectral

---

[4]https://heasarc.gsfc.nasa.gov/xanadu/xspec/manual/node319.html

fitting is XSPEC (Arnaud, 1996). The three main models from XSPEC used in this thesis are `apec`, `bbodyrad`, and `pegpwrlw`, which are described briefly below.

apec The `apec` (Astrophysical Plasma Emission Code) model is that of an emission spectrum from diffuse ionised gas around a source. The parameters for this model are the plasma temperature in keV, the metal abundances of the plasma, the redshift z of the source, and the normalisation of the model which is expressed as:

$$\text{norm} = \frac{10^{-14}}{4\pi[D_A(1+z)]^2} \int n_e n_H dV, \tag{2.13}$$

where n_e and n_H are the electron and hydrogen densities respectively, and D_A is the angular diameter distance.

bbodyrad The `bbodyrad` model is that of a normalised blackbody radiation spectrum expressed as:

$$A(E) = \frac{K \times 1.0344 \times 10^{-3} E^2 dE}{\exp(E/kT) - 1}. \tag{2.14}$$

The important parameters in this model are the temperature of the blackbody kT in keV, and the normalisation K.

pegpwrlaw The `pegpwrlw` model is a power-law model with pegged normalisation between two energy values. The model is simply:

$$A(E) = KE^{-\Gamma}. \tag{2.15}$$

The important parameters in this model are the photon index Γ which indicates how hard or soft the spectrum is, the upper and lower energy values in keV, and the normalisation K. In this model, the normalisation is the flux of the source in units of $10^{-12}\,\text{erg}\,\text{cm}^{-2}\,\text{s}^{-1}$ between the upper and lower energy values given.

It is important to note that all three of these models are affected by interstellar

absorption of the X-ray emission by the interstellar medium. This absorption is accounted for with the model `tbabs` provided in XSPEC. This model is a Tuebingen-Boulder interstellar medium absorption model that calculates the cross section of X-ray absorption by summing together the different factors contributing to the absorption cross section. These include absorption due to the gas, grains, and molecules in the interstellar medium. Notably, the molecular contribution to the X-ray absorption cross section only considers molecular hydrogen, meaning the hydrogen column density to an X-ray emitting source needs to be known. Additionally, the gas-phase contributions to the absorption cross section depend on the abundances of different gases in the interstellar medium, which are based on the abundances reported in Wilms et al. (2000).

2.4   Optical astronomy

Like X-ray telescopes, modern optical telescopes use CCDs for imaging. A series of mirrors are used to focus light from the source of interest onto the CCD to produce an electrical signal. For example, the Hubble Space Telescope uses a 2.4 m mirror and the *Gemini* observatories each use a 8.1 m mirror. This section presents a brief overview of photometry and spectroscopy using optical telescopes, mainly drawing on Howell (2006).

Reducing data collected with CCDs requires taking a set of images that are used for calibration in addition to images of the main science object. The three sets of calibration frames collected are called the bias, dark, and flat field frames. Additionally, in the case of spectroscopy, arc exposures (e.g., observing Ne/Ar, He/Ar, Th/Ar lamps) are needed for wavelength calibration. The bias frame is a frame where the camera shutter is closed and the CCD is just read out. It is used to determine the noise level for each frame. Dark frames are images taken for the same exposure time as the science frames, but with the shutter closed. They are used to correct for dark current, or thermal noise, in the CCD and can also give information about any bad pixels. Flat field frames are taken with the

CCD exposed to light to produce an image with uniform illumination and a high signal-to-noise ratio. Flat field frames correct for the pixel-to-pixel variations in the response of the CCD. Finally, science (or object) frames are observations of the actual science target. The exposure length of these frames can vary significantly depending on the brightness of the object and purpose of the observation. To produce a calibrated science frame, the mean bias or dark frame is subtracted from the science frame, and the result is then divided by a bias subtracted flat field frame. Below, optical photometry and optical spectroscopy are discussed, which are the two main forms of optical astronomy considered in this thesis.

2.4.1 Photometry

Optical photometry is the process of measuring the flux from an object within the optical range of the electromagnetic spectrum. The apparent magnitude of a target star m_1 can be calculated by comparing it to the magnitude of a reference star m_2 using:

$$m_1 - m_2 = -2.5 \log \frac{F_1}{F_2}, \tag{2.16}$$

where F_1 and F_2 are the optical fluxes of the target and reference star respectively. This can be converted to the absolute magnitude of the star, giving its total intrinsic brightness, through:

$$m_{app} - m_{abs} = 5 \log \frac{d}{10}, \tag{2.17}$$

where d is the distance to the source in parsecs.

It is also important to consider the effect that interstellar extinction, or reddening, has on the observed optical light from a source. Extinction occurs when dust in the interstellar medium along the line-of-sight scatters the incident light, removing the photons at shorter wavelengths and having the effect of causing the observed light to appear redder than it should. The colour excess of an object is

defined as:

$$E_{B-V} = (B-V)_{\text{observed}} - (B-V)_{\text{intrinsic}} \qquad (2.18)$$

where $(B-V)_{\text{observed}}$ is the observed $B-V$ colour of the object and $(B-V)_{\text{intrinsic}}$ is the theoretical $B-V$ colour of the object. The colour excess of the object can then be related to the interstellar absorption A_V to give an indication as to how much the observed light has been affected by extinction, and to correct for this effect. Extinction can also be caused by the Earth's atmosphere which is important to account for when performing absolute photometry. This effect can be mitigated by observing the science target and reference object at similar airmasses, and the extinction due to the atmosphere can be corrected for by using known tables published for different observatories[5].

Two of the types of photometry that can be performed on a source are absolute photometry and differential photometry. Absolute photometry is where the true flux of the source is measured to be converted into a total luminosity. This is particularly important for situations where the true intrinsic brightness of a source is needed, for example placing a star on a Hertzsprung-Russell diagram. For differential photometry, the true flux of the source is not needed, and the final flux measurement is compared relative to another source. When imaging, several sources can be observed at once, providing many reference sources that can be used for differential photometry. The main assumption when observing these reference sources is that they are not variable over the duration of the observation. Differential photometry is used most often when time series observations of a source are needed for comparison with other sources or other multiwavelength observations.

---

[5]For example, the differential atmospheric refraction table for La Silla and Paranal are available at http://www.eso.org/gen-fac/pubs/astclim/lasilla/diffrefr.html.

2.4.2 Spectroscopy

Optical spectroscopy is the process of measuring the observed intensity of a source as a function of wavelength. The most common use of spectroscopy in astronomical observations is the identification of spectral lines that an object exhibits. By identifying these spectral lines, the composition and temperature of stars can be determined. This is usually done by comparing an observed spectrum to template or model spectra. Once the properties of the star are known, unusual features in the spectrum, such as P-Cygni profiles or emission lines, can be identified.

There are different types of spectrographs that are used to collect optical spectra from sources. The most common technique is slit spectroscopy, where the light from the telescope is focused onto the slit. A collimator is then used to focus the incoming light onto a diffraction grating where it is dispersed into its component wavelengths, before a camera is used to focus the dispersed light onto a detector (usually a CCD in modern spectrographs). Other types of spectrographs are also used in modern telescopes. Multi-object spectrographs can be used to observe the spectra for many sources simultaneously, and integral field spectrometers can be used to take spectra as a function of position, either of an extended object such as a galaxy, or of several stars in a crowded field like a globular cluster.

2.5 Astrometry

Astrometry involves the precise measurements of the positions and proper motions of astronomical objects. This usually involves observing stars to accurately derive their positions. Some missions to perform accurate measurements of stars are the Tycho-2 catalogue (Høg et al., 2000), which measured the astrometric positions, proper motions, and photometric data of 2.5 million stars with the ESA *Hipparcos* satellite, and the *Gaia* catalogue (Gaia Collaboration et al., 2016, 2018, 2022) which presents the full astrometric solution for over one billion sources down to a limiting magnitude of 21.

An important use of astrometry is frame alignment. Each observatory has its own reference frame, and when observing the same source across multiple observatories at different frequencies, each with different filters and responses, it is important to make sure that it is actually the same source being observed. The way to do this is through frame alignment, and matching to a common reference frame by correcting for any proper motion. Each observation has its own epoch, which specifies that date and time that the observation was taken. When deriving the position of a source, it is in the epoch of the observation, and can then be corrected to a standard reference frame. The standardised equatorial coordinate system is the International Celestial Reference System (ICRS), which is fixed to stars as they would be seen from the solar system barycentre in the epoch J2000.0 (Julian date 2451545.0, or noon January 1 2000 UTC). By correcting observed coordinates to the ICRS, that is the coordinates in the epoch J2000.0, the position can be extrapolated to other epochs as needed, and comparisons between the observed coordinates of an object from different facilities can be done.

CHAPTER 3

SIMULTANEOUS *CHANDRA* AND VLA OBSERVATIONS OF THE TRANSITIONAL MILLISECOND PULSAR CANDIDATE NGC 6652B

This chapter is my own work except for the following. V. Tudor proposed for and acquired the radio and X-ray data, performed initial data reduction and calibration, originally identified the radio source, and calculated the radio spectral index. Optical spectroscopic data from the SOAR telescope were collected and calibrated by J. Strader, who also provided the text regarding the collection and calibration of this data. A. W. Shaw collected and performed initial calibration of the optical photometric data from the Gemini Acquisition camera. Discussions on the data reduction and implications of the results were contributed by my supervisory panel – A. Bahramian, J. C. A. Miller-Jones, and A. Kawka. Further discussions were also contributed by J. Strader, L. Chomiuk, C. O. Heinke, T. J. Maccarone, C. T. Britt, R. M. Plotkin, A. W. Shaw, L. Shishkovsky, E. Tremou, V. Tudor, and G. R. Sivakoff. I drafted the manuscript and distributed it to all co-authors for proofreading. All co-authors provided input and feedback on the manuscript until the final version was produced.

It is clear from Chapter 1 that GCs are an ideal environment to search for exotic binary systems containing BHs and other compact objects. The large stellar densities and encounter rates mean that these exotic binaries form at a much higher rate in GCs than the Galactic field, as evidenced by the overabundance of XRBs in GCs when compared to the Galactic field (Clark, 1975). In light of this, radio continuum observations of several Galactic GCs as part of the MAVERIC survey were taken, to provide deep radio coverage of these clusters and search for previously undiscovered exotic binary systems. The MAVERIC survey consists of a deep radio continuum survey of 50 Galactic globular clusters performed using the ATCA and the VLA (Tremou et al., 2018; Shishkovsky et al., 2020; Tudor et al., 2022), and is accompanied by a *Chandra*/ACIS catalogue of X-ray sources in 38 Galactic globular clusters (Bahramian et al., 2020). Numerous interesting sources were identified as part of this effort, some of which demanded further study to fully understand the nature of these objects. One of these sources is the

XRB NGC 6652B in the cluster NGC 6652.

NGC 6652 is a globular cluster with a mass of 5.2×10^4 M$_\odot$ located at a distance of 10 kpc (Harris, 1996; Baumgardt et al., 2019) in the Galactic bulge. It contains one bright LMXB (XB 1832-330 with $L_X \sim 10^{36}$ erg s^{-1}), in addition to several other lower luminosity X-ray binaries (Heinke et al., 2001; Stacey et al., 2012). Optical studies of the cluster by Deutsch et al. (1998) identified star 49, a faint, blue object first proposed as the optical counterpart to XB 1832-330. Subsequent *Chandra* observations indicated that this was not the case, and that star 49 was in fact associated with NGC 6652B, a new, faint LMXB (Heinke et al., 2001).

Strong optical variability from the source has been observed (Deutsch et al., 2000), although the claimed periodicity of this variability ($\sim$ 45 minutes) has been disputed (Heinke et al., 2001). Observations by Engel et al. (2012) showed optical variations by up to 1 magnitude in the *g'*-band on time-scales of hundreds of seconds. This strong blue variability also means that the apparent location of the optical counterpart on the main sequence is questionable.

Significant X-ray variability over similar time-scales has also been observed, in addition to evidence of X-ray spectral variability (Coomber et al., 2011; Stacey et al., 2012). The measured values of the hydrogen column density ($N_{\rm H}$) are consistent with the cluster foreground, and too low for obscuration by a disc to cause this spectral variation, with Stacey et al. (2012) suggesting that the cause of this variation is due to the propeller effect (Illarionov & Sunyaev, 1975). This is a scenario that arises when the magnetic field of the neutron star creates a centrifugal barrier that prevents accretion onto the neutron star surface. NGC 6652B was loosely classified as a very faint X-ray transient (VFXT), defined as a transient with a peak X-ray luminosity $< 10^{36}$ erg s^{-1} (Heinke et al., 2015).

As part of the MAVERIC survey, the cluster NGC 6652 was observed by the ATCA for a total of 26.1 hr in 2015. From these observations, a radio source at the position of the X-ray source NGC 6652B was identified (Tudor et al., 2022).

Observatory/Inst.	Obs. ID	Date	Duration
VLA (B configuration)	16A-325	2016 May 27	0.75 hr
		2016 May 29	0.75 hr
		2016 June 08	0.75 hr
		2016 June 11	0.67 hr
VLA (C configuration)	SI0399	2017 May 22	2.75 hr
Chandra /ACIS	18987	2017 May 22	10 ks
Gemini-North/AcqCam	GN-2017A-DD-7	2017 May 22	0.92 hr
SOAR/Goodman	-	2015 May 24	0.5 hr
		2015 May 28	1.83 hr
		2015 Aug 08	0.67 hr

Table 3.1: The multiwavelength data used in this study.

This source has an average 9 GHz radio flux density of 76 ± 4 μJy, and an inverted spectral index of $\alpha = 0.38 \pm 0.13$ ($S_\nu \propto \nu^\alpha$).

In this chapter, we present the results of a simultaneous monitoring campaign with *Chandra* and the VLA taken as follow-up observations to the MAVERIC survey, in addition to simultaneous optical observations with Gemini North and optical spectroscopy obtained using the Southern Astrophysical Research Telescope (SOAR) 4 m telescope. Based on the hard X-ray emission, variable H α emission, and brighter than expected radio luminosity for a neutron star, we conclude that NGC 6652B is a tMSP candidate.

3.1 Observations and data reduction

Following the detection of a radio counterpart to NGC 6652B, we obtained simultaneous radio and X-ray observations with the VLA and *Chandra* to investigate the relationship between the radio and X-ray emission from this source. The data used in this chapter are listed in Table 3.1, and in the following sections we describe the data reduction of these data.

3.1.1 Follow-up radio data

We observed NGC 6652B a total of five times with the VLA over the course of a year under two different project codes. The first set of observations under project code 16A-325 consists of four epochs of observations: three 0.75 hour observations on 2016 May 27, 2016 May 29, and 2016 June 8, and one 0.67 hour observation on 2016 June 11. The array was in the B configuration for these observations, and the target source was observed at C band with two 2 GHz basebands centred at 5.0 GHz and 7.0 GHz respectively. The flux density and bandpass calibrator for these observations was 3C48, and the complex gain calibrator was J1820-2528.

In addition to these four epochs, we observed NGC 6652B with the VLA on 2017 May 22 from 08:09-11:32 UTC under the project code SI0399, giving an on-target time of 2.75 hours. This observation was performed simultaneously with X-ray observations of the source made using the *Chandra* X-ray Observatory. The array was in the C configuration, and the target source was observed at X band with two 2 GHz basebands centred at 9.0 and 11.0 GHz, respectively. 3C286 was used as the flux density and bandpass calibrator, and J1820-2528 was used as the complex gain calibrator.

The data were imported into the Common Astronomy Software Application (CASA; McMullin et al., 2007) for data reduction and imaging. The data were reduced using the VLA CASA calibration pipeline version 5.6.2-3, which automatically flags and calibrates the data. Any remaining spurious data were manually flagged from the dataset before the calibration pipeline was re-run. Imaging was performed with the `tclean` task using Briggs weighting with a robust parameter of 0 to balance sensitivity and resolution. The flux density and position of the target source were determined using the CASA task `imfit`. The rms, clean beam size, and measured flux densities of NGC 6652B are shown in Table 3.2. This image is shown in Figure 3.1.

Date	Band	B_{maj} ($''$)	B_{min} ($''$)	B_{pa} ($°$)	rms (μJy/bm)	Flux density (μJy)
2016 May 27	C	2.81	0.73	21.98	9.41	46.3 ± 6.9
2016 May 29	C	2.89	0.74	23.72	8.04	39.6 ± 5.8
2016 June 08	C	2.66	0.73	19.49	8.81	69.9 ± 6.6
2016 June 11	C	2.50	0.75	17.62	8.82	88.4 ± 6.8
2017 May 22	X	3.89	1.38	1.51	3.73	79.2 ± 2.2

Table 3.2: The FWHM of the clean beam, consisting of the semi-major axis (B_{maj}), the semi-minor axis (B_{min}), and position angle (B_{pa}), and the central rms of the five VLA observations observations. The flux density of NGC 6652B and the frequency band of each observation are also listed. C band corresponds to 4-8 GHz and X band corresponds to 8-12 GHz.

3.1.2 X-ray data

NGC 6652B was observed with the *Chandra* X-ray Observatory on 2017 May 22 from 08:14-11:43 UTC during observing cycle 18 under the observation ID 18987, giving an exposure time of 10 ks. This observation was simultaneous with a radio observation with the VLA (Chapter 3.1.1). The observations were performed in Faint mode using ACIS-S and the target was positioned on chip S3 using a custom subarray of 128 rows to reduce pileup.

For data processing and analysis, we used CIAO 4.12.1 and CALDB 4.9.3 (Fruscione et al., 2006). The 0.3-10 keV image is shown in Figure 3.1. The *Chandra* data were reprocessed using `chandra_repro`, and `dmextract` was used to extract a light curve binned at 200 s from the data in the 0.3-10 keV energy range. Source and background spectra were extracted using `specextract`, with source and background regions chosen to avoid contamination by the bright LMXB XB 1832-330. A circular extraction region with a radius of $2''$ was used for the source, and an annulus with an inner radius of $2.5''$ and an outer radius of $7''$ was used for the background. Spectral analysis was performed using XSPEC 12.11 (Arnaud, 1996).

3.1.3 Optical data

3.1.3.1 Photometry

Optical observations of NGC 6652B were obtained with the Gemini North Acquisition Camera on 2017 May 22 from 10:35-11:30 UTC, giving 55 minutes of observations that were simultaneous with the VLA and *Chandra*. The observations were taken with the *V* filter under the project code GN-2017A-DD-7, and consisted of 1332 2 s snapshots for the purpose of fast photometry. The data were reduced using the PYTHON package CCDPROC (Craig et al., 2017) and astrometrically aligned for stacking and further analysis. For fast photometry and searching for variations, we used the software package ISIS 2.2 (Alard & Lupton, 1998; Alard, 2000). This image is shown in Figure 3.1.

3.1.3.2 Spectroscopy

We obtained spectra of NGC 6652B using SOAR/Goodman on three different nights: 2015 May 24, 2015 May 28, and 2015 Aug 18. All observations used a $400\,\mathrm{l\,mm^{-1}}$ grating and a $0.84''$ longslit, yielding a resolution of about 5.0 Å full-width at half-maximum (FWHM) over a nominal wavelength range ~ 3000–7000 Å (though the signal below ~ 3800 Å is very low). On 2015 May 24 we obtained a pair of 15-min exposures. On 2015 May 28 we first obtained a pair of 15-min exposures before taking two pairs of 20-min exposures, for six spectra total during this night. We obtained a final pair of 20-min exposures on 2015 Aug 18.

The spectra were all reduced and optimally extracted in the usual manner, and wavelength-calibrated using FeAr arc lamp exposures obtained immediately following the science spectra. Heliocentric velocity corrections were calculated using IRAF (Tody, 1986, 1993) using the package RVCORRECT and applied to the spectra. We searched for variability between the spectra and also stacked them to increase the signal-to-noise ratio for possible features originating from the accretion disc.
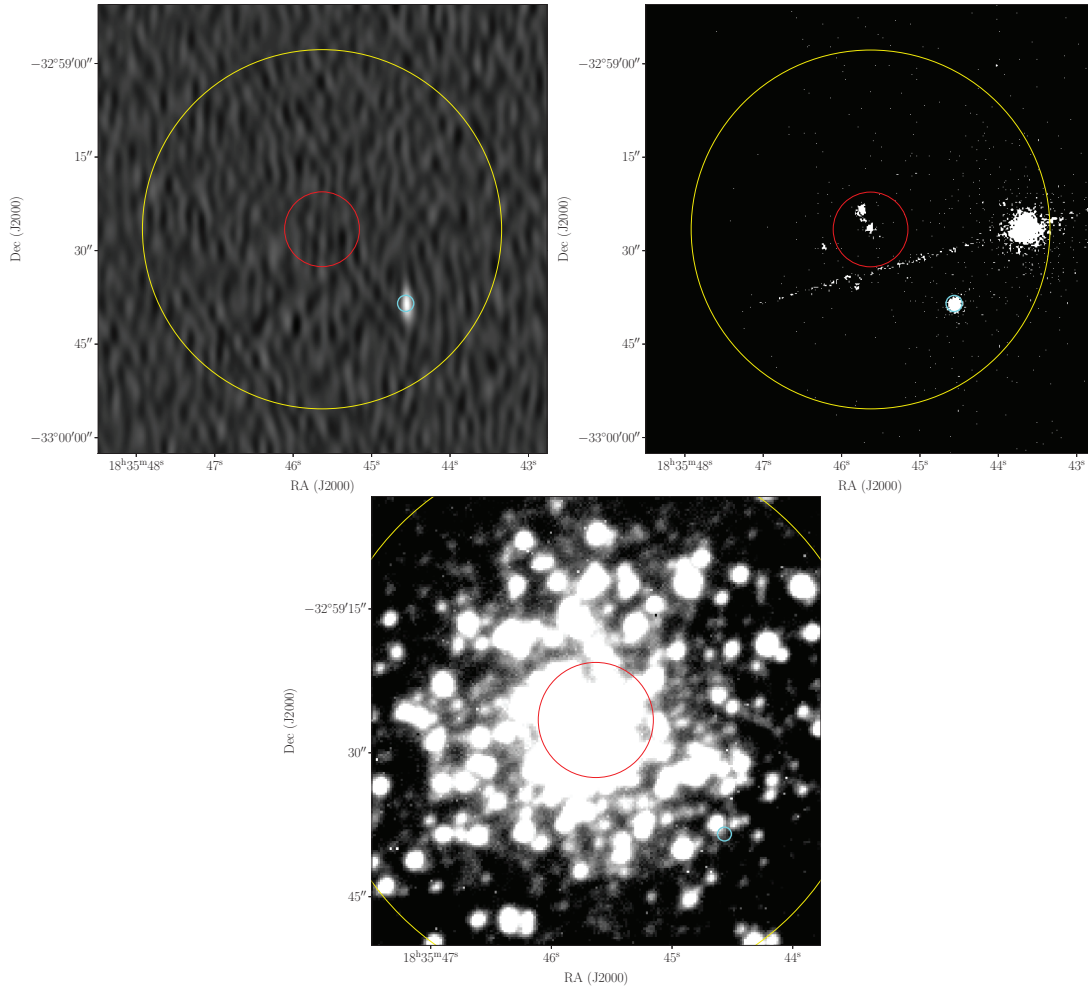
Figure 3.1: The 10 GHz VLA image (top left), the 0.3-10 keV *Chandra* image (top right), and the *V* filter Gemini image (bottom) of NGC 6652B and the surrounding field. NGC 6652B is highlighted by the cyan circle. The red and yellow circles indicate the core and half-light radii of the cluster NGC 6652 respectively.
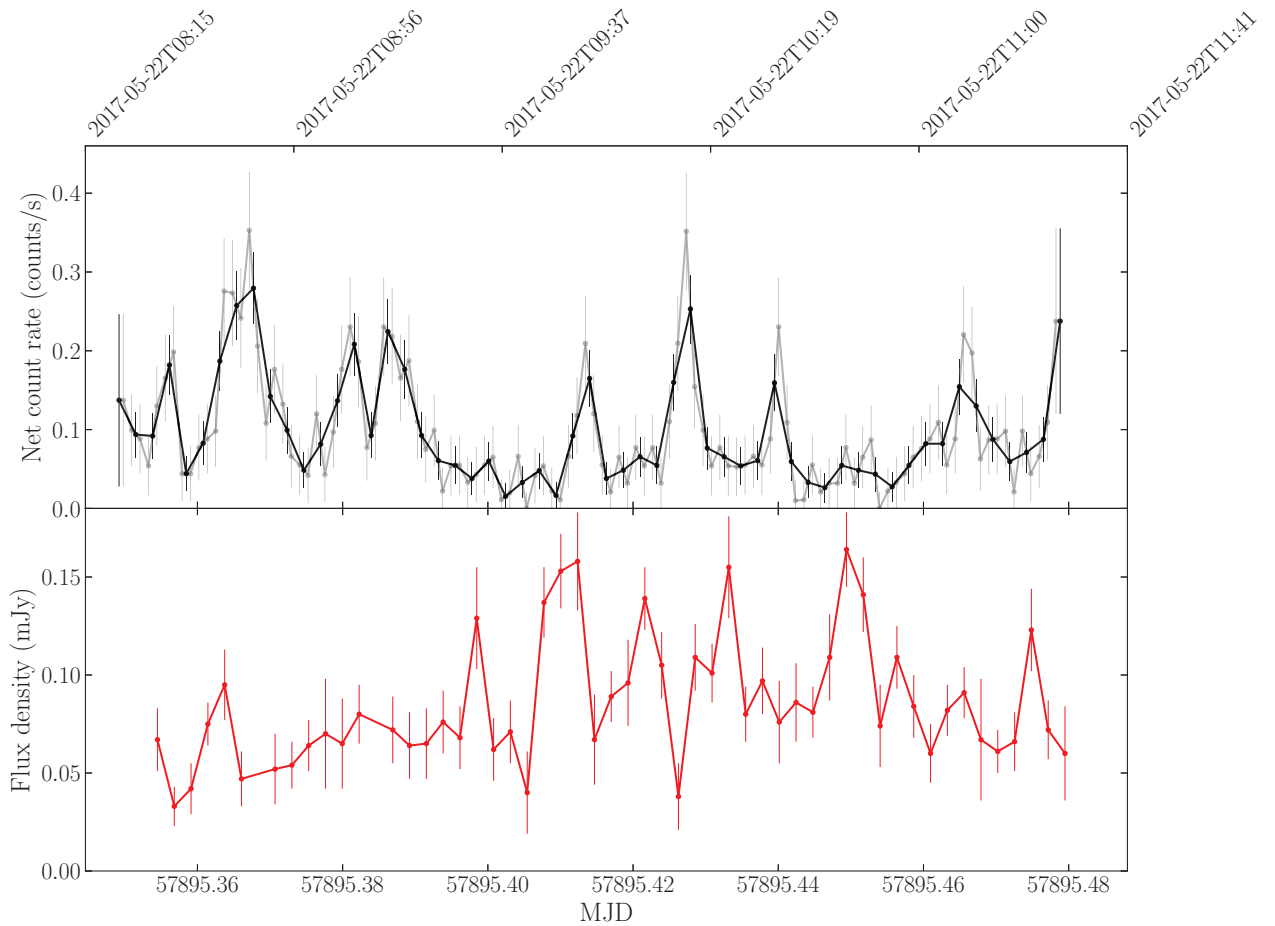
Figure 3.2: *Top*: The *Chandra* background subtracted light curve extracted in the 0.3-10 keV energy band with a binning of 200 s. This light curve is shown in black. The grey light curve shows the same data with a binning of 100 s. Numerous X-ray flares are seen over the duration of the observation. *Bottom*: The 8-12 GHz VLA light curve with a binning of 200 s. Some radio flares are visible in the later half of the observation.

3.2 Analysis and results

3.2.1 Searching for correlated variability in the radio and X-ray bands

To investigate whether there is any correlated variability between the radio and X-ray bands in NGC 6652B, we extracted a background subtracted light curve with a binning of 200 s in the 0.3-10 keV energy range from the *Chandra* X-ray data. This is shown in the top panel of Figure 3.2. The source shows variability over a time-scale of a few hours, with several flaring events with count rates > 0.1 counts/s present in the light curve. The fractional RMS variability amplitude for the X-ray light curve is 0.598, implying that the X-ray emission from the source is variable. The average 1-10 keV X-ray flux during this observation is $1.5 \pm 0.1 \times 10^{-12} \mathrm{\ erg\,s^{-1}\,cm^{-2}}$.

The bottom panel of Figure 3.2 shows the light curve extracted from the simultaneous VLA radio observation. This observation was split into several bins with a width of 200 s to match the timing resolution of the *Chandra* light curve and each bin was imaged. The task `imfit` was used to extract the flux density from these images. The fractional RMS variability for the radio light curve is 0.316, implying moderate variability. The average 10 GHz radio flux density of the source during this observation is 79.2 ± 2.2 µJy.

We calculated the Z-transformed discrete correlation function[1] (ZDCF; Alexander, 1997) of the two light curves to determine if there was any (anti-)correlation between them. The ZDCF was performed with a 200 s time bin. This cross-correlation function is shown in the top panel of Figure 3.3. To estimate the uncertainty on the cross-correlation function, we simulated 1000 light curves with the same power spectrum as the data, and calculated the ZDCF for each pair of simulated light curves. From this, we determined the 95% and 99% confidence intervals on the cross-correlation function. This showed that there is no

---

[1]https://webhome.weizmann.ac.il/home/tal/zdcf2.html
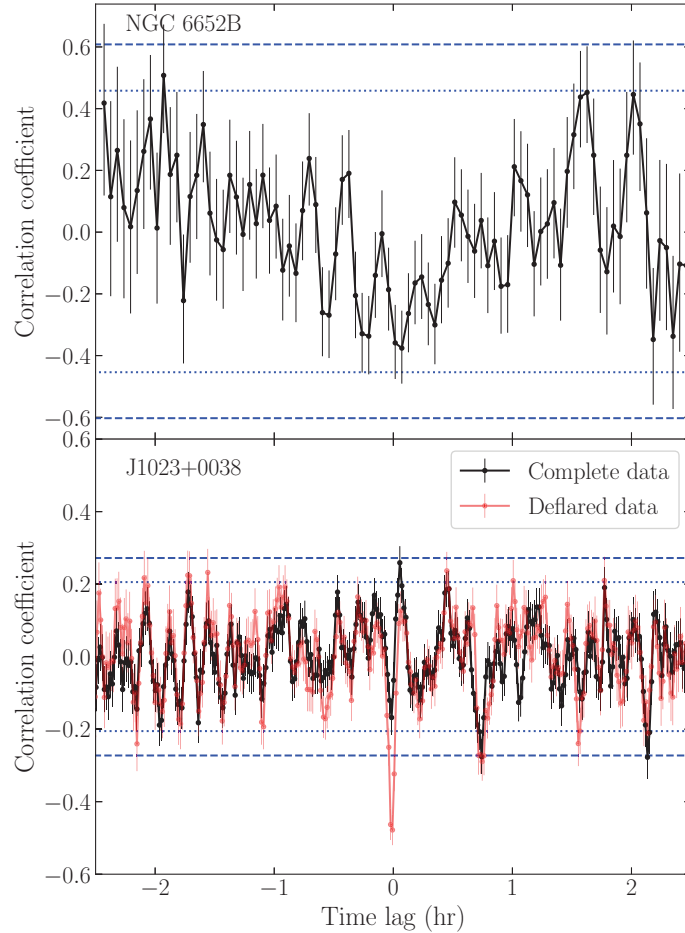
Figure 3.3: *Top*: The Z-transformed discrete correlation function of the radio and X-ray light curves of NGC 6652B. The 95% and 99% confidence intervals are shown as blue dotted and blue dashed lines respectively. No clear correlation is seen to > 99% confidence. *Bottom*: The Z-transformed discrete correlation function of the radio and X-ray light curves of J1023+0038 for two cases. The black line indicates the correlation function for the complete dataset, where the significant radio and X-ray flares seen in the light curves have been included in the dataset. In this complete dataset, no significant anti-correlation is seen between the radio and X-ray light curves. The red line indicates the correlation function for the dataset where the radio and X-ray flares have been removed, to leave only the high and low mode data. The blue dotted and dashed lines indicate the 95% and 99% confidence intervals respectively for this "deflared" dataset. With the flares removed from the dataset, anti-correlation is seen to > 99% confidence between the radio and X-ray light curves in the high and low mode data. This is discussed further in Chapter 3.3.3.

73

clear correlation between the simultaneous radio and X-ray light curves to > 99% confidence.

To investigate the behaviour of the source both during and outside an X-ray flaring event, we binned the X-ray and radio data based on periods of high (>0.09 counts/s) and low (≤ 0.09 counts/s) X-ray counts. From this we calculated the corresponding X-ray fluxes, using X-ray spectroscopy (see Chapter 3.2.3), and radio flux densities for these time periods. These results are shown in Table 3.3. By assuming the distance to the cluster NGC 6652 to be 10 kpc (Harris, 1996) and using a radio spectral index of 0.38 ± 0.13 for NGC 6652B, as measured in the original MAVERIC survey (Tudor et al., 2022), the 5 GHz radio luminosities and 1-10 keV X-ray luminosities were calculated, and the source was plotted on the radio–X-ray plane for accreting systems for different X-ray count rates (Figure 3.4). These radio and X-ray luminosities place NGC 6652B near the radio–X-ray correlation for accreting BHs (Gallo et al., 2014). Furthermore, NGC 6652B appears to show enhanced radio luminosity during periods of low X-ray counts and vice versa during our observations, however this behaviour only appears when considering the average flux densities during periods of high and low X-ray counts, that is the values shown in Table 3.3. However, as shown through the cross-correlation analysis, there is no correlation to > 99% confidence in the 200 s binned radio and X-ray light curves.

3.2.2   Longer term radio behaviour

The additional 4-8 GHz VLA observations taken a year before the simultaneous observations provide an opportunity to study the longer term radio behaviour of NGC 6652B. The measured 9 GHz flux density of the source in the original MAVERIC survey data from 2015 is 76 ± 4 µJy. The flux densities from our 4-8 GHz observations and 8-12 GHz observations were measured using the CASA task IMFIT and are shown in Table 3.2. The four 4-8 GHz observations show that the 6 GHz flux density of the source ranges between 40 and 88 µJy over the
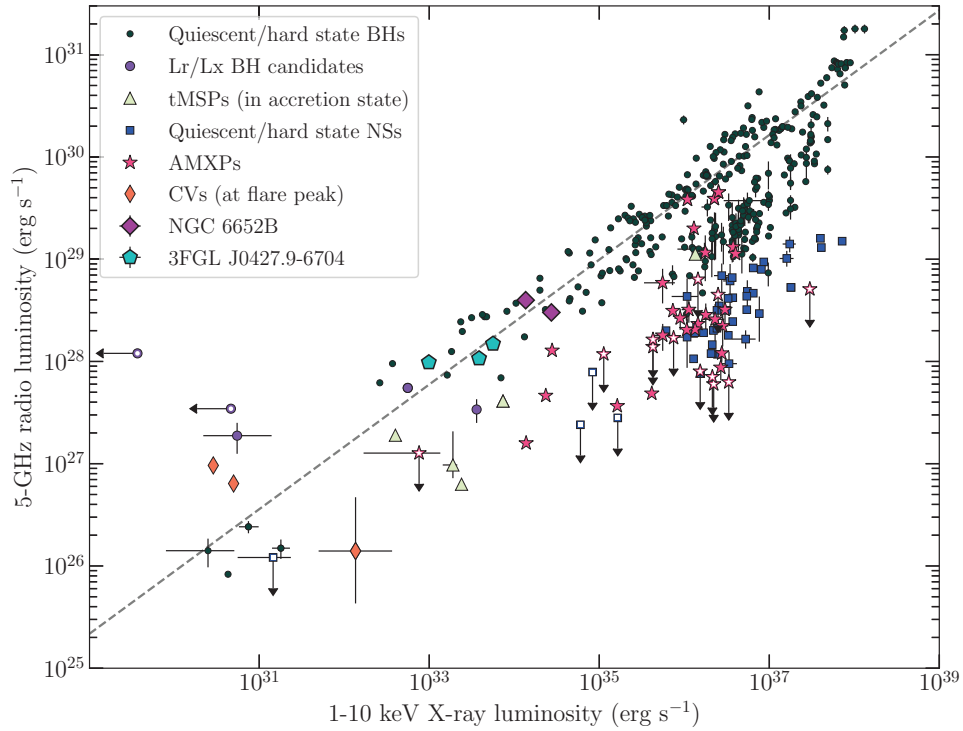
Figure 3.4: The radio–X-ray correlation for accreting systems, with the high and low X-ray count rate regimes of NGC 6652B plotted. Note the error bars are too small to be seen. The different coloured markers represent different types of accreting binaries from the database of Bahramian et al. (2018a), and the dashed line represents the correlation for accreting BHs (Gallo et al., 2014). NGC 6652B sits near the BH correlation, with this position changing for different X-ray count rate regimes. This behaviour is different to that of J0427.

course of two weeks. The 8-12 GHz observation taken a year later showed the source with a 10 GHz flux density of $79.2 \pm 2.2\,\mu Jy$. Only moderate variations by a factor of ~ 2 are seen, at similar levels to the variation seen within the radio light curve of the X band observation.

3.2.3 X-ray spectroscopy

X-ray spectra of NGC 6652B were extracted for intervals of high ($>0.09\,\text{counts/s}$) and low (≤ 0.09 counts/s) X-ray counts, and for the entire observation using `specextract`, with the source spectra binned to have 20 counts per bin. XSPEC 12.11 (Arnaud, 1996) was used for spectral analysis, assuming Wilms et al. (2000) abundance of elements and χ^2 statistics for inference. Previous X-ray spectral analysis of NGC 6652B has been done in-depth by Stacey et al. (2012). From a 47.5 ks *Chandra* observation, a variety of spectral models were fit to the spectrum of NGC 6652B, and it was found that a power-law model is a good fit to the data. In light of this, we preliminarily fit each spectrum with an absorbed power law model (`tbabs` $\times$ `pegpwrlw`), which indicated varying values of the hydrogen column density (N_{H}) between high and low X-ray counts, suggesting the presence of intrinsic absorption in the system. We also investigated whether our data were affected by pileup. For a 1/8 subarray we calculated the pileup to be $< 5\%$, and verified this by including pileup in our spectral models, where it had a minimal impact on the fitted parameters.

76

X-ray count rate threshold (counts/s)	Radio flux density (µJy)	Galactic N_H (10^{22} cm^{-2})	Intrinsic N_H (10^{22} cm^{-2})	Γ	Unabsorbed flux (10^{-12} erg s^{-1} cm^{-2})	χ^2_ν/d.o.f.	N.H.P.
> 0.09	65.6 ± 3.8	(0.078)	$< 0.086^*$	$1.45^{+0.15}_{-0.13}$	$2.29^{+0.19}_{-0.24}$	0.70/26	0.868
≤ 0.09	86.4 ± 2.7	(0.078)	$< 0.611^*$	$1.13^{+0.37}_{-0.33}$	$1.14^{+0.22}_{-0.19}$	0.38/13	0.976
Average	79.2 ± 2.2	(0.078)	$< 0.166^*$	$1.32^{+0.17}_{-0.12}$	$1.52^{+0.14}_{-0.14}$	0.72/41	0.912

Table 3.3: The results of the X-ray spectral fitting and the measured radio flux densities in the different X-ray count rate regimes. The radio flux densities are measured at 10 GHz, and the radio uncertainties reported are the 1σ values. All other uncertainties are reported at 90% confidence for a single parameter of interest. The values in parentheses indicated values that were frozen when fitting. The absorption column indicates the second absorption parameter included to test for intrinsic absorption, and the * indicates a 2.706 $\Delta\chi^2$ upper limit to these values (equivalent to a 90% confidence region for a single parameter of interest). The unabsorbed flux is in the 1-10 keV band. N.H.P. is the null hypothesis probability of the fit, where the null hypothesis is that the data are drawn from the model, meaning a higher probability is better.

To investigate the change in column density, we fit the high and low X-ray count rate spectra with an absorbed power law model with an additional absorption parameter to account for a possible intrinsic absorption (`tbabs` × `tbabs` × `pegpwrlw`). Foreground reddening in the direction of NGC 6652 is $E(B-V) = 0.09$ (Harris, 1996), and using the relations calculated by Bahramian et al. (2015) and Foight et al. (2016), we estimated the column density to the cluster to be $7.8 \times 10^{20}\,\mathrm{cm}^{-2}$. We set the first absorption component in the model to this value (representing the cluster foreground absorption), and allowed the second absorption parameter to vary to test the presence of intrinsic absorption. These results are shown in Table 3.3.

The spectra are hard ($\Gamma \sim 1.3$), indicating non-thermal emission is present, with the low count rate spectrum indicating slightly harder emission ($\Gamma \sim 1.1$). The measured photon indices are consistent within uncertainties. While the values of our second absorption parameter are consistent with zero for both the high and low X-ray count rates, we note that to a $\geq 1\,\sigma$ level the low count rate value is inconsistent with zero, indicating that there is marginal evidence for intrinsic absorption. This is highlighted in the contour plots for the high and low count rate spectra, shown in Figure 3.5.

3.2.4 Optical spectroscopy

We obtained ten optical spectra of NGC 6652B using the Goodman spectrograph on the SOAR 4 m telescope. These spectra are shown in Figure 3.6. An inspection of these spectra shows some stellar absorption features and some variable emission features typical of accreting X-ray binary systems. At $\sim 4300\,\text{Å}$ the G-band absorption feature is seen. The G-band is an absorption band due to the CH molecule, and is a feature of early F to early K-type stars. Other metallic absorption features are seen at $\sim 4530\,\text{Å}$ (Fe I), $\sim 5180\,\text{Å}$ (Mg I) and $\sim 5900\,\text{Å}$ (Na I doublet). The absorption line at $\sim 6290\,\text{Å}$ is potentially due to molecular oxygen from the Earth's atmosphere, with further telluric absorption features
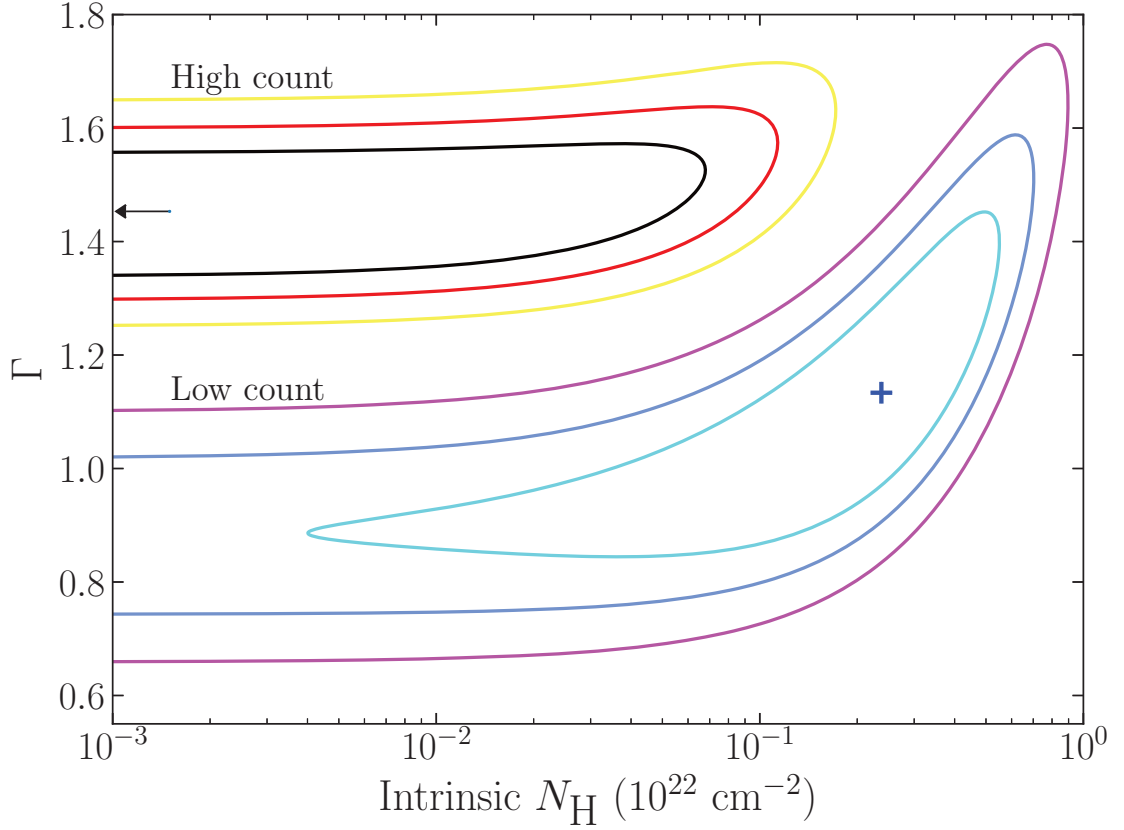
Figure 3.5: The contour plots for the high count (top left) and low count (bottom right) rate X-ray spectral fits. The different colour maps indicate that the contours are for two different datasets. The plot indicates how the χ^2 of the fit changes as the parameter space of the photon index and intrinsic column density is explored. The black arrow indicates that the best-fit parameters for the high X-ray count spectrum is beyond the x-axis limit of the plot, and the blue cross indicates the best-fit parameters for the low X-ray count rate spectrum. The contours indicate 1σ, 2σ, and 3σ levels for a single parameter of interest. The two fits are inconsistent with each other, and the intrinsic column density for the low X-ray count rate spectrum is inconsistent with zero at a $\geq 1\sigma$ level. This indicates there is some evidence for intrinsic absorption in the system during these periods of low X-ray counts.
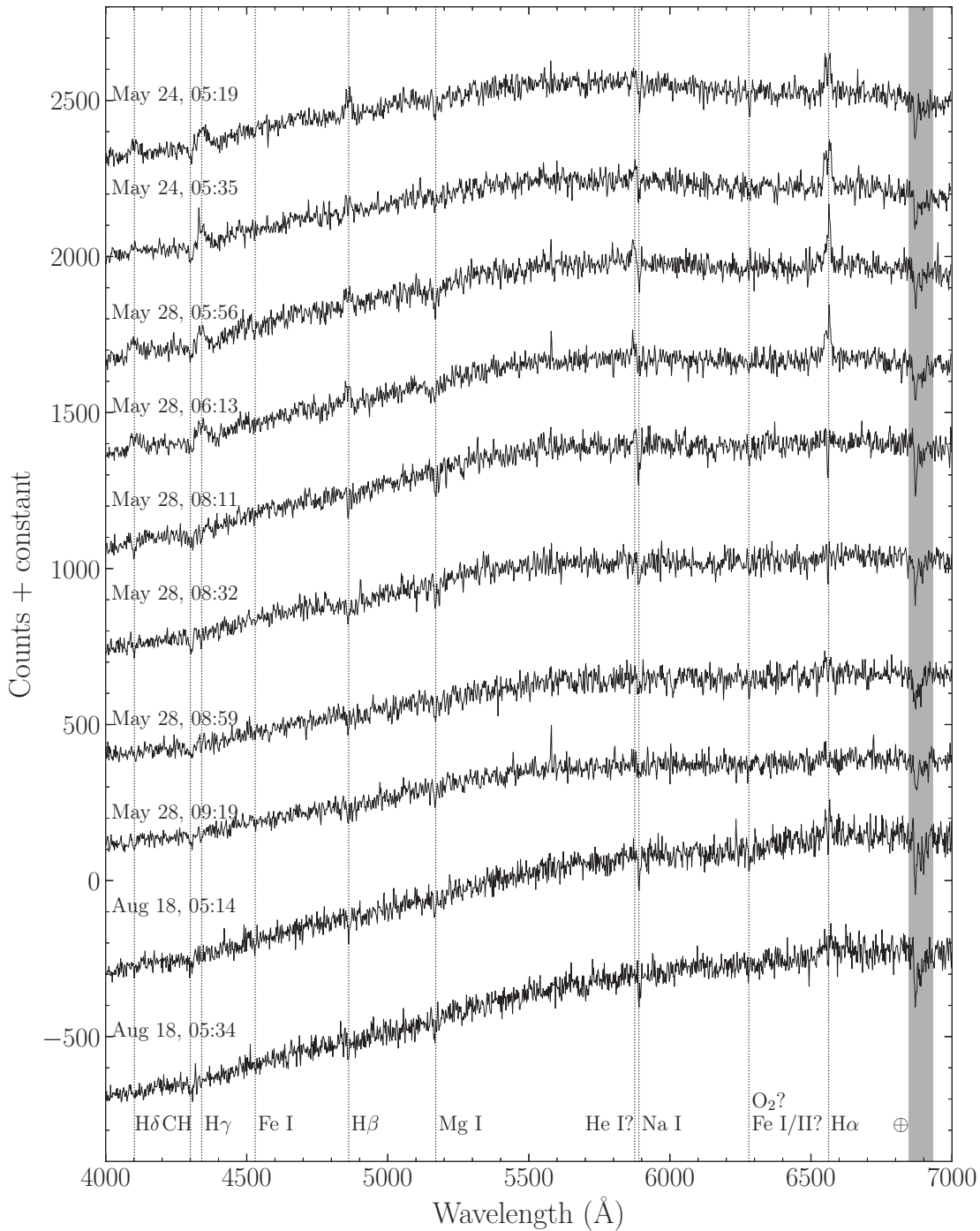
Figure 3.6: The ten optical spectra obtained of NGC 6652B. Several spectral features are shown with dashed lines. The first four Balmer features are seen, with prominent double-peaked H α emission visible in addition to H β, H γ, and H δ emission features seen in the first four observations before switching to absorption. Several stellar absorption features are visible, such as the G-band due to the CH molecule seen at ~ 4300 Å, and various other metallic absorption features such as Fe and Mg absorption lines. The shaded region indicates telluric absorption features.

seen from 6850 Å to 6930 Å. The first four Balmer features are seen and there is evidence of broad He I emission seen at ~ 5875 Å in some of the spectra. The presence of the G-band, and the indicated metallic absorption lines are consistent with an early to mid G-type star (see § 3.3.1), however robust identification of the optical counterpart is difficult due to potential contamination from the crowded region around the source.

Broad H α emission lines are prominent in the first four spectra, indicating that this source is most likely an accreting binary system (Casares, 2015, 2016). While for bona fide quiescent X-ray binaries, the relations of Casares (2015, 2016) can be used to estimate the projected radial velocity amplitude and the binary mass ratios using emission lines, these correlations have not been established to work for brighter objects, and do rely on the ionisation profile of the accretion disc being relatively similar to that of a quiescent system's accretion disc. Furthermore, the mass ratio estimates require averaging carefully over orbital phase, and with relatively strong variability, as we see for NGC 6652B, far more spectra are needed to give an appropriately weighted average of the data. Thus, this is not an appropriate situation for these correlations to be implemented.

The H α emission over our ten observations is shown in Figure 3.7. Prominent double-peaked emission features are seen over the two spectra taken on May 24 2015. This emission feature is also seen in the first two spectra taken on May 28 2015, although only one peak is seen. Between 06:13 and 08:11 on May 28 2015, the emission feature disappears and is replaced with an absorption feature, indicating a change in the source over a time-scale of less than two hours. The absorption feature persists for the rest of the spectra. This behaviour is also seen in the H β, H γ, H δ, and He I lines.

3.2.5   Optical photometry

We obtained 55 minutes of optical observations with the Gemini North Acquisition Camera that were simultaneous with our radio and X-ray observations to
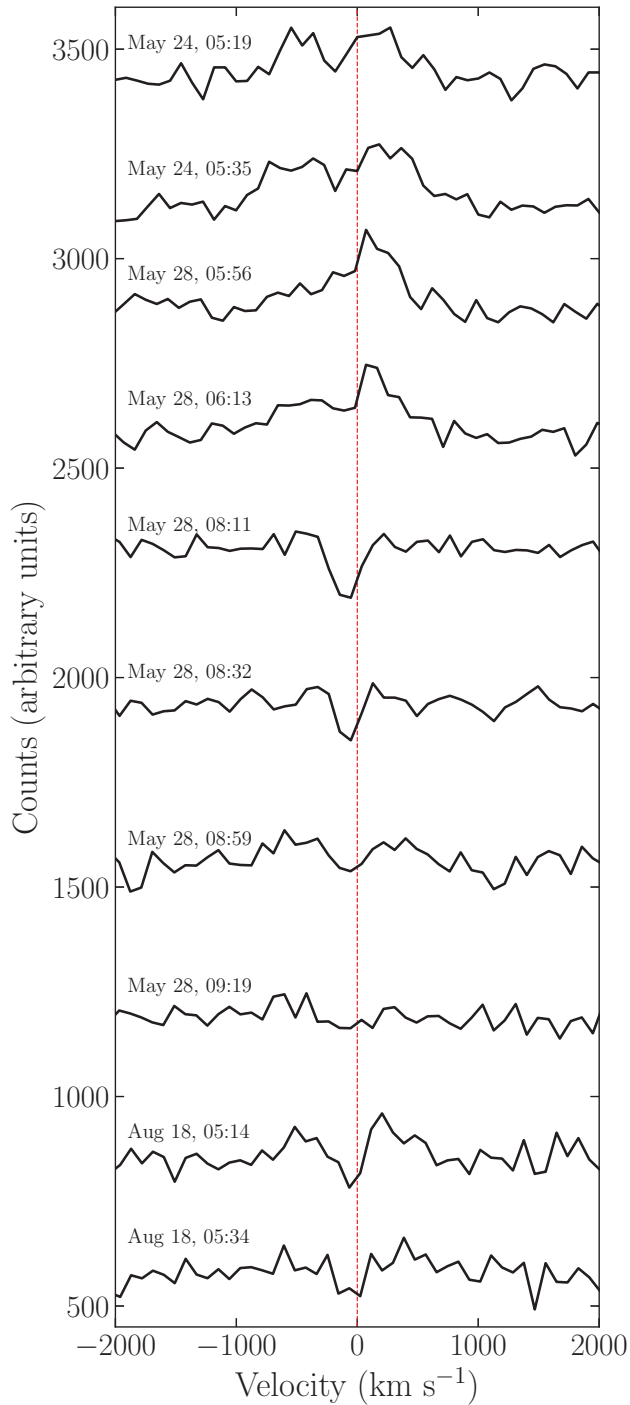
Figure 3.7: The variation in the H α line over ten spectra of NGC 6652B. The red dashed line indicates a velocity of $0\,\mathrm{km\,s^{-1}}$. The H α feature goes from double-peaked emission in the first observation to a single emission feature, before transitioning to full absorption in the fifth spectrum taken. The transition from emission to absorption occurs over a time-scale of a couple of hours.

search for variations in the V filter of NGC 6652B. The duration of each exposure was 2 s. The image subtraction software ISIS was used to extract the light curves of the source and three non-varying check sources in the field. The region near the source is crowded by bright, nearby sources, and the source is located in the point-spread function of a bright source, as highlighted by the image shown in Figure 3.1. Stacking the snapshots to derive a deep image of the field shows that the source is not detected down to a conservative V filter magnitude of ~ 17.7.

3.3   Discussion

We observed NGC 6652B simultaneously with *Chandra* and the VLA to investigate the correlation between the radio and X-ray behaviour of the source. Additional optical spectra obtained with SOAR provided a means to characterise the optical counterpart, and to search for signatures of accretion. These observations have provided several clues as to the classification of the system and the behaviours that are present.

Optical spectra obtained with SOAR have highlighted variation in the H α emission line, with a shift from double-peaked emission to absorption over a time scale of two hours as shown in Figure 3.7. Simultaneous radio and X-ray observations place NGC 6652B on the track mostly occupied by accreting BHs on the radio–X-ray luminosity plane (Figure 3.4), indicating that it has a higher radio luminosity than typical accreting NSs of a similar X-ray luminosity. Breaking these observations into intervals of high and low X-ray count rates hints that radio luminosity may decrease as X-ray luminosity increases and vice versa. This behaviour is only present when considering the average radio and X-ray luminosities during these regimes, and cross-correlation analysis indicates that there is no correlation between the simultaneous radio and X-ray light curves shown in Figure 3.2 to $> 99\%$ confidence. X-ray spectral analysis of NGC 6652B indicates a hard photon index ($\Gamma \sim 1.3$), resulting from non-thermal emission, and spectral fitting of the low count rate regime highlights weak evidence for

intrinsic absorption. These observational properties suggest that NGC 6652B is a dim variable X-ray source, with moderately variable radio emission.

NGC 6652B has been the subject of previous X-ray observations with *Chandra* (Coomber et al., 2011; Stacey et al., 2012). Through a 5 ks *Chandra* observation, Coomber et al. (2011) observed rapid flaring variability of the source, with flares up to $L_X = 9 \times 10^{34}\,\mathrm{erg\,s^{-1}}$ persisting for several minutes. The hardening of the X-ray emission during lower count rates suggested that the variability seen is caused by obscuration by an accretion disc with a high inclination angle. Stacey et al. (2012) further developed the X-ray picture of NGC 6652B with a 47.5 ks observation of the cluster. The variable, hard emission of the source was still present, and the X-ray luminosity of the source suggested a NS primary. A tentative increase in the column density N_H during low count rates was also observed, however it was concluded that this increase in column density was not sufficient enough to decrease the count rate, ruling out obscuration by the accretion disc as the cause of the source's variability. Instead, Stacey et al. (2012) suggested that the variability of the source was due to the propeller effect, where the rotating magnetosphere of the NS prevents accretion onto its surface (Illarionov & Sunyaev, 1975), and classified the source as a very faint X-ray transient, due to its peak X-ray luminosity falling in the range of $10^{34-36}\,\mathrm{erg\,s^{-1}}$.

3.3.1 The companion star

The presence of the optical counterpart on the main sequence has been noted in previous studies of the source. The optical counterpart appears to fall on the main sequence in *V-I* and *g-r* colour-magnitude diagrams (CMDs) of the cluster (Heinke et al., 2001; Engel et al., 2012), but to the blue side of the main sequence in a *U-B* CMD (Deutsch et al., 1998). The position of the source on the cluster CMD also rules out the possibility of a giant companion. The 1 magnitude variability, first seen by (Deutsch et al., 2000), was identified as prohibiting the optical counterpart from actually being a main sequence star as some component

of the system must be heated by X-rays, contributing a blue component to its colour (Heinke et al., 2001; Engel et al., 2012). The presence on the main sequence then suggests that the donor may be a redder object, such as a subgiant or red straggler star (Engel et al., 2012).

Based on the optical spectra shown in Figure 3.6, some conclusions can be made as to the nature of the companion star in NGC 6652B. To investigate the star class of the companion, we compared the stacked optical spectrum of NGC 6652B to example stellar spectra for F, G and K-type main sequence stars from the ESO library of stellar spectra[2] based on the stellar spectra catalogue produced by Pickles (1998). This comparison is shown in Figure 3.8.

From this comparison, we conclude that the most likely star class for the companion is an early to mid G-type star. The presence of the G-band means the star cannot be much cooler than a K2 star, and the other absorption features closely match what is seen in G-type stars. However, we note that we cannot be completely confident in this observational classification of the companion due to the possibility of spectral contamination. NGC 6652B is located in an optically crowded region, so it is possible that the absorption lines seen in our optical spectra could be contaminated by nearby bright sources. However, it is unlikely that there will be significant contamination of the variable H α emission as this would require several accreting sources within close proximity of NGC 6652B.

If the optical companion to NGC 6652B is a G-type star, it would be similar to that of J1023. J1023 contains a $\sim 0.2 M_\odot$ G-type star that is been irradiated by the pulsar in the system (Archibald et al., 2013). This source has also been observed to undergo spectral type changes from G5 to F6 depending on the side of the star that is observed (Shahbaz et al., 2019).

---

[2]Available from https://www.eso.org/sci/facilities/paranal/decommissioned/isaac/tools/lib.html
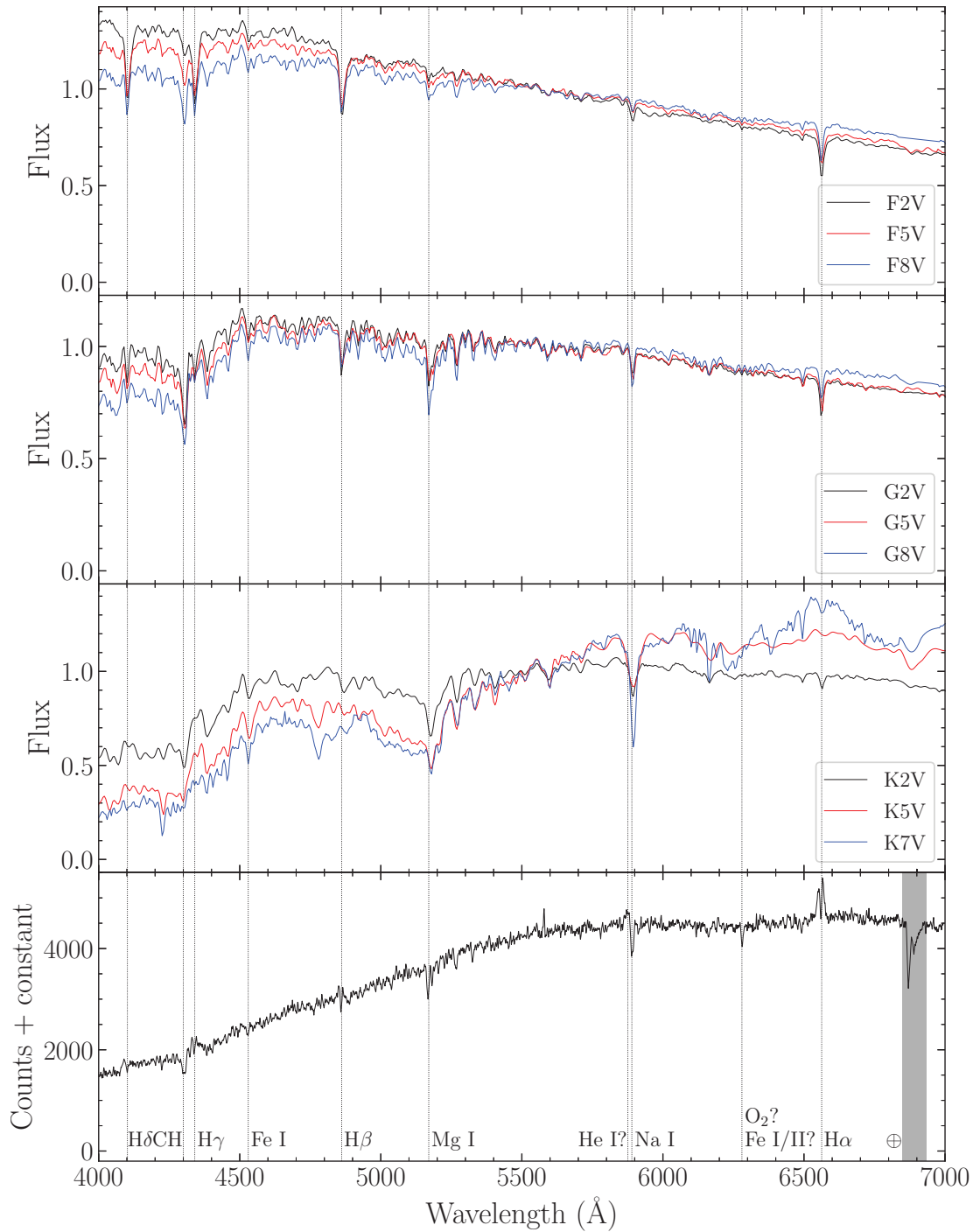
Figure 3.8: The stacked optical spectrum for NGC 6652B (bottom panel) compared to example stellar spectra for F, G and K-type main sequence stars. The identified spectral lines in the spectrum of NGC 6652B are indicated with black dashed lines. The spectrum of NGC 6652B best matches those of a G-type star.

3.3.2 Potential source classifications for NGC 6652B

NGC 6652B is located within the half-light radius of the cluster, and optical spectroscopy shows that the systematic velocity of the H α profile is consistent with the systematic velocity of the cluster NGC 6652 and offset from the field stars in that direction, meaning that it is unlikely to be a foreground star. The zero redshift of the spectral lines shows that it is not a background AGN. We identify the star as ID number 1676 in the HUGS catalogue (their photometric method 2) of Nardiello et al. (2018). Using proper motions between ACS and WFC3 epochs, the cluster membership probability of the star is estimated to be 97.8%, confirming that it is a cluster member.

There are many different types of X-ray sources within Galactic globular clusters, such as cataclysmic variables (CVs) and active binaries. CVs are prominent X-ray sources in clusters and can display X-ray variability. Three (rather extreme) examples of CVs are shown in the radio-X-ray luminosity plane in Figure 3.4: AE Aqr, AR Sco, and SS Cyg. The brightest of these in X-rays is SS Cyg with a peak X-ray luminosity of $\sim 10^{32} \, \mathrm{erg \, s^{-1}}$ (Russell et al., 2016), with the other two sources having X-ray luminosities $< 10^{31} \, \mathrm{erg \, s^{-1}}$ (Eracleous et al., 1991; Abada-Simon et al., 1993; Marsh et al., 2016). NGC 6652B has an average X-ray luminosity of $\sim 2 \times 10^{34} \, \mathrm{erg \, s^{-1}}$, which is two orders of magnitude higher than the observed X-ray luminosities of virtually all CVs other than intermediate polars (IPs). Furthermore, NGC 6652B has an average radio luminosity of $\sim 3 \times 10^{28} \, \mathrm{erg \, s^{-1}}$, which is an order of magnitude higher than the observed radio luminosity of AR Sco (Marsh et al., 2016) and two orders of magnitude higher than that of SS Cyg (Russell et al., 2016), meaning that based on radio luminosity it is unlikely that NGC 6652B is a CV.

In non-core-collapsed clusters there is a single faint CV population as seen through observations of the clusters ω Centauri and 47 Tucanae (Cool et al., 2013; Rivera Sandoval et al., 2018) collated by Belloni & Rivera Sandoval (2020), with the brightest of this population reaching an X-ray luminosity of $\sim 10^{33} \, \mathrm{erg \, s^{-1}}$.

This is an order of magnitude lower than that of NGC 6652B, again meaning that based on X-ray luminosity it is unlikely that NGC 6652B is a CV. The brightest CV in the X-rays in a GC, 1E1339.8+2837 in M3, occasionally shows similar levels of X-ray brightness, variability and spectral hardness as NGC 6652B. However, that source is distinctly different from NGC 6652B in optical/UV bands, with a very bright blue UV counterpart (Edmonds et al., 2004; Zhao et al., 2019), and is not detected in the radio band (Shishkovsky et al., 2020). Another population of X-ray bright CVs are intermediate polars (IPs), which radiate most of their accretion energy as X-rays at both low and high accretion rates (Patterson & Raymond, 1985). However, most IPs don't show substantial radio emission (Barrett et al., 2017), again making it unlikely that NGC 6652B could be classified as such.

Active binaries are tidally locked stars in close binaries which produce X-rays due to their high rate of rotation, and make up a large portion of faint X-ray sources in clusters. These systems generally have X-ray luminosities of $< 10^{31} \, \mathrm{erg \, s^{-1}}$ (Güdel, 2002). Additionally, the X-ray emission for coronally active stars when not flaring saturates at an X-ray luminosity of 10^{-3} of the bolometric luminosity (Vilhu & Walter, 1987). We have multiple X-ray observations of this object and have measured the average X-ray luminosity of NGC 6652B to be $\sim 2 \times 10^{34} \, \mathrm{erg \, s^{-1}}$. This makes it very unlikely that NGC 6652B is an active binary.

Given the position of NGC 6652B on the radio–X-ray luminosity plane in Figure 3.4, a possible explanation for the system is that it contains an accreting compact object. NGC 6652B shows behaviours that are different to known, typical NS X-ray binaries (NSXBs), such as Centaurus X-4 (Cen X-4). Cen X-4 is the closest NSXB at a distance of 1.2 ± 0.3 kpc (Chevalier et al., 1989), and is one of the few NSXB systems that can be studied in depth to understand how these systems behave. Cen X-4 has been in quiescence for over three decades (Hjellming et al., 1988), with its X-ray luminosity ($10^{32} \, \mathrm{erg \, s^{-1}}$) indicating low

level accretion is still occurring (Campana et al., 2000, 2004; Cackett et al., 2010; Bernardini et al., 2013). No radio emission has been seen in quiescence down to a radio luminosity limit of $\sim 10^{26}$ erg s^{-1} (Tudor et al., 2017). These observational properties are inconsistent with NGC 6652B. NGC 6652B has a 1-10 keV X-ray luminosity of $\sim 1.8 \times 10^{34}$ erg s^{-1}, and Cen X-4 only displays similar X-ray luminosities during a rise or fall between outburst and quiescence, which are short-lived phases. The radio luminosity of NGC 6652B is also at least two orders of magnitude higher than that of Cen X-4. Due to this, it is unlikely that NGC 6652B is a "typical" NSXB. NGC 6652B has a higher radio luminosity than any accreting NS observed at the same X-ray luminosity and its persistent X-ray luminosity ($\sim 10^{34}$) is a signature of unusual accretion.

Given that NGC 6652B displays observational properties inconsistent with typical NSXB, we can expand our comparison to more unusual classes of NS binaries, such as symbiotic X-ray binaries (SyXBs). SyXBs are a small subset of binary systems that contain a NS accreting from a late-type giant, with X-ray luminosities in the range of 10^{32-36} erg s^{-1} (Yungelson et al., 2019). The orbital periods of SyXBs can be several years. While the X-ray luminosity of NGC 6652B falls into the range expected for SyXBs, the source cannot be a SyXB. A CMD of the cluster NGC 6652 places the optical companion to NGC 6652B on the main sequence (Heinke et al., 2001; Engel et al., 2012), and not on the giant branch as would be needed to be classified as a SyXB. Our spectral classification of the companion to NGC 6652B as a G-type star is also inconsistent with the M-type stars expected in SyXBs. Due to these factors, NGC 6652B cannot be identified as a SyXB.

To test whether NGC 6652B could contain an accreting BH, we can compare this source to V404 Cygni, which is one of the most well studied BHXBs due to its proximity to Earth (2.39 ± 0.14 kpc, Miller-Jones et al., 2009) and well constrained orbital parameters (Casares et al., 1992; Khargharia et al., 2010). When the source transitioned into quiescence after its 2015 outburst, the X-ray

luminosity decreased to $\sim 10^{33}\,\mathrm{erg\,s^{-1}}$ and the photon index transitioned from $\Gamma \sim 1.6$ to $\Gamma \sim 2$ (Plotkin et al., 2017). The observed properties of NGC 6652B are inconsistent with these observations of V404 Cyg. NGC 6652B has a hard ($\Gamma \sim 1.3$) X-ray spectrum which is inconsistent with quiescent BHXBs which show $\Gamma \sim 2$ (Plotkin et al., 2013; Reynolds et al., 2014), making it unlikely to be a BHXB in quiescence. Further evidence against NGC 6652B containing a BH is the variable H α emission, unlike the broad H α emission BHs are expected to consistently exhibit (Casares, 2015, 2016). NGC 6652B shows double-peaked H α emission that transitions to complete absorption on a time-scale of a couple of hours as seen in Figure 3.7, which is inconsistent with known BH properties. The cause of this variation could be an intra-binary shock or changes in the ionisation of the material in the accretion disc.

3.3.3   NGC 6652B as a tMSP candidate

Based on the analysis presented in Chapter 3.2 and the inconsistencies with several "canonical" source classes in Chapter 3.3.2, a possible explanation for the dim, variable X-ray emission and radio emission seen from NGC 6652B is that this source may be a tMSP candidate in the accreting state. We observe multiple X-ray flares in the 1-10 keV band of $> 10^{34}\,\mathrm{erg\,s^{-1}}$ during the *Chandra* observation. The *Chandra* light curve in the top panel of Figure 3.2 shows that the source undergoes several X-ray flaring events on time-scales of 100s to 1000s of seconds, spending almost half of the observation in 1-10 keV X-ray flaring events up to $\sim 4.8 \times 10^{34}\,\mathrm{erg\,s^{-1}}$. The average 1-10 keV X-ray luminosity of the source during this observation is $\sim 1.8 \times 10^{34}\,\mathrm{erg\,s^{-1}}$. This is consistent with earlier observations of the source by both Coomber et al. (2011) and Stacey et al. (2012), who reported similar unusual variability on time-scales of $\sim 100\,\mathrm{s}$ and average X-ray luminosities of $\sim 2 \times 10^{34}\,\mathrm{erg\,s^{-1}}$ and $1.6 \times 10^{34}\,\mathrm{erg\,s^{-1}}$ respectively.

This behaviour is similar to the recently identified tMSP candidate 3FGL J0427.9-6704 (J0427, Li et al., 2020). J0427 was observed to be in the flaring

mode for the entirety of a 20 hr observation, exhibiting continuous flaring up to $\sim 2 \times 10^{34} \, \mathrm{erg \, s^{-1}}$ on time-scales of 10s to 100s of seconds. It is possible that we are also observing NGC 6652B in the flare-dominated accretion mode of tMSPs due to the magnitude and frequency of the flaring events over the course of the X-ray observation. The long-duration flaring behaviour of NGC 6652B is also similar to that of known tMSPs, such as XSS J12270-4859 (J12270) which has been shown to display several flares on time-scales of 100s of seconds during its accretion-dominated phase (de Martino et al., 2010, 2013), and J1023, which displayed a long flaring mode of duration $\sim$10 hr after its state transition in 2013 (Tendulkar et al., 2014).

NGC 6652B also displays similarities to the new tMSP candidate 4FGL J0540.0-7552 (Strader et al., 2021). This source displays a hard X-ray spectrum, and X-ray and optical variability. Additionally, the source appears to consistently be in an X-ray flaring mode, similar to the behaviour we observe in NGC 6652B and reported for J0427. This indicates that persistent flaring activity could be a common property in tMSPs.

The radio continuum behaviour of NGC 6652B is also consistent with that of J0427. NGC 6652B displays suggestive evidence for variability throughout the duration of the VLA observation, and J0427 shows some variation in radio emission with no flaring events (Li et al., 2020). This variation is also seen on longer time-scales, with previous observations of NGC 6652B from 2016 also showing similar moderate variability. Both sources show no evidence that the radio emission is eclipsed, which is consistent with steady radio outflow.

When we split the radio and X-ray light curves of NGC 6652B by X-ray count rate and split them into regimes of high ($>0.09 \, \mathrm{counts/s}$) and low ($\le 0.09$ counts/s) X-ray counts, there is a hint that radio luminosity may decrease as X-ray luminosity increases and vice versa. On the radio–X-ray luminosity plane (Figure 3.4), NGC 6652B sits on the track accreting BHs occupy, and the source displays the same behaviour as J1023, where its position on this plot changes

91

depending on what X-ray count rate regime it is in, allowing it to move above or below the BH correlation. However, it should be noted that this parallel with J1023 is not exact. The position of J1023 changes between the low and high mode, whereas it is unknown whether NGC 6652B has any X-ray modes other than the flaring mode. J0427 also changes position on the radio–X-ray luminosity plane, and sits on the accreting BH track. Both NGC 6652B and J0427 display a radio/X-ray luminosity ratio much higher than any known tMSP, however J0427 displays a higher radio luminosity with higher X-ray luminosities and instead undergoes marginal shifts along the BH correlation during changes in luminosity.

X-ray spectral analysis (Chapter 3.2.3) indicates that there is some evidence for changes in the hardness of the emission and column density during different X-ray count rate regimes. For low counts (≤ 0.09 counts/s) the X-ray emission is harder, while it is slightly softer emission at higher count rates. These properties have been previously observed, with both Coomber et al. (2011) and Stacey et al. (2012) observing a tendency for harder emission to be present in low count rate regimes. Additionally, there is marginal evidence that the column density towards the source changes subtly based on the X-ray count rate regime (intrinsic N_H in Table 3.3). While this inconsistency is only seen to a $\geq 1\sigma$ level as seen in the contour plots shown in Figure 3.5, this behaviour of NGC 6652B has also been previously noted by Coomber et al. (2011) and Stacey et al. (2012), with Stacey et al. (2012) concluding that these changes were due to an instability involving the propeller effect (Illarionov & Sunyaev, 1975). Furthermore, this conclusion was made before the confirmation of the existence of tMSPs, and since their discovery it has been discussed that the propeller effect may be present in these systems (Papitto & Torres, 2015; Deller et al., 2015). This suggests that we may be observing NGC 6652B in an accreting state similar to that of tMSPs where the propeller effect is present. The changes in column density and the presence of intrinsic absorption would then come from the propeller-driven outflow. This provides a more physical basis for identifying NGC 6652B as a possible tMSP

candidate.

Gamma-ray emission has been detected from NGC 6652 (The Fermi LAT collaboration, 2010), which would be consistent with a tMSP being present within the cluster. Accreting tMSPs are known to be gamma-ray sources, with the gamma-ray flux of these systems increasing by a factor of ~ 5 during a state change to the accreting state (Stappers et al., 2014; Deller et al., 2015). MSPs are also gamma-ray emitters, and NGC 6652 contains one known MSP (DeCesar et al., 2011, 2015) which is not associated with NGC 6652B. It is unclear whether the gamma-ray emission originates from one of these two sources or some other unidentified source, and further investigation into this emission is needed.

NGC 6652B also displays double-peaked H α emission, which is a signature for accreting binary systems (e.g., Casares, 2015, 2016). However, the H α emission is variable, and goes from double-peaked emission to full absorption over a time-scale of a couple of hours. This is similar to the behaviour of the NS binary J1417.7-4402 (J1417, Swihart et al., 2018). J1417 displays H α profiles that vary in amplitude and shape over the course of the 5.4 day orbital period of the binary system, and it was thought that these variations could be explained by the interactions between the pulsar wind, and a magnetically driven wind from the companion star. If such an intra-binary shock is present in NGC 6652B, it would disfavour the presence of an accretion disc. However, J1417 is a different kind of system to NGC 6652B (see Chapter 3.3.1), consisting of a giant companion in a wide orbit, and may display behaviours different to those present in NGC 6652B. These variations could also be caused by changes in the accretion disc. As the material in the disc becomes ionised, the emission features would disappear, potentially explaining the rapid change from emission to absorption seen in the H α profile of NGC 6652B.

While NGC 6652B displays many properties consistent with known tMSPs and tMSP candidates, there are some inconsistencies with this classification. A feature distinct to tMSPs, the bimodal X-ray flux distribution, is not seen in the

X-ray light curves of NGC 6652B. The lack of a bimodal X-ray flux distribution may be due to a combination of the light curve being dominated by flares and/or the effect of the relatively large distance.

Another feature distinct to tMSPs is the anti-correlation between the radio and X-ray emission between the "active" and "passive" modes. As shown by Bogdanov et al. (2018) through simultaneous *Chandra* and VLA observations of J1023, a transition into the X-ray low mode is accompanied with a corresponding increase in radio flux density, with the radio flux density decreasing as the X-ray count rate increases on the transition back to the high mode. A consequence of this behaviour is that during the X-ray low mode, tMSPs can enter parts of the radio–X-ray luminosity plane that were thought to be exclusive to accreting BHs.

We do not observe any clear evidence of anti-correlated behaviour between the radio and X-ray light curves of NGC 6652B (Figure 3.2). For a robust characterisation of the anti-correlation in and to test this method on tMSPs, we calculated the ZDCF for J1023, shown in the bottom panel of Figure 3.3, based on the radio and X-ray light curves presented in Bogdanov et al. (2018). The radio light curve is binned at 30 s, and the X-ray light curve is binned at 25 s. These light curves show an X-ray flare and several radio flares, so we investigated how the correlation function behaves when these flaring events are included in and removed from the datasets. The flares are those identified in Bogdanov et al. (2018). With the flares removed from the datasets, we see a strong anti-correlation between the two light curves at a time lag of ~ 0 hr. However, it is clear that the flares in tMSPs (which do not show any anti-correlation between the X-rays and radio data) can affect the correlation function, to a level where significant anti-correlation in a light curve dominated by flares could vanish entirely. When we calculate the ZDCF for J1023 using the full datasets (including the flares), the anti-correlation disappears (Figure 3.3). We do not see any clear anti-correlation in the correlation function of NGC 6652B to $> 99\%$. A possible reason for this is that NGC 6652B is much further away than J1023, such that we do not have sufficient sensitiv-

ity to differentiate between the canonical high and low modes. We also observe NGC 6652B in a largely X-ray flare dominated state, which may also explain why we don't observe any significant anti-correlation between any existing X-ray high and low mode, again lending credence that NGC 6652B, J0427, and 4FGL J0540.0-7552, can be considered "flare-type" tMSPs.

3.4 Conclusions and future work

We conclude based on simultaneous *Chandra* and VLA observations in addition to older optical spectra that NGC 6652B is best explained as a tMSP candidate in the accreting state. NGC 6652B displays similar behaviour to other tMSPs and tMSP candidates, most prominently several X-ray flares observed over the course of the *Chandra* observation. This behaviour is similar to the flaring behaviour of the tMSPs PSR J1023+0038 and XSS J12270-4859, and the new tMSP candidates 3FGL J0427.9-6704 (Li et al., 2020) and 4FGL J0540.0-7552 (Strader et al., 2021). This prolonged flaring behaviour suggests that we are observing NGC 6652B in a flare-dominated mode which is consistent with that observed from 3FGL J0427.9-6704 and 4FGL J0540.0-7552. The presence of doubled-peaked H α emission in previous optical spectra is indicative of the presence of an accretion disc in the system at one point in the past five years, further supporting the conclusion that we are observing NGC 6652B in the accreting state. However, we observe a transition to complete H α absorption, and an alternate explanation to this is that the H α profile in this system is caused by the shocks between the pulsar wind and the wind from the companion star, similar to those observed in J1417.7-4402 (Swihart et al., 2018).

Other scenarios as to the nature of NGC 6652B include a CV, an active binary, NSXB, and a BHXB; however each of these scenarios are considered less likely than a tMSP candidate explanation. NGC 6652B has a higher radio and X-ray luminosity than known CVs and a higher X-ray luminosity than known active binaries. NGC 6652B has a higher radio luminosity than NSs with similar X-ray

luminosities, and while NGC 6652B sits near the correlation for accreting BHs, it is unlikely to be a BHXB as it displays a hard X-ray spectrum.

An important caveat to the classification of NGC 6652B as a tMSP candidate is that we cannot confirm that it is a tMSP until a state change is observed. Further observations of the source are needed. In particular, NGC 6652B would need to be monitored for any transition into the rotation-powered MSP state, which would confirm its transitional nature. Additional simultaneous radio and X-ray observations would allow for any correlation between the radio and X-ray emission to be probed, and also indicate whether the source is still in a mode dominated by X-ray flares. Further optical spectroscopy with a larger (8 m) telescope would allow for a more detailed study of the optical counterpart. However, identifying new tMSP candidates such as NGC 6652B is still of great importance to tMSP science as it highlights the range of interesting multiwavelength behaviours that these sources exhibit, and again demonstrates the usefulness of simultaneous radio and X-ray observations for identifying known observational characteristics of tMSPs.

CHAPTER 4

THE FIRST RADIO AND X-RAY LIMITS ON THE DETACHED BLACK HOLES IN NGC 3201

Adapted from:

This chapter is my own work except for the following. Radio data acquisition was conducted by J. C. A Miller-Jones. Radio data were calibrated and images produced by V. Tudor. F. Göttgens provided the rotational velocities and the stellar radii for the stellar companions to the BHs in the cluster. S. Kamann assisted with the calculations of the rotation rates of some stellar companions to the BHs. J. C. A. Miller-Jones assisted with the calculations of the BH mass accretion rates. Discussions regarding the interpretation of the results were contributed by my supervisory panel – A. Bahramian, J. C. A. Miller-Jones, and A. Kawka. Further discussions were also contributed by F. Göttgens, J. Strader, L. Chomiuk, S. Kamann, S. Dreizler, C. O. Heinke, T. Husser, T. J. Maccarone, E. Tremou, and Y. Zhao. I drafted the manuscript and distributed it to all co-authors for proofreading. All co-authors provided input and feedback on the manuscript until the final version was produced.

Following the identification of an interesting radio and X-ray source for follow-up study in Chapter 3, we now turn our attention to another GC. The cluster that is the focus of this chapter is NGC 3201, which has a mass of $1.41 \times 10^5 M_\odot$ and is located at a distance of 4.74 ± 0.04 kpc (Baumgardt & Vasiliev, 2021). NGC 3201 has comprehensive radio, X-ray and optical coverage, making it ideal for searching for exotic binary systems. Our goal is to provide a comprehensive list of energetic sources within NGC 3201 through studying the radio and X-ray sources in the cluster, and exploring the radio and X-ray properties of interesting sources discovered through optical studies of the cluster.

NGC 3201 has recently become an important cluster for study of binary and BH dynamics in GCs, with the discovery of two detached BHs (and one candidate) in the cluster through observations using the MUSE instrument (Bacon et al., 2010). A large survey of several Galactic GCs is being conducted with MUSE enabling the spectra of several thousand stars per cluster to be obtained (Husser et al., 2016; Kamann et al., 2018). Through radial velocity variations of sources

within NGC 3201, Giesers et al. (2018, 2019) detected two BHs of mass $4.53 \pm 0.21 M_\odot$ and $7.68 \pm 0.5 M_\odot$, and one candidate BH of mass $4.4 \pm 2.8 M_\odot$. All three sources are in detached binary systems, meaning there is very little (if any) mass transfer onto the compact object. Further analyses of the MUSE data have investigated the binary population within the cluster (Giesers et al., 2019), and have categorised various emission line sources (Göttgens et al., 2019).

Beyond the expected populations of MSPs, CVs and ABs, another group of rare binaries also found in GCs are those with stripped companion stars. These systems are called sub-subgiants (SSGs) if these stars are fainter than subgiants but redder than a main sequence star when placed on a colour-magnitude diagram, and called red stragglers if they are brighter than subgiants but redder than normal giants (Geller et al., 2017a). These stars have been observed to be X-ray sources (van den Berg et al., 1999). A possible formation channel for these systems is through grazing tidal captures, resulting in a stripped, underluminous subgiant star (Ivanova et al., 2017; Shishkovsky et al., 2018). A total of 65 SSGs and red stragglers in 16 GCs have been identified (Geller et al., 2017a), with 23 of these sources being faint ($L_X \sim 10^{30-31}$erg/s) X-ray sources. Binary evolution is crucial in SSG formation, with this formation channel being the most prevalent, especially in GCs (Geller et al., 2017a,b).

In this chapter, we present the results of a multiwavelength study of exotic binaries in NGC 3201 using the MAVERIC survey and the MUSE GC survey. We identify 42 sources of various classes within the half-light radius of the cluster. We also present the first radio and X-ray limits on the detached BHs in NGC 3201. Section 4.1 details our catalogue selection and cross-matching taking into account coordinate uncertainties. Section 4.2 presents the sources considered in this chapter and possible interpretations of their natures. Section 4.3 presents a discussion of these results, including an interpretation as to what the radio and X-ray limits on the detached BHs imply for the presence of accretion in these systems, how the number of XRBs in the cluster compares to other clusters, and

an overview of the underluminous SSGs that are present in the cluster.

4.1 Data and Reduction

4.1.1 Catalogue selection

4.1.1.1 The MAVERIC Survey

The MAVERIC survey contains a list of both radio and X-ray sources that are present in NGC 3201. NGC 3201 has been observed for a total of 18.1 hr with the ATCA, and catalogues of sources detected with significance of $> 5\sigma$ and $> 3\sigma$ were compiled (Tudor et al., 2022). The 5σ catalogue represents radio sources that have a confident detection, and are the main radio sources we consider in this chapter. The sources in the 3σ catalogue are only considered if they have a multiwavelength counterpart (e.g., optical or X-ray) that provides further evidence that there is actually a source present at that location.

The X-ray source catalogue of NGC 3201 contains 47 sources that are associated with NGC 3201 characterised by a detection quality parameter. This parameter indicates the confidence of the source detection. This parameter is discussed in depth in Section 4.2 in Bahramian et al. (2020), and is calculated based on the minimum false probability value of the source and the source count rate. A minimum false probability value of $< 1\%$ and a net count ≥ 5 is a confident detection (detection quality is 0), whereas a minimum false probability value $< 1\%$ and a net count < 5 is a marginal detection (detection quality is 1). For this chapter, we consider all sources in the X-ray source catalogue for NGC 3201 with a detection quality of 0 or 1.

4.1.1.2 Optical surveys

In this chapter, optical surveys serve two purposes. Firstly, photometric surveys will allow us to construct colour-magnitude diagrams (CMDs) to investigate

where a source lies relative to other sources in the cluster. Secondly, spectroscopic studies will allow us to search for radial velocity variations and identify sources in binary systems, allowing us to estimate the orbital parameters and the mass of a possibly invisible companion.

To investigate the photometric properties of the cluster, we used data from the HST UV Globular Cluster Survey (HUGS, Piotto et al., 2015; Nardiello et al., 2018). This survey includes photometric catalogues of 56 GCs and one open cluster in five photometric bands (F275W, F336W, F438W, F606W, and F814W). These data give us insight into the stellar populations in NGC 3201, and where various sources will fall on the CMD.

To investigate the spectroscopic properties of sources within the cluster, we used catalogues created by MUSE. NGC 3201 has been studied extensively with MUSE since the first discovery of a detached BH candidate within the cluster (Giesers et al., 2018). For our purposes we have used data from the binary and emission line catalogues of NGC 3201 produced by MUSE (Giesers et al., 2019; Göttgens et al., 2019).

4.1.2   X-ray data reduction

NGC 3201 has been observed once by *Chandra* using ACIS-S in 2010 for $85\,\text{ks}$ under the observation ID 11031. To further investigate the X-ray properties of the cluster and perform X-ray spectroscopy beyond the scope of the analysis presented by Bahramian et al. (2020), we downloaded and reduced this dataset. The analysis in Bahramian et al. (2020) included X-ray spectral fitting of each X-ray source with three spectral models. The models considered were a power-law emission model, an apec emission spectrum from ionised diffuse gas, and a blackbody radiation model.

CIAO 4.12.1 and CALDB 4.9.3 (Fruscione et al., 2006) were used to reduce and reprocess the data. The data were reprocessed using `chandra_repro`, and source and background spectra were extracted using `specextract`. Background

and source regions varied depending on the position of the source in the X-ray image, and source crowding was not an issue. XSPEC 12.11 (Arnaud, 1996) was used to perform X-ray spectral analysis.

4.1.3 Catalogue cross-matching and source identification

Prior to any catalogue cross-matching, we first restricted the MAVERIC sample to only consider sources within the half-light radius of NGC 3201 (3.1'). Anything outside this radius was considered to have a higher chance of not being associated with the cluster, either as a foreground or background source. The MAVERIC survey listed 39 radio sources with a detection limit of 5σ associated with NGC 3201, of which 13 sources are within the half-light radius. The accompanying X-ray catalogue listed 24 X-ray sources with a detection quality of 0 or 1 within the half-light radius of the cluster.

To identify counterparts across the catalogues and surveys we are considering, we initially searched for matches within $1''$ of the input coordinates. This was a conservative threshold to account for the uncertainties associated with our radio and X-ray coordinates. The nominal uncertainty in the radio coordinates is $< 0.1''$. The uncertainty in the X-ray coordinates is a combination of the overall frame alignment and statistical precision of the individual X-ray sources. Through cross-matching with the HUGS catalogue, we determined that the uncertainty in the frame alignment is $\sim 0.3''$. The average uncertainty in the statistical precision of individual X-ray sources was determined by calculating the separation between the centroid X-ray coordinates (coordinates estimated through centroiding) and the reconstructed X-ray coordinates (coordinates estimated through X-ray image reconstruction[1]), with the coordinates provided in Bahramian et al. (2020). This value is $\sim 0.3''$, giving an overall uncertainty in X-ray coordinates of $\sim 0.42''$. For the optical/X-ray sources we discuss in § 4.2.3, we calculate the individual X-ray source uncertainty for each potential cross-match. Any matches identified

---

[1]This is a standard method used in the software package ACIS EXTRACT (Broos et al., 2010).

across multiple catalogues were also visually inspected to check the quality of the cross-match and identify any other possible candidate matches within errors. This also allowed us to reject any initial cross-matches between the catalogues with a difference between the input coordinates of $\gtrsim 0.5''$.

4.2 Results

Table 4.1: The 42 sources studied in this work, with the detached BHs listed first. The coordinates listed for the MUSE binary sources are taken from (Giesers et al., 2019). For the optical/X-ray sources and X-ray only sources, we take the X-ray coordinates from the MAVERIC X-ray source catalogue. For the remaining radio only sources, we give radio coordinates from the MAVERIC radio survey. The source type column indicates which survey the source is detected in. MUSE binaries are detected in the MUSE binary catalogue of NGC 3201 (Giesers et al., 2019), optical sources are detected in the HUGS survey (Piotto et al., 2015; Nardiello et al., 2018), X-ray sources are detected in the MAVERIC X-ray source catalogue (Bahramian et al., 2020), and radio sources are detected in the MAVERIC radio survey (Shishkovsky et al., 2020; Tudor et al., 2022). The final column indicates the likely nature of each source.

Source	RA	Dec	Source type	Likely nature
ACS ID #12560	10:17:37.090	-46:24:55.332	MUSE binary/detached BH	Cluster member
ACS ID #21859	10:17:39.233	-46:24:24.876	MUSE binary/detached BH	Cluster member

Continued on next page

Table 4.1 – continued from previous page

Source	RA	Dec	Source type	Likely nature
ACS ID #5132	10:17:36.082	-46:25:33.060	MUSE binary/detached BH	Cluster member
CXOU J101737.58-462352.2	10:17:37.589	-46:23:52.246	MUSE binary/X-ray source	Cluster member
CXOU J101735.57-462450.5	10:17:35.582	-46:24:50.562	MUSE binary/X-ray source	Cluster member
ACS ID #14749	10:17:33.146	-46:25:07.428	MUSE binary	Cluster member
ACS ID #11405	10:17:39.257	-46:25:11.892	MUSE binary	Cluster member
CXOU J101730.49-462442.4	10:17:30.489	-46:24:42.437	Optical/X-ray source	Cluster member
CXOU J101727.83-462500.6	10:17:27.836	-46:25:00.595	Optical/X-ray source	Background?
CXOU J101736.06-462422.5	10:17:36.070	-46:24:22.619	Optical/X-ray source	Cluster member
CXOU J101735.79-462418.1	10:17:35.795	-46:24:18.101	Optical/X-ray source	Cluster member
CXOU J101735.85-462346.1	10:17:35.842	-46:23:46.064	Optical/X-ray source	Cluster member
CXOU J101729.85-462440.6	10:17:29.824	-46:24:40.692	Radio source/X-ray source	Background
CXOU J101729.25-462644.0	10:17:29.259	-46:26:43.954	Radio source/X-ray source	Background
CXOU J101736.17-462539.5	10:17:36.173	-46:25:39.526	X-ray source	Background?
CXOU J101742.96-462509.1	10:17:42.939	-46:25:09.426	X-ray source	Background?
CXOU J101737.30-462332.0	10:17:37.313	-46:23:32.089	X-ray source	Background?

Table 4.1 – continued from previous page

Source	RA	Dec	Source type	Likely nature
CXOU J101730.77-462348.2	10:17:30.757	-46:23:48.286	X-ray source	Background?
CXOU J101741.33-462554.6	10:17:41.361	-46:25:55.006	X-ray source	Background?
CXOU J101730.60-462555.2	10:17:30.619	-46:25:55.121	X-ray source	Background?
CXOU J101725.45-462452.3	10:17:25.461	-46:24:52.434	X-ray source	Background?
CXOU J101739.24-462242.6	10:17:39.246	-46:22:42.625	X-ray source	Background?
CXOU J101726.64-462644.9	10:17:26.646	-46:26:45.276	X-ray source	Background?
CXOU J101722.88-462334.0	10:17:22.886	-46:23:33.994	X-ray source	Background?
CXOU J101730.66-462714.9	10:17:30.709	-46:27:14.796	X-ray source	Background?
CXOU J101739.49-462200.7	10:17:39.485	-46:22:00.617	X-ray source	Background?
CXOU J101723.71-462633.7	10:17:23.700	-46:26:33.590	X-ray source	Background?
CXOU J101727.26-462214.2	10:17:27.251	-46:22:14.315	X-ray source	Background?
CXOU J101749.73-462243.3	10:17:49.743	-46:22:43.129	X-ray source	Background?
ATCA J101742.667-462454.262	10:17:42.667	-46:24:54.262	Radio source	Background?
ATCA J101726.705-462504.558	10:17:26.705	-46:25:04.558	Radio source	Background?
ATCA J101732.309-462626.163	10:17:32.309	-46:26:26.163	Radio source	Background?

Table 4.1 – continued from previous page

Source	RA	Dec	Source type	Likely nature
ATCA J101731.164-462642.881	10:17:31.164	-46:26:42.881	Radio source	Background?
ATCA J101744.735-462631.964	10:17:44.735	-46:26:31.964	Radio source	Background?
ATCA J101746.690-462306.033	10:17:46.690	-46:23:06.033	Radio source	Background?
ATCA J101743.829-462236.644	10:17:43.829	-46:22:36.644	Radio source	Background?
ATCA J101723.716-462322.616	10:17:23.716	-46:23:22.616	Radio source	Background?
ATCA J101721.425-462536.169	10:17:21.425	-46:25:36.169	Radio source	Background?
ATCA J101748.939-462245.159	10:17:48.939	-46:22:45.159	Radio source	Background?
ATCA J101727.933-462712.667	10:17:27.933	-46:27:12.667	Radio source	Background?
ATCA J101749.983-462254.064	10:17:49.983	-46:22:54.064	Radio source	Background?
ATCA J101740.920-462144.955	10:17:40.920	-46:21:44.955	Radio source	Background?

Through cross-matching the MAVERIC survey with the HUGS survey and the MUSE binary and emission line catalogue we identified two MUSE binary sources that have X-ray emission, five X-ray sources within the HUGS survey, and two radio/X-ray counterparts from within the MAVERIC survey. We also identify 15 X-ray sources and 13 radio sources within the half-light radius of NGC 3201. These sources are shown in Table 4.1.

Throughout this chapter, there are multiple times where upper limits on the radio and X-ray luminosities are calculated. For consistency, we used the same approach for each source. To calculate a 3σ upper limit on the 5.5 GHz radio flux density, we take three times the central RMS noise of the 5.5 GHz image. This gives a 3σ upper limit of $11.7\,\mu\text{Jy}$ (Tudor et al., 2022). We note that Tremou et al. (2018) takes a different value 3σ upper limit for the radio images of NGC 3201. The value used by Tremou et al. (2018) is the 3σ upper limit of the stacked 7.25 GHz radio images. To retain sensitivity to steep spectrum sources, we have instead chosen to use the 5.5 GHz image and catalogue.

To calculate a 90% upper limit on the 1-10 keV X-ray flux of a source, we first determined the source and background counts. Source counts are determined from a circular region of radius $1.5''$ around the source coordinates, and background counts are determined using an annulus region of inner radius $1.9''$ and outer radius $12.3''$. The background counts are normalised, and we then took the 90% upper limit on the X-ray count rate using the method of Kraft et al. (1991). This count rate upper limit was converted to a flux upper limit using the exposure time of the *Chandra* observation and modelling the emission with a power law with an index of $\Gamma = 1.7$. The flux was converted to a luminosity upper limit using $4\pi d^2 F_\text{x}$. In all conversions to luminosity, the distance to NGC 3201 is assumed to be 4.74 kpc (Baumgardt et al., 2019).

Table 4.2: The 3σ 5.5 GHz radio upper limits and the 90% 1-10 keV X-ray upper limits of the two confirmed and one candidate BH in NGC 3201.

Source	5.5 GHz flux density (µJy)	5.5 GHz L_{R} (erg s^{-1})	1-10 keV X-ray flux (erg s^{-1} cm^{-2})	1-10 keV L_{X} (erg s^{-1})
ACS ID #12560	< 11.7	$< 1.7 \times 10^{27}$	$< 5.2 \times 10^{-16}$	$< 1.4 \times 10^{30}$
ACS ID #21859	< 11.7	$< 1.7 \times 10^{27}$	$< 3.2 \times 10^{-16}$	$< 8.6 \times 10^{29}$
ACS ID #5132	< 11.7	$< 1.7 \times 10^{27}$	$< 3.7 \times 10^{-16}$	$< 9.9 \times 10^{29}$
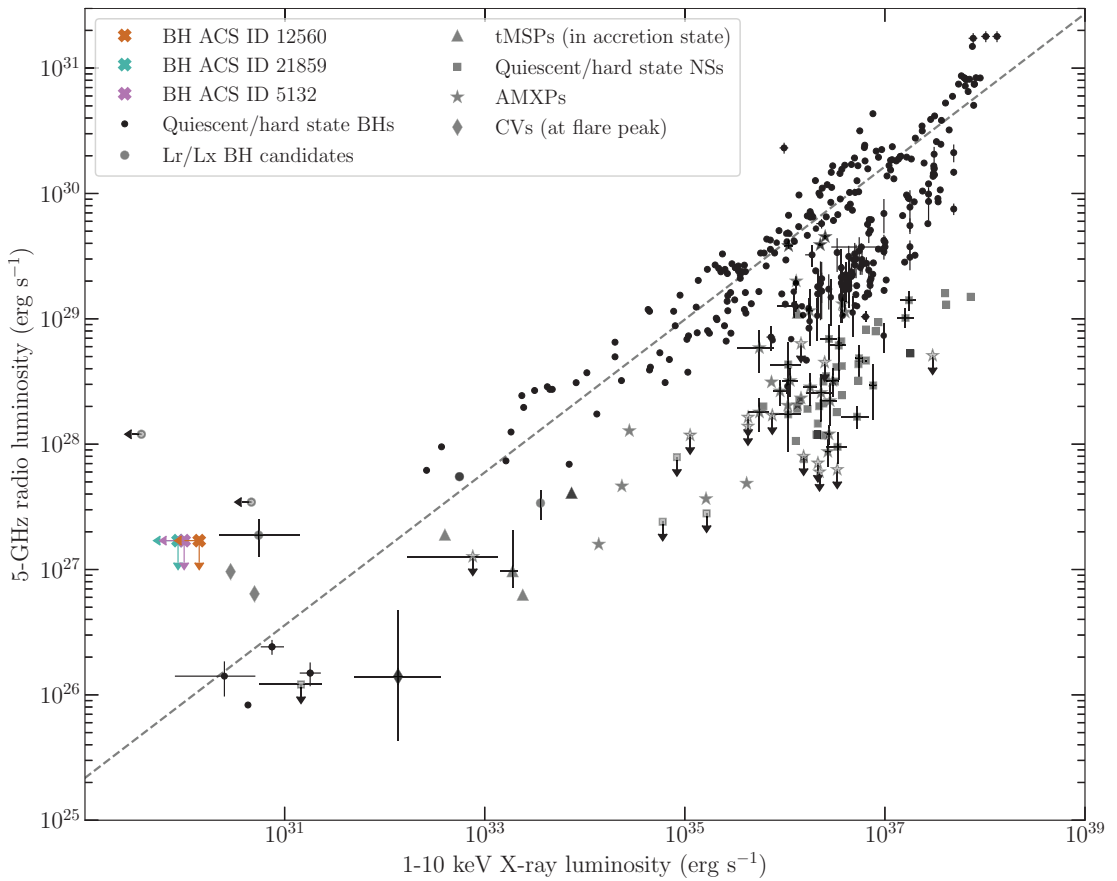
Figure 4.1: The 5 GHz radio and 1-10 keV X-ray luminosity limits for the BHs in NGC 3201 shown as crosses and indicated by their ACS ID numbers. The other points represent various other classes of accreting binary systems and are compiled from the database provided by Bahramian et al. (2018a).

4.2.1 Known BHs

NGC 3201 contains two dynamically confirmed BHs and one candidate BH. Here we discuss the available radio and X-ray data from the MAVERIC survey for these systems, and calculate upper limits on the radio and X-ray emission of these sources. These limits are listed in Table 4.2, and Figure 4.1 shows these sources on the radio–X-ray luminosity plane.

All three sources have no radio counterpart at 5.5 GHz. We take the 3σ upper limit on the 5.5 GHz radio flux density to be 11.7 µJy (three times the central RMS), which implies a 3σ 5.5 GHz radio luminosity upper limit of $1.7 \times 10^{27}\,\mathrm{erg\,s^{-1}}$. There is also no X-ray detection for any of the three sources, and we discuss the 90% 1-10 keV X-ray upper limits individually for each source.

ACS ID #12560 was the first BH discovered in NGC 3201 by Giesers et al. (2018). The source has a binary orbital period of 167.00 ± 0.09 days, with an eccentricity of 0.61 ± 0.02. The minimum mass of the BH is $4.53 \pm 0.21\ M_{\odot}$. The 90% 1-10 keV X-ray flux upper limit is $5.2 \times 10^{-16}\,\mathrm{erg\,s^{-1}\,cm^{-2}}$, corresponding to a 90% 1-10 keV X-ray luminosity upper limit of $1.4 \times 10^{30}\,\mathrm{erg\,s^{-1}}$.

ACS ID #21859 was discovered by Giesers et al. (2019). The binary orbital period is 2.2422 ± 0.0001 days, much shorter than the other two BHs, and the orbital eccentricity is 0.07 ± 0.04. The minimum mass of the BH is $7.68 \pm 0.5\ M_{\odot}$. The 90% upper limit on the 1-10 keV X-ray flux is $3.2 \times 10^{-16}\,\mathrm{erg\,s^{-1}\,cm^{-2}}$, giving a 90% 1-10 keV X-ray luminosity upper limit of $8.6 \times 10^{29}\,\mathrm{erg\,s^{-1}}$.

ACS ID #5132 is a candidate BH discovered by Giesers et al. (2019). The binary orbital period is 764 ± 11 days with an eccentricity of 0.28 ± 0.16. The minimum mass of the system is $4.40 \pm 2.82\ M_{\odot}$. The 90% upper limit on the 1-10 keV X-ray flux of the source is $3.7 \times 10^{-16}\,\mathrm{erg\,s^{-1}\,cm^{-2}}$, implying a 90% 1-10 keV X-ray luminosity upper limit of $9.9 \times 10^{29}\,\mathrm{erg\,s^{-1}}$.

4.2.2 Sub-subgiants and red stragglers

The MUSE binary catalogue (Giesers et al., 2019) lists four SSGs within the field-of-view of the survey, identified based on positions of the sources on the cluster CMD and by fitting the radial velocity variations observed with a Keplerian orbit. Two of these sources are also emission line sources as noted in the emission line catalogue (Göttgens et al., 2019). These four sources are discussed in depth below. Additionally, we have discovered one new candidate red straggler system with X-ray emission, based on its position on the cluster CMD. Here we discuss the multiwavelength properties of these systems.

4.2.2.1 CXOU J101730.49-462442.4

CXOU J101730.49-462442.4 is an X-ray source listed by the MAVERIC survey (Shishkovsky et al., 2020; Bahramian et al., 2020) that is consistent with an optical source in the HUGS survey (source R0001757). The optical and X-ray coordinates are consistent to within $< 0.1''$. Based on its position on the CMD of NGC 3201 constructed from the HUGS F606W and F814W magnitudes (see Figure 4.2), it is a red straggler system. We classify the source as a red straggler instead of a SSG as it is brighter than subgiants but lies redward of the giant branch. This source has a F606W magnitude of 16.8784, and a probability of 97.8% of being a cluster member (Piotto et al., 2015; Nardiello et al., 2018). The source is not covered by current MUSE observations of the cluster.

From the MAVERIC survey (Bahramian et al., 2020), this source is best fit by an apec emission spectrum from ionised diffuse gas, with a power-law model having a relative probability of 0.694. We fit an absorbed apec model (`tbabs`×`cflux`×`apec`) to the spectrum to calculate the 1-10 keV X-ray flux of the source. To estimate the cluster hydrogen column density, we use the $E(B-V)$ values estimated by Harris (1996), and the correlations estimated by Bahramian et al. (2015) and Foight et al. (2016). This gives a hydrogen column density of $N_H = 2 \times 10^{21}\,\mathrm{cm}^{-1}$. By freezing the absorption parameter in our model

to this value, the 1-10 keV X-ray flux is $5.8^{+2.8}_{-1.8} \times 10^{-15}$ erg s^{-1} cm^{-2} with an electron temperature of $kT = 3.9^{+6.2}_{-1.6}$ keV. This implies a 1-10 keV luminosity of 1.6×10^{31} erg s^{-1}. There is no radio detection of this source so we adopt a 3σ 5.5 GHz flux density upper limit of 11.7 µJy, corresponding to a 5.5 GHz luminosity upper limit of 1.7×10^{27} erg s^{-1}.

4.2.2.2   CXOU J101737.58-462352.2/ACS ID #22692

CXOU J101737.58-462352.2 is a SSG star detected by MUSE (Giesers et al., 2019). This system has an orbital period of 5.1038 ± 0.0004 days and a low eccentricity of 0.02 ± 0.03, with a F606W magnitude of 17.25. This source shows X-ray emission and varying Hα emission lines (Giesers et al., 2019; Göttgens et al., 2019).

This source is detected as an X-ray source in the MAVERIC survey, and its X-ray spectrum is best fit with a blackbody radiation model. We fit an absorbed blackbody radiation model (`tbabs`×`cflux`×`bbodyrad`) to the X-ray spectrum, with the hydrogen column density frozen to the cluster value, to calculate the 1-10 keV X-ray flux from the source. The 1-10 keV X-ray flux of the source is $1.1^{+0.6}_{-0.4} \times 10^{-15}$ erg s^{-1} cm^{-2}, corresponding to a 1-10 keV X-ray luminosity of 3.0×10^{30} erg s^{-1}, and the electron temperature is $kT = 0.3 \pm 0.1$ keV. This source has no radio counterpart, with a 3σ 5.5 GHz upper limit of 11.7 µJy, implying a 5.5 GHz luminosity upper limit of 1.7×10^{27} erg s^{-1}. The X-ray luminosity of this source is the highest for the SSGs detected by MUSE, which could be linked to its short orbital period.

The minimum invisible mass of this system is $0.35 \pm 0.03\ M_\odot$. By assuming that the minimum invisible mass has Gaussian errors and by isotropically sampling the inclination angle between $\cos 5°$ and $\cos 90°$, we use a Monte Carlo simulation to estimate the most probable mass of the unseen companion. We use a lower bound on the inclination angle of 5° as for inclination angles smaller than this, no radial velocity variations would be observed. The unseen companion has

a median mass of 0.408 $M_\odot$, with a 90% confidence interval of 0.322 $M_\odot$ to 1.104 $M_\odot$. This indicates that the companion object in this system is either a white dwarf or another type of star, such as a M dwarf.

4.2.2.3 CXOU J101735.57-462450.5/ACS ID #13438

CXOU J101735.57-462450.5 is a SSG star detected by MUSE (Giesers et al., 2019). The orbital period of this system is 5.9348 ± 0.0003 days, and the eccentricity is the same as the SSG discussed above at 0.02 ± 0.03. The F606W magnitude of this system is 17.17, and the source shows X-ray emission with several MUSE spectra of this star showing a partially filled in Hα absorption line (Giesers et al., 2019; Göttgens et al., 2019).

This source is listed as an X-ray source in the MAVERIC survey, and is best fit by an apec model. By fitting an absorbed apec model to the X-ray spectrum of this source (and freezing the hydrogen column density to the cluster value), we calculate the 1-10 keV X-ray flux of this source to be $5.0^{+4.5}_{-2.8} \times 10^{-16}$ erg s^{-1} cm^{-2}, with an electron temperature of $kT = 1.1^{+0.4}_{-0.3}$ keV. This X-ray flux implies a 1-10 keV X-ray luminosity of 1.3×10^{30} erg s^{-1}. There is no radio counterpart to this source, with a 3σ 5.5 GHz upper limit of 11.7 μJy, implying a 5.5 GHz luminosity upper limit of 1.7×10^{27} erg s^{-1}.

The minimum invisible mass of this system is the same as the above source, CXOU J101737.58-462352.2, at 0.35 ± 0.03 $M_\odot$. A similar Monte Carlo simulation as described above indicate that the median mass of the invisible companion is 0.408 $M_\odot$, with a 90% confidence interval of 0.322 $M_\odot$ to 1.104 $M_\odot$. Again, the companion object is either a white dwarf or another star.

4.2.2.4 ACS ID #14749

This SSG with ACS ID #14749 is a known SSG star with a reported period of 10.0037 ± 0.002 days (Kaluzny et al., 2016). This source is detected by MUSE with a period of 10.006 ± 0.002 days, an eccentricity of 0.09 ± 0.07, and a F606W

magnitude of 17.03. The source shows a partially filled in Hα absorption line (Giesers et al., 2019; Göttgens et al., 2019).

This source is not a detected radio or X-ray source in the MAVERIC survey. The 3σ 5.5 GHz radio upper limit is 11.7 µJy. The 90% upper limit for the 1-10 keV X-ray flux was calculated to be $4.6 \times 10^{-16}\,\mathrm{erg\,s^{-1}\,cm^{-2}}$.

The minimum invisible mass of this system is $0.53 \pm 0.04\ M_\odot$. Monte Carlo simulations indicate that the median companion mass is 0.618 $M_\odot$, with a 90% confidence interval of 0.493 $M_\odot$ to 1.648 $M_\odot$. The companion object in this system is either a white dwarf or another star, however if the system is more face-on, a NS companion becomes possible.

4.2.2.5 ACS ID #11405

This source (ACS ID #11405) is a SSG star with a longer orbital period than the other three SSGs detected by MUSE, with an orbital period of 17.219 ± 0.006 days and a higher eccentricity of 0.42 ± 0.08. The F606W magnitude of this star is 17.25, and the source shows a partially filled in Hα absorption line (Giesers et al., 2019; Göttgens et al., 2019).

This source has no radio or X-ray counterpart in the MAVERIC survey. The 3σ 5.5 GHz radio upper limit for this source is 11.7 µJy. The 90% 1-10 keV X-ray flux upper limit is $5.7 \times 10^{-16}\,\mathrm{erg\,s^{-1}\,cm^{-2}}$.

The minimum invisible mass of this source is lower than that for the other SSGs, at $0.15 \pm 0.02\ M_\odot$. The median mass indicated by Monte Carlo simulations is 0.179 $M_\odot$, with a 90% confidence interval of 0.128 $M_\odot$ to 0.476 $M_\odot$. Due to the low median mass, the companion is most likely another main sequence star or an extremely low-mass white dwarf.

4.2.3 Optical/X-ray sources

In addition to the candidate red straggler CXOU J101730.49-462442.4, there are four other HUGS sources that we identify X-ray counterparts for in the MAVERIC
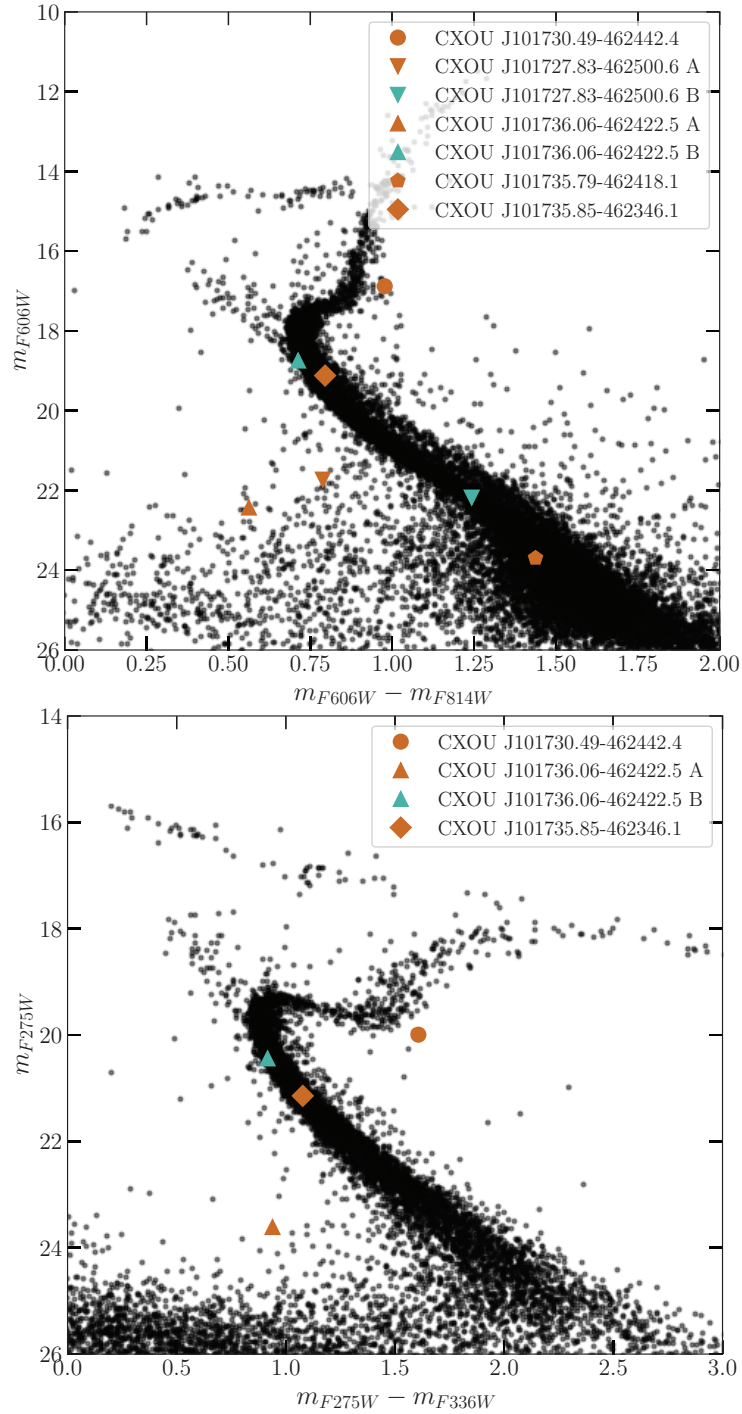
Figure 4.2: *Top*: The visible CMD of NGC 3201 constructed using the F606W and F814W photometric bands. *Bottom*: The UV CMD of NGC 3201 constructed using the F275W and F336W photometric bands. For both CMDs we indicate the most likely optical counterparts for the X-ray sources that have HUGS counterparts. Markers of the same shape with different colours are used to indicate where there is more than one possible optical counterpart for an X-ray source.

survey. Only two sources, CXOU J101736.06-462422.5 and CXOU J101735.79-462418.1, are covered by current MUSE observations of the cluster. Below we summarise the main results for each of these sources, and the position of each source on both the visible and UV CMD of the cluster, as shown in Figure 4.2. The X-ray properties of these sources are also shown in Table 4.3. For these sources, we also discuss the active galactic nuclei (AGN) probability and the cluster membership probability where listed in the HUGS survey. The AGN probability is a parameter included in the MAVERIC X-ray source catalogue, and is the probability that a source is a background AGN based solely on the source flux and the source position within the cluster, and ignores all other source information. More details about this parameter are provided in Section 4.7 of Bahramian et al. (2020).

Given the uncertainty of the X-ray coordinates, it is possible that any optical source with a position that is consistent with the X-ray source position could be a chance coincidence rather than the true counterpart. To estimate the number of chance coincidences, we follow the method outlined in Section 3.8.3 of Zhao et al. (2020a). We use the visible CMD, plotted for stars that have a cluster membership probability of > 0.9, to separate out the different stellar sub-populations in the cluster, shown in the left panel of Figure 4.3. The sub-populations were separated using polygon selection areas using the GLUEVIS software (Beaumont et al., 2015; Robitaille et al., 2017). The cluster was divided into several concentric annuli of radius $0.05'$, and the numbers of chance coincidences for the different sub-populations were calculated for each annulus by assuming that each sub-population was evenly distributed within the annulus. The number of chance coincidences is given by

$$N_{\mathrm{c}} = N_{\mathrm{total}} \frac{\overline{A_{\mathrm{err}}}}{A_{\mathrm{annulus}}}, \tag{4.1}$$

where N_{c} is the number of chance coincidences in a specific annulus, N_{total} is the total number of stars in a sub-population for the specific annulus, $\overline{A_{\mathrm{err}}}$ is roughly the uncertainty in the X-ray coordinates ($0.42''$), and A_{annulus} is the area of the

116

specific annulus. The number of chance coincidences within each annulus for each sub-population is shown in the right panel of Figure 4.3. For main sequence stars, the number of chance coincidences is relatively constant within the core radius of the cluster, before sharply decreasing outside of the core, a trend also seen in the other sub-populations. This is consistent with what is expected for non-core-collapsed clusters, such as NGC 3201. The drop-off seen at a radius of $\sim 2'$ is due to the ACS field-of-view. Within the core radius of the cluster, we expect the following numbers of chance coincidences for each sub-population: ≈ 4.91 for main sequence stars, ≈ 0.07 for blue stars, ≈ 0.27 for red stars, ≈ 0.09 for sub-giant stars, and ≈ 0.17 for red giant stars. Due to the small numbers of stars within the SSG and blue straggler sub-populations, we calculate the number of chance coincidences over the entire ACS field-of-view ($202'' \times 202''$) instead. This gives the number of chance coincidences for SSGs and blue stragglers as $\approx 4.5 \times 10^{-4}$ and $\approx 6.0 \times 10^{-4}$ respectively.

CXOU J101727.83-462500.6 is an X-ray source that falls outside the core radius of the cluster. The uncertainty on the X-ray coordinates is $\sim 0.31''$. The X-ray spectrum of the source is best fit by an apec model, and has a 0.5-10 keV X-ray luminosity of $2.6^{+0.7}_{-0.6} \times 10^{31}$ erg s^{-1}. Within the 0.31$''$ uncertainty of the X-ray coordinates, there are two optical sources from the HUGS catalogue: R0015163, and R0015164. R0015163 falls on the main sequence on the cluster CMD (listed as CXOU J101727.83-462500.6 B), making a chance coincidence with a main sequence star likely. R0015164 lies blueward of the main sequence (listed as CXOU J101727.83-462500.6 A) with a 606W magnitude of 21.7276, making a chance coincidence less likely, and has a separation between optical and X-ray coordinates of $< 0.1''$. Due to this, we favour R0015164 as the more likely counterpart. The AGN probability for this source is 1.0, and the HUGS survey has no listed cluster membership probability for this source. If the source is a cluster member, the X-ray luminosity and CMD position indicate that the source could be an XRB. However, given the lack of a secure optical counterpart and
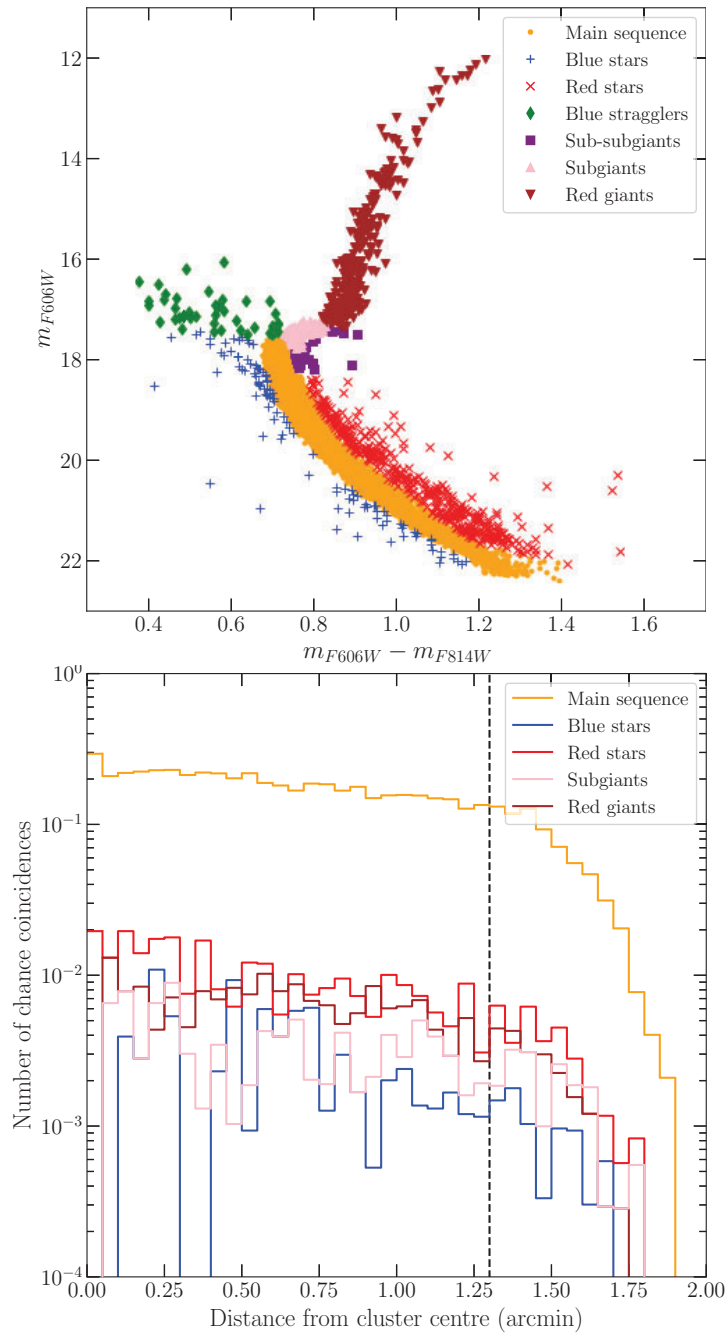
Figure 4.3: *Top*: The visible CMD of NGC 3201 plotted for stars with a cluster membership probability > 0.9. The different sub-populations are indicated with different markers. *Bottom*: The number of chance coincidences expected for each sub-population plotted against the distance in arcmin from the cluster centre. The vertical dashed line indicates the core radius of NGC 3201, and the drop-off seen at $\sim 2'$ is due to the ACS field-of-view. The number of chance coincidences for main sequence stars is roughly constant within the cluster core, before decreasing beyond the core. Within the core, we expect roughly five optical sources to be a chance coincidence with an X-ray source.

AGN probability, an AGN classification is the more feasible explanation.

CXOU J101736.06-462422.5 is an X-ray source listed in the MAVERIC survey which falls well within the core of the cluster. The uncertainty on the X-ray coordinates is $\sim 0.31''$. Its X-ray spectrum is best fit by an apec model, and has a 0.5-10 keV X-ray luminosity of $2.3^{+0.6}_{-0.5} \times 10^{31}$ erg s^{-1}. There are two optical sources from the HUGS survey within the X-ray uncertainty region: R0022094, and R0002240. R0022094 lies closer to the coordinates of the X-ray source ($\sim 0.1''$), and lies blueward of the main sequence on the cluster CMD (listed as CXOU J101736.06-462422.5 A) with a F606W magnitude of 22.427, making a chance coincidence less likely. This source is too faint to be detected by MUSE. R0002240 lies $\sim 0.18''$ from the X-ray source coordinates and is a likely radial velocity variable (probability ~ 0.7), but a Keplerian orbit could not be fitted to the data through Monte Carlo simulations using the software THE JOKER (Price-Whelan et al., 2017). This source sits on the main sequence of the cluster CMD (listed as CXOU J101736.06-462422.5 B), with a F606W magnitude of 18.7414 and a optical cluster membership probability of 0.971. Due to it falling on the main sequence, a chance coincidence is more likely for this source. However, given the radial velocity variations of this source, we favour R0002240 as the most likely optical counterpart to this X-ray source. This, along with its X-ray luminosity, indicate it could be an XRB or a CV.

CXOU J101735.79-462418.1 is an X-ray source within the core of the cluster. The uncertainty on the X-ray coordinates is $\sim 0.31''$. The X-ray spectrum of this source is best fit by a blackbody radiation model with a 0.5-10 keV X-ray luminosity of $4.0^{+0.8}_{-0.7} \times 10^{31}$ erg s^{-1}. Only one optical source falls within the X-ray uncertainty region, R0022891. R0022891 is $\sim 0.1''$ from the X-ray coordinates, has a F606W magnitude of 23.6928, and lies towards the lower end of the main sequence on the cluster CMD, meaning it could be a chance coincidence. The AGN probability of the X-ray source is 0.43. If R0022891 is the optical counterpart, then the X-ray luminosity and CMD position indicate it could either

be an XRB or a CV.

CXOU J101735.85-462346.1 is an X-ray source within $\sim 0.16''$ of the HUGS source R0027430. This source lies within the core of the cluster. The uncertainty on the X-ray coordinates is $\sim 0.51''$. The X-ray spectrum of the source is best fit with a power-law model, however further inspection of this fit indicates that it is not physical due to its shallow photon index. Given that we cannot distinguish between an apec and a blackbody radiation model, we default to a blackbody radiation model due to it being simpler. A blackbody model fit gives a 0.5-10 keV X-ray luminosity $8.3^{+89.0}_{-8.1} \times 10^{30}$ erg s^{-1}. The AGN probability of this source is listed as 0.39. This source lies on the main sequence of the cluster CMD with a F606W magnitude of 19.1185, meaning a chance coincidence is possible, and has an optical cluster membership probability of 0.978. If R0027430 is the optical counterpart, then the X-ray luminosity and CMD position indicate that an AB, CV, or XRB classification is feasible.

In addition to these four sources, there are a further three X-ray sources that have possible optical counterparts within the X-ray uncertainty regions. These X-ray sources are CXOU J101737.30-462332.0, CXOU J101725.45-462452.3, and CXOU J101730.77-462348.2. Upon visual inspection of these cross-matches, we find that it is unlikely that these optical sources are counterparts to the X-ray sources as they fall towards the edges of the respective X-ray uncertainty regions. Furthermore, an AGN classification is more feasible for CXOU J101725.45-462452.3 and CXOU J101730.77-462348.2 based on the AGN probability of the X-ray sources and the lack of an optical cluster membership probability for the optical sources.

4.2.4 Interesting radio sources

By comparing the radio and X-ray source catalogues in the MAVERIC survey, we identified two sources that have both radio and X-ray emission. Here we discuss the properties of each source in order to draw some conclusions about the source

class. The radio spectral index ($S_\nu \propto \nu^\alpha$) values and errors of these sources have been calculated in the initial MAVERIC survey (Tudor et al., 2022).

CXOU J101729.85-462440.6 has no optical counterpart within 0.5" of its radio or X-ray coordinates, and lies within the core of the cluster at a distance of 1.20' from the centre of the cluster. The X-ray spectrum of this source is best fit by a power-law model with a 0.5-10 keV X-ray flux of $4.3^{+13.4}_{-2.9} \times 10^{-15}$ erg s^{-1} cm^{-2}, implying a 0.5-10 keV X-ray luminosity of $1.2^{+3.8}_{-0.8} \times 10^{31}$ erg s^{-1} and a power-law index of $\Gamma = 2.2^{+1.5}_{-2.1}$. There is no spectral information below 1 keV so we do not have a good measure of how soft this source is. Either it is soft with a high absorption component, or hard with a low absorption component. The 5.5 GHz radio flux density of the source is 19.7 ± 3.9 µJy, corresponding to a 5.5 GHz radio luminosity of $(2.9 \pm 0.6) \times 10^{27}$ erg s^{-1}, and the spectral index for this source is $\alpha < 0.59 \pm 0.40$. The AGN probability for the X-ray source is 0.17, however the combined radio/X-ray luminosity ratio places it well above what is expected for accreting BHs ($L_\mathrm{R} \propto L_\mathrm{X}^{0.6}$; Gallo et al., 2014) and NSs. This, in addition to the lack of an optical counterpart to the source, makes it likely that this source is an AGN.

CXOU J101729.25-462644.0 is another radio/X-ray source identified in the MAVERIC survey with no optical counterpart within 1". This source is outside the core of the cluster and is 2.37' from the centre of the cluster. The X-ray spectrum of this source is best fit with an apec model with a 0.5-10 keV flux of $(1.5 \pm 0.3) \times 10^{-14}$ erg s^{-1} cm^{-2}, implying a 0.5-10 keV X-ray luminosity of $4.2^{+0.9}_{-0.7} \times 10^{31}$ erg s^{-1}. The source has a 5.5 GHz radio flux density of 133 ± 4 µJy, corresponding to a 5.5 GHz radio luminosity of $(2.0 \pm 0.1) \times 10^{28}$ erg s^{-1}, and the spectral index is $\alpha = -1.32 \pm 0.19$. Like the above source, it has a much higher radio/X-ray luminosity ratio than is expected from typical accreting systems, and the AGN probability of the X-ray source is 1.0. Combined with the lack of an optical counterpart, we conclude that this source is also most likely an AGN.

We also identify one radio source within the core radius of the cluster, ATCA

J101742.667-462454.262. This source has a 5.5 GHz radio flux density of 25.4±3.7 µJy corresponding to a radio luminosity of $(3.8 \pm 0.5) \times 10^{27} \, \mathrm{erg \, s^{-1}}$, and has a spectral index of $\alpha = -0.87 \pm 0.61$. There is no X-ray detection of this source. The 90% upper limit on the 1-10 keV X-ray flux is $7.4 \times 10^{-16} \, \mathrm{erg \, s^{-1} \, cm^{-2}}$, corresponding to a 90% 1-10 keV X-ray luminosity upper limit of $2.0 \times 10^{30} \, \mathrm{erg \, s^{-1}}$. We speculate that an AGN classification of this source is also plausible based on its radio spectrum.

4.2.5 X-ray sources

The MAVERIC survey lists 24 X-ray sources within the half-light radius of NGC 3201 that have a detection quality of 0 or 1. Of these 24 sources, two are known sub-subgiants in the cluster, five have optical counterparts, and two have radio counterparts. We list the remaining unclassified 15 sources with no multiwavelength counterparts in Table 4.3 and discuss them below.

Ten of these 15 sources have X-ray spectra that are best fit by power-law models. Four sources have spectra best fit by apec models, and the spectrum of CXOU J101739.49-462200.7 is best fit by a blackbody model. However, for all sources we cannot distinguish between the best-fitting model and second best-fitting model to > 99% confidence. All sources are within the half light radius of the cluster (3.1'), with only three sources, CXOU J101736.17-462539, CXOU J101742.96-462509, and CXOU J101737.30-462348.2, within the core (1.3'). The 0.5-10 keV X-ray luminosity of these sources falls in the range of $10^{29-31} \, \mathrm{erg \, s^{-1}}$, making them very faint X-ray sources.

We use the model from Georgakakis et al. (2008) to calculate the X-ray source counts in the 0.5-10 keV range. Using the 90% upper limit calculated for the BH ACD ID #12560 (see § 4.2.1) as a conservative upper limit on our sensitivity, we expect approximately 28 extra-galactic X-ray sources within an area of the sky the size of the half-light radius of NGC 3201. This means that it is possible that all the X-ray sources we observe can be attributed to background sources.

However, as shown in § 4.2.3, there are some X-ray sources that are confidently cluster members due to their optical counterparts. Thus, it is more likely that these 15 X-ray sources with no multiwavelength counterparts are background sources. However, if some sources are associated with the cluster, it is plausible that most of these sources are ABs due to their low X-ray luminosities. Only the brightest of these sources could potentially be CVs or XRBs.

Table 4.3: The list of X-ray sources discussed. This list contains the SSGs and candidate RS source discussed in Section 4.2.2, the four optical/X-ray sources discussed in § 4.2.3, and the 15 X-ray sources with no multiwavelength counterparts discussed in Section 4.2.5. For each source we list the distance from the centre of the cluster as a fraction of the core and half light radii, the AGN probability of the source (Section 4.2.5), and a variety of X-ray spectral model parameters. For a power-law (pl) model we list the photon index (Γ), for an apec model we list the plasma temperature (kT), and for a blackbody radiation (bbr) model we list the electron temperature (kT). For some sources (e.g. CXOU J101736.17-462539.5 and CXOU J101741.33-462554.6) the best-fit model parameters are not physical. We also list the X-ray luminosity for the best-fitting model for each source.

Counterpart	Source	R/R_c	R/R_h	AGN prob.	pl Γ	apec kT (keV)	bbr kT (keV)	Best-fit model	Best-fit L_X (erg s^{-1})
MUSE/X-ray	CXOU J101737.58-462352.2	0.68	0.29	0.19	$2.4^{+1.2}_{-0.8}$	$3.3^{+8.9}_{-1.6}$	0.3 ± 0.1	bbr	$3.0^{+1.6}_{-1.1} \times 10^{30}$
	CXOU J101735.57-462450.5	0.18	0.08	0.22	$3.0^{+0.7}_{-0.8}$	$1.1^{+0.4}_{-0.3}$	0.2 ± 0.1	apec	$1.3^{+1.2}_{-0.7} \times 10^{30}$

Table 4.3 – continued from previous page

Counterpart	Source	R/R_c	R/R_h	AGN prob.	pl Γ	apec kT (keV)	bbr kT (keV)	Best-fit model	Best-fit L_X (erg s^{-1})
Optical/X-ray	CXOU J101730.49-462442.4	0.84	0.35	0.25	$1.9^{+0.7}_{-0.5}$	$3.9^{+6.2}_{-1.6}$	0.6 ± 0.1	apec	$1.6^{+0.8}_{-0.5} \times 10^{31}$
	CXOU J101727.83-462500.6	1.21	0.51	1.00	1.9 ± 0.6	$7.5^{+13.4}_{-3.9}$	0.6 ± 0.1	apec	$2.6^{+0.7}_{-0.6} \times 10^{31}$
	CXOU J101736.06-462422.5	0.30	0.13	0.31	2.2 ± 0.7	$4.7^{+5.2}_{-1.7}$	0.5 ± 0.1	apec	$2.3^{+0.6}_{-0.5} \times 10^{31}$
	CXOU J101735.79-462418.1	0.37	0.15	0.43	1.2 ± 0.4	$15.3^{+10.7}_{-7.8}$	0.9 ± 0.1	bbr	$4.0^{+0.8}_{-0.7} \times 10^{31}$
	CXOU J101735.85-462346.1	0.76	0.32	0.39	$0.2^{+2.6}_{-1.0}$	$3.5^{+15.7}_{-3.4}$	$3.6^{+4.8}_{-3.6}$	bbr	$8.3^{+89.0}_{-8.1} \times 10^{30}$
Radio/X-ray	CXOU J101729.85-462440.6	0.92	0.39	0.17	$2.2^{+1.5}_{-2.1}$	$2.2^{+15.1}_{-1.7}$	$0.9^{+1.6}_{-0.5}$	pl	$1.2^{+3.8}_{-0.8} \times 10^{31}$
	CXOU J101729.25-462644.0	1.82	0.76	1.00	$1.2^{+0.4}_{-0.3}$	$12.4^{+12.6}_{-6.5}$	0.8 ± 0.1	apec	$4.2^{+0.9}_{-0.7} \times 10^{31}$
X-ray	CXOU J101736.17-462539.5	0.71	0.30	0.56	0.1 ± 0.6	$13.5^{+12.5}_{-8.9}$	$2.5^{+3.6}_{-1.1}$	pl	$2.6^{+1.6}_{-1.1} \times 10^{31}$
	CXOU J101742.96-462509.1	0.87	0.36	0.18	$1.4^{+1.6}_{-1.3}$	$10.6^{+13.5}_{-7.3}$	$1.2^{+1.2}_{-0.5}$	pl	$1.7^{+1.8}_{-0.7} \times 10^{31}$
	CXOU J101737.30-462332.0	0.94	0.39	0.21	$1.7^{+1.1}_{-0.8}$	$6.8^{+14.4}_{-4.3}$	$0.2^{+0.2}_{-0.1}$	pl	$1.8^{+0.9}_{-0.6} \times 10^{31}$
	CXOU J101730.77-462348.2	1.08	0.45	0.65	$2.6^{+1.0}_{-0.9}$	$2.1^{+8.9}_{-1.5}$	$0.3^{+0.1}_{-0.1}$	pl	$2.8^{+2.7}_{-1.3} \times 10^{30}$
	CXOU J101741.33-462554.6	1.08	0.45	1.00	$-0.1^{+2.5}_{-0.8}$	$8.6^{+14.6}_{-6.5}$	$4.7^{+4.0}_{-3.0}$	pl	$3.8^{+17.2}_{-2.0} \times 10^{31}$
	CXOU J101730.60-462555.2	1.22	0.51	0.76	$1.8^{+1.3}_{-1.2}$	$8.7^{+14.7}_{-6.1}$	$0.9^{+0.3}_{-0.2}$	pl	$1.7^{+1.9}_{-0.7} \times 10^{31}$
	CXOU J101725.45-462452.3	1.51	0.63	0.72	$1.2^{+1.2}_{-0.8}$	$8.2^{+15.2}_{-6.3}$	$0.7^{+0.6}_{-0.3}$	apec	$3.4^{+2.6}_{-1.5} \times 10^{30}$

Table 4.3 – continued from previous page

Counterpart	Source	R/R_c	R/R_h	AGN prob.	pl Γ	apec kT (keV)	bbr kT (keV)	Best-fit model	Best-fit L_X (erg s^{-1})
	CXOU J101739.24-462242.6	1.60	0.67	0.84	$1.2^{+2.1}_{-1.7}$	$5.2^{+14.7}_{-3.6}$	$1.9^{+3.7}_{-1.1}$	pl	$1.7^{+5.1}_{-1.0} \times 10^{31}$
	CXOU J101726.64-462644.9	2.05	0.86	0.64	$2.6^{+0.9}_{-0.6}$	$4.1^{+8.1}_{-1.9}$	0.3 ± 0.1	pl	$6.2^{+3.5}_{-2.0} \times 10^{30}$
	CXOU J101722.88-462334.0	2.06	0.86	0.68	$1.9^{+1.2}_{-0.8}$	$3.9^{+12.3}_{-2.3}$	0.6 ± 0.2	apec	$5.1^{+3.1}_{-2.2} \times 10^{30}$
	CXOU J101730.66-462714.9	2.09	0.88	0.75	$3.1^{+0.8}_{-1.3}$	$1.7^{+3.7}_{-1.0}$	0.5 ± 0.2	apec	$1.3^{+5.4}_{-0.7} \times 10^{31}$
	CXOU J101739.49-462200.7	2.13	0.75	0.92	$2.1^{+1.1}_{-1.0}$	$6.5^{+14.0}_{-4.1}$	$0.9^{+0.3}_{-0.2}$	bbr	$1.3^{+0.6}_{-0.4} \times 10^{31}$
	CXOU J101723.71-462633.7	2.23	0.94	1.00	$1.8^{+1.7}_{-1.9}$	$2.8^{+15.6}_{-2.0}$	$1.5^{+2.1}_{-0.7}$	pl	$2.5^{+10.8}_{-1.3} \times 10^{31}$
	CXOU J101727.26-462214.2	2.31	0.97	0.61	$2.2^{+1.4}_{-2.0}$	$1.2^{+8.4}_{-1.2}$	$0.2^{+1.6}_{-0.1}$	apec	$5.4^{+36940.0}_{-4.4} \times 10^{29}$
	CXOU J101749.73-462243.3	2.32	0.97	0.59	$1.3^{+1.8}_{-1.2}$	$5.2^{+15.5}_{-4.2}$	$0.6^{+1.5}_{-0.4}$	pl	$5.9^{+9.0}_{-3.9} \times 10^{30}$

4.2.6   Other radio sources

The MAVERIC survey lists 14 radio sources detected with a significance of $> 5\sigma$ within the half-light radius of NGC 3201. Of these, one source is also an X-ray source (CXOU J101729.25-462644.0). The remaining 13 sources are listed in Table 4.4. The source ATCA J101742.667-462454.262 is discussed in § 4.2.4, but is also included in Table 4.4.

The other radio sources in the cluster have 5.5 GHz flux densities of order $10\,\mu\text{Jy}$ with the exception of ATCA J101748.939-462245.159, which has a flux density of (182 ± 2) µJy. The spectral indices of these sources are consistent with being flat or negative, with only one source, ATCA J101723.716-462322.616, having an inverted spectrum of $\alpha < 1.16 \pm 0.41$, and these sources all fall at least $0.04'$ outside the core of the cluster.

To estimate the number of background sources we expect within the area of sky contained within the half-light radius of NGC 3201, we use the simulated source counts of Wilman et al. (2008). For the half-light radius of $3.1'$, we expect 19 background sources. This indicates that every radio source detected in NGC 3201 can be explained as a background source.

Table 4.4: The list of radio sources discussed, which includes the radio/X-ray sources discussed in Section 4.2.4, and the 15 radio sources with no multiwavelength counterpart discussed in Section 4.2.6. For each source we list the distance from the centre of the cluster as a fraction of the core and half-light radii, the 5.5 GHz radio flux density and the spectral index.

Counterpart	Source	R/R_c	R/R_h	5.5 GHz flux density (μJy)	Spectral index
Radio/X-ray	CXOU J101729.85-462440.6	0.92	0.39	19.7 ± 3.9	$< 0.59 \pm 0.40$
	CXOU J101729.25-462644.0	1.82	0.76	133 ± 4.0	-1.32 ± 0.19
Radio	ATCA J101742.667-462454.262	0.78	0.33	25.4 ± 3.7	-0.87 ± 0.61
	ATCA J101726.705-462504.558	1.36	0.57	26.6 ± 4.0	$< -0.13 \pm 0.31$
	ATCA J101732.309-462626.163	1.43	0.60	16.6 ± 3.9	0.47 ± 0.70
	ATCA J101731.164-462642.881	1.68	0.71	26.5 ± 4.2	$< 0.22 \pm 0.32$
	ATCA J101744.735-462631.964	1.73	0.73	24.6 ± 4.5	-0.15 ± 0.64
	ATCA J101746.690-462306.033	1.82	0.76	52.0 ± 4.5	-0.48 ± 0.41
	ATCA J101743.829-462236.644	1.89	0.79	28.7 ± 4.5	$< 0.60 \pm 0.32$

Continued on next page

128

Table 4.4 – continued from previous page

Counterpart	Source	R/R$_c$	R/R$_h$	5.5 GHz flux density (µJy)	Spectral index
	ATCA J101723.716-462322.616	2.03	0.85	24.9 ± 5.0	< 1.16 ± 0.41
	ATCA J101721.425-462536.169	2.15	0.90	30.1 ± 4.8	< −0.15 ± 0.33
	ATCA J101748.939-462245.159	2.22	0.93	182 ± 2.0	−0.30 ± 0.41
	ATCA J101727.933-462712.667	2.23	0.94	29.2 ± 4.9	< 0.65 ± 0.35
	ATCA J101749.983-462254.064	2.25	0.95	25.0 ± 5.5	< 0.74 ± 0.45
	ATCA J101740.920-462144.955	2.37	0.99	43.6 ± 5.5	< 0.29 ± 0.26

4.3 Discussion

Our main results are the non-detections of the two confirmed and one candidate BH in the GC NGC 3201. We report the 3σ radio luminosity upper limits at 5.5 GHz and the 90% 1-10 keV X-ray luminosity radio upper limits for these three sources. We list these values in Table 4.2 and discuss the implications of these results in § 4.3.1.

We also present a comprehensive list of multiwavelength sources within the half-light radius of NGC 3201. We identify two MUSE binary sources with X-ray emission, five optical sources with X-ray emission, two sources displaying both radio and X-ray emission, 15 X-ray sources with no other multiwavelength counterpart, and 13 radio sources with no other multiwavelength counterpart. The X-ray sources present in the cluster allow us to make some estimates as to the total population of XRBs in NGC 3201 (§ 4.3.3), and the detections of two known SSGs in the cluster allow us to briefly discuss the evolution of this class of object (§ 4.3.4).

4.3.1 Accretion limits on the detached black holes

4.3.1.1 Calculating the mass accretion limits from observations

Our upper limits on the radio and X-ray luminosities of the detached BHs in NGC 3201 (Table 4.2) allow us to constrain the mass accretion rates onto these sources. Using these upper limits, we can calculate the maximum mass accretion rate that would be visible in both the radio and X-ray bands. We calculate these limits both directly from the X-ray luminosity and by using the fundamental plane of BH activity (Merloni et al., 2003; Falcke et al., 2004).

The X-ray luminosity L_{X} is directly related to the mass accretion rate $\dot{M}$ through the standard equation

$$L_{\text{X}} = \epsilon \dot{M} c^2, \tag{4.2}$$

where ϵ is the radiative efficiency of the accretion and c is the speed of light. Thus for a given X-ray luminosity, we can constrain the observable product $\epsilon \dot{M}$ to which we would be sensitive.

The radio luminosity L_R allows us to provide a constraint on the mass accretion rate through the fundamental plane of BH activity. The fundamental plane describes the relation between the X-ray luminosity, radio luminosity, and the mass of hard state accreting BHs. This relationship spans several orders of magnitude in mass, ranging from stellar-mass BHs to supermassive BHs at the centres of galaxies (Merloni et al., 2003; Falcke et al., 2004; Plotkin et al., 2012). For this work, we use the following form of the fundamental plane (Miller-Jones et al., 2012; Plotkin et al., 2012)

$$\log L_\mathrm{X} = 1.44 \log L_\mathrm{R} - 0.89 \log M - 5.95, \tag{4.3}$$

where L_X and L_R are in $\mathrm{erg\,s^{-1}}$ and the BH mass M is in $M_\odot$. By substituting in the above relation for X-ray luminosity, we can again constrain the observable product $\epsilon \dot{M}$ to which we would be sensitive for a given radio luminosity and BH mass.

By using the radio and X-ray luminosity upper limits shown in Table 4.2 and the minimum BH masses given in Giesers et al. (2019), we can provide two constraints on the product $\epsilon \dot{M}$ that would be detectable: one from the X-ray luminosity upper limits, and one from the radio luminosity upper limits and BH masses. These constraints are shown in Table 4.5, and they represent the deepest such accretion limits onto a BH to date for a GC. The limits on $\epsilon \dot{M}$ derived from the X-ray luminosity are two orders of magnitude deeper than those derived from the fundamental plane.

Table 4.5: The limits on the product $\epsilon\dot{M}$, derived from X-ray luminosity limits and from the fundamental plane for BHs respectively. Our X-ray observations allow us to probe $\epsilon\dot{M}$ values two orders of magnitude deeper than our radio observations allow.

Source	$\epsilon\dot{M}$ from L_{X} $M_{\odot}$ yr^{-1}	$\epsilon\dot{M}$ from L_{R} and M $M_{\odot}$ yr^{-1}
ACS ID #12560	$< 2.5 \times 10^{-17}$	$< 8.4 \times 10^{-15}$
ACS ID #21859	$< 1.5 \times 10^{-17}$	$< 5.2 \times 10^{-15}$
ACS ID #5132	$< 1.7 \times 10^{-17}$	$< 8.6 \times 10^{-15}$

4.3.1.2 Estimating the expected mass accretion rates through stellar wind capture

With the limits on $\epsilon\dot{M}$ shown in Table 4.5, we can now place some constraints on the radiative efficiency of the accretion ϵ by making some assumptions as to what $\dot{M}$ is for these systems. A similar, but reversed calculation is shown in Breivik et al. (2019), where they estimate L_{X} based on assumptions over the wind mass-loss rate. For our case, as these systems are detached binary systems we expect that there will be no Roche-lobe overflow, as evidenced by the lack of an X-ray detection for any system. The formation of an accretion disc in a binary is dependent on the circularisation radius around the compact object. If the circularisation radius is smaller than the event horizon of the BH, no disc will be formed. In a stellar wind accretion regime, the circularisation radius can be expressed as (Frank et al., 2002)

$$\frac{R_{\mathrm{circ}}}{a} = \frac{M^3(M + M_2)}{16\lambda^4(a)M_2^4}\left(\frac{R_2}{a}\right)^4,$$ (4.4)

where M is the compact object mass, M_2 and R_2 are the mass and radius of the companion respectively, and a is the orbital separation of the binary. The term $\lambda(a)$ is the wind law describing the behaviour of the stellar winds from the companion. Due to the uncertainty over the wind law, we cannot confidently calculate the circularisation radii of the three BHs, as changing $\lambda(a)$ even by a factor of 2 drastically changes the result. Thus, we assume that the accretion

present in these systems, if any, is due to the capture of the stellar winds from the companion stars with no accretion disc formed. We do note, however, that the BH ACS ID # 21859 is the most likely system to form an accretion disc due to a shorter binary separation when compared to the other two BH systems.

The amount of the wind captured by the compact object can be expressed as a fraction of the wind mass loss rate of the companion star (Frank et al., 2002)

$$\frac{\dot{M}}{-\dot{M}_w} \cong \frac{1}{4}\left(\frac{M}{M_2}\right)^2\left(\frac{R_2}{a}\right)^2, \tag{4.5}$$

where $-\dot{M}_w$ is the mass loss rate of the companion, M is the compact object mass, M_2 and R_2 are the mass and radius of the companion respectively, and a is the orbital separation of the binary. Substituting in the orbital separation a from Kepler's Third Law reduces the above equation to

$$\frac{\dot{M}}{-\dot{M}_w} = \left(\frac{\pi^4}{4G^2}\right)^{1/3}\left(\frac{R_2}{M_2}\right)^2\left(\frac{M}{P}\right)^{4/3} \tag{4.6}$$

$$\sim 0.01412\left(\frac{R}{R_\odot}\right)^2\left(\frac{M_2}{M_\odot}\right)^{-2}\left(\frac{M}{M_\odot}\right)^{4/3}\left(\frac{P}{\text{days}}\right)^{-4/3}, \tag{4.7}$$

where P is the binary orbital period. The mass accretion rate is dependent on the mass loss rate due to stellar winds from the companion stars.

We adopt the relations from Johnstone et al. (2015b,a) to estimate the mass loss rate from the companion stars due to the stellar winds. The wind mass loss rate is expressed as

$$-\dot{M}_w = \dot{M}_\odot\left(\frac{R}{R_\odot}\right)^2\left(\frac{\Omega}{\Omega_\odot}\right)^{1.33}\left(\frac{M}{M_\odot}\right)^{-3.36}, \tag{4.8}$$

where the solar wind mass loss rate $\dot{M}_\odot = 1.4 \times 10^{-14} M_\odot \text{ yr}^{-1}$, the Carrington rotation rate $\Omega_\odot = 2.67 \times 10^{-6} \text{ rad s}^{-1}$, and R, Ω, and M are the radius, rotational velocity, and mass of the companion star respectively. By knowing the radius, rotational velocity, and mass of the companion stars, we can estimate

their wind mass loss rates.

The masses of the companion stars are given in Giesers et al. (2019). The radii of the companions are derived based on the effective temperature and an estimate of the luminosity of the companion. The radii of the companions are: $R = 1.62R_\odot$ for ACS ID# 12560, $R = 0.84R_\odot$ for ACS ID# 21859, and $R = 0.64R_\odot$ for ACS ID# 5132. Through full-spectrum fits, the rotational velocities of the companions can be estimated, however, this is limited to fast rotators only due to the spectral resolution of MUSE. The rotational velocities measured are: $\Omega \sin i \leq 2.42 \times 10^{-5}\,\mathrm{rad\,s^{-1}}$ for ACS ID# 12560, $\Omega \sin i \leq 5.12 \times 10^{-5}\,\mathrm{rad\,s^{-1}}$ for ACS ID# 21859, and $\Omega \sin i = 9.38 \times 10^{-5}\,\mathrm{rad\,s^{-1}}$ for ACS ID# 5132. In the case of the first two sources, we only have upper limits on the rotational velocity of the companions as the true rotation rates are likely below the detection threshold of MUSE, and the constraint on ACS ID# 5132 is only marginally above the detection threshold. Due to these uncertainties, we can use other theoretical models to predict what the actual rotation rates are.

For the systems ACS ID# 12560 and ACS ID# 5132, we can use the gyrochronology predictions of Epstein & Pinsonneault (2014) to provide a better constraint on the rotational velocity of the companions. Here, modern models predict that the rotational period will increase as age$^{-0.5}$, as predicted by Skumanich (1972), for stars older than 5 Gyr. For the companions in these two systems, we can expect rotation rates between 10 and 40 days, with an increase in period with stellar mass. Given the masses of the companions in ACS ID# 12560 and ACS ID# 5132, we adopt a predicted rotational period of 25 ± 5 days, implying a rotational velocitiy of $\Omega = 2.9 \times 10^{-6}\,\mathrm{rad\,s^{-1}}$. However, it is important to note that the companion star in ACS ID# 12560 is a sub-giant, and its rotational period will have been altered due to the expansion of its shell, likely resulting in a larger rotational period than an equally massive star on the main sequence. In this case, we note that applying the predictions of Epstein & Pinsonneault (2014) may not give an appropriate estimate of the rotational period,

and other gyrochronology models of sub-giant stars may need to be considered.

For the case of the BH system ACS ID #21859, due to the short orbital period of the system ($\sim$ 2 days, Giesers et al., 2019) we can constrain the rotational velocity based on the assumption that the system is tidally locked. The location of this source in a GC means it is likely that the orbit was not originally circular due to its formation through dynamical channels. Given that the orbit of this source is now circular ($e \sim 0.07$), it is reasonable to assume that the BH and companion are tidally locked, as tidal locking should occur prior to the circularisation of the binary orbit. We adopt the following equation for the rotational broadening for a star that is tidally locked from Wade & Horne (1988)

$$V_{\rm rot} \sin i \approx 0.462 K_2 q^{1/3} (1 + q)^{1/3}, \tag{4.9}$$

where K_2 is the semi-amplitude of the secondary and $q = M_2/M_1$. We do note that the caveat to using this relation to calculate the rotational velocity is that it assumes that the secondary is Roche-lobe filling, something that we have not assumed for our other calculations. From this, we estimate the rotational velocity of this star to be $\Omega \sin i = 1.09 \times 10^{-4} \, \rm rad \, s^{-1}$.

In Table 4.6 we present the fraction of the stellar wind captured by the BHs, the wind mass loss rates of the companions, and the final mass accretion rate into the BHs we estimate. As we expect, the mass accretion rates are low, consistent with there being no evidence of meaningful accretion in these systems. Notably, the mass accretion rate for ACS ID #21859 is approximately five orders of magnitude higher than that of the other BH systems. This is due to this system having a much shorter binary orbital period by a factor of $\sim$ 100, meaning the BH is expected to capture a higher fraction of the stellar wind from the companion.

4.3.1.3 Accretion efficiency constraints

These accretion limits now allow us to place some constraints on what the radiative efficiency ϵ must be in these systems. Previous studies (e.g., Maccarone,

Table 4.6: The mass accretion rate as a fraction of the stellar wind loss rate, the wind mass loss rate, and the mass accretion rate we estimate for each BH system. The mass accretion rate for ACS ID #21859 is at least five orders of magnitude higher than that of the other BH systems due to its much shorter binary orbital period.

Source	$\dot{M}/-\dot{M}_w$	$-\dot{M}_w$ $M_\odot \text{ yr}^{-1}$	$\dot{M}$ $M_\odot \text{ yr}^{-1}$
ACS ID #12560	4.61×10^{-4}	8.34×10^{-14}	3.85×10^{-17}
ACS ID #21859	1.39×10^{-1}	7.29×10^{-12}	1.01×10^{-12}
ACS ID #5132	1.46×10^{-5}	2.88×10^{-14}	4.20×10^{-19}

2005) have assumed that the accretion flow is radiatively inefficient. This is the case with advection-dominated accretion flows (Narayan & Yi, 1995). For low accretion rates ($\dot{M}/\dot{M}_{\text{Edd}} < 0.02$, Maccarone, 2003; Vahdat Motlagh et al., 2019), the efficiency scales with the accretion rate. This allows us to express the efficiency as

$$\epsilon = 0.1 \left(\frac{\dot{M}}{\dot{M}_{\text{Edd}}} /0.02 \right), \tag{4.10}$$

where $\dot{M}_{\text{Edd}}$ is the Eddington accretion rate, and $\dot{M}$ is usually expressed as some fraction (~ 0.03) of the Bondi accretion rate based on the observations from Pellegrini (2005).

For the case of the detached BHs in NGC 3201, we assume that the mass accretion rate is the fraction of the stellar wind captured by the BH (the $\dot{M}$ values in Table 4.6) with no accretion disc formed. Combining this with the accretion limits shown in Table 4.5, we can constrain the radiative efficiency by assuming $\epsilon \dot{M} = limit$. These constraints on the radiative efficiency are shown in Table 4.7. The BH ACS ID #21859 provides the best constraints on the radiative efficiency due to having a higher accretion rate from stellar winds. The lack of a radio and X-ray detection of this source indicates that it must be accreting below our sensitivity limits. The radio limit of this source constrains the efficiency to $< 5.1 \times 10^{-3}$, and the X-ray limit of this source constrains the efficiency to $< 1.5 \times 10^{-5}$. This provides a strong indication that either this source is not

Table 4.7: The constraints on the radiative efficiency of the accretion onto the BHs assuming the accretion is in the form of stellar winds from the companion stars. The only system for which we have good constraints is ACS ID #12560. The radiative efficiency of this system is less than 1%, indicating that the system is either not accreting, or the system is accreting extremely inefficiently. Entries consisting of a "-" indicate that no meaningful constraints on the radiative efficiency could be calculated due to the available depth of the radio and X-ray imaging.

Source	ϵ from L_{X}	ϵ from L_{R} and M
ACS ID #12560	$< 6.5 \times 10^{-1}$	-
ACS ID #21859	$< 1.5 \times 10^{-5}$	$< 5.1 \times 10^{-3}$
ACS ID #5132	-	-

accreting, or is accreting extremely inefficiently for there to be no multiwavelength detection. This efficiency limit is consistent with what is theoretically expected from Equation 4.10 for low mass accretion rates.

The constraints on the other two BHs are weaker, due to their lower expected accretion rates. Again, there is no multiwavelength detection of these sources, so the accretion must be below our sensitivity limits. Our radio observations are not deep enough to probe the expected accretion rates onto these BHs, and our X-ray observations only provide a constraint on the efficiency for ACS ID #12560 of $< 6.5 \times 10^{-1}$. For ACS ID #5132, the expected accretion rate is well below our sensitivity limits, so the radiative efficiency cannot be constrained.

Of course, these limits on the radiative efficiency are heavily dependent on the assumptions we have made, in particular that the accretion is purely from capturing a fraction of the companion's stellar winds with no accretion disc being formed, and the models we have assumed to calculate the wind mass loss rate from the stars. Furthermore, the rotational velocity of the source ACS ID #21859 has been calculated assuming the star is tidally locked with the binary orbit, and the rotational velocities of the other two systems have been predicted through gyrochronology. Any change in these assumptions would alter the constraints placed on the radiative efficiency. However, this is the first time that constraints have been placed on the accretion efficiency for dynamically-confirmed stellar-

mass BHs in a GC, and these show that any accretion is extremely inefficient. Any multiwavelength emission from this accretion would be very faint and would require large integration times to detect.

4.3.2 Detectability of the black holes with current and future instruments

The upper limits on the radio and X-ray luminosities of the BHs in NGC 3201 also allow us to comment on the detectability of these systems with current instruments. Plotting these limits on the radio–X-ray luminosity plane (Figure 4.1) shows that these sources lie well above the standard track occupied by accreting BHs ($L_\mathrm{R} \propto 0.6 L_\mathrm{X}$, Gallo et al., 2014). This indicates that while our X-ray observations of the cluster may be deep enough to potentially probe faint emission from weakly accreting systems, our current radio observations are too shallow by at least one order of magnitude.

We can now comment on whether these limits could potentially be reachable through observations with current radio facilities, such as the ATCA. The BH ACS ID #21859 has the deepest 1-10 keV X-ray limit of $8.6 \times 10^{29}\,\mathrm{erg\,s^{-1}}$. If we assume that any X-ray emission is on the verge of detectability with current data, the source falls on the standard accreting BH correlation, and that this correlation holds for these very low luminosities, the corresponding radio limit for this source is $7.7 \times 10^{25}\,\mathrm{erg\,s^{-1}}$, implying a 5.5 GHz radio flux density of $5.2 \times 10^{-1}\,\mathrm{\mu Jy}$ assuming a cluster distance of 4.74 kpc. The current 3σ radio upper limit for this BH is $9.5\,\mathrm{\mu Jy}$ from 18.1 hr of ATCA observations, a value approximately 17 times too shallow to reach even the radio limit of the standard accreting BH correlation. As RMS noise in radio images decreases as $\sqrt{\mathrm{time}}$, one would need to observe NGC 3201 for over 5200 hr of ATCA, observations assuming ideal conditions, to potentially detect emission at this limit from the system. This is not feasible for current generation instruments. Sub-$\mathrm{\mu Jy}$ radio noise levels would be possible for some clusters with a few hundred hours of ATCA observations assuming the

dynamic range of the observations is not limited, however, current instruments are not suited to probe the faintest BHs at these very low luminosities. These deep surveys, with noise levels on the order of hundreds of nJy, will be possible with next generation radio facilities such as the Next Generation VLA and the Square Kilometre Array (Murphy et al., 2018; Dewdney et al., 2009).

Additionally, observations of these faintly accreting sources may be feasible with the proposed next generation of X-ray facilities, such as the *Athena* X-ray Observatory (Nandra et al., 2013), and particularly the *Lynx* X-ray Observatory (The Lynx Team, 2018) due to its angular resolution. To push our current X-ray limits deeper with our current X-ray facilities, > 100 ks of *Chandra* observations would be needed.

4.3.3   Population of X-ray sources and encounter rate

Given we now have an estimate as to how many XRBs we expect in NGC 3201, we can now compare it to the stellar encounter rate (Verbunt & Hut, 1987) of the cluster ($\Gamma \propto \int \rho^2/\sigma$) to see if there is a significant (over)under-population of XRBs. The population of XRBs is expected to be different depending on whether the cluster has undergone a core-collapse, and whether the cluster has a larger or smaller stellar encounter rate (i.e. how dynamically active is the cluster). It has previously been shown that more XRBs are seen in clusters with higher stellar encounter rates (Heinke et al., 2003b; Pooley et al., 2003; Bahramian et al., 2013). It appears that core-collapsed clusters have fewer XRBs than non-core-collapsed clusters for the same encounter rate (Fregeau, 2008; Bahramian et al., 2013).

Figure 4.4 shows a plot of the number of XRBs in a cluster plotted against the stellar encounter rate of the cluster for a number of GCs. The number of XRBs for each cluster was collated from Pooley et al. (2003), and only includes X-ray sources that are brighter than $4 \times 10^{30} \, \mathrm{erg \, s^{-1}}$.

For NGC 3201, we are confident that one X-ray source is an XRB an associated with the cluster. This source is the candidate RS, CXOU J101730.49-462442.4.
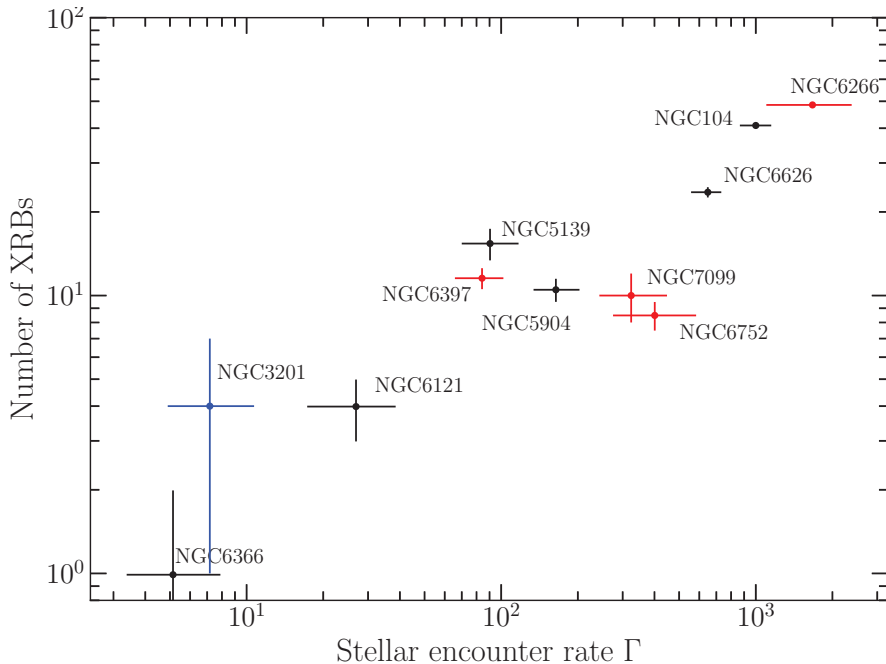
Figure 4.4: The number of XRBs plotted against the stellar encounter rate for a number of GCs. The clusters shown in red are core-collapsed clusters. NGC 3201 is shown in blue. The stellar encounter rate has been normalised so that the encounter rate of 47 Tucanae (NGC 104) is 1000.

Beyond this, three of the optical/X-ray sources discussed in § 4.2.3 are potential XRBs. Using the relations from Georgakakis et al. (2008), we expect there to be approximately 14 extra-galactic X-ray sources within the half-light radius of the cluster with a luminosity greater than 4×10^{30} erg s^{-1}. To estimate the most likely number of XRBs in the cluster, we assumed the number of background AGNs detected given the flux threshold follow a Poisson distribution with a Poisson rate corresponding to the 14 background sources expected within the cluster half-light radius, and that the likely number of XRBs cannot be less than the number of XRBs confirmed via multiwavelength observations. Thus, we estimate the likely number of XRBs to be 4 ± 3, based on the mode of the resulting distribution and 68% interval, as indicated in Figure 4.4.

In Figure 4.4, we see that NGC 3201 potentially contains more XRBs than would be expected for a cluster with a similar encounter rate. NGC 6366, which has an encounter rate of $\Gamma \sim 5.1$ compared to $\Gamma \sim 7.2$ for NGC 3201, only

contains one XRB while NGC 3201 potentially contains four or more XRBs. This is unusual as for these low encounter rate clusters we do not expect many XRBs to form, as one of the main formation channels, dynamical interactions, is mitigated due to the low encounter rate. The potential overabundance suggests we could be observing primordial binary systems, formed towards the beginning of the cluster's life cycle, instead of being formed dynamically throughout the lifetime of the cluster. It is not unfeasible for primordial binaries to survive in a cluster such as NGC 3201. The low encounter rate of the cluster combined with its large mass ($1.6 \times 10^5 M_\odot$; Baumgardt et al., 2019) when compared to NGC 6366 ($3.8 \times 10^4 M_\odot$; Baumgardt et al., 2019), means that it is less likely for these systems to be disrupted, as opposed to a more dynamically active cluster such as 47 Tucanae (NGC 104), where the higher encounter rate would make it difficult for primordial binaries to survive for long periods of time.

However, given that the lower limit for the number of XRBs is consistent with that of NGC 6366, it is also possible that NGC 3201 displays no overabundance of XRBs at all. If this is the case, then NGC 3201 would be displaying a number of XRBs which is expected for its stellar encounter rate. This would indicate that from an XRB perspective, NGC 3201 is a standard GC.

4.3.4 Evolution of sub-subgiants

In NGC 3201 we detect two of the SSGs identified in the MUSE binary catalogue as X-ray sources in the MAVERIC survey, and provide X-ray upper limits for the two other SSGs. We also identify an optical source with X-ray emission, which we conclude to be a RS system based on its position in the cluster CMD. This means that there is now a total of five systems in NGC 3201 that lie redward of the main sequence and are underluminous compared to normal (sub-)giant stars.

The X-ray luminosities of these systems are consistent with the expected luminosities of SSG systems. SSGs are expected to have very low X-ray luminosities on the order of 10^{30-31} erg s^{-1} (Geller et al., 2017a), and the three sources with

confident X-ray detections have X-ray luminosities within this range. Beyond the X-ray luminosities, the orbital periods of three of the four SSGs detected by MUSE are also consistent with the expected orbital periods for SSG systems, which have been observed to be $\lesssim 15$ days (Geller et al., 2017a). The SSG with a longer orbital period, ACS ID #11405 with a period of ~ 17 days, also has the largest eccentricity of any SSG, potentially indicating that it is in an earlier stage of its evolution prior to the orbit circularising, either through mass transfer or tidal forces.

Finally, the observed properties of these systems are also somewhat consistent with some speculative formation pathways for SSGs. Leiner et al. (2017) propose three methods for SSG formation: binary mass transfer, stripping of the star's envelope during a potential dynamical encounter, and strong magnetic fields causing underluminous stars. Binary mass transfer in the form of accretion onto a compact object would produce an X-ray signal, which we observe from two SSGs and our candidate RS indicating some accretion may be present in these systems. Another feasible explanation to the X-ray emission seen is that these two SSGs may be ABs, given that their X-ray luminosities fall in the range expected for these systems ($\lesssim 10^{31}$ erg s^{-1}; Güdel, 2002). All five of these systems are also underluminous in the optical bands when compared to normal (sub-)giant stars. It has also been suggested that the presence of underluminous stars in GCs could be indicative of BH presence (Ivanova et al., 2017), a statement that now has more merit given the presence of BHs in NGC 3201.

4.4 Conclusions

In this chapter, we present a catalogue of energetic sources in NGC 3201. We combine the radio and X-ray data from the MAVERIC survey (Shishkovsky et al., 2020; Bahramian et al., 2020) with the spectral binary and emission line catalogues of the cluster produced by MUSE (Giesers et al., 2019; Göttgens et al., 2019) and the HUGS catalogue (Piotto et al., 2015; Nardiello et al., 2018) to inves-

tigate any binary system or optical source that has radio and/or X-ray emission. From this, we consider 42 sources in this chapter. Three sources are known (or candidate) BHs and four sources are known SSGs (Giesers et al., 2019). Within the cluster half-light radius we also identify a new candidate red straggler system, four optical sources with X-ray emission, two sources with radio and X-ray emission, 15 X-ray sources with no other multiwavelength counterpart, and 13 radio sources with no other multiwavelength counterpart. We speculate that three of the four optical sources with X-ray emission are some type of X-ray emitting binary (e.g. AB, CV, or XRB) and, along with the candidate red straggler, are associated with the cluster. We suspect that the remaining radio and X-ray sources can be explained as background sources.

Importantly, we present the first radio and X-ray limits on the detached BHs in NGC 3201. All three sources are not detected in the 5.5 GHz radio band or the 0.5-10 keV X-ray band. The lack of a multiwavelength counterpart to these systems suggests that these systems are not accreting. From these limits, we are able to provide some constraints on the radiative efficiency of any accretion that is present in these, assuming that any accretion is through the capture of the companions' stellar winds. These calculations suggest that the accretion in these systems is extremely inefficient, with the limits on the BH ACS ID #21859 suggesting that the radiative efficiency is $\lesssim 1.5 \times 10^{-5}$, consistent with previous work suggesting that efficiency scales with accretion rate for low accretion rates (e.g., Maccarone, 2003; Vahdat Motlagh et al., 2019). Due to the extremely faint nature of these systems ($L_{\mathrm{X}} < 10^{30} \mathrm{erg\,s^{-1}}$), it is quite challenging to detect them with the current generation of radio facilities. Assuming that these BH systems follow the standard track for accreting BHs (Gallo et al., 2014), hundreds of observing hours would be required by either the ATCA or the VLA to reach the sub-µJy noise levels needed to probe any potential radio emission from these sources. However, these weakly accreting targets are prime candidates for deep surveys with the next generation of radio facilities, such as the Next Generation

VLA or the Square Kilometre Array, and observations of these sources may be feasible with the next generation of X-ray facilities.

NGC 3201 may also have a slight overpopulation of XRBs when compared to other GCs with similar stellar encounter rates. We speculate that this could be due to the presence of primordial binaries that have not been disrupted. However, if this overabundance is not true, then NGC 3201 contains a number of XRBs that would be expected for its stellar encounter rate.

CHAPTER 5

ULTRA-DEEP ATCA IMAGING OF 47 TUCANAE REVEALS A CENTRAL COMPACT RADIO SOURCE

Adapted from:

Chapter 5 of this thesis, "Ultra-deep ATCA imaging of 47 Tucanae reveals a central compact radio source", is a reproduction of a submitted manuscript by Paduano et al. ("Ultra-deep ATCA imaging of 47 Tucanae reveals a central compact radio source", The Astrophysical Journal). This is my own work except for the following. The radio data were acquired by me, A. Bahramian, J. C. A. Miller-Jones, and T. J. Galvin. T. J. Galvin assisted with the imaging of the data. The optical HST data, text describing the calibration of these data, and cluster CMDs were provided by L. Rivera Sandoval. A. Kawka performed HST/STIS UV data analysis, and provided text describing this. S. Kamann provided the MUSE spectra of the central stars in the cluster, the Hα flux image and residuals map of this region, and text outlining the collection and calibration of these data. J. Strader assisted with the astrometric alignment of the multiwavelength data and provided text outlining this process. The analysis of BY Dra stars from ZTF and VLASS was done by A. Bahramian, who also provided text outlining this process. Discussions regarding the interpretation of the results were contributed by my supervisory panel – A. Bahramian, J. C. A. Miller-Jones, and A. Kawka. Further discussions were also contributed by T. J. Galvin, L. Rivera Sandoval, S. Kamann, L. Chomiuk, C. O. Heinke, T. J. Maccarone, and S. Dreizler. I drafted the manuscript and distributed it to all co-authors for proofreading. All co-authors provided input and feedback on the manuscript until the final version was produced.

With the detection and dynamical confirmation of the BHs in NGC 3201, it has been shown that BHs can exist in GCs. This result has several implications. GCs are thought to be host environments of the progenitor systems to some of the binary BH merger events that produce gravitational waves (Morscher et al., 2013, 2015; Fragione et al., 2020), and understanding the population of BHs in clusters and how they evolve is key to constraining the theoretical simulations to predict the merger rates and the evolutionary pathways of these systems. BHs

are also thought to play a key role in the evolution of GCs, with some simulations suggesting that the size and surface brightness profile are determined by the BH content (Askar et al., 2020).

Related to the population of BHs in clusters is the population of pulsars. It has been suggested that the population of MSPs in a cluster is anticorrelated with the cluster's population of BHs (Ye et al., 2019), thus good estimates of the number of pulsars in a cluster can be used to constrain the suspected BH population. Some clusters, such as Terzan 5 and 47 Tuc, are known to contain large populations of MSPs making these clusters ideal laboratories to study pulsar properties.

On the heels of our exploration in Chapter 4 of the radio and X-ray properties of the detached BHs in NGC 3201 and the lack of any observable emission from these sources, it has become clear that our radio observations of GCs are not deep enough to probe any but the brightest quiescent accreting XRBs. In particular, we are only sensitive to the brightest BHs, should BHs follow the fundamental plane of BH activity (Merloni et al., 2003; Falcke et al., 2004; Plotkin et al., 2012; Gültekin et al., 2019). This motivated the need for a much deeper radio survey of a GC in order to push the radio limits of our observations down to the detectability of the population of very faintly accreting BHs.

With this in mind, we conducted an ultra-deep radio survey of 47 Tuc with the ATCA, obtaining 450 hr of new radio continuum observations to search for faintly accreting BHs and other exotic binary systems capable of producing radio emission, such as pulsars. 47 Tuc has been observed previously with the ATCA for various purposes. Observations by McConnell & Ables (2000) reached RMS noise levels of 42 and $46\,\mu\mathrm{Jy\,beam}^{-1}$ at 1.4 and 1.7 GHz respectively, enabling the detection of 11 radio sources within 5' of the cluster centre. These 11 sources included the detections of two pulsars with known positions. This initial survey was built upon by Fruchter & Goss (2000), who presented images with RMS noise levels of $32\,\mu\mathrm{Jy\,beam}^{-1}$. The survey by McConnell & Ables (2000) was extended

to include 170 hr of ATCA data the following year, pushing the RMS noise down to $18\,\mu\text{Jy beam}^{-1}$ (McConnell et al., 2001) and detecting nine radio sources in the cluster core. Following the bandwidth upgrade to the ATCA (Wilson et al., 2011), Lu & Kong (2011) obtained approximately 18 hr of ATCA data at 5.5 and 9.0 GHz in 2010, reaching an RMS noise level of $13.3\,\mu\text{Jy beam}^{-1}$ after stacking both bands. These observations were subsequently combined with the MAVERIC observations of 47 Tuc, reaching RMS noise levels of 4.4 and $5.7\,\mu\text{Jy beam}^{-1}$ at 5.5 and 9.0 GHz respectively, and used to identify the BH candidate X9 (Miller-Jones et al., 2015).

47 Tuc presented the best case for a deep radio continuum survey and exploration of radio sources due to several factors. The cluster is close, located at a distance of 4.52 ± 0.03 kpc (Baumgardt & Vasiliev, 2021), and has a very low extinction of $E(B-V) = 0.04\pm0.02$ (Salaris et al., 2007). These two points make the cluster an easy target for multi-wavelength studies, with 47 Tuc being studied extensively by the *Chandra* X-ray Observatory and Hubble Space Telescope (HST). 47 Tuc contains a rich population of over 300 known X-ray sources of various classes, including LMXBs, CVs, MSPs, and ABs (Heinke et al., 2005; Bhattacharya et al., 2017; Cheng et al., 2019). Of particular interest for this chapter is the X-ray source CXOGlb J002405.6$-$720452, also known as [GHE2001] W286 (hereafter W286, $\alpha = 00 : 24 : 05.697$, $\delta = -72 : 04 : 52.306$, Heinke et al. 2005; Bhattacharya et al. 2017), which falls within $1''$ of the photometric centre of 47 Tuc (as measured by Goldsbury et al. 2010). A potential optical counterpart was suggested for this source by Edmonds et al. (2003), corresponding to a BY Draconis variable Cl* NGC 104 EGG V32 (hereafter PC1-V32, $\alpha = 00 : 24 : 05.404$, $\delta = -72 : 04 : 52.316$) first identified by Albrow et al. (2001), with a period of 1.64 days. BY Draconis (BY Dra) sources are main sequence variable stars which exhibit luminosity variations due to chromospheric activity and the rotation of the star.

The existence of an IMBH in 47 Tuc has never been proven in previous lit-

erature. Freire et al. (2017) and Abbate et al. (2018) indicate that based on the pulsar accelerations in the cluster, a central IMBH is not needed, with an upper-limit on the mass of a central IMBH of $\sim 4000 M_\odot$ (Abbate et al., 2018). Velocity dispersion modelling by Mann et al. (2019) found that the velocity dispersion in the core of the cluster can be produced by the binaries and BHs in the core, such that an IMBH is not needed to explain the velocity dispersion. They found an IMBH mass of 40 ± 1650 $M_\odot$, and that a central IMBH is only needed if the retention fraction of stellar-mass BHs and NSs is very low. Further multimass modelling by Hénault-Brunet et al. (2020) also indicates that an IMBH is not required in 47 Tuc to explain various observational constraints. Additional modelling of the cluster by Ye et al. (2021) indicated approximately 200 BHs could be present, giving a total mass of BHs in 47 Tuc of $\sim 2000 M_\odot$. Radio continuum surveys have also contributed to placing mass upper limits on central IMBHs, with Lu & Kong (2011) and Tremou et al. (2018) placing 3σ upper mass limits of $520 - 4900 M_\odot$ and $1040 M_\odot$ respectively.

This ultra-deep radio continuum survey we have conducted has produced the deepest radio images ever made of a GC and ever made with the ATCA. It has reached RMS noise levels of $1.2\,\mu\mathrm{Jy\,beam}^{-1}$ at 5.5 GHz, $940\,\mathrm{nJy\,beam}^{-1}$ at 9.0 GHz, and $790\,\mathrm{nJy\,beam}^{-1}$ in a stacked 7.25 GHz image. These unparalleled image depths are the goals of next generation radio telescopes, such as the ngVLA and SKA. Through this survey we have detected several new radio sources that were too faint or variable to be detected in the original MAVERIC observations. This chapter focuses on the detection of a faint radio source at the photometric centre of 47 Tuc, ATCA J002405.702-720452.361 (ATCA J002405 hereafter). The following chapter, Chapter 6, will provide an overview of the other radio sources detected in 47 Tuc, and present the full catalogue of radio sources.

In this chapter, we discuss the first detection of the radio source ATCA J002405 at the centre of 47 Tuc, and search for multiwavelength counterparts to this source to constrain its properties. In Section 5.1, we describe the radio

149

observations taken as part of this radio survey, and detail our calibration and imaging techniques. We also describe the multiwavelength data analysed during this study. The results are presented in Section 5.2. In Section 5.3, we provide a discussion of our findings and step through the possible source classes for ATCA J002405, reaching the conclusion that this source is best explained as an undiscovered pulsar or an IMBH candidate. Finally, Section 5.4 presents our conclusions.

5.1 Observations and data reduction

5.1.1 ATCA observations

47 Tuc was observed by the ATCA under the project code C3427 over 41 epochs between 2021 March 31 and 2022 May 6. For all but five epochs, the array was in an extended 6-km configuration. This array configuration was chosen to maximise spatial resolution. For observations on 2021 December 28, 2021 December 30, 2022 January 2, and 2022 April 25, the array was in the 1.5-km configuration, and for 2022 May 6 the array was in the 750-m configuration. This was done to obtain shorter baseline coverage to improve our sensitivity to some extended sources in the field. A full overview of the date, duration, and array configuration of each epoch is shown in Table 5.1.

Observations were conducted in two bands simultaneously, using the Compact Array Broadband Backend (CABB) correlator (Wilson et al., 2011). The two bands each had a bandwidth of 2048 MHz, split into equal 1 MHz channels, and were centred on frequencies of 5.5 and 9 GHz. The source B1934-638 was used as the primary calibrator for bandpass and flux calibration, and the source B2353-686 was used as the secondary calibrator for amplitude and phase calibration. Occasionally, the source J0047−7530 was used as the secondary calibrator for times where B2353-686 had set. During each observation, after initial calibration on B1934-638 for approximately 15 minutes, we cycled between observing the

secondary calibrator and target for 1 minute and 15 minutes respectively. During poorer observing conditions, the target integration time was reduced to 5 minutes between secondary calibrator scans.

5.1.2   Radio data reduction and imaging

We reduced the data for each band separately. Data calibration was performed using standard procedures in MIRIAD (Sault et al., 1995), before we imported the *uv*-visibilities into the Common Astronomy Software Application (CASA Mc-Mullin et al., 2007) for imaging. We used the `tclean` task for imaging, and used a robust weighing factor of 1.0 to provide a good balance between image sensitivity and resolution. We used the multi-term multi-frequency synthesis deconvolver with two Taylor terms to account for the frequency-dependence of sources in the field, and the resulting images were primary beam corrected using the task `impbcor`. We used cell sizes of $0.3''$ and $0.15''$ and image sizes of 3072 and 5625 pixels for imaging the 5.5 and 9 GHz bands respectively. The image phase-centre was set to approximately $1'$ to the south of the cluster centre. These image sizes and this image phase-centre offset were applied to aid in the reconstruction and deconvolution of some bright, extended sources towards the edge of the image field at 5.5 GHz.

Primary beam corrected images were made at both 5.5 and 9 GHz. We also imaged a co-stack of these to bands, which resulted in an image with an apparent central frequency of 7.25 GHz and a lower image noise than the separate bands. To create the deepest possible images we stacked all 5.5 and 9 GHz epochs, excluding the data taken on 2021 April 7 and 2021 September 29 due to poor observing conditions. Again, we stacked and imaged both bands to produce a deep 7.25 GHz image of the field.

To verify our imaging techniques in CASA were producing reliable results, we also imaged our data using DDFACET (Tasse et al., 2018). DDFACET performs spectral deconvolution using image-plane faceting. Given the small field-of-view

Table 5.1: The ATCA observations of 47 Tuc taken under the project code C3427. For each epoch, the date and start time (in UTC), integration time, and array configuration are given.

Date	Start time (UTC)	Integration time (hr)	Array configuration
2021-03-31	21:00	11.66	6D
2021-04-01	20:00	11.56	6D
2021-04-05	22:00	9.63	6D
2021-04-07	01:30	9.12	6D
2021-04-08	21:30	10.87	6D
2021-04-09	20:30	11.54	6D
2021-04-11	20:00	11.58	6D
2021-04-14	17:00	11.53	6D
2021-04-15	20:00	11.45	6D
2021-04-16	17:00	11.50	6D
2021-04-17	20:00	11.69	6D
2021-04-23	23:00	10.00	6D
2021-06-29	18:30	9.72	6B
2021-06-30	17:30	10.83	6B
2021-07-01	17:30	10.62	6B
2021-09-09	06:00	11.52	6A
2021-09-12	09:00	11.49	6A
2021-09-17	05:00	11.20	6A
2021-09-19	12:00	11.24	6A
2021-09-20	10:00	11.35	6A
2021-09-21	08:30	11.48	6A
2021-09-22	08:30	11.56	6A
2021-09-23	08:30	12.40	6A
2021-09-25	07:30	11.62	6A
2021-09-26	09:00	11.36	6A
2021-09-28	06:00	11.97	6A
2021-09-29	08:30	9.64	6A
2021-10-01	07:30	11.68	6A
2021-11-17	13:00	2.75	6C
2021-11-22	07:00	8.91	6C
2021-12-28	06:00	7.68	1.5A
2021-12-30	02:00	11.75	1.5A
2022-01-02	02:00	10.11	1.5A
2022-01-22	00:30	11.68	6A
2022-01-26	00:00	5.31	6A
2022-01-27	00:00	11.41	6A
2022-01-28	00:00	11.96	6A
2022-01-30	00:00	12.82	6A
2022-01-30	23:30	13.81	6A
2022-04-25	18:00	11.53	1.5A
2022-05-06	15:30	13.64	750D

of this campaign and to improve computational efficiency, we imaged with four facets in a 2×2 configuration. All other imaging parameters such as robustness, image size and cell size were identical to those used in CASA. The images produced using DDFACET contained similar source distributions and noise structure, giving us confidence that our images were the correct representation of the data.

5.1.2.1 Archival radio data

To complement our survey, we searched the ATCA archive for previous observations of 47 Tuc. We combined our data with data taken by Lu & Kong (2011), Miller-Jones et al. (2015), and Bahramian et al. (2017), giving us an extra ~ 35 hr of on-target observations. These data were reduced in the same manner described in Section 5.1.2. The inclusion of these data allowed us to reach RMS noise levels of $1.19 \, \mu \mathrm{Jy} \, \mathrm{beam}^{-1}$ at 5.5 GHz and $940 \, \mathrm{nJy} \, \mathrm{beam}^{-1}$ at 9 GHz. In a stack of all the available data at 7.25 GHz the RMS noise is $790 \, \mathrm{nJy} \, \mathrm{beam}^{-1}$, representing the deepest image made to date with the ATCA.

5.1.3 X-ray data

We used the X-ray source catalogue of 47 Tuc compiled by Bhattacharya et al. (2017) as our main source catalogue to search for potential X-ray counterparts to radio sources. To investigate the X-ray properties of 47 Tuc beyond the scope of Bhattacharya et al. (2017), we queried the *Chandra* archive for previous X-ray observations of the cluster using the *Chandra* /ACIS detector. Nineteen observations of 47 Tuc were made using the *Chandra* /ACIS detector between 2000 and 2015, totalling more than 500 ks of data which we obtained for our analysis.

For data reprocessing and analysis, we used CIAO 4.14 with CALDB 4.9.7 (Fruscione et al., 2006). All X-ray data were reprocessed using `chandra_repro` before stacking. To stack the observations, we first corrected the coordinate system of each observation by using `wavdetect` for source detection, and then `wcs_match`

and `wcs_update` to create a matrix transformation to apply and correct the WCS parameters of each observation based on a single reference observation. When correcting the WCS parameters for stacking, we were only interested in the relative astrometry between each observation as our main aim for this X-ray analysis was to extract X-ray spectra. Considerations of the absolute astrometry are outlined in Section 5.1.6. We used the task `merge_obs` to stack the observations.

Given that 47 Tuc had not been observed by *Chandra* since 2015 prior to our ATCA campaign, we obtained new *Chandra* data of the cluster to search for signs of significant X-ray variability. Under Director's Discretionary Time 47 Tuc was observed for 9.62 ks on 2022 January 26 (Obs ID: 26229) and for 9.83 ks on 2022 January 27 (Obs ID: 26286), giving us almost 20 ks of new *Chandra* data of 47 Tuc for the first time since 2015. These data were reprocessed via the same method described above, and also stacked with the archival *Chandra* data.

5.1.4   HST Data

We used optical data from a variety of different sources in order to complement our survey and search for potential optical counterparts to radio sources detected. Primarily, we used data of 47 Tuc from the HST UV Globular Cluster Survey (HUGS, Piotto et al., 2015; Nardiello et al., 2018), to get an initial insight into the positions and properties of optical sources in the cluster. For further analysis, we used optical and UV data taken with the HST, specifically using the Space Telescope Imaging Spectrograph (STIS). STIS data were obtained from the Mikulski Archive for Space Telescopes (MAST). We used data under the program ID 8219 (PI: Knigge, Knigge et al. 2002) which were obtained between 1999 September 10 and 2000 August 16. Primarily, we looked at FUV data, which used the MIRFUV filter with the FUV-MAMA detector.

In this work we also used NUV and optical data from the programs GO 12950 and GO 9281. The NUV dataset was taken on 2013 August 13 and contains images in the F390W and F300X filters. The optical images were acquired over

three visits on 2002 September 20, 2002 October 2/3 and 2002 October 11 in the F435W (B), F625W (R) and F658N (Hα) filters. All images were calibrated and astrometrically corrected to the epoch J2000 as described in Rivera Sandoval et al. (2015), with PSF photometry carried out as mentioned in Rivera Sandoval et al. (2015, 2018). The optical data were aligned and photometrically analysed using using the software DOLPHOT (Dolphin, 2016). Photometry was obtained using the individual FLC images in the three filters simultaneously, and we used the combined DRC image in the B filter as a reference frame. The magnitude limits are magnitude 27 for the NUV data, magnitude 24.5 for the R and Hα data, and magnitude 25 for the B data.

5.1.5   MUSE integral field spectroscopy

47 Tuc was observed with MUSE (Bacon et al., 2010) in narrow-field mode (NFM) during the night of 2019-11-01, for a total exposure time of 4×600 s. In NFM, MUSE provides a field of view of 7.5×7.5 arcsec with a spatial sampling of 0.025 arcsec and uses the GALACSI module (Ströbele et al., 2012) in laser tomographic adaptive optics (LTAO) mode to achieve a spatial resolution of $\lesssim$0.1 arcsec. The spectral coverage is from 470 to 930 nm with a constant full-width at half maximum (FWHM) of 2.5 Å, corresponding to a spectral resolution of R~1700-3500. The observations were taken as part of the MUSE GTO survey of globular clusters (PI: Kamann/Dreizler), described in Kamann et al. (2018).

The data were reduced with version 2.8.1 of the standard MUSE pipeline (Weilbacher et al., 2020). The pipeline performs the basic reduction steps (such as bias subtraction, flat fielding, wavelength calibration, or flux calibration) on each individual exposure in order to create a pixtable, which contains the WCS coordinates, wavelength, flux, and flux uncertainty of every valid CCD pixel. In the last step, the individual pixtables are combined and resampled to the final data cube.

We extracted individual spectra from the data cube using PAMPELMUSE (Ka-

mann et al., 2013). PAMPELMUSE uses a reference catalog of sources in the observed field in order to measure the positions of the resolved stars and the point spread function (PSF) as a function of wavelength. This information is then used in order to deblend the spectra of the individual stars from the cube. The reference catalogue used in the analysis was published by Anderson et al. (2008) and is based on the HST/ACS survey of Galactic globular clusters presented in Sarajedini et al. (2007). In order to model the non-trivial shape of the MUSE PSF in NFM, we used the MAOPPY model by Fétick et al. (2019).

The extracted spectra were analysed as outlined in Husser et al. (2016). In particular, we measured stellar radial velocities from the extracted spectra by first cross-correlating each of them against a synthetic template spectrum with matched stellar parameters and then performing a full-spectrum fit. The templates used to perform the cross correlation as well as the full spectrum fitting were taken from the GLIB library presented in Husser et al. (2013). During the full-spectrum fitting, we also fitted for the effective temperature T_{eff} and the metallicity [M/H] of each star. The initial values for these parameters and the surface gravity $\log g$ (which was fixed during the analysis) were obtained from a comparison of the HST photometry available in the reference catalog and isochrones from the Bressan et al. (2012) database.

In order to search for any resolved Hα emission, we further created a residuals map from the MUSE data in the wavelength range around 656.3 nm. To do so, we first subtracted the contribution of each resolved star using its spectrum, position in the cube, and the MAOPPY PSF model valid for each wavelength step. In order to suppress any artefacts from the extraction process (like PSF residuals or faint stars missing in the catalog), we also created the residuals map for two wavelength ranges blue- and redwards of Hα. The two off-band residual maps were averaged and subtracted from the on-band residual map.

5.1.6 Astrometry

As we are combining data that have been taken several years apart, we need to consider the epochs that these data were taken in and shift the epochs in a manner such that the coordinates of different surveys can be compared. All source positions and surveys that we consider have coordinates in the equinox J2000.

The epoch of the radio data ranges from J2010.07 to J2022.34. To compare the coordinates of radio sources to other surveys from different epochs, we take the epoch of the radio data to be J2021.2, which corresponds to an average of all observation epochs weighted by the respective integration times.

The positions of the X-ray sources from Bhattacharya et al. (2017) were aligned in that paper with those of pulsars in the cluster based on Freire et al. (2003) and Freire et al. (2017), which are given in the epoch MJD 51600 ($\sim$J2000.16). The positions of optical sources from the HUGS survey are based on the epoch of *Gaia* DR1, which is J2015.0 (Nardiello et al., 2018). The position of the cluster centre has been adopted from Goldsbury et al. (2010) for this work. This position has been astrometrically corrected to the 2MASS (Skrutskie et al., 2006), but does not appear to have been shifted to a particular epoch. Thus, the astrometry is likely to be the epoch at which the data were taken, $\sim$J2006.2.

To check the astrometric frame of the ATCA data, we identified 11 millisecond pulsars (PSR C, D, E, J, L, M, O, Q, S, T, U) whose positions and proper motions have been measured at high precision using pulsar timing observations (Freire et al., 2017), which are detected at $> 3\sigma$ in the ATCA dataset, and which are not confused with other sources. We transformed the timing positions from their measured epoch (J2000.16) to the adopted ATCA epoch (J2021.2). The median offsets in right ascension and declination, in the sense PSR–ATCA, are -0.08 ± 0.05" and $+0.04 \pm 0.06$", respectively, where the uncertainties listed are the standard errors of the mean. The rms offsets in each coordinate are fully consistent with the median uncertainties in the ATCA positions of this sample.

These comparisons suggest that the ATCA absolute astrometry is accurate at least at the $\sim 0.05 - 0.06$" level and potentially better.

Separately, we checked the absolute astrometry of the HUGS optical data by cross-checking with *Gaia* DR3, finding no evidence for an offset and an rms scatter of only ~ 0.01" for bright stars. We also compared the HUGS positions of the four millisecond pulsars (S, T, U, V) with known optical counterparts (Rivera Sandoval et al., 2015) that are present in HUGS, finding very consistent astrometry between HUGS and the proper-motion corrected pulsar positions, with no evidence for an offset and an rms $\lesssim 0.01$". Together these checks show that the optical and radio frames are aligned to within a fraction of an HST pixel.

We re-checked the X-ray astrometry using the millisecond pulsars with precise positions and which Bhattacharya et al. (2017) identify as having relatively uncrowded X-ray data (pulsars C, D, E, H, J, M, N, O, Q, T, U, W, Y, Z, ab). In right ascension, there is indeed no offset (PSR–Chandra $= 0.00 \pm 0.01$"), but we find evidence for a small offset in declination of -0.08 ± 0.02". The overall rms scatter in the PSR–Chandra coordinates is 0.07". This is much less than the listed minimum 95% uncertainty in the *Chandra* X-ray coordinates, so does not meaningfully affect our results, but we do apply the declination offset to the position of the source W286 discussed below.

For the remainder of this chapter, to convert source positions to different epochs for comparison, we assume that the sources that are associated with the cluster move with the cluster proper motion of $\mu_\alpha = 5.25 \, \mathrm{mas \, yr^{-1}}$ and $\mu_\delta = -2.53 \, \mathrm{mas \, yr^{-1}}$. These proper motion values have been adopted from Baumgardt et al. (2019), who derive the mean proper motions of Galactic GCs from *Gaia* DR2.

5.2 Results

5.2.1 ATCA J002405.702-720452.361 − a possible radio counterpart to the X-ray source W286

Our deep ATCA imaging of 47 Tuc revealed a radio source, ATCA J002405.702-720452.361 (ATCA J002405 hereafter), at the photometric centre of the cluster as taken from Goldsbury et al. (2010). The 7.25 GHz image of the core of the cluster is seen in the top panel of Figure 5.1. ATCA J002405 has a 5.5 GHz radio flux density of 6.3 ± 1.2 µJy and a 9 GHz radio flux density of 5.4 ± 0.9 µJy. The radio spectral index ($S_\nu \propto \nu^\alpha$) is $\alpha = -0.31 \pm 0.54$, and is consistent with being flat. Table 5.2 shows the flux density measurements of ATCA J002405 for each of the three main subsets of our campaign, in addition to the full campaign. As the source was not detected in the January subset of the survey, we list the 3σ flux density upper limits of the source in Table 5.2. The source flux densities were measured using the CASA task `imfit` by assuming a point source model, and the 3σ flux density upper limits were calculated by taking three times the central RMS noise of each image.

The best position (in the epoch J2021.2) of ATCA J002405 is:

$$RA = 00 : 24 : 05.7018 \pm 0.0173 \text{ s}$$

$$Dec. = -72 : 04 : 52.631 \pm 0.112''.$$

This position was derived by using `imfit` to fit a point source model to the radio source, with uncertainties due to the thermal noise of the image. As shown in the bottom panel of Figure 5.1, ATCA J002405 is within the positional uncertainty region of the X-ray source W286. Additionally, the angular distance between ATCA J002405 and the cluster centre is less than 0.47 arcsec, which is the sum in quadrature of the Brownian motion radius for a $570 M_\odot$ BH (see Section 5.3.4 for details) and the positional uncertainty of the cluster centre.

Table 5.2: The flux density measurements of ATCA J002405 at 5.5, 7.25, and 9 GHz over the course of the survey. The RMS noise for each band is also listed. The flux density uncertainties also include the uncertainty due to the uncertainty in the calibration. The source was not detected in the January subset of our survey, so we list the 3σ flux density upper limits in this case.

Subset	Frequency (GHz)	S_ν (µJy)	RMS (µJy/beam)
Full survey	5.50	6.3 ± 1.2	1.19
	7.25	5.8 ± 0.8	0.79
	9.00	5.4 ± 0.9	0.94
April	5.50	7.8 ± 1.9	1.88
	7.25	6.5 ± 1.3	1.30
	9.00	3.7 ± 1.5	1.48
September	5.50	5.9 ± 1.7	1.71
	7.25	6.5 ± 1.1	1.11
	9.00	7.5 ± 1.3	1.35
January	5.50	< 6.87	2.29
	7.25	< 4.50	1.50
	9.00	< 5.52	1.84

ATCA J002405 may also display variability on a timescale of several months. The source is detected in a stacked image in at least one of the frequency bands during the April and September subsets of our survey, before not being detected at a significance of $> 3\sigma$ in the January subset. Given the source is only detected at a significance of $> 3\sigma$ in stacked images of the various subsets of the survey, we cannot comment on the intra-month variability of the source.

5.2.2   X-ray properties of W286

W286 was first identified as an X-ray source in 2005 (Heinke et al., 2005). To investigate the X-ray spectral properties of W286, we extracted a 0.3-10 keV X-ray spectrum from all the *Chandra* observations of 47 Tuc and combined them. A circular region with a radius of $1''$ was chosen to extract source counts. An annulus with an inner radius of $1.7''$ and an outer radius of $10''$ was chosen to be the background region, although parts of this annulus were then excluded due to containing other X-ray sources. Source and background spectra were extracted using the CIAO task `spec_extract`, and the task `combine_spectra` was used to

160
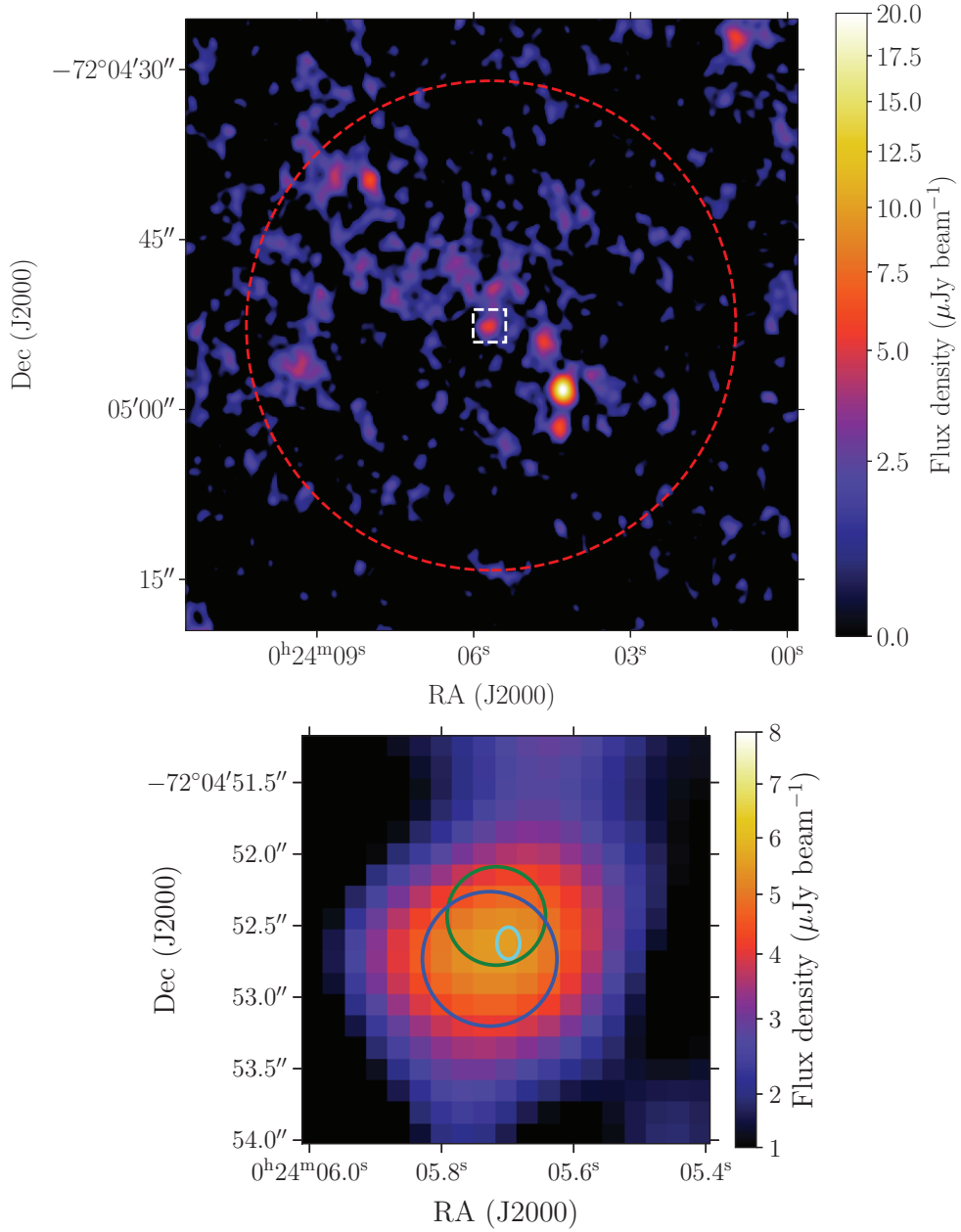
Figure 5.1: Top: The 7.25 GHz radio image of 47 Tuc. The RMS noise level in this image is $\sim 790\,\mathrm{nJy\,beam^{-1}}$. The core radius of 47 Tuc is shown by the dashed red circle. The white dashed box indicates the field of view of the bottom panel. Bottom: The 1σ radio position of ATCA J002405 shown in cyan, compared to the 90% X-ray position of the source W286 (green), and the cluster centre uncertainty plus Brownian motion radius for a $570 M_{\odot}$ BH added in quadrature (blue). All coordinates are in the epoch of the radio image ($\sim$J2021.80). ATCA J002405 is within the uncertainty region of the X-ray source and the cluster centre plus Brownian motion.

Table 5.3: The best-fit parameters of the different X-ray spectral models fit to the combined X-ray spectrum of W286. The photon index (Γ) is listed in the case of the power-law model, and the electron temperature ($\log(kT)$) is shown in the blackbody radiation and apec model cases. The relative probability indicates the probability of another model being preferred relative to the best-fitting model, which is the power-law model in this case. The relative probabilities are calculated using nested sampling to estimate the model evidence for each model fit.

Spectral fit	Γ	$\log(kT)$ (keV)	Relative probability
Power-law	2.1 ± 0.3	-	1.00
Bbodyrad	-	-0.5 ± 0.1	0.79
apec	-	0.6 ± 0.3	0.32

combine the individual spectra extracted for each observation into one stacked spectrum. Spectral analysis was performed using XSPEC 12.11.0m (Arnaud, 1996) and BXA (Buchner et al., 2014). The data were binned to have at least one count per bin, and fitting in XSPEC used C-stat statistics.

We fit three different models to the data: an absorbed power-law model (`tbabs`$\times$`pegpwrlw`), an absorbed blackbody radiation model (`tbabs`$\times$`bbodyrad`), and an absorbed apec (Astrophysical Plasma Emission Code) model from diffuse ionised gas around the source (`tbabs`$\times$`apec`). For all models, we froze the absorption parameter to the value of the hydrogen column density along the line-of-sight towards 47 Tuc, which is $3.5 \times 10^{20}\,\mathrm{cm}^{-2}$. This value is based on an $E(B-V) = 0.04$ from the Harris catalogue (Harris, 1996), assuming $R_V = 3.1$ and the $N_H - A_V$ correlation from Bahramian et al. (2015); Foight et al. (2016). From these, the power-law model was the best-fitting model, with a photon index of $\Gamma = 2.1 \pm 0.3$, and giving a 0.5-10 keV X-ray luminosity of $2.3^{+0.6}_{-0.5}10^{30}\,\mathrm{erg\,s}^{-1}$. A blackbody radiation model is the next best-fitting model with a relative probability to the power-law model of 0.79, followed by the apec model with a relative probability of 0.32. The fit parameters are shown in Table 5.3. The relative probabilities are calculated in BXA, which uses nested sampling to estimate the model evidence for each model fit, and then calculates relative probabilities.

We also visually inspected the X-ray spectrum to search for any distinctive features. In particular, we were searching for evidence of Fe L-shell emission,

which can be a useful feature in identifying the source class of the object (e.g., ABs). The X-ray spectrum of W286 is shown in Figure 5.2, and also shows the best-fit power-law model and the residuals between the model and the data. As can be seen, there is no evidence of an excess around 1 keV, where the Fe L-shell emission is expected. However, given the low number of source counts, any Fe L-shell emission may be too faint to be detected.
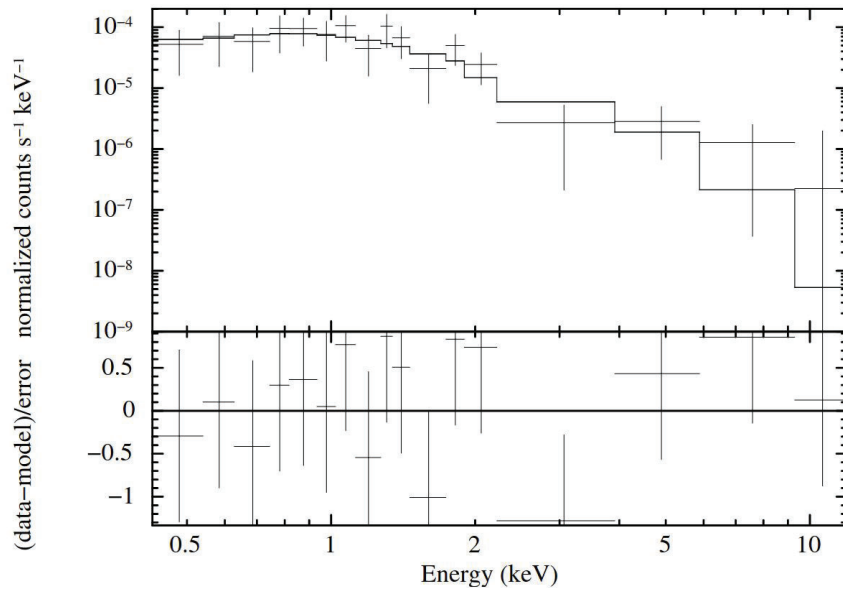
Figure 5.2: The X-ray spectrum of W286, fit with the best-fitting power-law model in the top panel. The bottom panel indicates the residuals between the model fit and the data. There is no evidence around 1 keV of Fe L-shell emission.

5.2.3 Optical and UV properties of W286

To identify possible optical counterparts to ATCA J002405, we use a combination of the HUGS survey and the HST image from the F300X filter. Optical sources in the F300X image have a positional uncertainty of $0.074''$ as outlined in Rivera Sandoval et al. (2015). The F300X HST image of the cluster centre is shown in Figure 5.3. We also consider the BY Dra PC1-V32 as a potential optical counterpart to ATCA J002405 given its previously-claimed association with the X-ray source W286.
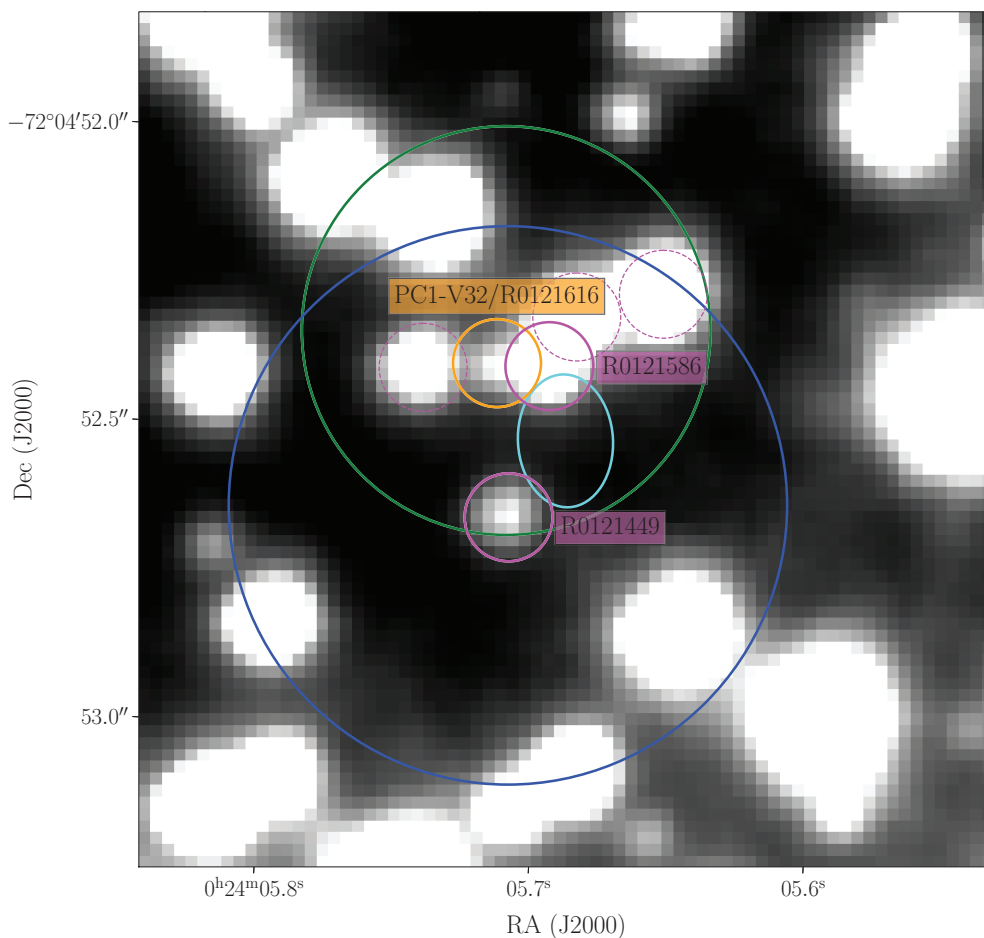
Figure 5.3: The UV (F300X) HST image of the cluster centre, with positions of the radio source ATCA J002405 (cyan), X-ray source W286 (green), and the cluster centre uncertainty and Brownian motion radius for a $\sim 570 M_\odot$ BH added quadrature (blue) plotted as regions. All regions are plotted with coordinates shifted to the epoch of the HST image, J2000. The magenta and orange regions represent positions of optical sources close to ATCA J002405. The solid magenta regions and labels indicate the HUGS sources that are within the 1σ uncertainty region of the radio source, with the dashed magenta regions indicating other nearby optical sources. The orange region and label represents the position of PC1-V32, which falls outside the radio uncertainty region.

From the HUGS survey, we identify three potential HUGS sources that fall within the 1σ uncertainty of ATCA J002405: R0121449, R0121586, and R0121617. Expanding this to 2σ includes PC1-V32 and the nearby HUGS source R0121517 within this uncertainty region. PC1-V32 appears to be associated with the HUGS source R0121616 based on the available photometric information of both sources,

and is located outside the 1σ uncertainty region of ATCA J002405. It is important to note that the sources R0121586 and R0121617 appear superimposed as one source. Upon further inspection, it is likely that the HUGS source R0121617 is not a real source. This source has no cluster membership information in the HUGS catalogue, and was identified in the F435W images in iteration six of the source finding. Upon further inspection of the individual images of the F435W and F336W filters, and the subtracted images in the UV filters, there is no evidence of this source. This, in addition to only one source being detected in the region of the sources R0121617 and R0121586 in the F300X filter, means we are confident that R0121617 is not a real source.

To investigate the properties of these optical sources, we constructed colour-magnitude diagrams (CMDs) of 47 Tuc for various combinations of filters. The filter combinations we considered were F390W vs F300X-F390W (UV), R vs Hα-R (Hα), and R vs B-R (optical). These CMDs are shown in Figure 5.4. PC1-V32 (R0121616) shows some Hα excess, and appears on the AB sequence in the Hα CMD and remains on the binary sequence in the UV CMD. R0121586 appears normal in the optical, UV and Hα, and R0121449 is is consistent with the main sequence in the optical and Hα CMDs, but near the binary sequence in the UV CMD.

We also used data from MUSE in narrow-field mode observations to investigate the optical sources in the X-ray uncertainty region. The narrow-band Hα image is shown in Figure 5.5, with the uncertainty regions of the cluster centre, ATCA J002405, W286, and the optical sources indicated. This figure also shows the residual image after the removal of starlight. From this figure, there are no signs of any extended Hα emission above the detection limit, and no significant Hα source is detected at the location of ATCA J002405.

To complete our optical and UV analysis, we checked to see whether there was a prominent FUV source at the cluster centre that was not present in the optical images. To do this, we visually inspected STIS images of the cluster. This
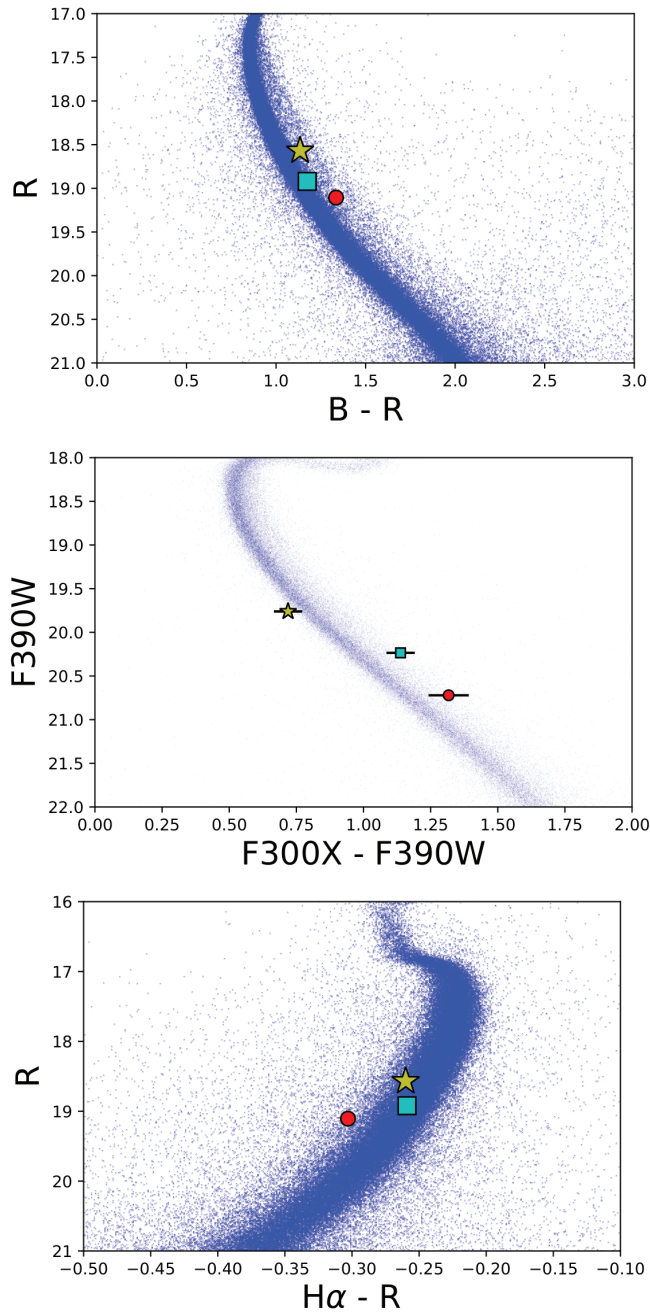
Figure 5.4: The optical, UV, and Hα CMDs of 47 Tuc, with our sources of interest also plotted. The BY Dra PC1-V32 which may be associated with the HUGS source R0121616 is denoted by the red circle, the HUGS source R0121449 is denoted by the cyan square, and the HUGS source R0121586 is denoted by the yellow star.

indicated that there was no evidence of any source within our regions of interest down to a magnitude limit of ~ 24 (the limiting magnitude given in the survey
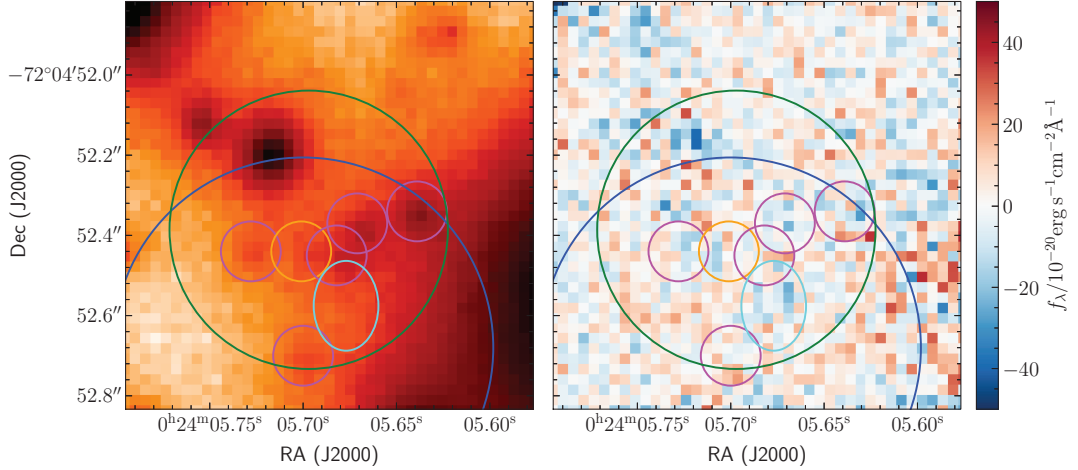
Figure 5.5: The left panel shows the narrow-band Hα image of 47 Tuc using a logarithmic flux map. The regions shown in this image are the same as Figure 5.3. The right panel shows the residuals in Hα after the subtraction of stellar spectra, with the linear flux scale indicated by the colourbar. The regions are the same as shown in Figure 5.3. There is no evidence of a resolved Hα source in the regions considered.

by Knigge et al. 2002).

5.3 Discussion

5.3.1 Possible optical counterparts

We investigated the possible optical counterparts to ATCA J002405, which include the two HUGS sources and PC1-V32 as mentioned in Section 5.2.3. Based on the available photometric data, PC1-V32 appears to be associated with the HUGS source R0121616. This source appears on the binary sequence in the Hα and UV CMDs, which is consistent with it being a BY Dra. PC1-V32 falls outside the 1σ radio position, as seen in Figure 5.3, meaning that while it remains possible it is unlikely that the radio emission observed from ATCA J002405 is associated with PC1-V32. We discuss the radio properties of PC1-V32 and other ABs further in Section 5.3.3.2.

We now consider the two other counterparts identified in the HUGS survey,

R0121449 and R0121586, as potential counterparts as the uncertainty regions on these sources overlap with the radio uncertainty region of ATCA J002405. R0121449 has typical colours for its brightness in the optical and Hα CMDs, and indicates no evidence of accretion. However, the source appears to be consistent within errors with the binary sequence in the UV CMD potentially indicating that it is a binary or variable star. R0121586 is normal in the optical and the Hα CMDs, and falls in the scatter of the main sequence in the UV CMD, again showing no strong evidence for accretion. This source may also be consistent within errors with the binary sequence, for which there are two possible explanations. R0121586 could be a binary that has a slightly bluish component, or the photometry is affected by crowding and this slight shift to the binary sequence is caused by contamination from the nearby PC1-V32 rather than being intrinsic behaviour of R0121586. These properties indicate that neither of these stars are obvious candidates for the source of the radio emission, and there is no obvious optical counterpart to our radio source.

5.3.2 The origin of the X-ray emission

We used the MUSE data to investigate the other optical sources (specifically R0121449 and R0121586) within the X-ray uncertainty region to see if there were any glaring features from these sources that could explain the X-ray emission. The Hα and residual images are shown in Figure 5.5. Some of the optical sources have no spectra extracted because they are too faint, including the source that corresponds to PC1-V32. From this figure, there are no signs of any Hα emission above the detection limit. This indicates that none of these sources show clear evidence of any accretion present in the system. The extracted spectra of the stars within this region also show no strong evidence for Hα emission lines, again indicating that none of these sources are accreting. Overall, none of the optical sources in this field show glaring features in the MUSE data that could favour emission of X-rays via accretion or a similar process. This points to either ATCA

J002405 or PC1-V32 being the source of the X-rays.

5.3.3 Possible radio source interpretations

Given the location of ATCA J002405 in a GC, there are several possible classifications for the source, depending on whether the X-ray emission is associated with the radio source or some other source. By assuming that the X-ray source W286 is associated with ATCA J002405, and a cluster distance of 4.52 kpc (Baumgardt & Vasiliev, 2021) we can plot the source on the radio/X-ray luminosity plane of accreting sources (Figure 5.6). ATCA J002405 falls well above the standard track for accreting stellar-mass BHs, and in a part of the parameter space that is occupied by the black hole X-ray binary (BHXB) candidates in M22 and M62 (Strader et al., 2012a; Chomiuk et al., 2013), and unusual radio-bright white dwarf (WD) systems. We can use this to identify plausible source classes that could be responsible for this radio emission.

5.3.3.1 Direct current (DC) offset in the correlator

For our observations, we chose our pointing centre prior to 2021 October 1 to coincide with that adopted by all other recent ATCA observations of the data, beginning with Lu & Kong (2011), for ease of stacking the data. However, this raises the possibility of a DC offset in the correlator creating a spurious source at the phase centre. If two waveforms are multiplied by a DC offset then the offsets can produce a signal, even if there is no correlation between the two signals.

While a DC offset artefact has not yet been observed in data using the CABB correlator on the ATCA, as soon as we found evidence for a source at the cluster centre we took steps to minimise the possibility that this source could be caused by a system error. For all observations after 2021 October 1 we adjusted the pointing centre of the 47 Tuc scans to the north by 3″. An analysis of the stacked data after 2021 October 1 indicated that no source was detected at the pointing centre of the imaged field. This, in addition to private communications with the
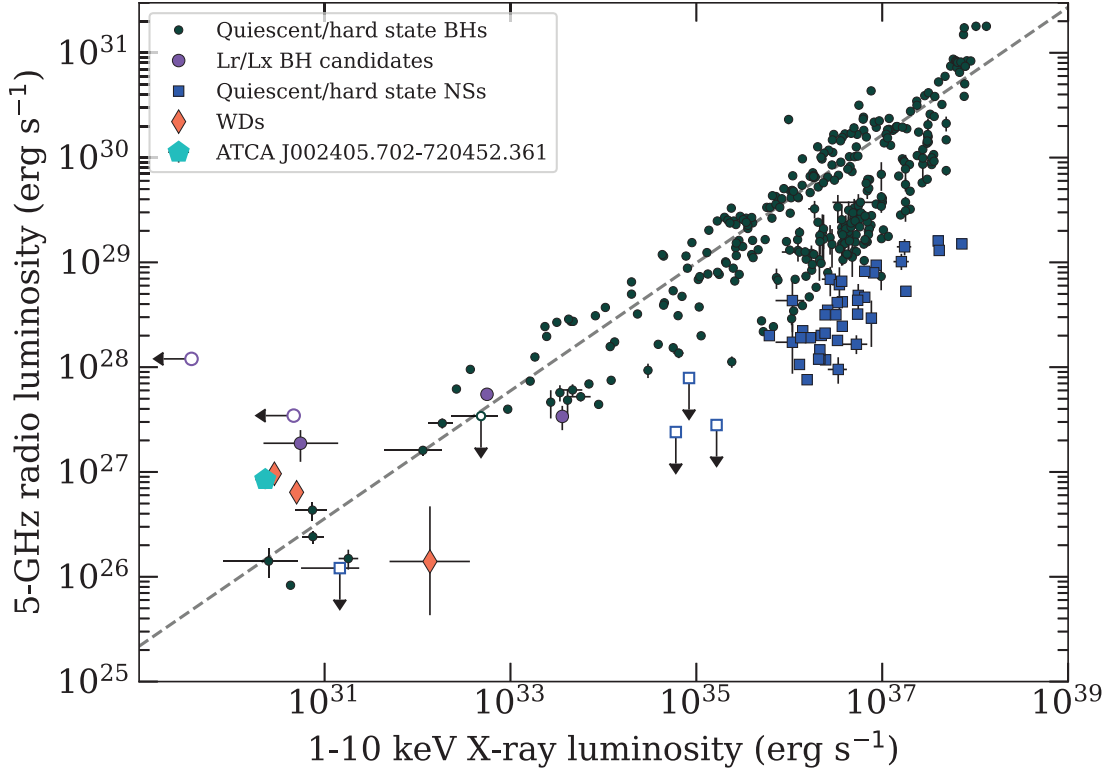
Figure 5.6: The radio/X-ray luminosity plane for several classes of stellar-mass accreting sources, compiled from Bahramian & Rushton (2022). The y-axis represents the quantity νL_ν where $\nu = 5\,\text{GHz}$. The dashed line in this figure indicates the $L_R \propto L_X^{0.6}$ correlation for BHs from Gallo et al. (2014). ATCA J002405 falls well above the standard track for accreting BHs, assuming that it is associated with the X-ray source W286, and a distance to 47 Tuc of 4.52 kpc (Baumgardt & Vasiliev, 2021). The error bars for this point are smaller than the marker size.

ATCA Senior Systems Scientist regarding previous experience with the CABB correlator, means we are confident in ruling out a DC offset as the origin of ATCA J002405.

5.3.3.2 Active binary

ABs, tidally locked stars producing X-ray emission, make up a large portion of the X-ray sources in GCs below $L_X < 10^{31}\ \text{erg s}^{-1}$ (Güdel, 2002). Furthermore, there is an observed relationship between the radio and X-ray emission of active stars of $L_X/L_R \approx 10^{15}$ (Guedel & Benz, 1993). We find it unlikely that ATCA J002405 is a type of AB. If we assume that the X-ray emission is associated with

the radio source, the source becomes a radio-bright outlier on the Güdel-Benz relation, as shown in Figure 5.7, by about an order of magnitude. If the X-ray emission is not associated with the radio source, then the upper limit on the X-ray luminosity will decrease making the source even more of an outlier on the Güdel-Benz relation.
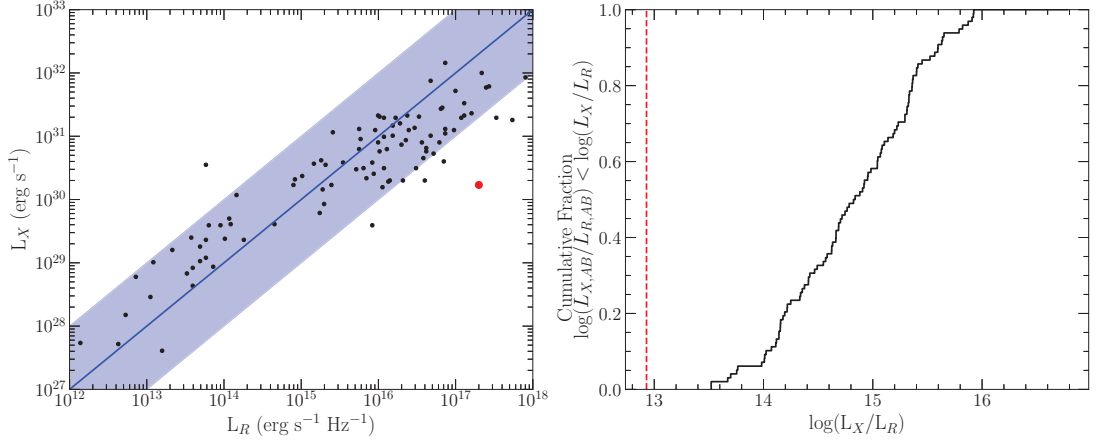
Figure 5.7: The left panel shows the radio/X-ray relation for ABs from Guedel & Benz (1993). The red circle indicates our radio detection of ATCA J002405, and that it is outside the scatter of the correlation. The right panel indicates the cumulative fraction of ABs for various L_X/L_R fractions, with the red dashed lined indicating the L_X/L_R fraction of ATCA J002405.

Additionally, we have discussed the possibility of the BY Dra PC1-V32 being associated with ATCA J002405. For a comparison to the radio properties of ATCA J002405, we also assessed the radio luminosities of a larger group of BY Dra systems, by constructing a sample based on radio and optical surveys. Our sample of BY Dra was chosen from the Zwicky Transient Facility (ZTF) catalogue of variables (Bellm et al., 2019), as classified by Chen et al. (2020), who identified a total of 84,697 BY Dra systems. To confine our comparison to the most confident subset of these, we only select sources with at least 200 observations and false alarm probability less than 10^{-5} in at least one band. This resulted in a total of 17,015 sources with a confident classification, and periods spanning from 0.15 to 44 days, fully encompassing the 1.64-day period of PC1-V32. We then cross-matched this subset with Gaia DR3 (Gaia Collaboration et al., 2022) using a

coordinate offset threshold of 0.1″, based on the estimated astrometric RMS of the ZTF survey[1] (Masci et al., 2019), yielding 10,237 systems. Of these systems, we retained only sources with parallax significance $> 10\sigma$ and located < 0.5 kpc from Earth, such that wide-area radio surveys such as the Very Large Array Sky Survey (VLASS; typical sensitivity ~ 128 to $145\,\mu$Jy beam^{-1}; Gordon et al., 2021) would be able to probe radio luminosities to sufficient depth. This resulted in a total of 1,403 BY Dra systems with high confidence classification, tightly constrained distances within 500 pc, and relatively deep constraints on radio luminosity. We then obtained $1' \times 1'$ cutout images around each source (using the NRAO VLASS Quick Look database[2]) and searched each of these cutouts statistically (searching for any pixels with peak flux densities above the 3σ of the $1' \times 1'$ cutout) and inspected each visually to verify presence/absence of a source. We found no significant radio sources within 1″ of any of these systems. Our 3σ radio luminosity upper limits are computed from the RMS values of the $1' \times 1'$ cutout images for each individual source, and are shown in Figure 5.8. We also compare our results to V* BY Draconis (the prototypical BY Dra variable), which is located at 16.5 pc with a consequently high proper motion of 374.74($\pm$0.04) mas yr^{-1} (Gaia Collaboration et al., 2022). V* BY Draconis is clearly detected in the VLASS survey at $\sim$6 mJy. However, this corresponds to a radio luminosity of $\sim 2 \times 10^{15}$ erg s^{-1} Hz^{-1}, over two orders of magnitude radio-fainter than ATCA J002405, further reducing the likelihood that PC1-V32 is the origin of the radio emission. In summary, we find that BY Dra variables are extremely unlikely to show strong radio emission.

5.3.3.3 Accreting white dwarf

Accreting WDs also account for a large number of the X-ray emitting sources in GCs (Grindlay et al., 2001; Pooley et al., 2002). Some WDs have been ob-

---

[1]Given that Gaia and ZTF surveys have been performed close in time, effects of displacement by high proper-motion are be negligible.

[2]https://archive-new.nrao.edu/vlass/quicklook/
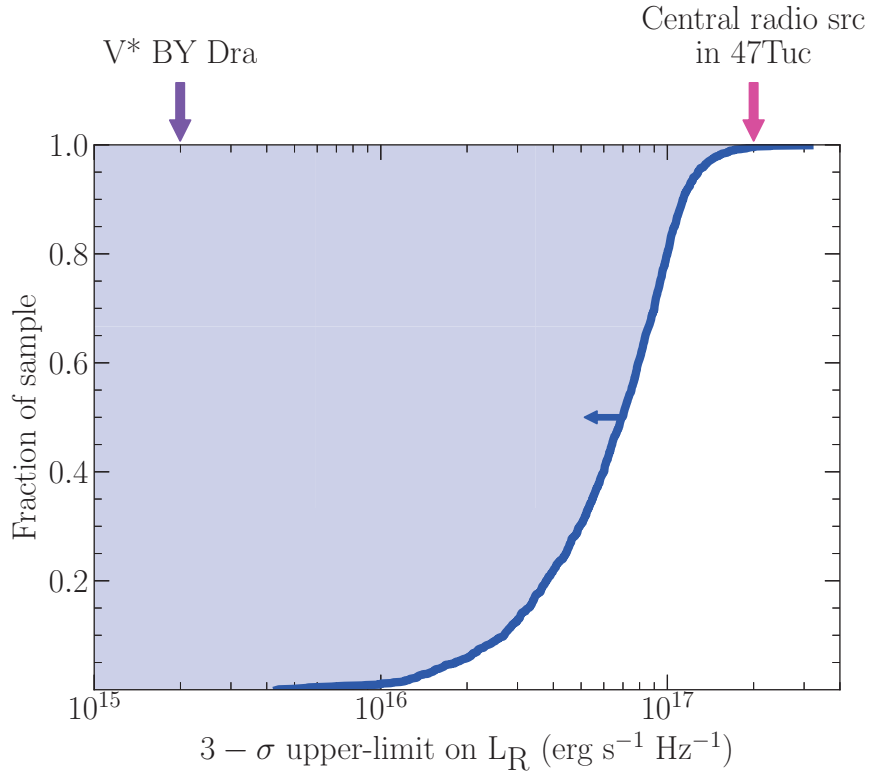
Figure 5.8: Cumulative distribution of radio luminosity upper-limits for BY Dra variables in the sample investigated in this work. The purple arrow indicates the detected radio luminosity of V* BY Draconis, and the pink arrow indicates the radio luminosity of ATCA J002405 in 47 Tuc. No known BY Dra variable has radio luminosity comparable to ATCA J002405.

served to reach the level of radio luminosity that we observe from ATCA J002405. However, these systems are only this radio bright during short radio flares and not persistently. While ATCA J002405 in 47 Tuc may display variability and is undetected in the January campaign of the survey, it was detected in April and September, and CV flares are not as long-lasting as these individual month-long subsets of the survey, or the time between the April and September campaigns. Furthermore, the two optical sources consistent with the radio position of the source show no evidence of being a CV candidate or some other type of radio bright WD as their colours are inconsistent with those of known WDs and CVs in 47 Tuc (Rivera Sandoval et al., 2018). Additionally no CV has been identified at this position despite extensive monitoring. Thus, we find it unlikely that

ATCA J002405 is a type of CV or other accreting WD. We do note, however, that photometry will be incomplete when going to fainter magnitudes at the centre of 47 Tuc. This means that a faint optical counterpart could still be present, even though it is not seen in the HST data.

5.3.3.4 Active galactic nucleus

Active galactic nuclei (AGN) account for a large portion of background sources in the radio sky, meaning that it is entirely possible that ATCA J002405 is an AGN that happens to be coincident with the cluster centre. However, it is unlikely that we would get a background AGN that is coincident with the centre of 47 Tuc. When considering the background differential source counts from Wilman et al. (2008), the number of AGN expected within one Brownian motion radius of the cluster centre for a $570M_\odot$ BH when taking uncertainties into account (0.47 arcsec) with a radio flux density greater than or equal to that of ATCA J002405 is 4×10^{-4}. This is shown in Figure 5.9. This indicates that it is very unlikely that ATCA J002405 is a background AGN.

5.3.3.5 Pulsar

47 Tuc is known for containing a rich collection of pulsars, including millisecond pulsars (MSPs) and other isolated and spider pulsars. To date, there are 29 known pulsars in 47 Tuc[3]. As we will show in Chapter 6, we have detected several known pulsars in continuum imaging meaning that it is possible we have detected a new pulsar very close to the cluster centre. Such a source may not have been detected in previous pulsar surveys due to its faint radio flux density, and the potential for it to be highly accelerated or hidden around part of its orbit. Spider pulsars, pulsars that are ablating their stellar companion, in particular can be hidden around parts of their orbit due to eclipsing or absorption (Roberts, 2013).

The radio spectral index of ATCA J002405 is $\alpha = -0.31 \pm 0.54$, which while

---

[3]http://www.naic.edu/~pfreire/GCpsr.html#47Tuc
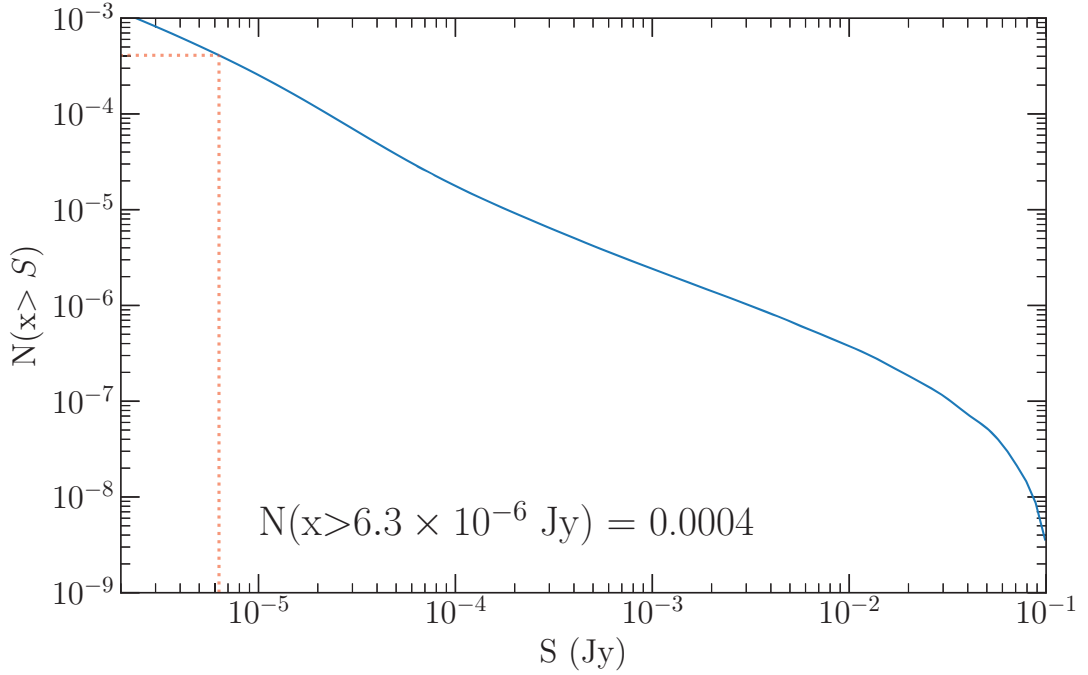
Figure 5.9: The number of AGN we expect within the sky area of interest with a radio flux density greater than a given threshold plotted against flux density. The red dashed line indicates the 5.5 GHz radio flux density of ATCA J002405. We expect the number of AGN within the sky area of interest with a flux density greater than this to be 4×10^{-4}, making it unlikely that ATCA J002405 is an AGN.

consistent with a flat spectrum object, is also consistent with the tail-end of the pulsar spectral index distribution. A recent examination of the radio spectra of Galactic MSPs by Aggarwal & Lorimer (2022) have shown that the population of MSPs has a mean spectral index of -1.3 with a standard deviation of 0.43. Further to this, Martsen et al. (2022) have shown that the MSPs in Terzan 5 have a spectral index distribution with a mean of -1.35 and a standard deviation of 0.53, indicating that the MSPs in GCs seem broadly consistent with the overall MSP population as shown in Figure 5.10. The spectral index of ATCA J002405 is consistent with both of these distributions. The probability of obtaining a spectral index > -0.85 (the lower uncertainty bound on our spectral index measurement) from the distribution of Aggarwal & Lorimer (2022) is 0.14. Similarly, the probability of obtaining a spectral index > -0.85 from the distribution of

Martsen et al. (2022) is 0.17. This indicates that based on its spectral index
ATCA J002405 could be an undiscovered pulsar at the centre of the cluster. Fur-
ther deep observations would be needed by other facilities such as MeerKAT to
detect pulsations from and derive a timing solution for this potential pulsar. For
a typical pulsar spectral index of –1.35, its predicted 1.4 GHz flux density would
be able 40 μJy, which while faint is within the range of pulsars previously de-
tected in 47 Tuc (Camilo et al., 2000), while a flatter spectral index, as measured
(–0.31), would imply a 1.4 GHz flux density of only $\sim 10\mu$Jy.
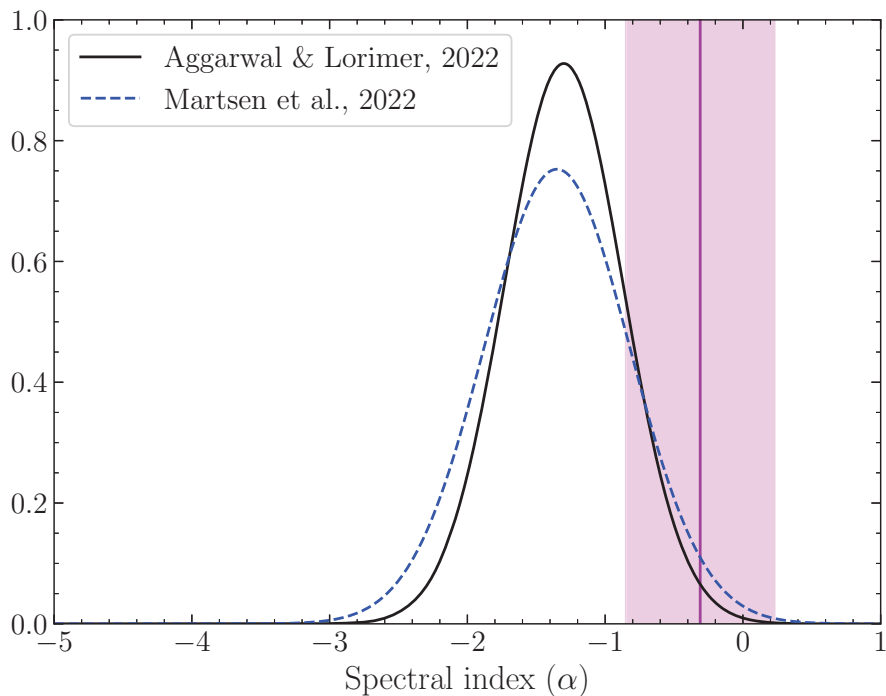
Figure 5.10: The spectral index distribution for a Galactic sample of MSPs from
Aggarwal & Lorimer (2022) shown in black, and that for a sample of MSPs in
Terzan 5 from Martsen et al. (2022) shown in blue. The radio spectral index
of ATCA J002405 is shown as the magenta vertical line, with the shaded region
indicating the 1σ uncertainty on this value. The spectral index of ATCA J002405
is consistent with the tail-end of the pulsar spectral index distribution.

5.3.3.6   Stellar-mass black hole

After decades of debate, we now know that GCs do contain stellar-mass BHs
(e.g., Giesers et al., 2018, 2019). 47 Tuc contains the ultra-compact candidate

BH X-ray binary 47 Tuc X9 (Miller-Jones et al., 2015; Bahramian et al., 2017), indicating that 47 Tuc may indeed contain some number of stellar-mass BHs. Modelling by Ye et al. (2021) has indicated that 47 Tuc could presently contain around 200 stellar-mass BHs, with a total BH mass in the cluster of $\sim 2300 M_\odot$. Due to the number of BHs expected in 47 Tuc, it is possible that ATCA J002405 is a stellar-mass BH in an XRB that has undergone some brightening. A *Chandra* DDT observation taken on 2022 January 26 and 27 indicates no increase in X-ray emission from W286 over what was detected in 2015 (albeit this non-detection also corresponds to the radio non-detection in the January subset of the observing campaign), and an analysis of *Swift* X-ray data over the past year shows no increase in total cluster X-ray luminosity, meaning a flaring X-ray transient $> 10^{33}$ $\mathrm{erg\,s^{-1}}$ can be ruled out.

On the radio/X-ray luminosity plane (Figure 5.6), ATCA J002405 falls above the standard correlation for accreting BHs. This is in the same part of the parameter space as the stellar-mass BH candidates in the clusters M22 (Strader et al., 2012a) and M62 (Chomiuk et al., 2013), indicating that the radio/X-ray luminosity ratio of ATCA J002405 is similar to other BH candidates in clusters. Other stellar-mass BHs in quiescence have also been shown to occupy this part of the parameter space, specifically MAXI J1348-630 (Carotenuto et al., 2022). The radio spectrum of ATCA J002405 is consistent with being flat, which is what is expected from stellar-mass BHXBs. Furthermore, the best-fitting model to the X-ray spectrum of W286 is a power-law model with a photon index of $\Gamma = 2.1 \pm 0.3$. This means that if W286 is associated with the radio source, its X-ray spectrum is consistent with an accreting BH in quiescence (Plotkin et al., 2017).

While the radio and X-ray properties of the source may be consistent with a stellar-mass BH, we have found no clear optical counterpart to ATCA J002405, although we again note that a counterpart too faint to be detected in HST data could have been missed. As discussed in Section 5.3.1, the two optical sources

consistent with ATCA J002405 show no significant evidence of accretion, or show any significant discrepancy from the single star main sequence within uncertainties. This is at odds with what has been observed in other stellar-mass BHXB systems. For quiescent BHXBs, it is expected to observe some emission from the outer accretion disk. For example, the disk emission component in the X-ray transient A0620-00 is estimated as at least 10% of the total light in the near-infrared (Cantrell et al., 2010). Thus, for an accreting BHXB we would not expect the optical counterpart to fall on the main sequence of the cluster CMD. Due to this inconsistency in the optical properties of the source, we cannot conclusively confirm a stellar-mass BH as the classification of ATCA J002405, despite the supportive radio and X-ray behaviours.

5.3.4   A central intermediate-mass black hole

The multi-wavelength properties of ATCA J002405 do provide evidence that the source could be a candidate IMBH. The position of the source within the radius of Brownian motion of the photometric cluster centre is where IMBHs in GCs would be expected to be located - they are the heaviest objects in the cluster and should have migrated to the cluster centre by dynamical friction. The radio spectrum of the ATCA J002405 is also flat, consistent with what is expected for an IMBH in a low-luminosity state. Although ATCA J002405 does show evidence of variability, some radio variability is expected in quiescence (Plotkin et al., 2019) and has been observed previously in other BH systems, such as V404 Cygni and Sgr A*.

We can make some estimates as to the mass of a potential IMBH through the fundamental plane of BH activity. We adopt the following form of the fundamental plane with mass as the dependent variable as shown in Miller-Jones et al. (2012):

$$\log M_{BH} = (1.638 \pm 0.070) \log L_R - (1.136 \pm 0.077) \log L_X$$
$$- (6.863 \pm 0.790),$$

(5.1)

where the BH mass is in solar masses, and the radio and X-ray luminosities are in $\mathrm{erg\,s^{-1}}$.

For the case where the X-ray emission from W286 is associated with the radio emission from ATCA J002405, we can get a direct estimate of the BH mass from the radio and X-ray luminosity. The 5.5 GHz flux density of the source is $6.3\,\mu\mathrm{Jy}$, corresponding to a 5.5 GHz luminosity of $8.47 \times 10^{26}\,\mathrm{erg\,s^{-1}}$ at a distance of 4.52 kpc (Baumgardt & Vasiliev, 2021), and the 0.5-10 keV X-ray luminosity of W286 is then $2.3 \times 10^{30}\,\mathrm{erg\,s^{-1}}$. This corresponds to a BH mass of $570^{+430}_{-260}M_\odot$. This uncertainty is the statistical uncertainty and was calculated by considering only the errors on the radio and X-ray luminosities. We note that the scatter of the fundamental plane will also increase the uncertainty on the mass estimate. While Miller-Jones et al. (2012) found a scatter in the residuals of Equation 5.1 of 0.44 dex, a more robust examination of the intrinsic scatter in the fundamental plane was performed by Gültekin et al. (2019). Through Markov Chain Monte Carlo simulations, Gültekin et al. (2019) found a systematic uncertainty in this relation of ~ 1 dex. It is this more conservative estimate of 1 dex that we take to represent the intrinsic scatter in the fundamental plane. This means that our mass estimate of any BH is uncertain by at least a further order of magnitude, giving a nominal 1σ mass range of $60 - 6000 M_\odot$. Additionally, studies of the pulsar accelerations in 47 Tuc provide a BH mass upper limit of $\sim 4000 M_\odot$ (Abbate et al., 2018) meaning that the effective mass range to consider is $60 - 4000 M_\odot$, which is broadly consistent with an IMBH.

It is worth noting that because of this scatter in the fundamental plane, our mass estimate cannot currently be made any more certain. It appears that the scatter in the mass direction for this relation is largely driven by AGN, and it is unknown how this scatter translates to lower mass BHs such as IMBHs, which represent unexplored parts of the fundamental plane parameter space. A better mass estimate for any central BH could be achieved if an orbiting companion is identified, allowing for the mass to be dynamically measured. Alternatively, one

could attempt to use the $M_{BH} - \sigma$ relation from Greene & Ho (2006) to estimate the BH mass. The reported intrinsic scatter in this relation is $0.4\,$dex, meaning it is better than that of the fundamental plane. However, this method is difficult to apply in a GC because of shot noise, meaning that there are not enough stars within the BH's sphere of influence to accurately measure the velocity dispersion (see, e.g., de Vita et al. 2017). Overall, despite its large intrinsic scatter, the fundamental plane still remains the only currently viable method to estimate the mass of this source.

If we consider our best estimate for the IMBH mass ($570 M_\odot$), the Brownian motion radius can be estimated as $\langle x^2 \rangle = (2/9)(M_*/M_{BH}\ r_c^2)$, where M_* is the average mass of a star in the cluster core (taken to be $\sim 1 M_\odot$) and r_c is the core radius of the cluster (see Strader et al. 2012b and Tremou et al. 2018). Using $M_{BH} = 570 M_\odot$, the Brownian motion radius would be $0.43''$. Since this radius scales as M_{BH}^{-1}, the systematic uncertainty on the fundamental plane relation could increase or decrease this value by up to an order of magnitude. This allows a large angular area within which an IMBH can be perturbed from the cluster centre due to interactions with stars and stellar remnants.

The mass estimate above only considers the case where both the radio emission from ATCA J002405 and the X-ray emission from W286 are associated with a central IMBH. It is important to also consider the case where the X-ray emission from W286 is not associated with ATCA J002405 and is instead associated with PC1-V32, in which case we can again use the fundamental plane to estimate a BH mass lower-limit. This can be calculated using the measured radio luminosity of the source, and an upper-limit on the X-ray luminosity from the source. Given that the radio source position falls within the uncertainty region of W286, we adopt the X-ray luminosity of W286 as the X-ray luminosity upper-limit. This then corresponds to a BH mass lower limit of $> 570 M_\odot$. Again, this value represents our best estimate as to the BH mass lower limit in this case and this estimate is affected by the intrinsic $1\,$dex scatter on the fundamental plane,

meaning that our 1σ BH mass lower limit is effectively $> 60 M_\odot$.

It is also important to consider the case where both the radio emission from ATCA J002405 and the X-ray emission from W286 are not associated with a candidate IMBH. Because the of the presence of a radio source within the Brownian motion region, it is possible that the radio emission from a potential IMBH could be hiding in the wings of the radio emission from ATCA J002405. In this case, we can use the flux density of ATCA J002405, in addition to an estimation of the X-ray emission expected from an IMBH accreting from the intra-cluster gas, to derive a mass upper-limit for a central IMBH in 47 Tuc. This process follows the methodology outlined in Strader et al. (2012b) and Tremou et al. (2018). The X-ray luminosity of a source is related to its accretion rate ($L_X = \epsilon \dot{M} c^2$), and for accretion rates less than 2% of the Eddington rate the radiative efficiency ϵ scales with accretion rate (Maccarone, 2003; Vahdat Motlagh et al., 2019) and can be expressed as:

$$\epsilon = 0.1 \left(\frac{\dot{M}}{\dot{M}_{Edd}}/0.02 \right). \tag{5.2}$$

The accretion rate $\dot{M}$ is assumed to be some fraction of the Bondi accretion rate, usually ~ 0.03 (Pellegrini, 2005; Maccarone et al., 2007). To compute the Bondi accretion rate we take the gas number density to be $n = 0.2$ cm^{-3}, consistent with pulsar measurements (Abbate et al., 2018). We also assume that the gas is fully ionised with a temperature $T = 10^4$ K and a mean molecular mass $\mu = 0.59$ which is typical for fully ionised gas (Fall & Rees, 1985). For consistency with Strader et al. (2012b) and Tremou et al. (2018), we only consider the $\gamma = 1$ isothermal case, although we note that the $\gamma = 5/3$ adiabatic case will result in a higher mass upper-limit.

Using the flux density of ATCA J002405 (6.3 µJy) gives a mass upper limit of $< 860 M_\odot$ on the presence of a central IMBH in 47 Tuc in the isothermal case, which is lower than that calculated by Tremou et al. (2018) due to the unparalleled image depth we have achieved. However, as with previous mass estimates in this section, this value only represents our best estimate of the mass upper limit,

and this estimate is affected by the intrinsic scatter in the fundamental plane, effectively increasing it to an upper limit of $< 4000 M_\odot$ as constrained by the pulsar accelerations.

5.4 Conclusion

In this chapter, we present the deepest radio image of the globular cluster 47 Tucanae. Our ultra-deep imaging campaign with the Australia Telescope Compact Array at 5.5 and 9 GHz has allowed us to reach an RMS noise level of $790\,\mathrm{nJy\,beam^{-1}}$, representing the deepest radio continuum image made of a globular cluster and the deepest radio image ever made by the Australia Telescope Compact Array.

Based on analysis of these data, we have identified ATCA J002405.702-720452.361, a flat-spectrum, variable radio source that falls within the uncertainty region of the faint X-ray source W286 and the cluster centre. This source has a 5.5 GHz flux density of 6.3 ± 1.2 µJy and a spectral index of $\alpha = -0.31 \pm 0.54$. We consider several possible explanations for the origin of the radio and X-ray emission, and conclude that the radio source does not originate from the previously proposed counterpart to W286, a BY Draconis source (PC1-V32), and that the X-ray emission from W286 is associated with either PC1-V32 or this newly discovered radio source. We consider several possible source class explanations for ATCA J002405.702-720452.361, which are summarised in Table 5.4, and we find that the most likely classifications for the source are either an undiscovered pulsar or a candidate intermediate-mass black hole. A stellar-mass black hole appears less likely than these other explanations but cannot be ruled out.

It is not unsurprising that a pulsar at the cluster centre may have been missed. ATCA J002405.702-720452.361 is very faint, meaning that it may have been invisible to previous low-frequency pulsar surveys of 47 Tucanae. Additionally, the pulsar could be highly accelerated or hidden for parts of its orbit, either through absorption or eclipsing by a binary companion, again rendering it invis-

182

ible. Further deep observations with MeerKAT would be needed to fully explore this possibility, in addition to potential higher or lower-frequency detections to attempt to further constrain the spectral index of the source. These observations would allow us to test whether ATCA J002405.702-720452.361 is another member of 47 Tucanae's large pulsar population.

In the event that ATCA J002405.702-720452.361 is a candidate intermediate-mass black hole, we use the fundamental plane of black hole activity to estimate the mass of the source. In the event that the radio and X-ray emission are associated the black hole mass is $570^{+430}_{-260}M_\odot$, which is significantly lower than previous mass constraints on the presence of an intermediate-mass black hole in 47 Tucanae. However, as discussed in-depth in Section 5.3.4, this value only represents our best estimate of the BH mass. The fundamental plane has an intrinsic scatter of ~ 1 dex, giving a nominal 1σ uncertainty range of $60-6000M_\odot$, which is further reduced at the upper end by the pulsar accelerations of the cluster imposing a mass upper limit of $4000M_\odot$. An intermediate-mass black hole with mass $\sim 570M_\odot$ would have a sphere of influence of $\sim 0.8''$. It would be valuable to get proper motions for as complete as possible a sample of stars within this sphere of influence, either with ground-based adaptive optics data or with the James Webb Space Telescope. This would allow the presence of a central intermediate-mass black hole to be tested, either through dynamical modelling or through searching for a potential companion star.

Table 5.4: Comparison of explanations for the origin of the radio emission.

Source class	Possibility	Comment
Active binary	?	Radio emission is too bright for an active binary at this distance (Section 5.3.3.2)
White dwarf	?	Colours of optical counterparts are inconsistent with known WDs (Section 5.3.3.3)
AGN	?	Unlikely to have an AGN at this flux density this close to the cluster centre (Section 5.3.3.4)
Stellar-mass BH	✓	L_R/L_X ratio can be consistent with other BH candidates, no clear optical counterpart (Section 5.3.3.6)
Pulsar	✓✓	Spectral index is consistent with pulsar spectral index distribution (Section 5.3.3.5)
IMBH	✓✓	Radio source is located at the cluster centre, mass estimates $> 100 M_\odot$ (Section 5.3.4)

CHAPTER 6

A RADIO SOURCE CATALOGUE OF 47 TUCANAE

Chapter 6 of this thesis, "A radio source catalogue of 47 Tucanae", is as yet unpublished. This is my own work except for the following. The analysis of 47 Tuc W41 was the result of discussions with T. J. Maccarone and will be published in a manuscript in preparation by Maccarone et al.. This discussion has been synthesised into this chapter. Discussions regarding the interpretation of the results were contributed by my supervisory panel – A. Bahramian, J. C. A. Miller-Jones, and A. Kawka. Further discussions were also contributed by T. J. Maccarone, and J. Strader.

In Chapter 5, we described a deep, 480 hr ATCA survey of 47 Tuc to search for faintly accreting BHs and other exotic binary systems producing in radio emission. This culminated in the detection of ATCA J002405, which we proposed as either an undiscovered pulsar or an IMBH candidate. However, while this source is the most high impact result to come out of this survey, the reduction in RMS noise has given us sensitivity to several faint radio sources that were invisible in

the initial MAVERIC survey, and allows us to explore other science goals. For example, the large pulsar population of 47 Tuc can be probed, allowing for further spectral constraints to be placed on known pulsars and to search for new pulsars that are in potentially highly accelerated or eclipsed systems that would have been missed by traditional pulsar timing searches.

On the heels of our discovery in Chapter 5, we explore and catalogue the population of radio sources in 47 Tuc in this chapter. While some of these radio sources have been detected previously (see e.g., Miller-Jones et al. 2015; Tudor et al. 2022), several of these sources have been detected for the first time as they were either too faint or variable to be detected in previous surveys of 47 Tuc. In Section 6.1 we describe our data collection and imaging procedures, and discuss our source detection methodology. In Section 6.2 we present the catalogue of radio sources detected in 47 Tuc, and discuss the catalogue completeness and spectral properties of the sources detected. In Section 6.3 we explore the multiwavelength properties of the radio sources detected by searching for X-ray counterparts to these sources, and also use our catalogue to determine whether we have any detections of the pulsar population in 47 Tuc. Finally, Section 6.4 presents a discussion of a new candidate redback pulsar, 47 Tuc W41, that was identified through our radio survey, and Section 6.5 presents our conclusions.

6.1 Data collection, imaging, and source finding

The collection and imaging of these data are described more comprehensively in Chapter 5.1, however a brief overview is also presented here for completeness. 47 Tuc was observed with the ATCA under the project code C3427 for a total of 41 epochs between 2021 March 31 and 2022 May 6. The array was predominantly in an extended 6-km configuration to provide the best possible angular resolution except for the following five epochs. The array was in the 1.5-km configuration on 2021 December 28, 2021 December 30, 2022 January 2, and 2022 April 25; and in the 750-m configuration on 2022 May 6. These more compact configurations

were obtained to provide more short baseline coverage to improve the sensitivity to some larger, extended sources in the image field. The source B1934-638 was used as the primary calibrator, with the source B2352-686 used as the main secondary calibrator. The source J0047-7530 was also occasionally used as the secondary calibrator for times when B2352-686 had set.

The data were reduced and imaged using standard procedures in MIRIAD (Sault et al., 1995) and CASA version 5.6.2-3 (McMullin et al., 2007). Imaging used the task `tclean` with a robust weighting factor of 1.0, and image sizes of 3072 and 5625 and cell sizes of 0.3 arcsec and 0.15 arcsec respectively at 5.5 and 9.0 GHz. All images were primary beam corrected and then stacked to produce the deepest possible image at each frequency. We also used the imaging software DDFACET (Tasse et al., 2018) to verify that our images were producing reliable results.

To perform source finding on the 5.5, 9.0 and stacked 7.25 GHz images from the ultra-deep ATCA survey of 47 Tuc, we use the source extraction software PYBDSF (Mohan & Rafferty, 2015). PYBDSF performs source finding by first using a sliding box algorithm to estimate the background RMS and mean images, and then by finding islands of source emission and fitting them with multiple elliptical Gaussians to approximate the source shape. We used PYBDSF to obtain (Gaussian) shape parameters, source position and uncertainty, and peak flux and uncertainty for detections in each band.

For consistency with the previous source catalogue of 47 Tuc extracted as part of the MAVERIC survey (Shishkovsky et al., 2020; Tudor et al., 2022), we used the same parameters for source finding with PYBDSF. The sliding box used to estimate background RMS and mean images had a size of 150×150 pixels, with steps of 30 pixels. For brighter sources (SNR> 50), the sliding box instead had a size of 50×50 pixels and moves in steps of 10 pixels. This is done to account for the artefacts around bright sources. Source finding was performed on the primary-beam corrected images to ensure that accurate source fluxes were calculated as

PYBDSF identified sources away from the maximum response of the primary beam. While source finding was performed over the entire image, we are only interested in sources that fall within the half-light radius of 47 Tuc (190.2 arcsec). This is because these sources are most likely to be cluster members. As we move beyond the half-light radius, the probability of a source being a cluster member reduces. We created two source catalogues: a catalogue of radio sources detected with a significance of $> 5\sigma$, and a catalogue of sources detected to $> 3\sigma$. Sources detected with a significance of $> 5\sigma$ represent confident detections, while 3σ are marginal and can be helpful in cross-matching with multiwavelength catalogues with the presence of external evidence.

6.2   A radio source catalogue of 47 Tucanae

Within the half-light radius of 47 Tuc, we detect 81 sources at a significance $> 5\sigma$, of which 21 sources have counterparts at both 5.5 and 9.0 GHz, meaning that spectral indices for these sources can be calculated. The 5σ source catalogue, and a description of the data it contains, is shown in Appendix B in Table B.1. Also shown in Appendix B are the images of the cluster at 5.5, 7.25, and 9.0 GHz. The radial distribution from the cluster centre of the radio sources detected is shown in the top panel of Figure 6.1. This histogram is a function of the increasing area probed by larger annuli for bins further away from the cluster centre. Background sources should have a roughly constant sky density and will scale with area, whereas the density of cluster sources will fall off further from the core. These two effects combined gives the resulting distribution in Figure 6.1. The bottom panel of Figure 6.1 shows the number of sources detected per unit area for each histogram bin. Within the core radius of the cluster, we see that there are more sources detected per unit area, indicating that there is evidence for an excess of sources towards the cluster centre.
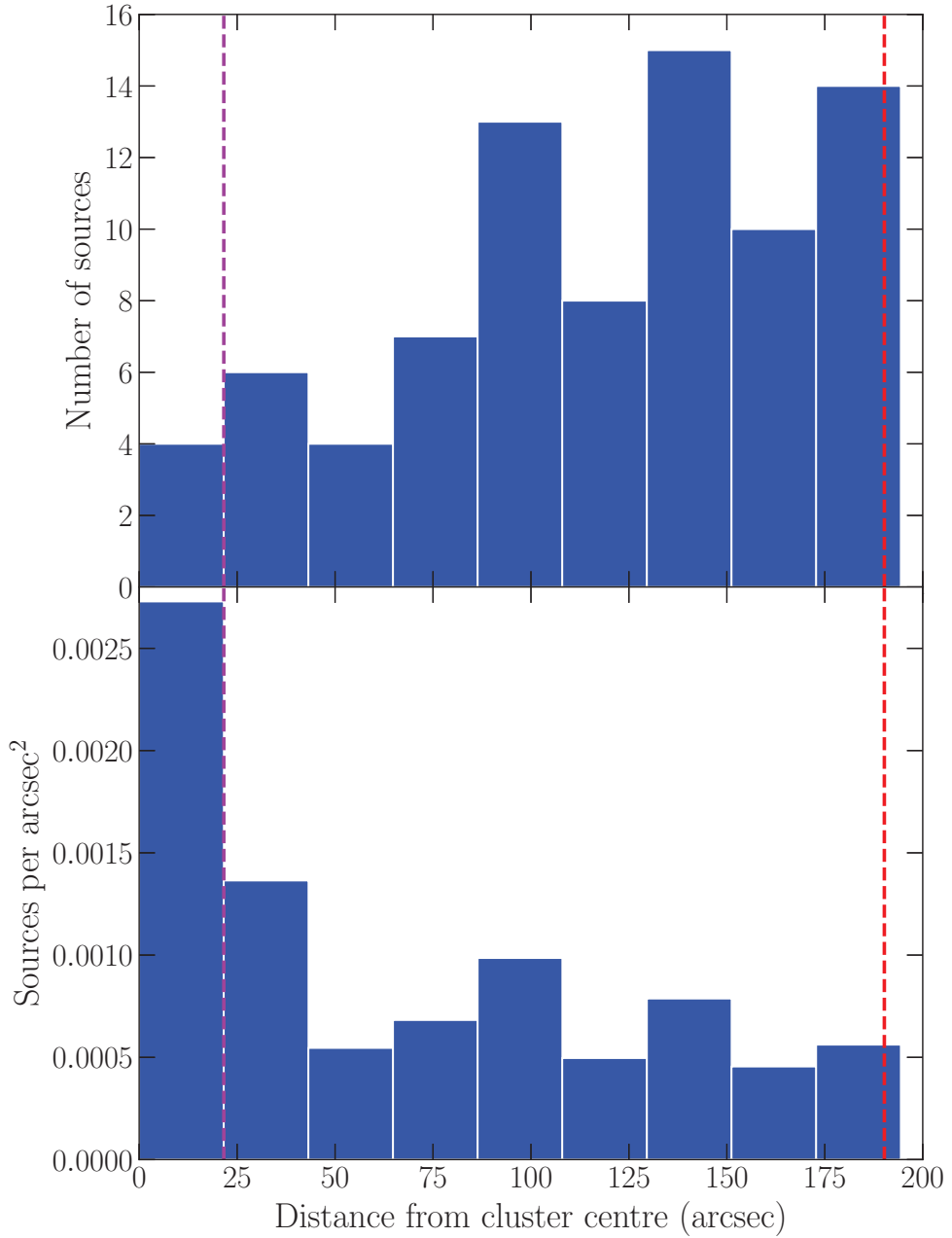
Figure 6.1: Top: A histogram showing the radial distribution from the cluster centre of the 81 sources detected in 47 Tuc. The magenta dashed line indicates the core radius of 21.6 arcsec and the red dashed line indications the half-light radius of 190.2 arcsec. Bottom: A histogram showing the number of sources detected per unit area for each histogram bin. The magenta and red dashed lines indicate the same as in the top panel. It can be seen that there are more sources detected per unit area within the cluster core, indicating that there is evidence for an excess of radio sources towards the cluster centre.

6.2.1 Completeness and false detections

The completeness of our source extraction is dependent on the RMS noise of the input images. Our RMS noise for each band is $1.1\,\mu\text{Jy beam}^{-1}$ for 5.5 GHz, $790\,\text{nJy beam}^{-1}$ at 7.25 GHz, and $940\,\text{nJy beam}^{-1}$ at 9.0 GHz. For our 5σ catalogue, this means that the faintest sources we are sensitive to have flux densities of $5.5\,\mu\text{Jy}$ at 5.5 GHz, $4.0\,\mu\text{Jy}$ at 7.25 GHz, and $4.7\,\mu\text{Jy}$ at 9.0 GHz. A visual inspection of the image overlaid with the regions of the extracted sources indicates that the sources that were missed by the source extraction algorithm were either just below the 5σ threshold, or in more crowded places in the image with noiser structure around the source, potentially interfering with how PYBDSF spawns islands to then fit with Gaussians. This is particularly true towards the edges of the images. The extensive investigations of Tudor et al. (2022) in deep MAVERIC radio images, including source injection tests, showed that a 5σ threshold provided a catalogue that was complete to above the 90% level, whereas a 3σ threshold was only complete to a $\sim 40\%$ level. Since our images are not significantly affected by artefacts, we adopt the estimates of Tudor et al. (2022) for our completeness thresholds.

For the 3σ catalogue, the faintest sources we are sensitive to have flux densities of $3.3\,\mu\text{Jy}$ at 5.5 GHz, $2.4\,\mu\text{Jy}$ at 7.25 GHz, and $2.8\,\mu\text{Jy}$ at 9.0 GHz. As indicated above, completeness will be more of an issue for this fainter source catalogue, as it will be easier for true sources to hide among the noise structure of the image and be missed by the detection algorithm, and there is a higher chance of noise spikes being detected as spurious sources. Thus, care needs to be taken when using the 3σ catalogues. A visual inspection of the image field would assist in discerning which sources may be spurious, and additional evidence (such as an optical or X-ray counterpart) is needed to reliably infer the presence of a radio source.

190

6.2.2 Spectral indices

There are 21 radio sources that have counterparts at 5.5 and 9.0 GHz within an angular separation of 1 arcsec, meaning that a spectral index for these sources can be calculated. The spectral index α is calculated as:

$$\alpha = \frac{\log S_1 - \log S_2}{\log \nu_1 - \log \nu_2}, \tag{6.1}$$

where $\nu_1 = 5.5\,\text{GHz}$, $\nu_2 = 9.0\,\text{GHz}$, and S_1 and S_2 are the source flux densities at these frequencies respectively. The uncertainty in spectral index $\delta\alpha$ is calculated through standard error propagation. These 21 sources and their spectral indices are shown in Table 6.1 and also in the full catalogue in Table B.1 for completeness, and the distribution of spectral indices for these sources is plotted in Figure 6.2. The distribution of spectral indices ranges between a minimum of -1.94 and a maximum of -0.18, and has a mean spectral index of -1.22 and a standard deviation of 0.47. This indicates that a large fraction of the sources we identify at both frequencies are likely pulsars, given the negative spectral indices (Aggarwal & Lorimer, 2022), or AGN, that are expected to have canonical spectral indices around -0.7 (Condon et al., 2002).

Table 6.1: The spectral indices of the 21 radio sources with detections at 5.5 and 9.0 GHz.

Source	$S_{5.5}$	$\delta S_{5.5}$	$S_{9.0}$	$\delta S_{9.0}$	α	$\delta\alpha$
ATCA J002435.006-720501.764	31.6	1.5	12.2	1.8	-1.94	0.72
ATCA J002427.989-720603.846	28.7	1.3	15.9	1.5	-1.20	0.50
ATCA J002424.196-720259.877	13.0	1.4	9.6	1.7	-0.61	0.97
ATCA J002422.552-720532.146	12.1	1.2	6.4	1.3	-1.30	1.04
ATCA J002422.249-720408.702	16.1	1.3	6.9	1.2	-1.71	0.91

Continued on next page

Table 6.1 – continued from previous page

Source	$S_{5.5}$	$\delta S_{5.5}$	$S_{9.0}$	$\delta S_{9.0}$	α	$\delta\alpha$
ATCA J002418.146-720619.392	29.6	1.4	12.0	1.4	-1.84	0.58
ATCA J002417.272-720559.496	11.9	1.4	6.8	1.2	-1.15	1.01
ATCA J002413.963-720431.731	16.1	1.3	7.6	1.2	-1.53	0.83
ATCA J002413.312-720332.769	82.4	1.4	39.8	1.3	-1.48	0.17
ATCA J002413.520-720605.282	14.6	1.3	7.5	1.2	-1.35	0.88
ATCA J002413.306-720225.217	18.1	1.5	12.3	1.8	-0.79	0.80
ATCA J002410.334-720741.358	79.8	1.6	38.4	1.3	-1.49	0.27
ATCA J002408.584-720708.177	30.7	1.5	16.9	1.7	-1.21	0.51
ATCA J002404.272-720458.087	21.6	1.3	19.7	1.1	-0.18	0.39
ATCA J002403.340-720234.852	27.0	1.4	18.0	1.7	-0.82	0.50
ATCA J002359.037-720603.590	12.8	1.2	8.0	1.3	-0.94	0.87
ATCA J002357.479-720559.959	15.2	1.3	7.4	1.4	-1.47	0.96
ATCA J002352.437-720356.174	29.5	1.2	15.1	1.2	-1.37	0.43
ATCA J002349.247-720538.170	20.7	1.2	10.7	1.4	-1.34	0.66
ATCA J002341.759-720522.089	9.8	1.4	8.9	1.4	-0.18	0.99
ATCA J002340.881-720511.592	172.3	1.5	74.8	1.5	-1.70	0.10

6.2.3 Source counts

Radio source counts have been used to test the viability of different cosmological models. The source counts distribution is the cumulative distribution of the number of sources N brighter than a certain flux density S. Extragalactic radio sources, such as AGN, are expected to form a large portion of the background sources detected in radio surveys. To test if a particular radio survey contains an excess of radio sources, it is important to consider how many background radio sources one expects to be contaminating a survey. The differential source count $n(S_i)$ is the number of radio sources per unit flux density per unit sky area, and
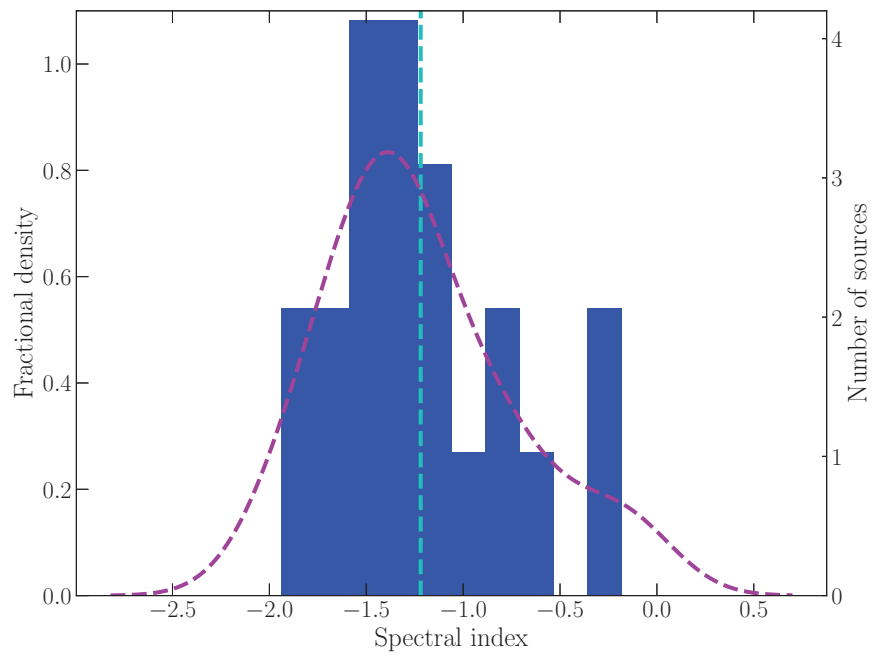
Figure 6.2: The distribution of the spectral indices of radio sources detected at both 5.5 and 9.0 GHz shown in blue. The magenta dashed curve indicates a kernel density estimate of the histogram (using Gaussian kernels and a binwidth of 0.54), and the cyan dashed line indicates the mean of the spectral index distribution of -1.22 and a standard deviation of 0.47.

is expressed as:

$$n(S_i) = \frac{dN}{dSd\Omega}.$$

(6.2)

Differential source counts are used in radio astronomy population statistics as they are less prone to instrumental and observational biases (Crawford et al., 1970). The number of background sources expected per steradian can be calculated by integrating from the RMS noise of an image up to the maximum flux density recorded.

$$\frac{n(> S_{min})}{\text{sr}} = \int_{S_{min}}^{\infty} \frac{dN}{dS} dS.$$

(6.3)

We use the source count simulation from Wilman et al. (2008) to estimate the number of background sources we expect to be detected within our survey. Wilman et al. (2008) performed a semi-empirical simulation of the radio continuum sky to estimate the distribution of extragalactic radio sources. This simulation is complete down to a radio flux density limit of 10 nJy and covers various frequencies ranging from 151 MHz to 18 GHz, including a frequency of 4.86 GHz which is the closest frequency in this simulation to our observed frequency of 5.5 GHz. We use this particular source count distribution to estimate the number of background sources we expect within the half-light radius of 47 Tuc (3.17′) that have a flux density greater than five times the RMS noise of our 5.5 GHz image (5.5 µJy). This value was chosen as it represents the faintest source in the 5.5 GHz image that we could detect to 5σ significance, results in approximately 109 background sources expected within the half-light radius, assuming they are spatially isotropic.

We can now compare this number of expected background sources with the total number of sources we detect in our survey. At 5.5 GHz, we detect 68 sources to $> 5\sigma$ significance and 337 sources to $> 3\sigma$ significance, meaning a number of these sources can be expected to be background sources like AGN rather than being associated with the cluster. Of course, some of these sources have already been identified as cluster members, such as X9, W41, and various pulsars, with

the caveat that these sources are well within the half-light radius of the cluster. However, for the remaining sources, careful multiwavelength follow-up would be needed to confirm whether these sources are indeed cluster members, or whether they are background sources. When going to fainter sources like those listed in the 3σ source catalogue, again most sources can be attributed to background sources, with the remaining sources again needing follow-up analysis to confirm whether they are true sources and whether they are cluster members. However, to properly interpret the findings associated with this fainter source catalogue, the completeness and false detection rate statistics would be needed.

What this analysis does indicate, in conjunction with Figure 6.1, is that there is evidence of an excess of radio sources towards the core of the cluster. The sources further away from the cluster core are more likely to be attributed to background sources. However, further follow-up analysis, in particular attempting to identify an optical counterpart, is crucial in determining whether the radio sources detected in clusters are indeed cluster members.

6.3   Searching for multiwavelength counterparts

Prior to cross-matching with any multiwavelength catalogues, we first verified that the astrometric frame of the radio data was correct. This is outlined in Chapter 5, where we identified MSPs that are detected to $> 3\sigma$ significance in our dataset, and compared their continuum positions, as localised in our survey, with their timing positions from Freire et al. (2017). This indicated that the median offsets in RA and Dec are < 0.1 arcsec, meaning that the ATCA astrometry is accurate to well below 0.1 arcsec.

We compared our radio source catalogue with other multiwavelength source catalogues to search for potentially interesting exotic objects, such as XRBs and MSPs. The main catalogue used for this cross-match is the X-ray source catalogue of Bhattacharya et al. (2017). This catalogue was chosen as it used *Chandra* to produce an X-ray source catalogue of 47 Tuc, meaning it has sufficient angular

resolution to resolve faint X-ray sources in the crowded centre of the cluster. Additionally, we also search for radio continuum detections of the known pulsar population in 47 Tuc.

6.3.1 X-ray sources in 47 Tuc

X-ray observations of 47 Tuc have shown that it contains more than 300 X-ray sources of various source classes including LMXBs, MSPs, CVs, and ABs (Heinke et al., 2005; Bhattacharya et al., 2017). A large number of these X-ray sources do not have confident identifications, and some sources have potentially been misclassified. This was the case for 47 Tuc X9, which was initially classified as a CV (Paresce et al., 1992), before the identification of a radio counterpart and further X-ray studies indicated that the source was better explained as an ultracompact BHXB (Miller-Jones et al., 2015; Bahramian et al., 2017). We can use our radio source catalogue to search for X-ray sources with previously unidentified radio counterparts, allowing us to search for new XRBs in the cluster.

We used the X-ray source catalogue of Bhattacharya et al. (2017) as our main catalogue for comparison. This is an X-ray point source catalogue that detected 370 X-ray sources within the half-mass radius of 47 Tuc. This catalogue was made by combining *Chandra* ACIS observations from 2000, 2002, 2014, and 2015 to create a deep X-ray dataset. The X-ray source detection was performed using the CIAO task `wavdetect`, a source detection algorithm using Mexican-Hat based wavelets (Freeman et al., 2002). This catalogue was also astrometrically corrected using the positions of known pulsars in the cluster, and matched the X-ray and radio positions of the pulsars to a standard deviation of 0.16 arcsec in RA and 0.08 arcsec in Dec (Bhattacharya et al., 2017).

We used TOPCAT (Tools for OPerations on Catalogues And Tables; Taylor 2005) to search for radio and X-ray sources with coordinates that matched within an angular separation of 1 arcsec. We used the catalogue of 3σ radio sources at 5.5 and 9.0 GHz for this cross-match as identifying an X-ray source that is consistent

with a 3σ radio source indicates that the radio emission is probably real and not a noise spike.

We identify 45 3σ radio sources that have X-ray counterparts from Bhattacharya et al. (2017) within 1 arcsec. These sources are shown in Table 6.2, which also presents the following information:

1. Source name with the ATCA J prefix

2. Source name with the CXOGlb prefix from Bhattacharya et al. (2017)

3. Separation between the radio and X-ray coordinates in arcsec

4. 5.5 GHz radio flux density in µJy (sources which have their 7.25 or 9.0 GHz flux densities listed instead are denoted with $S_{7.25}$ and $S_{9.0}$ respectively in the notes column)

5. 0.5-6.0 keV X-ray luminosity in units of $10^{30} \, \mathrm{erg \, s^{-1}}$ from Bhattacharya et al. (2017), calculated assuming a distance of 4.53 kpc

6. X-ray W source number from Bhattacharya et al. (2017)

7. Notes about the X-ray sources from Bhattacharya et al. (2017).

Table 6.2: The $> 3\sigma$ radio sources in 47 Tuc that have X-ray counterparts within an angular separation of 1 arcsec, within the half-light radius of the cluster.

ATCA J	CXOGlb	Sep	S_ν	L_X (0.5-6.0 keV)	W	Notes
		(arcsec)	(μJy)	($10^{30}\,\mathrm{erg\,s^{-1}}$)		
002435.006-720501.764	002435.0-720502	0.055	31.6	10.3	132	
002434.487-720335.507	002434.5-720335	0.423	11.4	1.0	366	
002434.141-720333.332	002434.2-720333	0.191	10.2	2.5	193	
002419.458-720334.733	002419.4-720335	0.434	7.1	24.5	114	
002418.146-720619.392	002418.1-720619	0.500	29.6	0.4	231	
002417.272-720559.496	002417.1-720559	0.761	11.9	0.4	232	
002416.550-720425.499	002416.5-720425	0.426	4.7	1.9	104	MSP-Q
002415.962-720426.755	002415.9-720436	0.566	4.2	96.1	2	X13, $S_{9.0}$
002415.708-720306.472	002415.7-720307	0.629	8.3	2.4	166	
002414.582-720654.017	002414.4-720653	0.990	4.8	0.4	240	$S_{9.0}$
002413.915-720443.720	002413.9-720444	0.211	15.8	2.7	67	MSP-D
002413.808-720302.316	002413.8-720302	0.150	5.4	18.5	117	$S_{7.25}$

Continued on next page

198

Table 6.2 – continued from previous page

ATCA J	CXOGlb	Sep (arcsec)	S_ν (μJy)	L_X (0.5-6.0 keV) ($10^{30}\,\mathrm{erg\,s^{-1}}$)	W	Notes
002413.312-720332.769	002413.2-720333	0.444	82.4	0.7	380	
002413.520-720605.282	002413.6-720605	0.328	14.6	0.8	375	
002411.682-720517.046	002411.7-720518	0.827	3.7	1.0	249	$S_{9.0}$
002411.546-720224.390	002411.5-720224	0.119	14.8	10.2	118	
002411.179-720520.169	002411.1-720520	0.323	8.1	3.1	7	MSP-E
002411.085-720620.471	002411.1-720620	0.513	10.1	17.1	120	
002409.849-720359.879	002409.8-720360	0.283	8.4	3.1	11	MSP-U
002408.617-720439.024	002408.5-720439	0.447	5.3	1.0	105	MSP-T
002408.584-720708.177	002408.6-720708	0.113	30.7	0.6	186	
002407.982-720439.779	002407.9-720440	0.224	6.4	4.2	19	MSP-G,I
002407.428-720416.846	002407.5-720418	0.942	5.7	0.3	270	$S_{7.25}$
002405.812-720345.892	002406.0-720346	0.967	3.8	4.3	168	
002407.125-720507.494	002407.2-720507	0.550	3.3	2.0	200	$S_{9.0}$
002406.131-720724.495	002406.0-720725	0.953	6.5	0.4	284	$S_{9.0}$

Continued on next page

Table 6.2 – continued from previous page

ATCA J	CXOGlb	Sep (arcsec)	S_ν (µJy)	L_X (0.5-6.0 keV) ($10^{30}\,\mathrm{erg\,s^{-1}}$)	W	Notes
002405.702-720452.361	002405.7-720452	0.530	6.3	1.7	286	J002405 from Chapter 5
002405.095-720429.319	002405.2-720430	0.773	3.1	0.5	395	$S_{9.0}$
002404.657-720453.988	002404.6-720454	0.274	8.0	6.1	39	MSP-O
002404.272-720458.087	002404.3-720458	0.147	21.6	1151.9	42	X9
002404.347-720501.237	002404.3-720501	0.117	9.8	14.4	41	Discussed in Section 6.4
002404.217-720420.605	002404.2-720420	0.454	4.4	2.4	142	$S_{7.25}$
002403.725-720456.919	002403.8-720457	0.334	4.3	7.5	106	MSP-L
002403.981-720442.851	002404.0-720442	0.484	4.7	3.7	352	MSP-S
002402.675-720538.547	002402.6-720539	0.170	4.6	3.1	52	
002401.252-720504.819	002401.4-720504	0.771	3.8	1.1	306	$S_{9.0}$
002359.427-720358.843	002359.4-720359	0.102	17.2	7.5	63	MSP-J
002357.685-720501.951	002357.7-720502	0.056	4.5	58.1	64	
002354.533-720531.089	002354.5-720531	0.439	4.1	1.8	107	MSP-M
002353.418-720708.502	002353.4-720708	0.726	4.9	1.9	188	

Table 6.2 – continued from previous page

ATCA J	CXOGlb	Sep (arcsec)	S_ν (µJy)	L_X (0.5-6.0 keV) ($10^{30}\,\mathrm{erg\,s^{-1}}$)	W	Notes
002350.404-720431.561	002350.4-720431	0.259	13.4	1.1	108	MSP-C
002349.247-720538.170	002349.2-720538	0.487	20.7	0.2	341	
002346.155-720714.874	002346.2-720714	0.620	15.4	1.9	355	
002344.865-720602.368	002344.8-720602	0.431	4.1	15.5	126	$S_{9.0}$
002340.881-720511.592	002341.0-720511	0.636	172.3	0.6	384	

As seen in Table 6.2, we have radio detections of 12 MSPs that also have X-ray emission in 47 Tuc. Beyond this, the only other notable X-ray sources we detect are the BHXB candidate X9, the source ATCA J002405 discussed in Chapter 5, the X-ray source W41 (discussed in Section 6.4), and the X-ray source 47 Tuc X13. The majority of the remaining X-ray sources in the catalogue cross-match have X-ray luminosities $< 10^{31}\,\mathrm{erg\,s^{-1}}$, consistent with a low-level accreting WD or AB classification in the event they are not foreground or background sources. Some of these sources could also be quiescent BHs or NSs, but further interrogation of available multiwavelength data would be needed to determine if any such sources could be identified.

6.3.2   Millisecond pulsars in 47 Tuc

47 Tuc has the second largest known pulsar population in a GC, behind only Terzan 5. Of the 29 known pulsars in 47 Tuc, only 25 have reliable positions. The positions of 47 Tuc ae and 47 Tuc af are unpublished, and there are currently no exact positions for 47 Tuc ac and 47 Tuc ad given the scintillation affecting their detections, although these two sources are probably within 0.5 arcmin of the cluster centre (Ridolfi et al., 2021). Given the radio detections of 12 MSPs with X-ray emission, we cross-matched our 3σ radio source catalogues at 5.5 GHz and 9.0 GHz with the known locations of these 25 pulsars to search for continuum flux detections. We used the same methodology from Section 6.3.1, where TOPCAT was used to search for radio sources in our catalogue that are within an angular separation of 1 arcsec of the known pulsar timing positions.

At 5.5 GHz, we have continuum flux detections of 12 known MSPs, with the MSPs M and S detected for the first time in continuum imaging. These pulsars are listed in Table 6.3, and the positions of these pulsars are also shown in Figure 6.3. With the exception of the MSPs C, D, and J, the 5.5 GHz flux density of these MSPs is $< 10\,\mathrm{\mu Jy}$. These pulsars would have been missed by previous radio continuum surveys of 47 Tuc at these frequencies, and it is only

ATCA J	Pulsar	Sep (arcsec)	$S_{5.5}$	$\delta S_{5.5}$	$S_{9.0}$	$\delta S_{9.0}$	α	$\Delta\alpha$
002350.404-720431.561	C	0.262	13.4	1.2	-		-	-
002413.915-720443.720	D	0.213	15.5	1.2	3.8	1.0	-2.85	0.56
002411.179-720520.169	E	0.412	7.0	1.2	3.5	1.1	-1.41	0.73
002407.982-720439.779	G/I	0.332	6.4	1.5	4.7	1.7	-0.63	0.61
002359.427-720358.843	J	0.114	17.2	1.3	-		-	-
002403.725-720456.919	L	0.213	4.3	1.3	-		-	-
002354.533-720531.089	M	0.406	4.1	1.0	-		-	-
002404.657-720453.988	O	0.250	7.8	1.4	-		-	-
002416.550-720425.499	Q	0.445	4.7	1.2	-		-	-
002403.981-720442.851	S	0.509	4.7	1.4	-		-	-
002408.617-720439.024	T	0.331	5.4	1.4	-		-	-
002409.849-720359.879	U	0.192	8.0	1.3	-		-	-

Table 6.3: The known MSPs in 47 Tuc that we have detections for 5.5 GHz and 9.0 GHz. Listed in the table are the ATCA J source names for each pulsar from our radio source catalogue, the pulsar name, the separation between the radio continuum and pulsar timing coordinates in arcsec, the 5.5 and 9.0 GHz flux densities, and the spectral indices if they can be calculated.

due to the unparalleled image depths that we reach in our survey that we are able to detect these pulsars, and in particular M and S for the first time, in continuum images. We also detect 9.0 GHz counterparts for three known MSPs: D, E, and G/I. For these pulsars we can calculate a meaningful spectral index, which is also included in Table 6.3. These spectral indices are steep, typical for pulsars, and are consistent with the values presented in McConnell et al. (2001), however this is mainly due to the large uncertainties in the spectral indices presented by McConnell et al. (2001). The 9.0 GHz flux densities for these sources are < 5 µJy again indicating that our radio survey is the first survey capable of detecting this emission at these higher frequencies.

6.4 W41 - a case study

47 Tuc W41 (CXOGlb J002404.3-720501) is a faint ($L_X \sim 10^{31}$ erg s^{-1}) X-ray source in the core of 47 Tuc (Heinke et al., 2005; Bhattacharya et al., 2017). The optical counterpart to the source was first identified in 2001 as the source PC1-
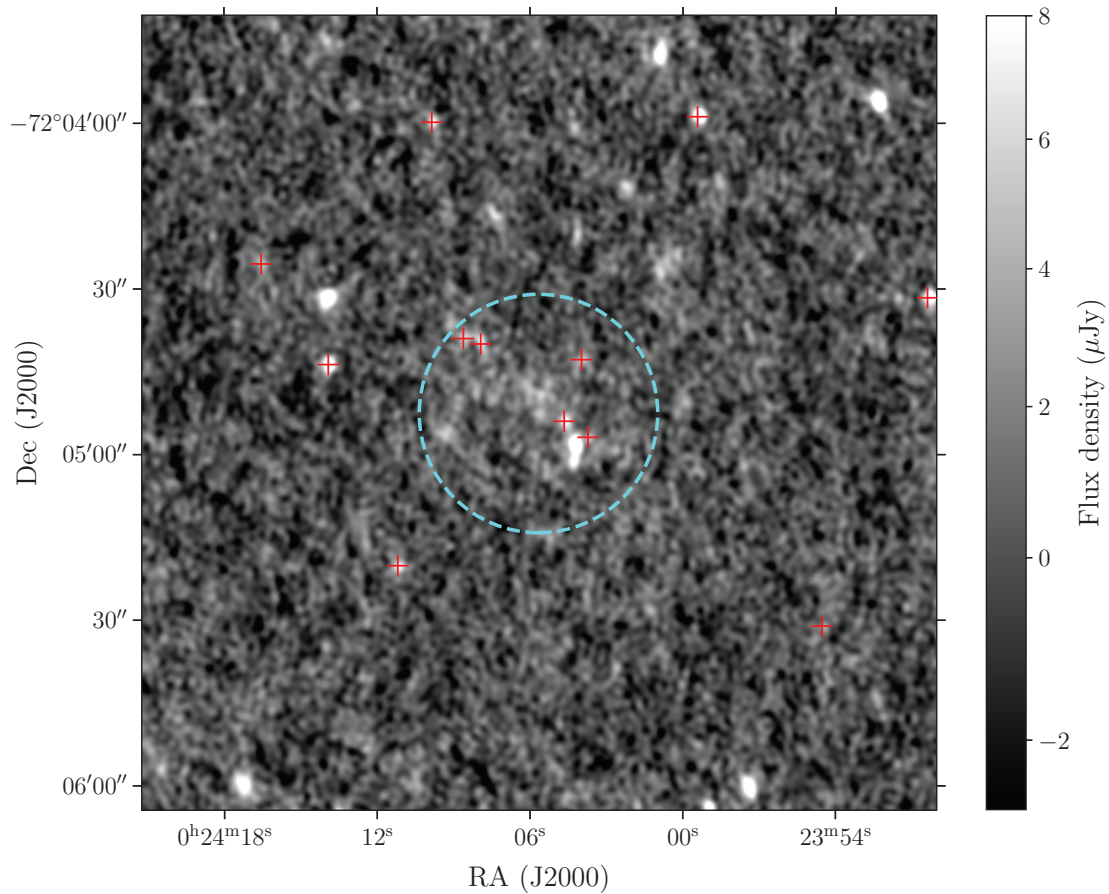
Figure 6.3: The positions of the known MSPs detected in our radio catalogue. These are shown by the red crosses. The dashed and solid cyan circles indicate the core and half-light radii of 47 Tuc respectively. All sources have been plotted on the 5.5 GHz image.

V19, a variable source with a period of 0.4145 days, which Albrow et al. (2001) classify as a W Ursa Majoris (W UMa) system. W UMa sources are eclipsing binary stars that share a common envelope and are in contact with each other, allowing them to transfer mass. PC1-V19 was proposed as the optical counterpart to W41 based on work done by Edmonds et al. (2003), who also noted that while the optical source appeared fainter than other W UMa sources in the cluster, the X-ray luminosity seemed to be too bright for this classification and attributed it to a flaring episode.

During our deep radio survey of 47 Tuc, we identified a radio counterpart for W41 for the first time, within 0.15 arcsec of the X-ray coordinates. The source has a 5.5 GHz radio flux density of 9.8 ± 1.3 µJy and a 9.0 GHz flux density of 4.0 ± 1.1 µJy, yielding a spectral index of the source of $\alpha = -1.84 \pm 0.64$. We divided our data into three subsets to search for variability in the source. No variability within the noise limits was found.

There are some inconsistencies that indicate that the initial classification of W41 as an AB may have been incorrect. Longer term *Chandra* data have indicated that the source only has an X-ray variability of about a factor of 2, indicating that the initial X-ray detection of W41 was not in a flaring state, and hence that this source has a persistently higher X-ray luminosity than expected for a W UMa variable. Coronal activity for ABs saturates at $L_X/L_{\mathrm{Bol}} = 10^{-3}$ (Vilhu & Walter, 1987), which is exceeded in the case of W41, meaning that the X-ray emission from the source is not purely coronal.

Because this source is too X-ray bright for an AB classification, other source classifications can now be considered. In light of the new radio detection of the source, the L_R/L_X ratio of the source falls slightly above the BH correlation as shown in Figure 6.4. This indicates that a binary system containing either a BH or pulsar are possible explanations for this source. However, the steep spectral index of $\alpha = -1.84 \pm 0.64$ rules out a BH, which are expected to display generally flat radio spectra (Plotkin et al., 2017), and argues much more strongly in favour
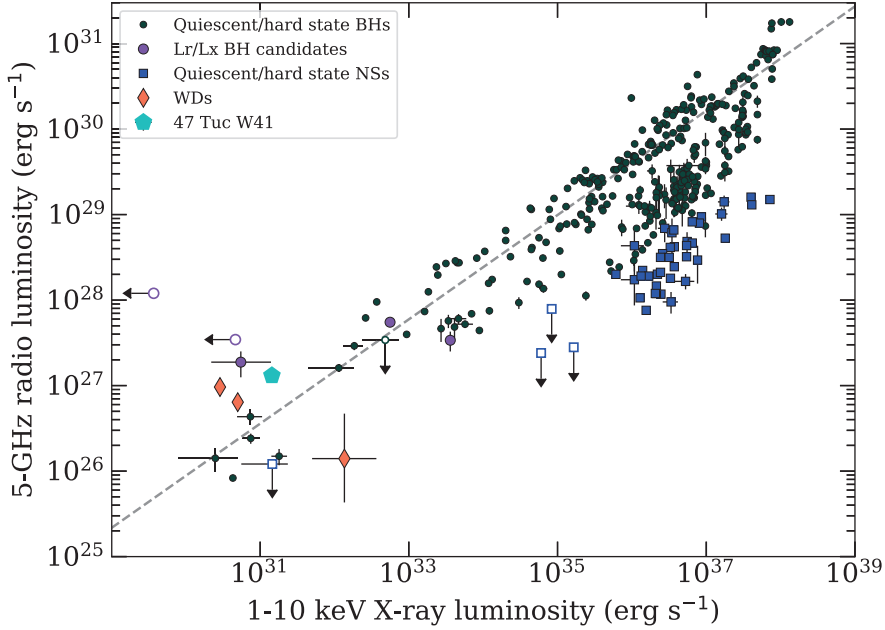
Figure 6.4: W41 plotted on the radio/X-ray luminosity plane. The source falls slightly above the BH correlation.

of a pulsar explanation. Given the fainter than expected optical counterpart for this source, it is possible that the source is a redback pulsar. Redback pulsars are pulsars where the pulsar wind ablates the companion star (Roberts, 2013), providing a means to generate X-rays through intra-binary shocks and rendering the companion underluminous due to its stripped nature. Many heavy NSs are also found in redback pulsar systems (Strader et al., 2019a).

To confirm the pulsar nature of W41, further radio observations at lower frequencies such as L-band would be needed. The spectral index of W41 implies a L-band flux density of $\sim 80\,\mu$Jy, which should be easily detectable with instruments such as MeerKAT. Indeed, the TRAPUM project (Ridolfi et al., 2021) has already identified new pulsars in 47 Tuc, including two pulsars that are yet to have published positions, meaning one of these two pulsars may actually be a detection of W41. Long, low frequency VLBI observations could also be used to study this object to test its pulsar nature. VLBI would be needed in order to resolve this source from the other bright pulsars in the cluster.

Overall, the detection of W41 as a radio source highlights the value of deep

radio surveys of GCs. W41 was initially dismissed as a slightly unusual W Uma source, and only drew our interest due to its new detection as a radio source. This potentially indicates that there could be other interesting sources in other GCs hiding as ABs whose classifications could be revisited if new deep radio observations indicate radio emission is present.

6.5 Summary and conclusions

In this chapter, we have built upon the work presented in Chapter 5 and have used our ultra-deep ATCA survey to produce a radio source catalogue of 47 Tuc. Within the half-light radius of 47 Tuc, we have detected 81 sources to a significance of $> 5\sigma$. Of these sources, 21 have detections at both 5.5 and 9.0 GHz allowing spectral indices to be calculated. The spectral indices of these sources have a mean spectral index of -1.22 and a standard deviation of 0.47, indicating that these sources are likely pulsars or AGN.

We searched for X-ray counterparts to the detected radio sources, and find that 45 detected radio sources have an X-ray counterpart within 1 arcsec. Some notable X-ray sources that we detect a radio counterpart to are X9, the source ATCA J002405 from Chapter 5, W41, and X13, in addition to 12 MSPs. Spurred on by the radio continuum detections of 12 MSPs with X-ray emission, we also searched for radio continuum emission from the 25 pulsars in the cluster with good timing positions. We detected 12 MSPs at 5.5 GHz and, for the first time, detect radio continuum emission from the MSPs M and S.

Finally, motivated by the detection of a radio counterpart, we present a case study of the X-ray source W41, which has been previously classified as a W UMa system. This is the first time that a radio counterpart to this source has been detected. The source has a 5.5 GHz radio flux density of 9.8 ± 1.3 µJy and a 9.0 GHz flux density of 4.0 ± 1.1 µJy, resulting in a spectral index of the source of $\alpha = -1.84 \pm 0.64$. We show that based on this radio spectral information, brighter than inspected X-ray emission from a W UMa, and faint

optical counterpart, W41 is unlikely to be a W UMa source and is instead better explained as a previously undetected redback pulsar. Further observations with MeerKAT and low frequency VLBI facilities will be able to confirm if this is the case.

Overall, this radio source catalogue has highlighted the value of deep radio observations of GCs. We have detected several radio sources that were invisible to previous radio surveys of 47 Tuc due to the next-generation sensitivities we have achieved. This has allowed for the detection of new radio counterparts to a number of X-ray sources and the first radio continuum detection of two known MSPs, and has shown that some X-ray sources in the cluster may have been misclassified as in the case of W41.

CHAPTER 7

DISCUSSION, FUTURE PROSPECTS AND CONCLUSIONS

GCs are ideal targets for deep radio observations due to the number of exotic sources that they contain. Previous radio continuum surveys, such as the MAVERIC survey (Shishkovsky et al., 2020; Tudor et al., 2022) have characterised the radio source population in clusters, and have detected several interesting sources like BHs and pulsars. Targeted, follow-up observations of these sources are needed to properly understand their properties and populations within GCs.

To continue building upon the foundation laid by the MAVERIC survey, I have been conducting further deep radio studies of GCs to reveal and characterise exotic BH and NS in these clusters. In Chapter 3, I presented the results of a simultaneous radio and X-ray observing campaign of the XRB NGC 6652B. This source was initially identified as a radio source in the MAVERIC survey after being a known X-ray source since 2001 (Heinke et al., 2001), and these follow-up simultaneous observations provided an opportunity to investigate the relationship between the radio and X-ray emission. Based on these new follow-up data, I concluded that NGC 6652B is best explained as a tMSP candidate due to

its persistent X-ray flaring behaviour and its radio and X-ray luminosities. This highlights the value of obtaining follow-up radio observations of GCs, as NGC 6652B was just thought to be a VFXT with an X-ray luminosity $LX < 10^{36}\,\mathrm{erg\,s^{-1}}$ prior to the discovery of its radio counterpart.

Chapter 4 presents a multiwavelength study of the first dynamically-confirmed BHs detected in a GC in NGC 3201. Using the available data from the MAVERIC survey, we searched for radio and X-ray emission from these BHs, emission which is expected if the source is accreting. There was no radio or X-ray detection in any of the three sources. Using the calculated observational upper limits on the sources, I constrained the mass accretion rate and radiative efficiency of the accretion in these sources, indicating that the BHs in NGC 3201 are detached and not accreting.

Chapters 5 and 6 present the results of an ultra-deep radio survey of the GC 47 Tuc. This survey combined 480 hr of radio data from the ATCA to produce a radio image with an RMS noise of $790\,\mathrm{nJy\,beam^{-1}}$, the deepest existing radio image of a GC and the deepest radio image ever produced by the ATCA. Chapter 5 presents the detection of ATCA J002405, a faint radio source at the photometric centre of 47 Tuc. Based on its multiwavelength properties, I conclude that this source is best explained as either an undiscovered pulsar, or a candidate IMBH with a mass of $\sim 600 M_\odot$ as calculated from the fundamental plane of BH activity (although the intrinsic 1 dex scatter in this relation means that this value could be uncertain by an order of magnitude). Chapter 6 presents an overview of the full survey, including the sources detected at each frequency and cross-matching with other multiwavelength catalogues. There are 45 radio detections of known X-ray sources, and 12 radio continuum detections of known MSPs in 47 Tuc. I also present a case study of the X-ray source W41, showing that it is a candidate redback pulsar system and not a W UMa AB as was initially hypothesised.

7.1 Discussion

7.1.1 Improvements on the MAVERIC survey

The MAVERIC survey provided deep radio source catalogues of 50 GCs (Shishkovsky et al., 2020; Tudor et al., 2022) and deep X-ray source catalogues of 38 GCs (Bahramian et al., 2020). Through these catalogues, a number of potential stellar-mass BH candidates were identified (e.g., Chomiuk et al. 2013; Miller-Jones et al. 2015; Shishkovsky et al. 2018; Zhao et al. 2020b). However, the majority of the detected radio sources were not fully characterised. In this thesis, I have exploited the initial MAVERIC survey by conducting targeted follow-up of interesting sources detected in the survey (e.g. NGC 6652B) and of the GC 47 Tuc, demonstrating the science results that can be achieved by improving the sensitivity of our radio observations. I also use the MAVERIC survey to follow-up sources identified through other studies (e.g., the BHs in NGC 3201 Giesers et al. 2018, 2019).

Of course, the main area where we improved on the MAVERIC survey is through our ultra-deep radio survey of 47 Tuc. The initial survey of 47 Tuc managed to achieve RMS noise levels of $3.8\,\mu\mathrm{Jy\,beam^{-1}}$ at 5.5 GHz, $4.7\,\mu\mathrm{Jy\,beam^{-1}}$ at 9.0 GHz, and $3.2\,\mu\mathrm{Jy\,beam^{-1}}$ in a stacked 7.25 GHz image. Our survey significantly improves on this by reaching RMS noise levels of $1.2\,\mu\mathrm{Jy\,beam^{-1}}$, $940\,\mathrm{nJy\,beam^{-1}}$, and $790\,\mathrm{nJy\,beam^{-1}}$ respectively for the same frequencies. This reduction in RMS noise allows for the confident detection of several new radio sources in the cluster, and allows us to probe to L_R/L_X ratios much deeper than the initial MAVERIC survey could, rendering us sensitive to very faintly accreting BHs that were previously undetectable. Consequentially, it also allows us to begin searching for very faint radio emission from a potential central IMBH in the cluster, something that was previously not possible as prior radio surveys did not achieve the sensitivities needed to search for IMBHs with masses $\lesssim 1000 M_\odot$. This shows that while the MAVERIC survey is good for characterising the population

of faint to moderately bright radio sources in GCs, a targeted approach with long integration times is needed to search for the very faintest sources, sources which have now been detected through our survey of 47 Tuc.

7.1.2 Intermediate-mass black holes in globular clusters

Our ultra-deep radio survey of 47 Tuc allows us to probe the possibility of very faintly accreting IMBHs being present at the centres of clusters. There have been previous radio continuum surveys of certain GCs searching for accretion signatures of BHs, but there have been no candidates detected as of yet. Lu & Kong (2011) used the ATCA to search for accretion signatures in 47 Tuc and ω Cen, reaching 3σ radio upper limits of $40\,\mu\mathrm{Jy\,beam}^{-1}$ and $20\,\mu\mathrm{Jy\,beam}^{-1}$ respectively. There was evidence of a 2.5σ detection of a radio source at both cluster centres and, using the fundamental plane of BHs, place 3σ mass upper limits on a central IMBH of $520 - 4900 M_\odot$ for 47 Tuc and $1100 - 5200 M_\odot$ for ω Cen. Strader et al. (2012b) used deep (RMS noise levels of $1.5 - 2.1\,\mu\mathrm{Jy\,beam}^{-1}$) VLA observations of M15, M19, and M22 to show that there were no sources detected at the centres of these clusters, and place 3σ mass upper limits of $360 - 980 M_\odot$. While not a Galactic GC, the same method was applied to the cluster G1 in M31, showing that a previously detected central radio source was not present (Miller-Jones et al., 2012). The most comprehensive application of this method was the MAVERIC survey (Tremou et al., 2018) showing that 50 Galactic GCs show no evidence of a central radio source, indicating that IMBHs $> 1000 M_\odot$ do not exist in GCs or are rare, or that either the gas density in GCs is much lower or the accretion process is less efficient than assumed.

Despite radio continuum searches indicating no strong evidence for IMBHs to exist in GCs, and that any that do exist must be light, there have been claims of IMBH candidates through various techniques such as pulsar timing, modelling of pulsar accelerations, and velocity dispersion modelling. The most robust IMBH candidate in a Galactic GC is in NGC 6624. Through 25 years of timing observa-

tions of the MSP PSR B1820-30A, it was concluded that the pulsar is most likely orbiting a central IMBH with a mass $> 7500 M_\odot$ (Perera et al., 2017). While this result has been questioned (e.g., Gieles et al. 2018; Baumgardt et al. 2019) it still remains the most convincing candidate IMBH in a Galactic GC. Other claims include a $4.7 \times 10^4 M_\odot$ IMBH in ω Cen identified through velocity dispersion modelling (Noyola et al., 2010), and a $\sim 2300 M_\odot$ IMBH 47 Tuc identified through modelling of the pulsar accelerations in the cluster (Kızıltan et al., 2017). Both of these claims have since been shown to be incorrect through X-ray observations and N-body simulations in the case of ω Cen, and further analysis of the pulsar accelerations in the case of 47 Tuc (Freire et al., 2017; Abbate et al., 2018).

For the case of 47 Tuc specifically, there have been several studies that have put limits on the presence of a central BH, through both radio continuum observations (discussed above) and theoretical modelling. Through ATCA observations, Tremou et al. (2018) placed a mass upper limit of $< 1040 M_\odot$ from images with an RMS noise of $3.7\,\mu\text{Jy beam}^{-1}$. Beyond the pulsar acceleration modelling discussed above, there have been further modelling studies of 47 Tuc investigating the presence of a central BH in the cluster. Modelling of the stellar proper motions in the core of 47 Tuc by Mann et al. (2019) indicated that the velocity dispersion of these stars can be explained by binaries and other (as yet undetected) stellar-mass BHs in the core, and gave a mass estimate on a potential IMBH of $40 \pm 1650 M_\odot$ indicating that an IMBH is unlikely to be present in the cluster. Further modelling by Hénault-Brunet et al. (2020) also indicates that an IMBH is not needed to produce a multi-mass model that best fits the cluster's observational constraints. Finally, Monte Carlo simulations by Ye et al. (2021) indicate that 47 Tuc could contain ~ 200 BHs and that this group of stellar-mass BHs can reproduce the pulsar accelerations in the cluster, reinforcing the view of earlier modelling studies that an IMBH is not needed to reproduce the observed parameters of the cluster.

All of these studies indicate that either an IMBH is not needed to explain the cluster properties, or that if an IMBH does exist it is in the mass range of $\sim 10^3 M_\odot$. Such low-mass IMBHs are very difficult to observe at radio and X-ray frequencies. The only way to probe down to these lighter masses with radio continuum surveys is to push down to deeper RMS noise levels. This has been achieved through our ultra-deep radio survey of 47 Tuc, allowing us to probe down to IMBH masses below the threshold set by Tremou et al. (2018). Our radio survey pushed the boundaries of what can be achieved with the current generation of radio facilities and resulted in the deepest integration ever made with the ATCA, allowing us to be sensitive to extremely faint radio sources in 47 Tuc. Such a result will not be able to be feasibly improved on until next generation facilities, such as the SKA, are operational. The detection of a central radio source, which could be a candidate IMBH, has shown that GCs may potentially contain low-mass IMBHs in the range of $10^{2-3} M_\odot$, which have lower masses than the previous IMBH claims discussed earlier in this section. As a consequence of this, if the fundamental plane of BH activity is valid for these low-mass IMBHs, the radio emission from such an IMBH is expected to be fainter than previously expected. The only reason that we managed to detect ATCA J002405 is because we pushed the noise level of our image down with hundreds of hours of observing. If all IMBHs in GCs are similarly light, then long radio integrations on clusters with candidate IMBHs will be needed to detect any potential very faint radio emission from them.

The potential existence of a very low-mass IMBH in 47 Tuc has some important implications for the theoretical modelling of compact objects in GCs. It was suggested by Ye et al. (2019) that the number of MSPs in a GC is anti-correlated with the number of BHs retained. This presents an interesting conundrum in the case of 47 Tuc, which has a large MSP population, indicating that there should be a very low number of BHs retained in the cluster, contributing a very small fraction of the total cluster mass. If an IMBH with a mass $\sim 600 M_\odot$ does exist

in the cluster, then this could indicate that, beyond 47 Tuc X9, very few other stellar-mass BHs exist in the cluster as most of the cluster BH mass is locked up in an IMBH. Simulations of the BH population in 47 Tuc have already been performed (e.g., Hénault-Brunet et al. 2020; Ye et al. 2021) and the results of these indicate vastly different final BH populations in the cluster which appear to be dependent on the initial mass function initially specified in the simulations. The detection of ATCA J002405 could be used to help inform future simulations of 47 Tuc, and help to break the degeneracy in these modelling assumptions.

Additionally, the existence of a $\sim 600 M_\odot$ IMBH in 47 Tuc raises some interesting questions as to whether a central BH is needed to reproduce the observed dynamics of the cluster, as some previous studies have indicated that such a source is not needed. As mentioned above, modelling of the observed velocity dispersion of the stars in the core of the cluster by Mann et al. (2019) indicated that a central BH is not needed to reproduce this signal, with an IMBH mass estimate of $40 \pm 1650 M_\odot$. While a $\sim 600 M_\odot$ IMBH is consistent with this, it is still not required to explain the kinematics of the cluster, and further studies would be needed to see if a BH of this mass could actually impact the kinematics in a meaningful way or it its mass is too low. Further to this, Hénault-Brunet et al. (2020) show that the cluster should contain a total BH mass of $430^{+386}_{-301} M_\odot$ while containing very few BHs and no IMBH. A single IMBH of $\sim 600 M_\odot$ is consistent with this total BH mass, but leaves room for only a handful of extra BHs. Further simulations of 47 Tuc are needed to see if the observed properties of the cluster are compatible with a single light IMBH at the cluster centre, with a few other scattered BHs remaining well mixed within the core.

7.1.3 Lack of radio-detected black holes in globular clusters

The results from Giesers et al. (2018, 2019) have shown that a population of BHs can be retained in GCs. These dynamical identifications follow years of BH

candidates being identified in Galactic GCs through radio continuum observations (e.g., Strader et al. (2012a); Chomiuk et al. (2013); Miller-Jones et al. (2015)). Currently, there have been two types of BHs in binary systems that exist in GCs, ranging between ultracompact BHXB systems like 47 Tuc X9 and the detached BHs in NGC 3201, although it is still unknown if the BHs in M22 and M62 fall under these classifications. The nature of X9 as an ultracompact BHXB, with an orbital period of $\sim$ 28 minutes (Bahramian et al., 2017) and a white dwarf donor, results in there being substantial mass transfer in the system, resulting in detectable radio and X-ray emission. This is in contrast to the detached BHs in NGC 3201. These systems have orbital periods longer than at least 2 days, resulting in very low mass transfer rates onto the BHs. As shown in Chapter 4, the product of the radiative efficiency and the mass accretion rate ($\epsilon\dot{M}$) is constrained to $\lesssim 10^{-15}$ $M_\odot yr^{-1}$ for all three BH systems. The result of these long orbital periods and very low mass transfer rates is that there is no detectable radio or X-ray emission observed from these systems, meaning that either there is no accretion present or it is extremely inefficient.

Preliminary analysis of our ultra-deep radio survey of 47 Tuc has indicated that, beyond ATCA J002405, no new BHs have been identified in the cluster. This has importance consequences for the total population of BHs in the cluster, indicating that either 47 Tuc contains very few BHs, as suggested in the simulations by Hénault-Brunet et al. (2020), or that the majority of the BHs in the cluster are detached systems like those found in NGC 3201. Aside from X9, this suggests that any BHs that do exist may have very low mass transfer rates and binary orbital periods on a timescale of days to hundreds of days. This is supported by the lack of any new BH detections (apart from ATCA J002405) in an extremely deep ATCA image, indicating that the mass transfer rates of any detached binary must be extremely low (potentially even lower than those in the detached systems in NGC 3201). One conclusion that can be drawn from this is that the majority of BHs in binary systems in GCs appear to be detached

binaries, with very low mass transfer rates meaning that there is no observable radio or X-ray emission. A consequence of this would be that radio and X-ray observations of GCs may by ill-suited for probing for detached BHs, something that has now been shown more quantitatively by the non-detection of the BHs in NGC 3201 in Chapter 4 and the amount of radio data needed to detect a ATCA J002405 in 47 Tuc in Chapter 5. Instead, methods that aim to measure the mass of potential invisible companions to stars are much more suited to searching for hidden BHs in GCs, like those already successfully applied in NGC 3201. An obvious outlier to this claim that all cluster BHs are detached is X9 which, as an ultracompact system, is the very opposite of a detached system. However, the orbital periods of ultracompact systems will increase as they age and it is suspected that these systems could eventually evolve to become detached with very faint emission due to a reduction in the mass accretion rate from the donor (van Haaften et al., 2012, 2013).

7.1.4 Transitional millisecond pulsars and redback pulsars in globular clusters

Out of the three confirmed tMSPs, only M28I resides in a GC. M28 (NGC 6626) is a cluster located at a distance of $\sim 5\,\mathrm{kpc}$ (Baumgardt & Vasiliev, 2021), and M28I was originally identified in 2013 as an X-ray transient by *INTEGRAL* with a position identical to the known pulsar PSR J1824-2452I in the cluster (Papitto et al., 2013). While there are very few tMSPs actually known, the fact that one is within a GC could indicate that there is a potential overabundance of tMSPs in GCs. It is already known that GCs contain an overabundance of XRBs by a factor of ~ 100 when compared to the Galactic field, so it is feasible to consider that this overabundance extends to tMSPs (which are technically XRBs themselves). The identification of Terzan 5 CX1 as a tMSP candidate also adds credence to the possibility of tMSPs being common in GCs. Terzan 5 CX1 is a variable X-ray source in the Galactic GC Terzan 5 that showed a dimming then re-brightening

in *Chandra* data from 2003 to 2017, and has a radio counterpart detected with the VLA (Bahramian et al., 2018b). It was concluded that the two states seen in Terzan 5 CX1 are consistent with that of a tMSP.

In Chapter 3 we show that the radio and X-ray properties of NGC 6652B are consistent with those of a tMSP candidate. While no state transitions have been observed in this system, the X-ray flaring behaviour of the source is similar to the recently identified tMSP candidates such as 3FGL J0427.9-6704 (Li et al., 2020) and 4FGL J0540.0-7552 (Strader et al., 2021). All three of these candidates show prolonged X-ray flaring, indicating that some tMSPs could remain in the X-ray flaring mode for prolonged periods of time. Additionally, the radio/X-ray luminosity ratio of NGC 6652B is similar to that of 3FGL J0427.9-6704, with both sources venturing onto the BH correlation in the radio/X-ray luminosity plane. The known tMSP J1023+0038 has also been known to be as radio-loud as some BHs during its X-ray low modes.

The identification of another tMSP candidate in a Galactic GC lends further support to the idea that tMSPs may be abundant in GCs. However, the study of NGC 6652B also highlights some issues with studying these sources in clusters. NGC 6652 is 10 kpc away meaning it is quite distant and much more extinguished than the parts of the Galactic field where other tMSPs and tMSP candidates reside. As a result, studying these sources in clusters can be difficult. This is highlighted most obviously when searching for anti-correlated variability between the radio and X-ray emission in NGC 6652B. As shown in Chapter 3, no evidence of this anti-correlated variability is observed, despite simultaneous observations using the same facilities as those used to observe this anti-correlated behaviour in J1023+0038 (Bogdanov et al., 2018). The main difference between these two sources is that J1023+0038 is very close at 1.3 kpc (Deller et al., 2012), meaning that extinction is not as much of an issue as for NGC 6652B and we are simply much more sensitive to emission from this system given how much closer it is in constrast to NGC 6652B. This means that the anti-correlated behaviour is much

more easily observable in J1023. While GCs are superb environments to search for new tMSPs, we are limited in the means we can use to both study them and confirm their tMSP nature, with transitions between the two states remaining the most robust method for confirming new tMSPs.

Furthermore, all three confirmed tMSPs are redback pulsar systems. These are MSPs with low mass companions where the pulsar wind is ablating the companion star (Strader et al., 2019b). This is worth mentioning, as we have identified a new candidate redback pulsar system in 47 Tuc (47 Tuc W41). The overall properties of redbacks are still somewhat unknown, and thus identifying new candidates to increase the sample size is useful for the ongoing study of these systems. This also provides additional evidence that GCs are prime environments for hosting and studying redback pulsars and thus tMSPs.

7.1.5 Importance of deep radio observations of globular clusters

Several of the sources discussed in this thesis indicate the value of deep radio observations of GCs for identifying new and interesting sources for future study. These observations have allowed us to revisit the previous classifications of several sources through the identification of new radio counterparts. An example of this is 47 Tuc X9. X9 was initially identified as a CV based on X-ray observations (Heinke et al., 2005), however the identification of a radio counterpart to this source allowed for this classification to be revisited and this source has now been reclassified as a BH candidate (Miller-Jones et al., 2015).

Through deep radio observations of several clusters, we have also managed to revisit the previous classifications of several sources. NGC 6652B has now been identified as a tMSP candidate based on the detection of a radio counterpart. Through our ultra-deep survey of 47 Tuc, we have also been able to revisit the classifications of two other sources. W41 was initially identified as the brightest AB in 47 Tuc, however the identification of a new radio counterpart to this source

has indicated that this source could be a redback pulsar candidate instead. W286 was also initially classified as an AB, but the identification of ATCA J002405 as its radio counterpart has meant that this source is likely either a pulsar or BH candidate (Chapter 5). These sources having their previous classifications revisited following the detection of new radio counterparts suggests that there could be other sources in GCs that have been misclassified. In order to properly understand the source populations in GCs, further multiwavelength observations are needed. In particular, radio continuum observations are very useful in this regard, as the studies of NGC 6652B, W41, and W286 have shown.

7.2 Future work

The deep ATCA observations of 47 Tuc have highlighted the value of deep radio observations of GCs, and have demonstrated the sources the types of sources that can be detected from such an observing campaign. There are a handful of other GCs for which deep radio observations would be feasible.

The pending BIGCAT upgrade to the ATCA correlator will double the available bandwidth in the 4-cm band, improving the sensitivity by a factor of $\sqrt{2}$. This upgrade to the ATCA will allow other clusters in the southern sky to be targeted in an expansion of these very large surveys, with fewer observing hours needed due to the sensitivity improvements. Given the improved sensitivity of the VLA over ATCA, and its pending upgrade in the form of the ngVLA which will increase the sensitivity of the facility by a factor of 10 (Murphy et al., 2018), choosing to observe clusters with the VLA would allow us to probe to unparalleled image depths that are unfeasible to achieve with the ATCA.

M4 (NGC 6121) would be an ideal cluster to conduct ultra-deep radio observations of due to being one of the closest GCs (1.85 kpc; Baumgardt & Vasiliev 2021). This means it would require less integration time (about 100 hr with the ATCA) to reach similar luminosity sensitivities that we achieved with 47 Tuc, making such an observing campaign fro very faint accreting systems much less

intensive. Another GC worth considering is M10. Previous MAVERIC observations of M10 (Shishkovsky et al., 2018) have identified several interesting sources, including a potential BH candidate. Further deep observations would allow this candidate to be studied for any potential variability, and allow the cluster to be probed for very faint radio sources which could be weakly accreting BHs. NGC 6397 is another close GC (2.48 kpc; Baumgardt & Vasiliev 2021) that would be a good target for observations with an upgraded ATCA. NGC 6397 is also a core-collapsed cluster, meaning it would be a good test to see if it also contains a faint central radio source similar to that of 47 Tuc (although testing the properties of core-collapsed vs. non core-collapsed clusters would require a larger sample size).

It may be tempting to think that Terzan 5 would be a good target for deep radio observations, given that it contains several MSPs and other interesting objects like 47 Tuc. However, there are a few issues with Terzan 5 that make it difficult to achieve high quality observations. While Terzan 5 is visible to both the ATCA and the VLA given its declination of $-24°$, both facilities have some shortcomings when observing this cluster. The maximum baseline length of the ATCA of 6 km is insufficient to resolve the radio sources in the core of the cluster at 5.5 and 9 GHz, meaning that the VLA is needed to achieve the required angular resolution (see Urquhart et al. 2020 for a VLA image of the crowded core). However, the declination of Terzan 5 means that it is not visible to the VLA at high elevations, resulting in a very elliptical beam and sparser (u, v) coverage at the desired frequencies around 5-10 GHz. Again, this effect can be seen in the radio images produced of the cluster by Urquhart et al. (2020). For these reasons, Terzan 5 is a challenging target for a similar deep radio survey.

Beyond conducting deep radio observations on other GCs to search for faintly accreting sources and potential central IMBHs, there are also several objects in 47 Tuc that were identified during our deep survey that can be studied further. The most obvious of these (aside from the candidate IMBH) is X9. Beyond its 28 minute orbital period, X9 has also been shown to display a 6.8 day superor-

bital modulation in archival X-ray data (Bahramian et al., 2017). It would be interesting to use the now comprehensive radio coverage of X9 to search for any evidence of this superorbital modulation in the radio, which could help confirm or reject whether this modulation is caused by effects such as precession or a warped accretion disk. In addition to X9, W41 is also worth studying further to confirm whether it is indeed a redback pulsar. This would need to be confirmed with timing observations of the cluster with MeerKAT, to see if pulses with a valid timing solution are detected at the position of W41. There are 45 X-ray sources in 47 Tuc that have a radio counterpart detected in our deep radio survey (including X9, X13, W41, and W286), making these sources ideal for future studies. While a large fraction of them are consistent with some known pulsars or background AGN, the remaining sources will be cluster members for which candidate optical counterparts can be identified. These sources are the most likely to be new detections of XRBs in 47 Tuc, that have only been detected due to the depth of our radio survey. It would also be worth observing the cluster further with MeerKAT in both timing and imaging mode to try and identify any of these remaining radio/X-ray matches as potential new pulsars in 47 Tuc.

Obviously, the central radio source ATCA J002405 is an ideal source for further study. Given that we could not confidently constrain the nature of the object, there are follow-up observations that can be conducted that can help with this. The best way to confirm whether ATCA J002405 is an IMBH is to measure the proper motion for a sample of stars within its sphere of influence. Such observations would be challenging due to the crowded nature of the core of 47 Tuc. Either ground-based observations with adaptive optics or JWST would be needed to conduct these observations. If the proper motions of these stars show evidence that they are consistent with the presence of a central massive object, the IMBH nature of ATCA J002405 would almost certainly be confirmed. On the other hand, there is also the possibility of ATCA J002405 being a pulsar. The best way to test this would be to use MeerKAT to search for pulsations from this source.

MeerKAT has already discovered several new pulsars in 47 Tuc and, given the sensitivities that it can reach, is the best instrument to use to search for pulsations from ATCA J002405. With regards to future continuum observations of this source, given the declination of 47 Tuc, only the ATCA and eventually SKA-mid would be able to take observations at 5.5 and 9 GHz. While the BIGCAT upgrade to the ATCA would allow us to acquire new, more sensitive radio observations, it would take over 200 hr of new observations to get a $\sqrt{2}$ sensitivity improvement when stacked with the current data. Thus, we would need to wait for SKA-mid to be operational to feasibly improve on the existing continuum data.

Beyond future deep radio studies of other GCs, there is also the potential for follow-up observations of NGC 6652B to attempt to confirm its tMSP nature. By observing a state transition between the accreting state and the pulsar state, we would be able to confirm the source as a tMSP. There are two ways this could be achieved: a pulsar search to look for pulsations turning on at the position of the source, or a continuing monitoring campaign with the VLA, to see if the continuum radio emission disappears. The latter also has the advantage of providing us with additional data on NGC 6652, which can be stacked to search for faint radio sources. Another possibility for future observations with the ngVLA is to search for anti-correlated radio and X-ray emission. The ngVLA would provide us with the short timescale sensitivity required to accurately determine if there is radio behaviour that is suggestive of the anti-correlation being present. This would potentially provide us with another piece of evidence in favour of a tMSP if this can be achieved.

7.3 Conclusions

The purpose of this thesis was to investigate the BHs and NSs that exist in binary systems in Galactic GCs. GCs provide a fantastic environment within which to search for these exotic binary systems due to their forming XRBs at a much higher rate than that of the Galactic field. I used multiwavelength observations

of several clusters to study these exotic binary systems. I also built upon the MAVERIC survey (Shishkovsky et al., 2020; Tudor et al., 2022) by conducting further radio continuum observations of the GC 47 Tuc with the ATCA, producing radio images that were more four times more sensitive than the previous radio images of 47 Tuc and the deepest images ever made with the ATCA.

We presented simultaneous radio and X-ray observations of the XRB NGC 6652B to search for correlated variability between the radio and X-ray emission in this system. Based on the short term X-ray flaring behaviour, and radio and X-ray luminosities, we conclude that this source is best explained as a tMSP candidate. This adds another tMSP candidate to a short list of confirmed and other candidate tMSPs. Given the rarity of these sources, identifying even another candidate is worthwhile to the field. This identification also indicates that GCs could potentially contain a large number of tMSPs.

Following the identification of three dynamically-confirmed BHs in the GC NGC 3201, we used the MAVERIC radio observations and existing X-ray data of the cluster to search for any multiwavelength emission from these BHs. No such signal was detected. We used these luminosity limits to constrain the mass accretion rates onto these BHs, showing that either there is no accretion present in these detached binary systems or that any accretion is extremely inefficient. These radio and X-ray limits indicate that the detached BHs that are present in GCs do not emit strong radio or X-ray signals, meaning they are challenging to detect with the current generation of radio and X-ray facilities.

In an attempt to detect this very faint radio emission expected from these detached BHs in GCs, we conducted the deepest ever radio survey of the cluster 47 Tuc with the ATCA. Through approximately 480 hours of radio data, we were able to produce a radio image with an RMS noise of $790\,\text{nJy}\,\text{beam}^{-1}$; the deepest radio image of a GC and the deepest radio image ever made with the ATCA. This unprecedented imaging depth allowed us to detect a very faint radio source at the photometric centre of the cluster. By combining our radio data

with available optical and X-ray data, we conclude that this faint radio source is best explained as an undetected pulsar at the cluster centre, or a candidate IMBH. Such an IMBH would have a mass $\sim 600 M_\odot$ (although the systematic uncertainty in the fundamental plane relation used to estimate this means this value could be uncertain by a further order of magnitude) and, if confirmed, would represent the first direct radio detection of an IMBH. This challenges the current modelling studies of 47 Tuc, with many indicating that an IMBH is not needed to explain the observational properties of the cluster. Beyond the detection of this radio source, we used our ultra-deep coverage of 47 Tuc to produce a radio source catalogue of 47 Tuc. Preliminary analysis of this catalogue has revealed that the X-ray source 47 Tuc W41 may actually be a candidate redback pulsar system.

This ultra-deep survey of 47 Tuc has highlighted the potential of deep radio continuum imaging of clusters. The detection of several radio counterparts to previously known sources has allowed us to challenge the current classifications of these sources. The detection of an IMBH candidate at the centre of a GC has many implications on the theoretical modelling of the BH population in GCs, and how this population forms, evolves, impacts the observed properties of the cluster. The nJy noise levels that have been achieved through our imaging campaign of 47 Tuc highlights what will be possible once next generation radio facilities, such as the SKA and ngVLA, are constructed and fully operational, paving the way for several other astrophysical fields of study beyond the study of XRBs to be probed and investigated in revolutionary new ways.

Appendices

APPENDIX A

FUNDAMENTAL PLANE MASS ESTIMATES OF BLACK HOLES

The fundamental plane of BH activity links the radio and X-ray luminosities of a BH with its mass (Merloni et al., 2003; Falcke et al., 2004; Plotkin et al., 2012). From Plotkin et al. (2012) the fundamental plane has the form:

$$\log L_X = (1.45 \pm 0.04) \log L_R - (0.88 \pm 0.06) \log M_{BH} - (6.07 \pm 1.10). \quad \text{(A.1)}$$

This relation also has an intrinsic scatter of $\sim 1\,\text{dex}$ (Gültekin et al., 2019). By knowing the radio and X-ray luminosity of a BH system, the mass of the BH can be determined. In the case of radio continuum searches for IMBHs in GCs (e.g., Strader et al. 2012b; Tremou et al. 2018), the mass (or mass upper-limit) of a BH can be estimated using only a radio detection (or non-detection), in addition to some assumptions about the nature of the X-ray emission. The fundamental plane rearranged to give mass as the dependent variable, as used in Tremou et al.

(2018), is:

$$\log M_{BH} = (1.638 \pm 0.070) \log L_R - (1.136 \pm 0.077) \log L_X - (6.863 \pm 0.790). \quad \text{(A.2)}$$

In the event that there is no X-ray emission detected, we can estimate the expected X-ray luminosity of an IMBH by making some assumptions about the accretion rate and environment within the GC. X-ray luminosity is given by:

$$L_X = \epsilon \dot{M} c^2, \quad \text{(A.3)}$$

where below 2% of the Eddington rate we can say that efficiency scales as (Maccarone, 2003; Vahdat Motlagh et al., 2019):

$$\epsilon = \frac{0.1}{0.02} \frac{\dot{M}}{\dot{M}_{Edd}}, \quad \text{(A.4)}$$

giving the following expression for L_X:

$$L_X = \frac{0.1}{0.02} \frac{\dot{M}}{\dot{M}_{Edd}} c^2. \quad \text{(A.5)}$$

Hence, by knowing (or estimating) what $\dot{M}$ and $\dot{M}_{Edd}$ are, L_X can be estimated.

To determine $\dot{M}$, we assume that the source is accreting from the surrounding medium and that the accretion rate is given by some fraction of the Bondi accretion rate. This is usually expressed as $\dot{M} = 0.03 \dot{M}_{Bondi}$ (Pellegrini, 2005). The Bondi accretion rate is:

$$\dot{M}_{Bondi} = \pi G^2 M_{BH}^2 \rho c_s^{-3} \left(\frac{2}{5 - 3\gamma} \right)^{\frac{5-3\gamma}{2(\gamma-1)}}. \quad \text{(A.6)}$$

γ is the adiabatic index, which varies from 1 in the isothermal case to 5/3 in the adiabatic case; M_{BH} is the mass of the central BH; and ρ is the gas density where $\rho = n \mu m_H$ where n is the gas number density (usually assumed to be $0.2 \, \text{cm}^{-3}$; Freire et al. 2001), μ is the mean molecular mass (usually assumed to be 0.59 for

fully ionised gas Fall & Rees 1985), and m_H is the mass of hydrogen. c_s is the sound speed of the gas and is given by:

$$c_s = \sqrt{\frac{\gamma k_B T}{\mu m_p}}, \tag{A.7}$$

where T is the temperature of the gas.

The Eddington accretion rate $\dot{M}_{Edd}$ can be derived from the Eddington luminosity. We can write:

$$\dot{M}_{Edd} = \frac{L_{Edd}}{\epsilon c^2} = \frac{4\pi G M_{BH} m_p c}{\sigma_T \epsilon c^2}, \tag{A.8}$$

where σ_T is the Thompson cross-section. The efficiency ϵ in this case is assumed to be 0.1, typical for Eddington rates.

With these expressions for $\dot{M}$ and $\dot{M}_{Edd}$, we can now express L_X in terms of the BH mass. We assume the isothermal case (in order to be consistent with Strader et al. 2012b; Tremou et al. 2018) meaning that $\gamma = 1$ and the quantity $\left(\frac{2}{5-3\gamma}\right)^{(5-3\gamma)/2(\gamma-1)} = e^{3/2}$, and we assume a temperature of 10^4 K.

$$L_X = \frac{0.1}{0.02} \frac{\dot{M}}{\dot{M}_{Edd}} c^2, \tag{A.9}$$

$$= \frac{0.1 \times 0.03^2}{0.02} c^3 (\pi G^2 M_\odot \frac{n \mu m_H}{c_s^3} e^{3/2})^2 (\frac{M_{BH}}{M_\odot})^3 \frac{0.1\sigma_T}{4\pi G M_\odot m_p}, \tag{A.10}$$

$$= 1.125 \times 10^{-4} \pi e^3 \frac{c^3 G^3 M_\odot^3 n^2 \mu^2 m_H^2 \sigma_T}{m_p c_s^6} (\frac{M_{BH}}{M_\odot})^3, \tag{A.11}$$

$$= A(\frac{M_{BH}}{M_\odot})^3, \tag{A.12}$$

where:

$$A = 1.125 \times 10^{-4} \pi e^3 \frac{c^3 G^3 M_\odot^3 n^2 \mu^2 m_H^2 \sigma_T}{m_p c_s^6}. \tag{A.13}$$

We can now combine this with the fundamental plane in order to estimate

M_{BH}. From above, we can write:

$$\log L_X = 3 \log M_{BH} + \log A. \tag{A.14}$$

Additionally, we can write a similar relationship for the radio luminosity $L_R = 4\pi d^2 \nu S_\nu$ to give:

$$\log L_R = \log(4\pi\nu) + 2\log d + \log(S_\nu), \tag{A.15}$$

where d is the distance to the radio source, ν is the observing frequency, and S_ν is the radio flux density. Substituting this into the fundamental plane gives us the following equation:

$$\log M_{BH} = 0.37 \log(4\pi\nu) + 0.74 \log d + 0.37 \log S_\nu - 0.257 \log A - 1.53. \tag{A.16}$$

APPENDIX B

A RADIO SOURCE CATALOGUE OF 47 TUCANAE

This Appendix presents the source catalogue of 47 Tuc, where 81 sources are detected within the half-light radius of 47 Tuc to $> 5\sigma$ significance. Also included in this Appendix are the radio images of 47 Tuc at 5.5, 7.25, and 9.0 GHz. In these images, the cyan dashed circle represents the core radius of the cluster, and the cyan solid circle represents the half-light radius of the cluster.

1. Source name with the ATCA J prefix (ATCA J)

2. Right Ascension (RA)

3. 1σ error in RA (δRA) in arcsec

4. Declination (Dec)

5. 1σ error in Dec (δDec) in arcsec

6. Peak flux density at 5.5 GHz ($S_{5.5}$) in µJy

7. Peak flux density error at 5.5 GHz ($\delta S_{5.5}$) in µJy

8. Peak flux density at 7.25 GHz ($S_{7.25}$) in µJy

9. Peak flux density error at 7.25 GHz ($\delta S_{7.25}$) in µJy

10. Peak flux density at 9.0 GHz ($S_{9.0}$) in µJy

11. Peak flux density error at 9.0 GHz ($\delta S_{9.0}$) in µJy

12. Spectral index (α) for the sources detected at both 5.5 and 9.0 GHz

13. Spectral index error ($\delta\alpha$)

14. MAVERIC source name if the source was detected in Tudor et al. (2022)

Table B.1: The radio source catalogue of sources within the half-light radius of

47 Tuc to greater than 5σ significance.

ATCA J	RA	δRA	Dec	δDec	$S_{5.5}$	$\delta S_{5.5}$	$S_{7.25}$	$\delta S_{7.25}$	$S_{9.0}$	$\delta S_{9.0}$	α	$\delta\alpha$	MAVERIC
002444.382-720416.074	00:24:44.382	0.135	-72:04:16.074	0.181	9.4	1.6	7.6	1.6					
002435.123-720458.096	00:24:35.123	0.262	-72:04:58.096	0.154	10.8	1.6	9.9	1.4					
002435.006-720501.764	00:24:35.006	0.038	-72:05:01.764	0.059	31.6	1.5	23.0	1.4	12.2	1.8	-1.94	0.72	47Tuc-ATCA11
002434.656-720514.175	00:24:34.656	0.128	-72:05:14.175	0.258	8.3	1.5	6.8	1.2					
002434.487-720335.507	00:24:34.487	0.153	-72:03:35.507	0.244	11.4	1.5	6.7	1.0					
002434.141-720333.332	00:24:34.141	0.080	-72:03:33.332	0.147	10.2	1.4							
002433.409-720502.078	00:24:33.409	0.228	-72:05:02.078	0.387	7.0	1.5							
002430.841-720333.651	00:24:30.841	0.194	-72:03:33.651	0.380	8.9	1.5							
002427.989-720603.846	00:24:27.989	0.035	-72:06:03.846	0.057	28.7	1.3	22.6	1.1	15.9	1.5	-1.20	0.50	47Tuc-ATCA8
002425.525-720220.672	00:24:25.525	0.183	-72:02:20.672	0.055			6.9	1.4					
002425.115-720613.218	00:24:25.115	0.117	-72:06:13.218	0.161			4.4	1.0					
002424.922-720614.336	00:24:24.922	0.079	-72:06:14.336	0.164			5.3	1.0					

Continued on next page

235

Table B.1 – continued from previous page

ATCA J	RA	δRA	Dec	δDec	$S_{5.5}$	$\delta S_{5.5}$	$S_{7.25}$	$\delta S_{7.25}$	$S_{9.0}$	$\delta S_{9.0}$	α	$\delta\alpha$	MAVERIC
002424.196-720259.877	00:24:24.196	0.084	-72:02:59.877	0.128	13.0	1.4	10.5	1.1	9.6	1.7	-0.61	0.97	
002422.552-720532.146	00:24:22.552	0.074	-72:05:32.146	0.121	12.1	1.2	9.1	1.0	6.4	1.3	-1.30	1.04	
002422.249-720408.702	00:24:22.249	0.095	-72:04:08.702	0.146	16.1	1.3	10.9	0.9	6.9	1.2	-1.71	0.91	47Tuc-ATCA5
002420.097-720701.563	00:24:20.097	0.101	-72:07:01.563	0.158	8.1	1.3	6.0	1.2					
002419.458-720334.733	00:24:19.458	0.184	-72:03:34.733	0.142	7.1	1.3	5.2	1.0					
002418.976-720253.901	00:24:18.976	0.080	-72:02:53.901	0.183	12.8	1.4	8.5	1.1					
002418.146-720619.392	00:24:18.146	0.047	-72:06:19.392	0.073	29.6	1.4	19.2	1.0	12.0	1.4	-1.84	0.58	47Tuc-ATCA6
002417.272-720559.496	00:24:17.272	0.138	-72:05:59.496	0.206	11.9	1.4	8.3	0.9	6.8	1.2	-1.15	1.01	
002417.071-720323.670	00:24:17.071	0.074	-72:03:23.670	0.148			5.0	0.9					
002416.643-720742.367	00:24:16.643	0.244	-72:07:42.367	0.451	7.7	1.6							
002415.708-720306.472	00:24:15.708	0.208	-72:03:06.472	0.256	8.3	1.4	6.8	1.1					
002413.963-720431.731	00:24:13.963	0.091	-72:04:31.731	0.110	16.1	1.3	11.2	0.9	7.6	1.2	-1.53	0.83	
002413.915-720443.720	00:24:13.915	0.056	-72:04:43.720	0.095	15.8	1.2	8.3	0.9					47Tuc-ATCA2
002413.808-720302.316	00:24:13.808	0.183	-72:03:02.316	0.300			5.4	1.1					
002413.312-720332.769	00:24:13.312	0.016	-72:03:32.769	0.019	82.4	1.4	58.8	1.0	39.8	1.3	-1.48	0.17	47Tuc-ATCA4

Table B.1 – continued from previous page

ATCA J	RA	δRA	Dec	δDec	$S_{5.5}$	$\delta S_{5.5}$	$S_{7.25}$	$\delta S_{7.25}$	$S_{9.0}$	$\delta S_{9.0}$	α	$\delta\alpha$	MAVERIC
002413.520-720605.282	00:24:13.520	0.060	-72:06:05.282	0.115	14.6	1.3	10.7	1.0	7.5	1.2	-1.35	0.88	
002413.306-720225.217	00:24:13.306	0.064	-72:02:25.217	0.143	18.1	1.5	14.3	1.4	12.3	1.8	-0.79	0.80	47Tuc-ATCA15
002411.546-720224.390	00:24:11.546	0.082	-72:02:24.390	0.119	14.8	1.4	10.3	1.3					
002411.561-720635.364	00:24:11.561	0.079	-72:06:35.364	0.150	9.5	1.2	6.2	1.0					
002411.179-720520.169	00:24:11.179	0.135	-72:05:20.169	0.138	8.1	1.2	5.1	1.0					
002411.085-720620.471	00:24:11.085	0.094	-72:06:20.471	0.158	10.1	1.3	7.4	1.0					
002410.334-720741.358	00:24:10.334	0.014	-72:07:41.358	0.023	79.8	1.6	62.9	1.3	38.4	2.1	-1.49	0.27	47Tuc-ATCA17
002409.849-720359.879	00:24:09.849	0.076	-72:03:59.879	0.164	8.4	1.2	5.8	0.9					
002408.584-720708.177	00:24:08.584	0.041	-72:07:08.177	0.059	30.7	1.5	23.8	1.1	16.9	1.7	-1.21	0.51	47Tuc-ATCA12
002407.982-720439.779	00:24:07.982	0.090	-72:04:39.779	0.161			5.6	0.9					
002407.791-720704.370	00:24:07.791	0.132	-72:07:04.370	0.346	7.8	1.5	5.3	1.0					
002407.428-720416.846	00:24:07.428	0.085	-72:04:16.846	0.131			5.7	0.8	5.1	1.0			
002404.657-720453.988	00:24:04.657	0.157	-72:04:53.988	0.258	8.0	1.4							
002404.272-720458.087	00:24:04.272	0.041	-72:04:58.087	0.082	21.6	1.3	20.0	1.1	19.7	1.1	-0.18	0.39	47Tuc-ATCA1
002404.347-720501.237	00:24:04.347	0.088	-72:05:01.237	0.150	9.8	1.3	6.1	1.0					

Table B.1 – continued from previous page

ATCA J	RA	δRA	Dec	δDec	$S_{5.5}$	$δS_{5.5}$	$S_{7.25}$	$δS_{7.25}$	$S_{9.0}$	$δS_{9.0}$	α	δα	MAVERIC
002404.217-720420.605	00:24:04.217	0.096	-72:04:20.605	0.264			4.4	0.8					
002403.340-720234.852	00:24:03.340	0.039	-72:02:34.852	0.062	27.0	1.4	22.6	1.1	18.0	1.7	-0.82	0.50	47Tuc-ATCA13
002402.877-720205.503	00:24:02.877	0.156	-72:02:05.503	0.134	10.4	1.5	8.5	1.4					
002402.271-720411.699	00:24:02.271	0.202	-72:04:11.699	0.243	6.7	1.3	4.6	0.9					
002401.009-720427.276	00:24:01.009	0.159	-72:04:27.276	0.193			5.0	0.9					
002401.091-720151.120	00:24:01.091	0.224	-72:01:51.120	0.161	8.7	1.6							
002400.966-720347.642	00:24:00.966	0.071	-72:03:47.642	0.195	13.8	1.3							
002400.849-720426.238	00:24:00.849	0.370	-72:04:26.238	0.522	5.5	1.2							
002359.427-720358.843	00:23:59.427	0.059	-72:03:58.843	0.073	17.2	1.3	9.9	0.9					
002359.037-720603.590	00:23:59.037	0.067	-72:06:03.590	0.104	12.8	1.2	10.2	1.0	8.0	1.3	-0.94	0.87	
002357.479-720559.959	00:23:57.479	0.073	-72:05:59.959	0.152	15.2	1.3	10.5	1.0	7.4	1.4	-1.47	0.96	
002353.796-720622.823	00:23:53.796	0.267	-72:06:22.823	0.177			4.4	1.3					
002353.581-720624.724	00:23:53.581	0.143	-72:06:24.724	0.195	11.8	1.5	8.7	1.4					
002353.991-720621.804	00:23:53.991	0.238	-72:06:21.804	0.323	7.9	1.5							
002353.542-720712.882	00:23:53.542	0.110	-72:07:12.882	0.215	9.3	1.4							

Continued on next page

238

Table B.1 – continued from previous page

ATCA J	RA	δRA	Dec	δDec	$S_{5.5}$	$\delta S_{5.5}$	$S_{7.25}$	$\delta S_{7.25}$	$S_{9.0}$	$\delta S_{9.0}$	α	$\delta\alpha$	MAVERIC
002352.437-720356.174	00:23:52.437	0.041	-72:03:56.174	0.032	29.5	1.2	22.2	0.9	15.1	1.2	-1.37	0.43	47Tuc-ATCA3
002350.404-720431.561	00:23:50.404	0.069	-72:04:31.561	0.112	13.6	1.2	8.3	0.9					
002349.247-720538.170	00:23:49.247	0.044	-72:05:38.170	0.082	20.7	1.2	15.9	1.0	10.7	1.4	-1.34	0.66	
002346.367-720640.240	00:23:46.367	0.132	-72:06:40.240	0.155	8.8	1.4	6.7	1.2					
002346.155-720714.874	00:23:46.155	0.069	-72:07:14.874	0.118	15.4	1.5	11.5	1.4					47Tuc-ATCA16
002343.346-720446.855	00:23:43.346	0.341	-72:04:46.855	0.473	6.6	1.3							
002341.759-720522.089	00:23:41.759	0.089	-72:05:22.089	0.246	9.8	1.4	9.1	1.1	8.9	1.4	-0.18	0.99	
002340.881-720511.592	00:23:40.881	0.006	-72:05:11.592	0.010	172.3	1.5	126.2	1.4	74.8	1.5	-1.70	0.10	47Tuc-ATCA7
002338.912-720610.076	00:23:38.912	0.108	-72:06:10.076	0.236	9.2	1.5	8.0	1.3					
002338.187-720231.737	00:23:38.187	0.139	-72:02:31.737	0.113	14.7	1.8	10.3	1.6					
002336.504-720355.291	00:23:36.504	0.082	-72:03:55.291	0.144	12.5	1.5	8.3	1.2					
002335.315-720610.864	00:23:35.315	0.171	-72:06:10.864	0.240	11.8	1.7	8.5	1.4					
002335.153-720248.108	00:23:35.153	0.137	-72:02:48.108	0.201			6.8	1.4					
002334.217-720625.073	00:23:34.217	0.075	-72:06:25.073	0.118	17.9	1.7	13.5	1.6					
002332.475-720530.081	00:23:32.475	0.136	-72:05:30.081	0.212			5.4	1.2					

ATCA J	RA	δRA	Dec	δDec	$S_{5.5}$	$\delta S_{5.5}$	$S_{7.25}$	$\delta S_{7.25}$	$S_{9.0}$	$\delta S_{9.0}$	α	$\delta\alpha$	MAVERIC
002332.423-720614.106	00:23:32.423	0.268	-72:06:14.106	0.199	10.0	1.8	8.8	1.7					
002332.381-720617.520	00:23:32.381	0.501	-72:06:17.520	0.343	6.7	1.8							
002331.595-720611.402	00:23:31.595	0.178	-72:06:11.402	0.268	9.3	1.8	7.6	1.6					
002331.268-720609.468	00:23:31.268	0.170	-72:06:09.468	0.177	7.2	1.5							
002330.624-720502.658	00:23:30.624	0.207	-72:05:02.658	0.246	11.0	1.6	8.4	1.3					
002329.650-720357.908	00:23:29.650	0.058	-72:03:57.908	0.112	18.2	1.5	13.4	1.4					
002328.626-720353.421	00:23:28.626	0.072	-72:03:53.421	0.070	25.0	1.7	16.7	1.5					47Tuc-ATCA18
002327.870-720349.005	00:23:27.870	0.129	-72:03:49.005	0.306	9.2	1.7							
002327.597-720459.231	00:23:27.597	0.126	-72:04:59.231	0.137			7.3	1.4					

Figure B.1: The 5.5 GHz radio image of 47 Tuc. The dashed and solid cyan circles indicate the core and half-light radii of 47 Tuc respectively.
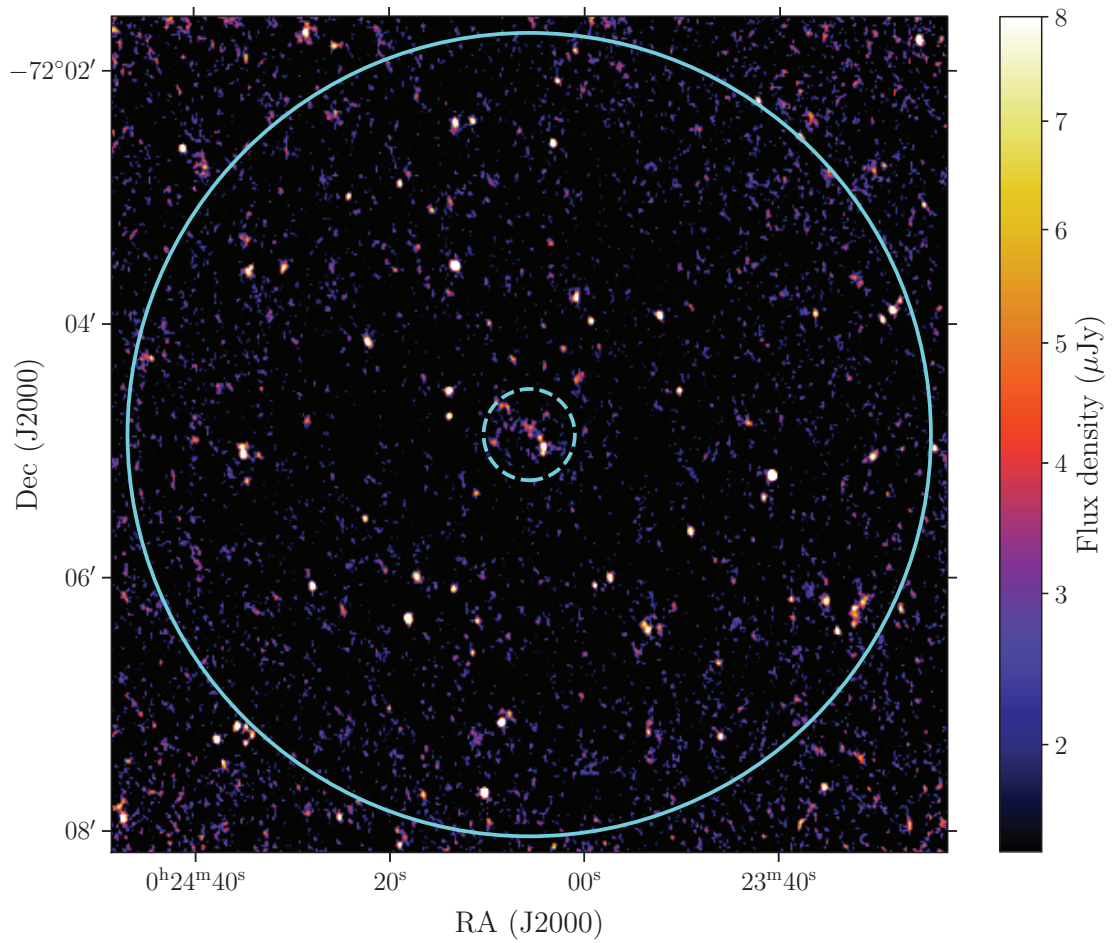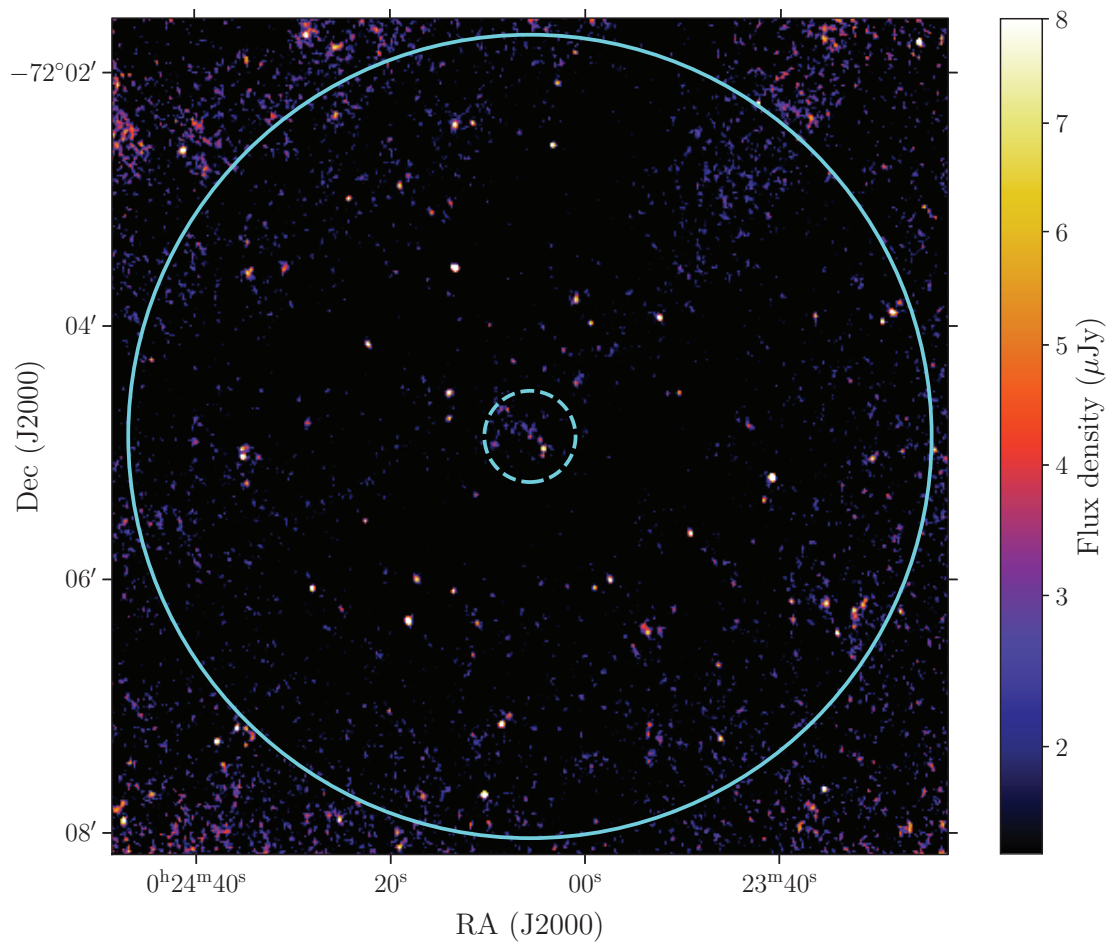
Figure B.2: The 7.25 GHz radio image of 47 Tuc. The dashed and solid cyan circles indicate the core and half-light radii of 47 Tuc respectively.
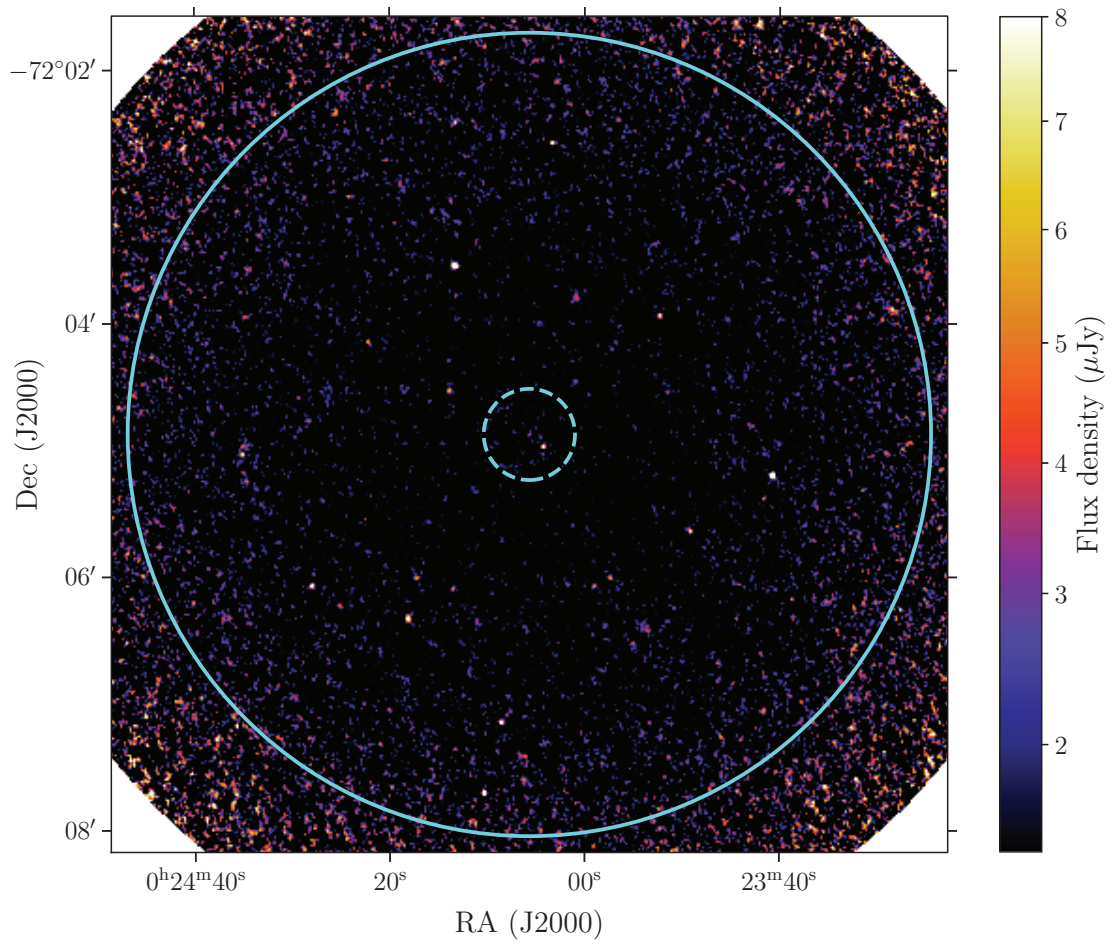
Figure B.3: The 9.0 GHz radio image of 47 Tuc. The dashed and solid cyan circles indicate the core and half-light radii of 47 Tuc respectively.

APPENDIX C

CO-AUTHOR PERMISSIONS

To whom it may concern,

I, Alessandro Paduano, have outlined my contributions and the contributions of Co-Authors to the chapters in this thesis that have been adapted from published papers (Chapter 3, "The MAVERIC Survey: Simultaneous Chandra and VLA observations of the transitional millisecond pulsar candidate NGC 6652B"; Chapter 4, "The MAVERIC Survey: The first radio and X-ray limits on the detached black holes in NGC 3201"; and Chapter 5, "Ultra-deep ATCA imaging of 47 Tucanae reveals a central compact radio source") and to Chapter 6, "A radio source catalogue of 47 Tucanae".

_____

(Signature of candidate)

I, as a Co-Author, endorse that the level of contribution indicated by the candidate as in the "Statement of contribution by Co-Authors" is appropriate.

Arash Bahramian
_____   _____

(Full name of Co-author)   (Signature of Co-author)

To whom it may concern,

I, Alessandro Paduano, have outlined my contributions and the contributions of Co-Authors to the chapters in this thesis that have been adapted from published papers (Chapter 3, "The MAVERIC Survey: Simultaneous Chandra and VLA observations of the transitional millisecond pulsar candidate NGC 6652B"; Chapter 4, "The MAVERIC Survey: The first radio and X-ray limits on the detached black holes in NGC 3201"; and Chapter 5, "Ultra-deep ATCA imaging of 47 Tucanae reveals a central compact radio source") and to Chapter 6, "A radio source catalogue of 47 Tucanae".

(Signature of candidate)

I, as a Co-Author, endorse that the level of contribution indicated by the candidate as in the "Statement of contribution by Co-Authors" is appropriate.

Christopher Britt

(Full name of Co-author)   (Signature of Co-author)

To whom it may concern,

I, Alessandro Paduano, have outlined my contributions and the contributions of Co-Authors to the chapters in this thesis that have been adapted from published papers (Chapter 3, "The MAVERIC Survey: Simultaneous Chandra and VLA observations of the transitional millisecond pulsar candidate NGC 6652B"; Chapter 4, "The MAVERIC Survey: The first radio and X-ray limits on the detached black holes in NGC 3201"; and Chapter 5, "Ultra-deep ATCA imaging of 47 Tucanae reveals a central compact radio source") and to Chapter 6, "A radio source catalogue of 47 Tucanae".

‾‾‾‾‾‾‾‾‾‾‾‾‾‾‾‾‾‾‾‾‾‾‾‾‾‾‾‾‾‾‾‾‾‾‾‾
(Signature of candidate)

I, as a Co-Author, endorse that the level of contribution indicated by the candidate as in the "Statement of contribution by Co-Authors" is appropriate.

Laura Chomiuk
‾‾‾‾‾‾‾‾‾‾‾‾‾‾‾‾‾‾‾‾‾‾‾‾‾   ‾‾‾‾‾‾‾‾‾‾‾‾‾‾‾‾‾‾‾‾‾‾‾‾‾
(Full name of Co-author)   (Signature of Co-author)

To whom it may concern,

I, Alessandro Paduano, have outlined my contributions and the contributions of Co-Authors to the chapters in this thesis that have been adapted from published papers (Chapter 3, "The MAVERIC Survey: Simultaneous Chandra and VLA observations of the transitional millisecond pulsar candidate NGC 6652B"; Chapter 4, "The MAVERIC Survey: The first radio and X-ray limits on the detached black holes in NGC 3201"; and Chapter 5, "Ultra-deep ATCA imaging of 47 Tucanae reveals a central compact radio source") and to Chapter 6, "A radio source catalogue of 47 Tucanae".
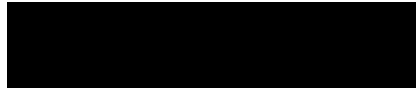
███████████████

_____

(Signature of candidate)

I, as a Co-Author, endorse that the level of contribution indicated by the candidate as in the "Statement of contribution by Co-Authors" is appropriate.

Stefan Dreizlor   ███████████████

(Full name of Co-author)   (Signature of Co-author)

To whom it may concern,

I, Alessandro Paduano, have outlined my contributions and the contributions of Co-Authors to the chapters in this thesis that have been adapted from published papers (Chapter 3, "The MAVERIC Survey: Simultaneous Chandra and VLA observations of the transitional millisecond pulsar candidate NGC 6652B"; Chapter 4, "The MAVERIC Survey: The first radio and X-ray limits on the detached black holes in NGC 3201"; and Chapter 5, "Ultra-deep ATCA imaging of 47 Tucanae reveals a central compact radio source") and to Chapter 6, "A radio source catalogue of 47 Tucanae".
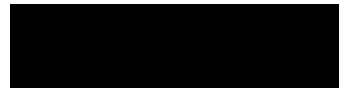
_____

(Signature of candidate)

I, as a Co-Author, endorse that the level of contribution indicated by the candidate as in the "Statement of contribution by Co-Authors" is appropriate.

Timothy James Galvin
_____
(Full name of Co-author)   (Signature of Co-author)

To whom it may concern,

I, Alessandro Paduano, have outlined my contributions and the contributions of Co-Authors to the chapters in this thesis that have been adapted from published papers (Chapter 3, "The MAVERIC Survey: Simultaneous Chandra and VLA observations of the transitional millisecond pulsar candidate NGC 6652B"; Chapter 4, "The MAVERIC Survey: The first radio and X-ray limits on the detached black holes in NGC 3201"; and Chapter 5, "Ultra-deep ATCA imaging of 47 Tucanae reveals a central compact radio source") and to Chapter 6, "A radio source catalogue of 47 Tucanae".
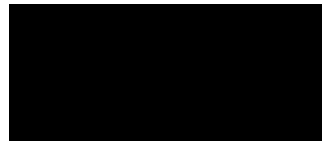
████████████████████████

(Signature of candidate)

I, as a Co-Author, endorse that the level of contribution indicated by the candidate as in the "Statement of contribution by Co-Authors" is appropriate.

Fabian Göttgens

(Full name of Co-author)

████████████████████████

(Signature of Co-author)

To whom it may concern,

I, Alessandro Paduano, have outlined my contributions and the contributions of Co-Authors to the chapters in this thesis that have been adapted from published papers (Chapter 3, "The MAVERIC Survey: Simultaneous Chandra and VLA observations of the transitional millisecond pulsar candidate NGC 6652B"; Chapter 4, "The MAVERIC Survey: The first radio and X-ray limits on the detached black holes in NGC 3201"; and Chapter 5, "Ultra-deep ATCA imaging of 47 Tucanae reveals a central compact radio source") and to Chapter 6, "A radio source catalogue of 47 Tucanae".

_____
(Signature of candidate)

I, as a Co-Author, endorse that the level of contribution indicated by the candidate as in the "Statement of contribution by Co-Authors" is appropriate.

Craig Heinke
_____   _____
(Full name of Co-author)   (Signature of Co-author)

To whom it may concern,

I, Alessandro Paduano, have outlined my contributions and the contributions of Co-Authors to the chapters in this thesis that have been adapted from published papers (Chapter 3, "The MAVERIC Survey: Simultaneous Chandra and VLA observations of the transitional millisecond pulsar candidate NGC 6652B"; Chapter 4, "The MAVERIC Survey: The first radio and X-ray limits on the detached black holes in NGC 3201"; and Chapter 5, "Ultra-deep ATCA imaging of 47 Tucanae reveals a central compact radio source") and to Chapter 6, "A radio source catalogue of 47 Tucanae".
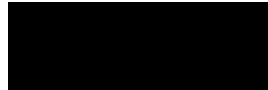
███████████████████

_____

(Signature of candidate)

I, as a Co-Author, endorse that the level of contribution indicated by the candidate as in the "Statement of contribution by Co-Authors" is appropriate.

Tim-Oliver Husser   ███████████████
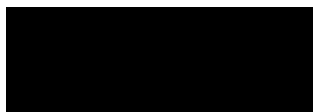
(Full name of Co-author)   (Signature of Co-author)

To whom it may concern,

I, Alessandro Paduano, have outlined my contributions and the contributions of Co-Authors to the chapters in this thesis that have been adapted from published papers (Chapter 3, "The MAVERIC Survey: Simultaneous Chandra and VLA observations of the transitional millisecond pulsar candidate NGC 6652B"; Chapter 4, "The MAVERIC Survey: The first radio and X-ray limits on the detached black holes in NGC 3201"; and Chapter 5, "Ultra-deep ATCA imaging of 47 Tucanae reveals a central compact radio source") and to Chapter 6, "A radio source catalogue of 47 Tucanae".

_____

(Signature of candidate)

I, as a Co-Author, endorse that the level of contribution indicated by the candidate as in the "Statement of contribution by Co-Authors" is appropriate.

Sebastian Kamann
_____   _____

(Full name of Co-author)   (Signature of Co-author)

To whom it may concern,

I, Alessandro Paduano, have outlined my contributions and the contributions of Co-Authors to the chapters in this thesis that have been adapted from published papers (Chapter 3, "The MAVERIC Survey: Simultaneous Chandra and VLA observations of the transitional millisecond pulsar candidate NGC 6652B"; Chapter 4, "The MAVERIC Survey: The first radio and X-ray limits on the detached black holes in NGC 3201"; and Chapter 5, "Ultra-deep ATCA imaging of 47 Tucanae reveals a central compact radio source") and to Chapter 6, "A radio source catalogue of 47 Tucanae".
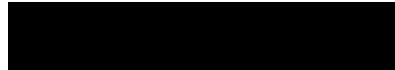
_____

(Signature of candidate)

I, as a Co-Author, endorse that the level of contribution indicated by the candidate as in the "Statement of contribution by Co-Authors" is appropriate.

Adela Kawka
_____

(Full name of Co-author)   (Signature of Co-author)

To whom it may concern,

I, Alessandro Paduano, have outlined my contributions and the contributions of Co-Authors to the chapters in this thesis that have been adapted from published papers (Chapter 3, "The MAVERIC Survey: Simultaneous Chandra and VLA observations of the transitional millisecond pulsar candidate NGC 6652B"; Chapter 4, "The MAVERIC Survey: The first radio and X-ray limits on the detached black holes in NGC 3201"; and Chapter 5, "Ultra-deep ATCA imaging of 47 Tucanae reveals a central compact radio source") and to Chapter 6, "A radio source catalogue of 47 Tucanae".

_____
(Signature of candidate)

I, as a Co-Author, endorse that the level of contribution indicated by the candidate as in the "Statement of contribution by Co-Authors" is appropriate.

Thomas Joseph Maccarone
(Full name of Co-author)

(Signature of Co-author)

To whom it may concern,

I, Alessandro Paduano, have outlined my contributions and the contributions of Co-Authors to the chapters in this thesis that have been adapted from published papers (Chapter 3, "The MAVERIC Survey: Simultaneous Chandra and VLA observations of the transitional millisecond pulsar candidate NGC 6652B"; Chapter 4, "The MAVERIC Survey: The first radio and X-ray limits on the detached black holes in NGC 3201"; and Chapter 5, "Ultra-deep ATCA imaging of 47 Tucanae reveals a central compact radio source") and to Chapter 6, "A radio source catalogue of 47 Tucanae".

_____
(Signature of candidate)

I, as a Co-Author, endorse that the level of contribution indicated by the candidate as in the "Statement of contribution by Co-Authors" is appropriate.

James C.A. Miller-Jones
_____
(Full name of Co-author)

(Signature of Co-author)

To whom it may concern,

I, Alessandro Paduano, have outlined my contributions and the contributions of Co-Authors to the chapters in this thesis that have been adapted from published papers (Chapter 3, "The MAVERIC Survey: Simultaneous Chandra and VLA observations of the transitional millisecond pulsar candidate NGC 6652B"; Chapter 4, "The MAVERIC Survey: The first radio and X-ray limits on the detached black holes in NGC 3201"; and Chapter 5, "Ultra-deep ATCA imaging of 47 Tucanae reveals a central compact radio source") and to Chapter 6, "A radio source catalogue of 47 Tucanae".
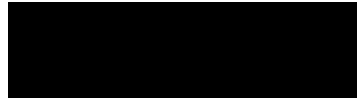
_____
(Signature of candidate)

I, as a Co-Author, endorse that the level of contribution indicated by the candidate as in the "Statement of contribution by Co-Authors" is appropriate.

Richard Plotkin
_____   _____
(Full name of Co-author)   (Signature of Co-author)

To whom it may concern,

I, Alessandro Paduano, have outlined my contributions and the contributions of Co-Authors to the chapters in this thesis that have been adapted from published papers (Chapter 3, "The MAVERIC Survey: Simultaneous Chandra and VLA observations of the transitional millisecond pulsar candidate NGC 6652B"; Chapter 4, "The MAVERIC Survey: The first radio and X-ray limits on the detached black holes in NGC 3201"; and Chapter 5, "Ultra-deep ATCA imaging of 47 Tucanae reveals a central compact radio source") and to Chapter 6, "A radio source catalogue of 47 Tucanae".
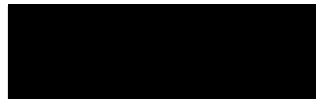
███████████████

_____

(Signature of candidate)

I, as a Co-Author, endorse that the level of contribution indicated by the candidate as in the "Statement of contribution by Co-Authors" is appropriate.

███████████████

Dr. Liliana Rivera Sandoval

_____   _____

(Full name of Co-author)   (Signature of Co-author)

To whom it may concern,

I, Alessandro Paduano, have outlined my contributions and the contributions of Co-Authors to the chapters in this thesis that have been adapted from published papers (Chapter 3, "The MAVERIC Survey: Simultaneous Chandra and VLA observations of the transitional millisecond pulsar candidate NGC 6652B"; Chapter 4, "The MAVERIC Survey: The first radio and X-ray limits on the detached black holes in NGC 3201"; and Chapter 5, "Ultra-deep ATCA imaging of 47 Tucanae reveals a central compact radio source") and to Chapter 6, "A radio source catalogue of 47 Tucanae".

_____

(Signature of candidate)

I, as a Co-Author, endorse that the level of contribution indicated by the candidate as in the "Statement of contribution by Co-Authors" is appropriate.

Aarran Shaw
_____   _____

(Full name of Co-author)   (Signature of Co-author)

To whom it may concern,

I, Alessandro Paduano, have outlined my contributions and the contributions of Co-Authors to the chapters in this thesis that have been adapted from published papers (Chapter 3, "The MAVERIC Survey: Simultaneous Chandra and VLA observations of the transitional millisecond pulsar candidate NGC 6652B"; Chapter 4, "The MAVERIC Survey: The first radio and X-ray limits on the detached black holes in NGC 3201"; and Chapter 5, "Ultra-deep ATCA imaging of 47 Tucanae reveals a central compact radio source") and to Chapter 6, "A radio source catalogue of 47 Tucanae".
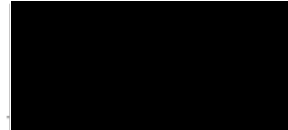
███████████████████████

_____

(Signature of candidate)

I, as a Co-Author, endorse that the level of contribution indicated by the candidate as in the "Statement of contribution by Co-Authors" is appropriate.

Laura Shishkovsky
_____   █████████████████████

(Full name of Co-author)   (Signature of Co-author)

To whom it may concern,

I, Alessandro Paduano, have outlined my contributions and the contributions of Co-Authors to the chapters in this thesis that have been adapted from published papers (Chapter 3, "The MAVERIC Survey: Simultaneous Chandra and VLA observations of the transitional millisecond pulsar candidate NGC 6652B"; Chapter 4, "The MAVERIC Survey: The first radio and X-ray limits on the detached black holes in NGC 3201"; and Chapter 5, "Ultra-deep ATCA imaging of 47 Tucanae reveals a central compact radio source") and to Chapter 6, "A radio source catalogue of 47 Tucanae".

_____
(Signature of candidate)

I, as a Co-Author, endorse that the level of contribution indicated by the candidate as in the "Statement of contribution by Co-Authors" is appropriate.

Gregory R. Sivakoff
_____   _____
(Full name of Co-author)   (Signature of Co-author)

To whom it may concern,

I, Alessandro Paduano, have outlined my contributions and the contributions of Co-Authors to the chapters in this thesis that have been adapted from published papers (Chapter 3, "The MAVERIC Survey: Simultaneous Chandra and VLA observations of the transitional millisecond pulsar candidate NGC 6652B"; Chapter 4, "The MAVERIC Survey: The first radio and X-ray limits on the detached black holes in NGC 3201"; and Chapter 5, "Ultra-deep ATCA imaging of 47 Tucanae reveals a central compact radio source") and to Chapter 6, "A radio source catalogue of 47 Tucanae".
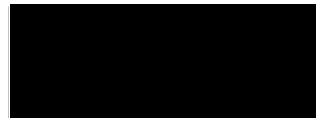
_____
(Signature of candidate)

I, as a Co-Author, endorse that the level of contribution indicated by the candidate as in the "Statement of contribution by Co-Authors" is appropriate.

_____Jay Strader_____
(Full name of Co-author)

(Signature of Co-author)

To whom it may concern,

I, Alessandro Paduano, have outlined my contributions and the contributions of Co-Authors to the chapters in this thesis that have been adapted from published papers (Chapter 3, "The MAVERIC Survey: Simultaneous Chandra and VLA observations of the transitional millisecond pulsar candidate NGC 6652B"; Chapter 4, "The MAVERIC Survey: The first radio and X-ray limits on the detached black holes in NGC 3201"; and Chapter 5, "Ultra-deep ATCA imaging of 47 Tucanae reveals a central compact radio source") and to Chapter 6, "A radio source catalogue of 47 Tucanae".

████████████████████████

_____
(Signature of candidate)

I, as a Co-Author, endorse that the level of contribution indicated by the candidate as in the "Statement of contribution by Co-Authors" is appropriate.

████████████████

Evangelia Tremou_____   __████████████████____
(Full name of Co-author)   (Signature of Co-author)

To whom it may concern,

I, Alessandro Paduano, have outlined my contributions and the contributions of Co-Authors to the chapters in this thesis that have been adapted from published papers (Chapter 3, "The MAVERIC Survey: Simultaneous Chandra and VLA observations of the transitional millisecond pulsar candidate NGC 6652B"; Chapter 4, "The MAVERIC Survey: The first radio and X-ray limits on the detached black holes in NGC 3201"; and Chapter 5, "Ultra-deep ATCA imaging of 47 Tucanae reveals a central compact radio source") and to Chapter 6, "A radio source catalogue of 47 Tucanae".
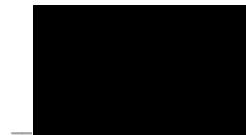
_____

(Signature of candidate)

I, as a Co-Author, endorse that the level of contribution indicated by the candidate as in the "Statement of contribution by Co-Authors" is appropriate.

Vlad Tudor

_____   _____

(Full name of Co-author)   (Signature of Co-author)

To whom it may concern,

I, Alessandro Paduano, have outlined my contributions and the contributions of Co-Authors to the chapters in this thesis that have been adapted from published papers (Chapter 3, "The MAVERIC Survey: Simultaneous Chandra and VLA observations of the transitional millisecond pulsar candidate NGC 6652B"; Chapter 4, "The MAVERIC Survey: The first radio and X-ray limits on the detached black holes in NGC 3201"; and Chapter 5, "Ultra-deep ATCA imaging of 47 Tucanae reveals a central compact radio source") and to Chapter 6, "A radio source catalogue of 47 Tucanae".
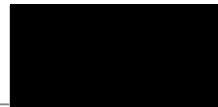
_____

(Signature of candidate)

I, as a Co-Author, endorse that the level of contribution indicated by the candidate as in the "Statement of contribution by Co-Authors" is appropriate.

Yue Zhao

_____   _____

(Full name of Co-author)   (Signature of Co-author)

BIBLIOGRAPHY

M. Abada-Simon, et al. (1993). 'The Spectrum and Variability of Radio Emission from AE Aquarii'. *The Astrophysical Journal* **406**:692–700.

F. Abbate, et al. (2018). 'Internal Gas Models and Central Black Hole in 47 Tucanae Using Millisecond Pulsars'. *Monthly Notices of the Royal Astronomical Society* **481**:627–638.

R. Abbott, et al. (2020). 'GW190521: A Binary Black Hole Merger with a Total Mass of 150 M⊙'. *Physical Review Letters* **125**:101102.

R. Abbott, et al. (2020). 'Properties and Astrophysical Implications of the 150 M$_\odot$ Binary Black Hole Merger GW190521'. *The Astrophysical Journal Letters* **900**(1):L13.

K. Aggarwal & D. R. Lorimer (2022). 'On the Radio Spectra of Galactic Millisecond Pulsars'. *arXiv:2203.05560 [astro-ph]* .

C. Alard (2000). 'Image Subtraction Using a Space-Varying Kernel'. *Astronomy and Astrophysics Supplement Series* **144**:363–370.

C. Alard & R. H. Lupton (1998). 'A Method for Optimal Image Subtraction'. *The Astrophysical Journal* **503**:325–331.

M. D. Albrow, et al. (2001). 'The Frequency of Binary Stars in the Core of 47 Tucanae'. *The Astrophysical Journal* **559**:1060–1081.

T. Alexander (1997). 'Is AGN Variability Correlated with Other AGN Properties? ZDCF Analysis of Small Samples of Sparse Light Curves'. In D. Maoz, A. Sternberg, & E. M. Leibowitz (eds.), *Astronomical Time Series*, vol. 218 of *Astrophysics and Space Science Library*, p. 163.

M. A. Alpar, et al. (1982). 'A New Class of Radio Pulsars'. *Nature* **300**:728–730.

F. Ambrosino et al. (2017). 'Optical Pulsations from a Transitional Millisecond Pulsar'. *Nature Astronomy (2017), published on-line on October 2, 2017* **1**(12):854–858.

J. Anderson, et al. (2008). 'The Acs Survey of Globular Clusters. V. Generating a Comprehensive Star Catalog for Each Cluster'. *The Astronomical Journal* **135**:2055–2073.

F. Antonini, et al. (2019). 'Black hole growth through hierarchical black hole mergers in dense star clusters: implications for gravitational wave detections'. *Monthly Notices of the Royal Astronomical Society* **486**(4):5008–5021.

A. M. Archibald et al. (2009). 'A Radio Pulsar/X-ray Binary Link'. *Science* **324**:1411.

A. M. Archibald, et al. (2013). 'Long-Term Radio Timing Observations of the Transition Millisecond Pulsar PSR˜J1023+0038'. *arXiv e-prints* **1311**:arXiv:1311.5161.

K. A. Arnaud (1996). 'XSPEC: The First Ten Years' **101**:17.

A. Askar, et al. (2020). 'Stellar-Mass Black Holes in Globular Clusters: Dynamical Consequences and Observational Signatures' **351**:395–399.

R. Bacon, et al. (2010). 'The MUSE Second-Generation VLT Instrument'. In \procspie, vol. 7735 of *Society of Photo-Optical Instrumentation Engineers (SPIE) Conference Series*, p. 773508.

A. Bahramian, et al. (2015). 'Limits on Thermal Variations in a Dozen Quiescent Neutron Stars over a Decade'. *Monthly Notices of the Royal Astronomical Society* **452**:3475–3488.

A. Bahramian, et al. (2014). 'Discovery of the Third Transient X-Ray Binary in the Galactic Globular Cluster Terzan 5'. \apj **780**(2):127.

A. Bahramian, et al. (2013). 'Stellar Encounter Rate in Galactic Globular Clusters'. *The Astrophysical Journal* **766**:136.

A. Bahramian, et al. (2017). 'The Ultracompact Nature of the Black Hole Candidate X-ray Binary 47 Tuc X9'. *Monthly Notices of the Royal Astronomical Society* **467**:2199–2216.

A. Bahramian, et al. (2018a). *Radio/X-ray Correlation Database for X-ray Binaries*.

A. Bahramian & A. Rushton (2022). 'bersavosh/XRB-LrLx_pub: update 220808'.

A. Bahramian, et al. (2018b). 'The MAVERIC Survey: A Transitional Millisecond Pulsar Candidate in Terzan 5'. *The Astrophysical Journal* **864**:28.

A. Bahramian, et al. (2020). 'The MAVERIC Survey: Chandra/ACIS Catalog of Faint X-Ray Sources in 38 Galactic Globular Clusters'. *The Astrophysical Journal* **901**:57.

R. Barnard, et al. (2011). 'Four New Black Hole Candidates Identified in M31 Globular Clusters with Chandra and XMM-Newton'. \apj **734**(2):79.

P. E. Barrett, et al. (2017). 'A Jansky VLA Survey of Magnetic Cataclysmic Variable Stars. I. The Data'. *The Astronomical Journal* **154**:252.

C. G. Bassa et al. (2014). 'A State Change in the Low-Mass X-ray Binary XSS J12270-4859'. *Mon. Not. Roy. Astron. Soc.* **441**(2):1825–1830.

H. Baumgardt (2017). 'N -body modelling of globular clusters: masses, mass-to-light ratios and intermediate-mass black holes'. *Monthly Notices of the Royal Astronomical Society* **464**(2):2174–2202.

H. Baumgardt, et al. (2019). 'No evidence for intermediate-mass black holes in the globular clusters ω Cen and NGC 6624'. *Monthly Notices of the Royal Astronomical Society* **488**(4):5340–5351.

H. Baumgardt, et al. (2019). 'Mean Proper Motions, Space Orbits, and Velocity Dispersion Profiles of Galactic Globular Clusters Derived from Gaia DR2 Data'. *Monthly Notices of the Royal Astronomical Society* **482**:5138–5155.

H. Baumgardt & E. Vasiliev (2021). 'Accurate Distances to Galactic Globular Clusters through a Combination of Gaia EDR3, HST and Literature Data'. *arXiv:2105.09526 [astro-ph]* .

C. Beaumont, et al. (2015). 'Hackable User Interfaces In Astronomy with Glue' **495**:101.

E. C. Bellm, et al. (2019). 'The Zwicky Transient Facility: System Overview, Performance, and First Results'. *Publications of the Astronomical Society of the Pacific* **131**:018002.

D. Belloni & L. E. Rivera Sandoval (2020). 'Properties of Cataclysmic Variables in Globular Clusters'. *arXiv e-prints* **2008**:arXiv:2008.12772.

F. Bernardini, et al. (2013). 'Daily Multiwavelength Swift Monitoring of the Neutron Star Low-Mass X-ray Binary Cen X-4: Evidence for Accretion and Reprocessing during Quiescence'. *Monthly Notices of the Royal Astronomical Society* **436**:2465–2483.

S. Bhattacharya, et al. (2017). 'Chandra Studies of the Globular Cluster 47 Tucanae: A Deeper X-ray Source Catalogue, Five New X-ray Counterparts to Millisecond Radio Pulsars, and New Constraints to r-Mode Instability Window'. *Monthly Notices of the Royal Astronomical Society* **472**:3706–3721.

R. D. Blandford & D. G. Payne (1982). 'Hydromagnetic flows from accretion disks and the production of radio jets.'. *Monthly Notices of the Royal Astronomical Society* **199**:883–903.

R. D. Blandford & R. L. Znajek (1977). 'Electromagnetic extraction of energy from Kerr black holes.'. *Monthly Notices of the Royal Astronomical Society* **179**:433–456.

S. Bogdanov, et al. (2018). 'Simultaneous Chandra and VLA Observations of the Transitional Millisecond Pulsar PSR J1023+0038: Anti-correlated X-ray and Radio Variability'. *Astrophys. J.* **856**(1):54.

S. Bogdanov & J. P. Halpern (2015). 'Identification of the High-energy Gamma-ray Source 3fgl J1544.6–1125 as a Transitional Millisecond Pulsar Binary in an Accreting State'. *Astrophys. J.* **803**(2):L27.

J. R. Bond, et al. (1984). 'The Evolution and Fate of Very Massive Objects'. *The Astrophysical Journal* **280**:825–847.

N. J. Brassington, et al. (2010). 'The X-ray Spectra of the Luminous LMXBs in NGC 3379: Field and Globular Cluster Sources'. \apj **725**(2):1805–1823.

P. G. Breen & D. C. Heggie (2013). 'Dynamical Evolution of Black Hole Subsystems in Idealized Star Clusters'. *Monthly Notices of the Royal Astronomical Society* **432**:2779–2797.

K. Breivik, et al. (2019). 'Constraining Compact Object Formation with 2M0521'. *The Astrophysical Journal* **878**:L4.

A. Bressan, et al. (2012). 'PARSEC: Stellar Tracks and Isochrones with the PAdova and TRieste Stellar Evolution Code'. *Monthly Notices of the Royal Astronomical Society* **427**:127–145.

D. S. Briggs (1995). *High fidelity deconvolution of moderately resolved sources.* Ph.D. thesis, New Mexico Institute of Mining and Technology.

P. S. Broos, et al. (2010). 'Innovations in the Analysis of Chandra-ACIS Observations'. *The Astrophysical Journal* **714**:1582–1605.

J. Buchner, et al. (2014). 'X-Ray Spectral Modelling of the AGN Obscuring Region in the CDFS: Bayesian Model Selection and Catalogue'. *Astronomy and Astrophysics* **564**:A125.

E. M. Cackett, et al. (2010). 'Quiescent X-ray Emission From Cen X-4: A Variable Thermal Component'. *The Astrophysical Journal* **720**:1325–1332.

F. Camilo, et al. (2000). 'Observations of 20 Millisecond Pulsars in 47 Tucanae at 20 Centimeters'. *The Astrophysical Journal* **535**(2):975–990.

S. Campana, et al. (2004). 'The Variable Quiescence of Centaurus X-4'. *The Astrophysical Journal* **601**:474–478.

S. Campana, et al. (2000). 'BeppoSAX Observation of Cen X-4 in Quiescence'. *Astronomy and Astrophysics* **358**:583–586.

A. G. Cantrell, et al. (2010). 'The Inclination of the Soft X-Ray Transient A0620-00 and the Mass of Its Black Hole'. *The Astrophysical Journal* **710**:1127–1141.

F. Carotenuto, et al. (2022). 'The black hole X-ray binary MAXI J1348−630 in quiescence'. *arXiv e-prints* p. arXiv:2208.00100.

J. Casares (2015). 'A FWHM-K2 Correlation in Black Hole Transients'. *The Astrophysical Journal* **808**:80.

J. Casares (2016). 'Mass Ratio Determination from H α Lines in Black Hole X-Ray Transients'. *The Astrophysical Journal* **822**:99.

J. Casares, et al. (1992). 'A 6.5-Day Periodicity in the Recurrent Nova V404 Cygni Implying the Presence of a Black Hole'. *Nature* **355**:614–617.

W. Cash (1979). 'Parameter estimation in astronomy through application of the likelihood ratio.'. *The Astrophysical Journal* **228**:939–947.

X. Chen, et al. (2020). 'The Zwicky Transient Facility Catalog of Periodic Variable Stars'. *The Astrophysical Journal Supplemental* **249**(1):18.

Z. Cheng, et al. (2019). 'Exploring the Mass Segregation Effect of X-Ray Sources in Globular Clusters: The Case of 47 Tucanae'. *The Astrophysical Journal* **876**(1):59.

C. Chevalier, et al. (1989). 'Optical Studies of Transient Low-Mass X-ray Binaries in Quiescence. I - Centaurus X-4: Orbital Period, Light Curve, Spectrum and Models for the System'. *Astronomy and Astrophysics* **210**:114–126.

L. Chomiuk, et al. (2013). 'A Radio-selected Black Hole X-Ray Binary Candidate in the Milky Way Globular Cluster M62'. *The Astrophysical Journal* **777**:69.

G. W. Clark (1975). 'X-Ray Binaries in Globular Clusters.'. \apjl **199**:L143–L145.

J. J. Condon, et al. (2002). 'Radio Sources and Star Formation in the Local Universe'. *The Astronomical Journal* **124**(2):675–689.

A. M. Cool, et al. (2013). 'HST/ACS Imaging of Omega Centauri: Optical Counterparts of Chandra X-Ray Sources'. *The Astrophysical Journal* **763**(2):126.

G. Coomber, et al. (2011). 'The Unusual X-Ray Binaries of the Globular Cluster NGC 6652'. *The Astrophysical Journal* **735**:95.

J. M. Corral-Santana, et al. (2016). 'BlackCAT: A Catalogue of Stellar-Mass Black Holes in X-ray Transients'. *Astronomy & Astrophysics, Volume 587, id.A61, <NUMPAGES>20</NUMPAGES> pp.* **587**:A61.

G. Costa, et al. (2021). 'Formation of GW190521 from stellar evolution: the impact of the hydrogen-rich envelope, dredge-up, and ^{12}C$(\alpha, \gamma)^{16}$O rate on the pair-instability black hole mass gap'. *Monthly Notices of the Royal Astronomical Society* **501**(3):4514–4533.

F. Coti Zelati, et al. (2019). 'Prolonged Sub-Luminous State of the New Transitional Pulsar Candidate CXOU J110926.4-650224'. *Astronomy and Astrophysics* **622**:A211.

M. Craig, et al. (2017). 'astropy/ccdproc: v1.3.0.post1'.

D. F. Crawford, et al. (1970). 'Maximum-Likelihood Estimation of the Slope from Number-Flux Counts of Radio Sources'. *The Astrophysical Journal* **162**:405.

D. Cseh, et al. (2010). 'Radio Observations of NGC 6388: An Upper Limit on the Mass of Its Central Black Hole'. *Monthly Notices of the Royal Astronomical Society* **406**:1049–1054.

D. de Martino, et al. (2013). 'X-Ray Follow-Ups of XSSJ12270-4859: A Low-Mass X-ray Binary with Gamma Ray FERMI-LAT Association'. *Astronomy & Astrophysics* **550**:A89.

D. de Martino, et al. (2010). 'The Intriguing Nature of the High-Energy Gamma Ray Source XSS J12270-4859'. *Astronomy and Astrophysics* **515**:A25.

R. de Vita, et al. (2017). 'Prospects for detection of intermediate-mass black holes in globular clusters using integrated-light spectroscopy'. *Monthly Notices of the Royal Astronomical Society* **467**(4):4057–4066.

M. E. DeCesar, et al. (2015). 'A Highly Eccentric 3.9 Millisecond Binary Pulsar in the Globular Cluster NGC 6652'. *The Astrophysical Journal Letters* **807**:L23.

274

M. E. DeCesar, et al. (2011). 'A Search for Millisecond Pulsars in Fermi LAT-Detected Globular Clusters'. *arXiv:1111.0365 [astro-ph]* .

A. T. Deller, et al. (2012). 'A Parallax Distance and Mass Estimate for the Transitional Millisecond Pulsar System J1023+0038'. *apjl* **756**:L25.

A. T. Deller, et al. (2015). 'Radio Imaging Observations of PSR J1023+0038 in an LMXB State'. *Astrophys. J.* **809**(1):13.

E. W. Deutsch, et al. (1998). 'A Search for the Optical Counterpart of the Luminous X-Ray Source in NGC 6652'. *The Astronomical Journal* **116**:1301–1307.

E. W. Deutsch, et al. (2000). 'Ultracompact X-Ray Binaries in Globular Clusters: Variability of the Optical Counterpart of X1832-330 in NGC 6652'. *The Astrophysical Journal Letters* **530**:L21–L24.

P. E. Dewdney, et al. (2009). 'The Square Kilometre Array'. *IEEE Proceedings* **97**:1482–1496.

A. Dolphin (2016). 'DOLPHOT: Stellar photometry'. Astrophysics Source Code Library, record ascl:1608.013.

P. D. Edmonds, et al. (2003). 'An Extensive Census of Hubble Space Telescope Counterparts to Chandra X-Ray Sources in the Globular Cluster 47 Tucanae. I. Astrometry and Photometry'. *The Astrophysical Journal* **596**:1177–1196.

P. D. Edmonds, et al. (2004). 'Hubble Space Telescope Discovery of an Optical Counterpart to the Supersoft X-Ray Source in the Globular Cluster M3'. *The Astrophysical Journal* **611**:413–417.

P. P. Eggleton (1983). 'Aproximations to the Radii of Roche Lobes.'. *apj* **268**:368–369.

M. C. Engel, et al. (2012). 'A 2.15 Hr Orbital Period for the Low-mass X-Ray Binary XB 1832-330 in the Globular Cluster NGC 6652'. *The Astrophysical Journal* **747**:119.

C. R. Epstein & M. H. Pinsonneault (2014). 'How Good a Clock Is Rotation? The Stellar Rotation-Mass-Age Relationship for Old Field Stars'. *The Astrophysical Journal* **780**:159.

M. Eracleous, et al. (1991). 'X-Ray Spectra of Cataclysmic Variables from the Einstein Observatory'. *The Astrophysical Journal* **382**:290–300.

A. C. Fabian, et al. (1975). 'Tidal Capture Formation of Binary Systems and X-ray Sources in Globular Clusters.'. *\mnras* **172**:15.

H. Falcke, et al. (2004). 'A Scheme to Unify Low-Power Accreting Black Holes. Jet-dominated Accretion Flows and the Radio/X-ray Correlation'. *Astronomy and Astrophysics* **414**:895–903.

S. M. Fall & M. J. Rees (1985). 'A Theory for the Origin of Globular Clusters.'. *The Astrophysical Journal* **298**:18–26.

R. Farmer, et al. (2020). 'Constraints from Gravitational-wave Detections of Binary Black Hole Mergers on the $^{12}C(\alpha, \gamma)^{16}O$ Rate'. *The Astrophysical Journal Letters* **902**(2):L36.

R. P. Fender, et al. (2004). 'Towards a Unified Model for Black Hole X-Ray Binary Jets'. *Mon. Not. Roy. Astron. Soc.* **355**:1105–1118.

R. J. L. Fétick, et al. (2019). 'Physics-Based Model of the Adaptive-Optics-Corrected Point Spread Function. Applications to the SPHERE/ZIMPOL and MUSE Instruments'. *Astronomy & Astrophysics, Volume 628, id.A99, <NUMPAGES>11</NUMPAGES> pp.* **628**:A99.

D. R. Foight, et al. (2016). 'Probing X-Ray Absorption and Optical Extinction in the Interstellar Medium Using Chandra Observations of Supernova Remnants'. *The Astrophysical Journal* **826**:66.

W. A. Fowler & F. Hoyle (1964). 'Neutrino Processes and Pair Formation in Massive Stars and Supernovae.'. *The Astrophysical Journal Supplement Series* **9**:201.

G. Fragione & O. Bromberg (2019). 'Eccentric binary black hole mergers in globular clusters hosting intermediate-mass black holes'. *Monthly Notices of the Royal Astronomical Society* **488**(3):4370–4377.

G. Fragione, et al. (2022). 'Merger Rates of Intermediate-Mass Black Hole Binaries in Nuclear Star Clusters'. *arXiv:2204.03745 [astro-ph]* .

G. Fragione, et al. (2020). 'On the Origin of GW190521-like Events from Repeated Black Hole Mergers in Star Clusters'. *The Astrophysical Journal* **902**(1):L26.

G. Fragione & J. Silk (2020). 'Repeated mergers and ejection of black holes within nuclear star clusters'. *Monthly Notices of the Royal Astronomical Society* **498**(4):4591–4604.

J. Frank, et al. (2002). *Accretion Power in Astrophysics: Third Edition.*

P. E. Freeman, et al. (2002). 'A Wavelet-Based Algorithm for the Spatial Analysis of Poisson Data'. *The Astrophysical Journal Supplemental* **138**(1):185–218.

J. M. Fregeau (2008). 'X-Ray Binaries and the Current Dynamical States of Galactic Globular Clusters'. *The Astrophysical Journal Letters* **673**:L25.

P. C. Freire, et al. (2003). 'Further results from the timing of the millisecond pulsars in 47 Tucanae'. *Monthly Notices of the Royal Astronomical Society* **340**(4):1359–1374.

P. C. Freire, et al. (2001). 'Detection of Ionized Gas in the Globular Cluster 47 Tucanae'. *The Astrophysical Journal* **557**:L105–L108.

P. C. C. Freire, et al. (2017). 'Long-Term Observations of the Pulsars in 47 Tucanae - II. Proper Motions, Accelerations and Jerks'. *Monthly Notices of the Royal Astronomical Society* **471**:857–876.

A. S. Fruchter & W. M. Goss (1990). 'The Integrated Flux Density of Pulsars in Globular Clusters'. *The Astrophysical Journal Letters* **365**:L63–L66.

A. S. Fruchter & W. M. Goss (2000). 'Deep Radio Imaging of Globular Clusters and the Cluster Pulsar Population'. *The Astrophysical Journal* **536**:865–874.

A. Fruscione, et al. (2006). 'CIAO: Chandra's Data Analysis System'. In *procspie*, vol. 6270 of *Society of Photo-Optical Instrumentation Engineers (SPIE) Conference Series*, p. 62701V.

Gaia Collaboration, et al. (2018). 'Gaia Data Release 2. Summary of the Contents and Survey Properties'. *aap* **616**:A1.

Gaia Collaboration, et al. (2016). 'The Gaia Mission'. *aap* **595**:A1.

Gaia Collaboration, et al. (2022). 'Gaia Data Release 3: Summary of the content and survey properties'. *arXiv e-prints* p. arXiv:2208.00211.

E. Gallo, et al. (2014). 'The Radio/X-ray Domain of Black Hole X-ray Binaries at the Lowest Radio Luminosities'. *mnras* **445**(1):290–300.

A. M. Geller, et al. (2017a). 'On the Origin of Sub-subgiant Stars. I. Demographics'. *The Astrophysical Journal* **840**:66.

A. M. Geller, et al. (2017b). 'On the Origin of Sub-subgiant Stars. III. Formation Frequencies'. *The Astrophysical Journal* **842**:1.

A. Georgakakis, et al. (2008). 'A New Method for Determining the Sensitivity of X-ray Imaging Observations and the X-ray Number Counts'. *Monthly Notices of the Royal Astronomical Society* **388**:1205–1213.

M. Gieles, et al. (2018). 'Mass models of NGC 6624 without an intermediate-mass black hole'. *Monthly Notices of the Royal Astronomical Society* **473**(4):4832–4839.

B. Giesers, et al. (2018). 'A Detached Stellar-Mass Black Hole Candidate in the Globular Cluster NGC 3201'. *Monthly Notices of the Royal Astronomical Society* **475**:L15–L19.

B. Giesers, et al. (2019). 'A Stellar Census in Globular Clusters with MUSE: Binaries in NGC 3201'. *Astronomy and Astrophysics* **632**:A3.

R. Goldsbury, et al. (2010). 'The ACS Survey of Galactic Globular Clusters. X. New Determinations of Centers for 65 Clusters'. *The Astronomical Journal* **140**:1830–1837.

Y. A. Gordon, et al. (2021). 'A Quick Look at the 3 GHz Radio Sky. I. Source Statistics from the Very Large Array Sky Survey'. *The Astrophysical Journal Supplemental* **255**(2):30.

F. Göttgens, et al. (2019). 'A Stellar Census in Globular Clusters with MUSE: A Spectral Catalogue of Emission-Line Sources'. *Astronomy and Astrophysics* **631**:A118.

J. E. Greene & L. C. Ho (2006). 'The M_{BH}-σ_* Relation in Local Active Galaxies'. *The Astrophysical Journal Letters* **641**(1):L21–L24.

J. E. Greene, et al. (2020). 'Intermediate-Mass Black Holes'. *Annual Review of Astronomy and Astrophysics* **58**:257–312.

J. E. Grindlay, et al. (2001). 'High-Resolution X-ray Imaging of a Globular Cluster Core: Compact Binaries in 47Tuc'. *Science* **292**(5525):2290–2295.

M. Güdel (2002). 'Stellar Radio Astronomy: Probing Stellar Atmospheres from Protostars to Giants'. \araa **40**:217–261.

M. Guedel & A. O. Benz (1993). 'X-Ray/Microwave Relation of Different Types of Active Stars'. *The Astrophysical Journal* **405**:L63.

S. Guillot, et al. (2009). 'Chandra Observation of Quiescent Low-Mass X-Ray Binaries in the Globular Cluster NGC 6304'. *The Astrophysical Journal* **699**:1418–1422.

K. Gültekin, et al. (2019). 'The Fundamental Plane of Black Hole Accretion and Its Use as a Black Hole-Mass Estimator'. *The Astrophysical Journal* **871**(1):80.

K. Gültekin, et al. (2004). 'Growth of Intermediate-Mass Black Holes in Globular Clusters'. *The Astrophysical Journal* **616**(1):221–230.

K. Gültekin, et al. (2006). 'Three-Body Dynamics with Gravitational Wave Emission'. *The Astrophysical Journal* **640**(1):156–166.

T. T. Hamilton, et al. (1985). 'A Search for Millisecond Pulsars in Globular Clusters'. *The Astronomical Journal* **90**:606–608.

W. E. Harris (1996). 'A Catalog of Parameters for Globular Clusters in the Milky Way'. \aj **112**:1487.

A. Heger, et al. (2003). 'How Massive Single Stars End Their Life'. *The Astrophysical Journal* **591**:288–300.

D. C. Heggie & M. Giersz (2008). 'Monte Carlo Simulations of Star Clusters - V. The Globular Cluster M4'. *Monthly Notices of the Royal Astronomical Society* **389**:1858–1870.

C. O. Heinke, et al. (2015). 'The Nature of Very Faint X-ray Binaries: Hints from Light Curves'. \mnras **447**(4):3034–3043.

C. O. Heinke, et al. (2001). 'Identification of the Low-Mass X-Ray Binary and Faint X-Ray Sources in NGC 6652'. *The Astrophysical Journal* **562**:363–367.

C. O. Heinke, et al. (2003a). 'A Chandra X-Ray Study of the Dense Globular Cluster Terzan 5'. *The Astrophysical Journal* **590**:809–821.

C. O. Heinke, et al. (2005). 'A Deep Chandra Survey of the Globular Cluster 47 Tucanae: Catalog of Point Sources'. *The Astrophysical Journal* **625**:796–824.

C. O. Heinke, et al. (2003b). 'A Chandra X-Ray Study of the Globular Cluster M80'. *The Astrophysical Journal* **598**:516–526.

C. O. Heinke, et al. (2006). 'Faint X-Ray Sources in the Globular Cluster Terzan 5'. *The Astrophysical Journal* **651**:1098–1111.

V. Hénault-Brunet, et al. (2020). 'On the Black Hole Content and Initial Mass Function of 47 Tuc'. *Monthly Notices of the Royal Astronomical Society* **491**:113–128.

P. Hertz & J. E. Grindlay (1983). 'An X-ray Survey of Globular Clusters and Their X-ray Luminosity Function'. *The Astrophysical Journal* **275**:105–119.

A. B. Hill, et al. (2011). 'The Bright Unidentified γ-Ray Source 1FGL J1227.9-4852: Can It Be Associated with a Low-Mass X-ray Binary?'. *Monthly Notices of the Royal Astronomical Society* **415**:235–243.

J. G. Hills (1976). 'The Formation of Binaries Containing Black Holes by the Exchange of Companions and the X-ray Sources in Globular Clusters.'. *mnras* **175**:1P–4P.

R. Hirai & I. Mandel (2021). 'Conditions for accretion disc formation and observability of wind-accreting X-ray binaries'. *Publications of the Astronomical Society of Australia* **38**:e056.

R. M. Hjellming, et al. (1988). 'Transient Radio Emission from the X-ray Nova ASM 2000+25'. *The Astrophysical Journal Letters* **335**:L75–L78.

E. Høg, et al. (2000). 'The Tycho-2 catalogue of the 2.5 million brightest stars'. *Astronomy and Astrophysics* **355**:L27–L30.

J. A. Högbom (1974). 'Aperture Synthesis with a Non-Regular Distribution of Interferometer Baselines'. *Astronomy and Astrophysics Supplement Series* **15**:417.

K. Holley-Bockelmann, et al. (2008). 'Gravitational Wave Recoil and the Retention of Intermediate-Mass Black Holes'. *The Astrophysical Journal* **686**(2):829–837.

S. B. Howell (2006). *Handbook of CCD Astronomy*, vol. 5.

T.-O. Husser, et al. (2016). 'MUSE Crowded Field 3D Spectroscopy of over 12,000 Stars in the Globular Cluster NGC 6397 - I. The First Comprehensive Spectroscopic HRD of a Globular Cluster'. *Astronomy & Astrophysics* **588**:A148.

T.-O. Husser, et al. (2013). 'A New Extensive Library of PHOENIX Stellar Atmospheres and Synthetic Spectra'. *Astronomy & Astrophysics, Volume 553, id.A6, <NUMPAGES>9</NUMPAGES> pp.* **553**:A6.

R. Ibata, et al. (2009). 'Density and Kinematic Cusps in M54 at the Heart of the Sagittarius Dwarf Galaxy: Evidence for A 10^4 M $_{sun}$ Black Hole?'. *The Astrophysical Journal Letters* **699**(2):L169–L173.

A. F. Illarionov & R. A. Sunyaev (1975). 'Why the Number of Galactic X-ray Stars Is so Small?'. *Astronomy and Astrophysics* **39**:185.

G. Illiano, et al. (2022). 'Investigating the origin of optical and X-ray pulsations of the transitional millisecond pulsar PSR J1023+0038'. *arXiv e-prints* p. arXiv:2211.12975.

J. A. Irwin, et al. (2010). 'Evidence for a Stellar Disruption by an Intermediate-mass Black Hole in an Extragalactic Globular Cluster'. \apjl **712**(1):L1–L4.

N. Ivanova, et al. (2017). 'Formation of Black Hole X-Ray Binaries with Non-degenerate Donors in Globular Clusters'. *The Astrophysical Journal Letters* **843**:L30.

H. M. Johnson (1976). 'Radio Sources in the Field of Globular Clusters'. *The Astrophysical Journal* **208**:706–708.

H. M. Johnson, et al. (1977). 'Radio and X-ray Observations of NGC 1851 and NGC 1904'. *The Astrophysical Journal* **212**:112–116.

T. J. Johnson, et al. (2015). 'Discovery of Gamma-Ray Pulsations from the Transitional Redback PSR J1227-4853'. *The Astrophysical Journal* **806**:91.

C. P. Johnstone, et al. (2015a). 'Stellar Winds on the Main-Sequence. II. The Evolution of Rotation and Winds'. *Astronomy and Astrophysics* **577**:A28.

C. P. Johnstone, et al. (2015b). 'Stellar Winds on the Main-Sequence. I. Wind Model'. *Astronomy and Astrophysics* **577**:A27.

J. Kaluzny, et al. (2016). 'The Clusters AgeS Experiment (CASE). Variable Stars in the Field of the Globular Cluster NGC 3201'. *Acta Astronomica* **66**:31–53.

S. Kamann, et al. (2018). 'A Stellar Census in Globular Clusters with MUSE: The Contribution of Rotation to Cluster Dynamics Studied with 200 000 Stars'. *Monthly Notices of the Royal Astronomical Society* **473**:5591–5616.

S. Kamann, et al. (2013). 'Resolving Stellar Populations with Crowded Field 3D Spectroscopy'. *Astronomy & Astrophysics, Volume 549, id.A71, <NUMPAGES>19</NUMPAGES> pp.* **549**:A71.

J. Khargharia, et al. (2010). 'Near-Infrared Spectroscopy of Low-mass X-ray Binaries: Accretion Disk Contamination and Compact Object Mass Determination in V404 Cyg and Cen X-4'. *The Astrophysical Journal* **716**:1105–1117.

B. Kızıltan, et al. (2017). 'An Intermediate-Mass Black Hole in the Centre of the Globular Cluster 47 Tucanae'. *Nature* **542**:203–205.

C. Knigge, et al. (2008). 'Stellar Exotica in 47 Tucanae'. *The Astrophysical Journal* **683**(2):1006–1030.

C. Knigge, et al. (2002). 'A Far-Ultraviolet Survey of 47 Tucanae. I. Imaging'. *The Astrophysical Journal* **579**(2):752–759.

R. P. Kraft, et al. (1991). 'Determination of Confidence Limits for Experiments with Low Numbers of Counts'. *The Astrophysical Journal* **374**:344–355.

O. Krause, et al. (2008). 'The Cassiopeia A Supernova Was of Type IIb'. *Science* **320**:1195.

K. Kremer, et al. (2018). 'How Black Holes Shape Globular Clusters: Modeling NGC 3201'. *The Astrophysical Journal Letters* **855**:L15.

S. R. Kulkarni, et al. (1993). 'Stellar Black Holes in Globular Clusters'. \nat **364**(6436):421–423.

B. Lanzoni, et al. (2013). 'The Velocity Dispersion Profile of NGC 6388 from Resolved-star Spectroscopy: No Evidence of a Central Cusp and New Constraints on the Black Hole Mass'. *The Astrophysical Journal* **769**(2):107.

E. Leiner, et al. (2017). 'On the Origin of Sub-subgiant Stars. II. Binary Mass Transfer, Envelope Stripping, and Magnetic Activity'. *The Astrophysical Journal* **840**:67.

K.-L. Li, et al. (2018). 'Multiwavelength Observations of a New Redback Millisecond Pulsar Candidate: 3FGL J0954.8-3948'. \apj **863**:194.

K.-L. Li, et al. (2020). 'The Flare-dominated Accretion Mode of a Radio-bright Candidate Transitional Millisecond Pulsar'. *The Astrophysical Journal* **895**:89.

M. Linares (2014). 'X-Ray States of Redback Millisecond Pulsars'. *The Astrophysical Journal* **795**:72.

M. Linares, et al. (2018). 'Peering into the Dark Side: Magnesium Lines Establish a Massive Neutron Star in PSR J2215+5135'. *The Astrophysical Journal* **859**:54.

Q. Z. Liu, et al. (2007). 'A Catalogue of Low-Mass X-ray Binaries in the Galaxy, LMC, and SMC (Fourth Edition)'. \aap **469**(2):807–810.

T.-N. Lu & A. K. H. Kong (2011). 'Radio Continuum Observations of 47 Tucanae and ω Centauri: Hints for Intermediate-mass Black Holes?'. *The Astrophysical Journal* **729**:L25.

N. Lützgendorf, et al. (2015). 'Re-evaluation of the central velocity-dispersion profile in NGC 6388'. *Astronomy and Astrophysics* **581**:A1.

N. Lützgendorf, et al. (2011). 'Kinematic signature of an intermediate-mass black hole in the globular cluster NGC 6388'. *Astronomy and Astrophysics* **533**:A36.

T. J. Maccarone (2003). 'Do X-ray Binary Spectral State Transition Luminosities Vary?'. *Astronomy and Astrophysics, v.409, p.697-706 (2003)* **409**:697.

T. J. Maccarone (2004). 'Radio Emission as a Test of the Existence of Intermediate-Mass Black Holes in Globular Clusters and Dwarf Spheroidal Galaxies'. *Monthly Notices of the Royal Astronomical Society* **351**:1049–1053.

T. J. Maccarone (2005). 'Constraints on Jet X-ray Emission in Low/Hard-State X-ray Binaries'. *Monthly Notices of the Royal Astronomical Society* **360**:L68–L72.

T. J. Maccarone, et al. (2007). 'A Black Hole in a Globular Cluster'. \nat **445**(7124):183–185.

T. J. Maccarone, et al. (2011). 'A New Globular Cluster Black Hole in NGC 4472'. \mnras **410**(3):1655–1659.

T. J. Maccarone & M. Servillat (2008). 'Radio Observations of NGC 2808 and Other Globular Clusters: Constraints on Intermediate-Mass Black Holes'. *Monthly Notices of the Royal Astronomical Society* **389**:379–384.

A. D. Mackey, et al. (2008). 'Black Holes and Core Expansion in Massive Star Clusters'. *Monthly Notices of the Royal Astronomical Society* **386**:65–95.

C. R. Mann, et al. (2019). 'A Multimass Velocity Dispersion Model of 47 Tucanae Indicates No Evidence for an Intermediate-mass Black Hole'. *The Astrophysical Journal* **875**:1.

P. Marchant & T. J. Moriya (2020). 'The impact of stellar rotation on the black hole mass-gap from pair-instability supernovae'. *Astronomy and Astrophysics* **640**:L18.

T. R. Marsh, et al. (2016). 'A Radio-Pulsing White Dwarf Binary Star'. *Nature* **537**:374–377.

A. R. Martsen, et al. (2022). 'Pulse Profiles and Polarization of Terzan 5 Pulsars'.

F. J. Masci, et al. (2019). 'The Zwicky Transient Facility: Data Processing, Products, and Archive'. **131**(995):018003.

D. McConnell & J. G. Ables (2000). 'Radio Sources near the Core of the Globular Cluster 47 Tucanae'. *Monthly Notices of the Royal Astronomical Society* **311**:841–845.

D. McConnell, et al. (2001). 'Radio Images of the Globular Cluster 47 Tucanae'. *Publications of the Astronomical Society of Australia* **18**:136–139.

J. P. McMullin, et al. (2007). 'CASA Architecture and Applications'. In *Astronomical Data Analysis Software and Systems XVI*, vol. 376, p. 127.

A. Merloni, et al. (2003). 'A Fundamental Plane of Black Hole Activity'. *Monthly Notices of the Royal Astronomical Society* **345**:1057–1076.

J. M. Miller, et al. (2020). 'A New Candidate Transitional Millisecond Pulsar in the Sub-luminous Disk State: 4FGL J0407.7–5702'. *arXiv e-prints* **2009**:arXiv:2009.09054.

M. C. Miller & D. P. Hamilton (2002). 'Four-Body Effects in Globular Cluster Black Hole Coalescence'. *The Astrophysical Journal* **576**:894–898.

J. C. A. Miller-Jones, et al. (2009). 'The First Accurate Parallax Distance to a Black Hole'. *The Astrophysical Journal Letters* **706**:L230–L234.

J. C. A. Miller-Jones, et al. (2015). 'Deep Radio Imaging of 47 Tuc Identifies the Peculiar X-ray Source X9 as a New Black Hole Candidate'. *Monthly Notices of the Royal Astronomical Society* **453**:3918–3931.

J. C. A. Miller-Jones, et al. (2012). 'The Absence of Radio Emission from the Globular Cluster G1'. *The Astrophysical Journal Letters* **755**:L1.

A. P. Milone, et al. (2012). 'The ACS Survey of Galactic Globular Clusters. XII. Photometric Binaries along the Main Sequence'. *Astronomy and Astrophysics* **540**:A16.

N. Mohan & D. Rafferty (2015). 'PyBDSF: Python Blob Detection and Source Finder'. Astrophysics Source Code Library, record ascl:1502.007.

K. Moody & S. Sigurdsson (2009). 'Modeling the Retention Probability of Black Holes in Globular Clusters: Kicks and Rates'. *The Astrophysical Journal* **690**:1370–1377.

M. Morscher, et al. (2015). 'The Dynamical Evolution of Stellar Black Holes in Globular Clusters'. *The Astrophysical Journal* **800**:9.

M. Morscher, et al. (2013). 'Retention of Stellar-mass Black Holes in Globular Clusters'. *The Astrophysical Journal Letters* **763**:L15.

E. J. Murphy, et al. (2018). 'The ngVLA Science Case and Associated Science Requirements' **517**:3.

K. Nandra, et al. (2013). 'The Hot and Energetic Universe: A White Paper Presenting the Science Theme Motivating the Athena+ Mission'.

R. Narayan & I. Yi (1995). 'Advection-Dominated Accretion: Underfed Black Holes and Neutron Stars'. *The Astrophysical Journal* **452**:710.

D. Nardiello, et al. (2018). 'The Hubble Space Telescope UV Legacy Survey of Galactic Globular Clusters - XVII. Public Catalogue Release'. *Monthly Notices of the Royal Astronomical Society* **481**:3382–3393.

E. Noyola, et al. (2010). 'Very Large Telescope Kinematics for Omega Centauri: Further Support for a Central Black Hole'. *The Astrophysical Journal Letters* **719**(1):L60–L64.

W. W. Ober, et al. (1983). 'Evolution of Massive Pregalactic Stars - Part Two - Nucleosynthesis in Pair Creation Supernovae and Pregalactic Enrichment'. *Astronomy and Astrophysics, Vol.119, P. 61, 1983* **119**:61.

A. Paduano, et al. (2022). 'The MAVERIC Survey: The First Radio and X-ray Limits on the Detached Black Holes in NGC 3201'. *Monthly Notices of the Royal Astronomical Society* **510**:3658–3673.

A. Paduano, et al. (2021). 'The MAVERIC Survey: Simultaneous Chandra and VLA Observations of the Transitional Millisecond Pulsar Candidate NGC 6652B'. *Monthly Notices of the Royal Astronomical Society* **506**:4107–4120.

A. Papitto et al. (2013). 'Swings between Rotation and Accretion Power in a Millisecond Binary Pulsar'. *Nature* **501**:517–520.

A. Papitto & D. F. Torres (2015). 'A Propeller Model for the Sub-Luminous Disk State of the Transitional Millisecond Pulsar PSR J1023+0038'. *arXiv:1504.05029 [astro-ph]* .

F. Paresce, et al. (1992). 'Possible cataclysmic variable in the core of the globular cluster 47 Tucanae'. *Nature* **360**(6399):46–48.

J. Patterson & J. C. Raymond (1985). 'X-Ray Emission from Cataclysmic Variables with Accretion Disks. I - Hard X-rays. II - EUV/Soft X-ray Radiation'. *The Astrophysical Journal* **292**:535–558.

S. Pellegrini (2005). 'Nuclear Accretion in Galaxies of the Local Universe: Clues from Chandra Observations'. *The Astrophysical Journal* **624**:155–161.

B. B. P. Perera, et al. (2017). 'Evidence for an Intermediate-Mass Black Hole in the Globular Cluster NGC 6624'. *Monthly Notices of the Royal Astronomical Society* **468**:2114–2127.

A. J. Pickles (1998). 'A Stellar Spectral Flux Library: 1150-25000 Å'. *Publications of the Astronomical Society of the Pacific* **110**:863–878.

G. Piotto, et al. (2015). 'The Hubble Space Telescope UV Legacy Survey of Galactic Globular Clusters. I. Overview of the Project and Detection of Multiple Stellar Populations'. *The Astronomical Journal* **149**:91.

R. M. Plotkin, et al. (2013). 'The X-Ray Spectral Evolution of Galactic Black Hole X-Ray Binaries toward Quiescence'. *The Astrophysical Journal* **773**:59.

R. M. Plotkin, et al. (2012). 'Using the Fundamental Plane of Black Hole Activity to Distinguish X-ray Processes from Weakly Accreting Black Holes'. *Monthly Notices of the Royal Astronomical Society* **419**:267–286.

R. M. Plotkin, et al. (2019). 'Radio Variability from a Quiescent Stellar-mass Black Hole Jet'. *The Astrophysical Journal* **874**:13.

R. M. Plotkin, et al. (2017). 'The 2015 Decay of the Black Hole X-Ray Binary V404 Cygni: Robust Disk-jet Coupling and a Sharp Transition into Quiescence'. *The Astrophysical Journal* **834**:104.

D. Pooley, et al. (2003). 'Dynamical Formation of Close Binary Systems in Globular Clusters'. \apjl **591**(2):L131–L134.

D. Pooley, et al. (2002). 'Optical Identification of Multiple Faint X-Ray Sources in the Globular Cluster NGC 6752: Evidence for Numerous Cataclysmic Variables'. *The Astrophysical Journal* **569**:405–417.

S. F. Portegies Zwart & S. L. W. McMillan (2002). 'The Runaway Growth of Intermediate-Mass Black Holes in Dense Star Clusters'. *The Astrophysical Journal* **576**(2):899–907.

A. M. Price-Whelan, et al. (2017). 'The Joker: A Custom Monte Carlo Sampler for Binary-star and Exoplanet Radial Velocity Data'. *The Astrophysical Journal* **837**:20.

N. Rea, et al. (2017). 'Multiband Study of RX J0838-2827 and XMM J083850.4-282759: A New Asynchronous Magnetic Cataclysmic Variable and a Candidate Transitional Millisecond Pulsar'. *Monthly Notices of the Royal Astronomical Society* **471**:2902–2916.

M. T. Reynolds, et al. (2014). 'The Quiescent X-ray Spectrum of Accreting Black Holes'. *Monthly Notices of the Royal Astronomical Society* **441**:3656–3665.

A. Ridolfi, et al. (2021). 'Eight New Millisecond Pulsars from the First MeerKAT Globular Cluster Census'. *Monthly Notices of the Royal Astronomical Society* **504**:1407–1426.

L. E. Rivera Sandoval, et al. (2018). 'New Cataclysmic Variables and Other Exotic Binaries in the Globular Cluster 47 Tucanae'. *Monthly Notices of the Royal Astronomical Society* **475**(4):4841–4867.

L. E. Rivera Sandoval, et al. (2015). 'Discovery of Near-Ultraviolet Counterparts to Millisecond Pulsars in the Globular Cluster 47 Tucanae'. *Monthly Notices of the Royal Astronomical Society* **453**:2707–2717.

M. S. E. Roberts (2013). 'Surrounded by Spiders! New Black Widows and Redbacks in the Galactic Field'. In J. van Leeuwen (ed.), *Neutron Stars and Pulsars: Challenges and Opportunities after 80 Years*, vol. 291 of *IAU Symposium*, pp. 127–132.

T. Robitaille, et al. (2017). 'Glueviz v0.13.1: Multidimensional Data Exploration'. *Zenodo* .

R. W. Romani, et al. (2022). 'PSR J0952-0607: The Fastest and Heaviest Known Galactic Neutron Star'. *The Astrophysical Journal* **934**:L17.

R. T. Rood, et al. (1978). 'Radio Sources in Globular Cluster Fields.'. *The Astrophysical Journal* **225**:804–807.

T. D. Russell, et al. (2016). 'The Reproducible Radio Outbursts of SS Cygni'. *Monthly Notices of the Royal Astronomical Society* **460**:3720–3732.

M. Salaris, et al. (2007). 'Deep Near-Infrared Photometry of the Globular Cluster 47 Tucanae. Reconciling Theory and Observations'. *Astronomy and Astrophysics, Volume 476, Issue 1, December II 2007, pp.243-253* **476**(1):243.

A. Sarajedini, et al. (2007). 'The ACS Survey of Galactic Globular Clusters. I. Overview and Clusters without Previous Hubble Space Telescope Photometry'. *The Astronomical Journal* **133**:1658–1672.

R. J. Sault, et al. (1995). 'A Retrospective View of Miriad'. *4th Annual Astronomical Data Analysis Software and Systems Conference Conference (ADASS 94) Baltimore, Maryland, September 25-28, 1994* **77**:433–436.

T. Shahbaz, et al. (2019). 'The Binary Millisecond Pulsar PSR J1023+0038 - II. Optical Spectroscopy'. *Monthly Notices of the Royal Astronomical Society* **488**:198–212.

N. I. Shakura & R. A. Sunyaev (1973). 'Black holes in binary systems. Observational appearance.'. *Astronomy and Astrophysics* **24**:337–355.

I. C. Shih, et al. (2010). 'A Variable Black Hole X-ray Source in an NGC 1399 Globular Cluster'. *apj* **721**(1):323–328.

L. Shishkovsky, et al. (2018). 'The MAVERIC Survey: A Red Straggler Binary with an Invisible Companion in the Galactic Globular Cluster M10'. *The Astrophysical Journal* **855**:55.

L. Shishkovsky, et al. (2020). 'The MAVERIC Survey: Radio Catalogs and Source Counts from Deep Very Large Array Imaging of 25 Galactic Globular Clusters'. *The Astrophysical Journal, Volume 903, Issue 1, id.73, <NUMPAGES>14</NUMPAGES> pp.* **903**(1):73.

S. Sigurdsson & L. Hernquist (1993). 'Primordial Black Holes in Globular Clusters'. \nat **364**(6436):423–425.

M. F. Skrutskie, et al. (2006). 'The Two Micron All Sky Survey (2MASS)'. *The Astronomical Journal* **131**(2):1163–1183.

A. Skumanich (1972). 'Time Scales for Ca II Emission Decay, Rotational Braking, and Lithium Depletion'. *The Astrophysical Journal* **171**:565.

J. Spitzer, Lyman (1969). 'Equipartition and the Formation of Compact Nuclei in Spherical Stellar Systems'. \apjl **158**:L139.

W. S. Stacey, et al. (2012). 'An Examination of the X-Ray Sources in the Globular Cluster NGC 6652'. *The Astrophysical Journal* **751**:62.

B. W. Stappers et al. (2014). 'A State Change in the Missing Link Binary Pulsar System PSR J1023+0038'. *Astrophys. J.* **790**(1):39.

J. Strader, et al. (2012a). 'Two Stellar-Mass Black Holes in the Globular Cluster M22'. *Nature* **490**:71–73.

J. Strader, et al. (2012b). 'No Evidence for Intermediate-mass Black Holes in Globular Clusters: Strong Constraints from the JVLA'. *The Astrophysical Journal Letters* **750**:L27.

J. Strader, et al. (2019a). 'Optical Spectroscopy and Demographics of Redback Millisecond Pulsar Binaries'. *The Astrophysical Journal* **872**:42.

J. Strader, et al. (2019b). 'Optical Spectroscopy and Demographics of Redback Millisecond Pulsar Binaries'. *The Astrophysical Journal* **872**:42.

J. Strader, et al. (2021). 'Multiwavelength Evidence for a New Flare-Mode Transitional Millisecond Pulsar'. *arXiv:2106.07657 [astro-ph]* .

S. Ströbele, et al. (2012). 'GALACSI System Design and Analysis' **8447**:844737.

W. Sutantyo (1975). 'The Formation of Globular Cluster X-ray Sources through Neutron Star - Giant Collisions.'. *aap* **44**:227–230.

S. J. Swihart, et al. (2018). 'A Multiwavelength View of the Neutron Star Binary 1FGL J1417.7-4402: A Progenitor to Canonical Millisecond Pulsars'. *apj* **866**:83.

C. Tasse, et al. (2018). 'Faceting for Direction-Dependent Spectral Deconvolution'. *Astronomy & Astrophysics, Volume 611, id.A87, <NUMPAGES>15</NUMPAGES> pp.* **611**:A87.

T. M. Tauris & E. P. J. van den Heuvel (2006). 'Formation and Evolution of Compact Stellar X-ray Sources'. In *In: Compact Stellar X-ray Sources. Edited by Walter Lewin & Michiel van Der Klis. Cambridge Astrophysics Series, No. 39. Cambridge, UK: Cambridge University Press, ISBN 978-0-521-82659-4, ISBN 0-521-82659-4, DOI: 10.2277/0521826594, 2006, p. 623 - 665*, vol. 39, pp. 623–665.

G. B. Taylor, et al. (1999). 'Synthesis Imaging in Radio Astronomy II' **180**.

M. B. Taylor (2005). 'TOPCAT & STIL: Starlink Table/VOTable Processing Software'. In P. Shopbell, M. Britton, & R. Ebert (eds.), *Astronomical Data Analysis Software and Systems XIV*, vol. 347 of *Astronomical Society of the Pacific Conference Series*, p. 29.

S. P. Tendulkar, et al. (2014). 'NuSTAR Observations of the State Transition of Millisecond Pulsar Binary PSR J1023+0038'. *The Astrophysical Journal* **791**:77.

Y. Terzian & E. K. Conklin (1977). 'Radio Sources in the Direction of Globular Clusters.'. *The Astronomical Journal* **82**:468–470.

B. E. Tetarenko, et al. (2016). 'WATCHDOG: A Comprehensive All-sky Database of Galactic Black Hole X-ray Binaries'. *The Astrophysical Journal Supplement Series* **222**:15.

The Fermi LAT collaboration (2010). 'A Population of Gamma-Ray Emitting Globular Clusters Seen with the Fermi Large Area Telescope'. *Astronomy & Astrophysics* **524**:A75.

The Lynx Team (2018). 'The Lynx Mission Concept Study Interim Report'.

A. R. Thompson, et al. (2017). *Interferometry and Synthesis in Radio Astronomy, 3rd Edition*.

T. A. Thompson, et al. (2019). 'A Noninteracting Low-Mass Black Hole–Giant Star Binary System'. *Science* **366**(6465):637–640.

D. Tody (1986). 'The IRAF Data Reduction and Analysis System'. *Instrumentation in astronomy VI* **627**:733.

D. Tody (1993). 'IRAF in the Nineties' **52**:173.

E. Tremou, et al. (2018). 'The MAVERIC Survey: Still No Evidence for Accreting Intermediate-mass Black Holes in Globular Clusters'. *The Astrophysical Journal* **862**:16.

V. Tudor, et al. (2017). 'Disc-Jet Coupling in Low-Luminosity Accreting Neutron Stars'. *Monthly Notices of the Royal Astronomical Society* **470**:324–339.

V. Tudor, et al. (2022). 'The MAVERIC Survey: A Catalogue of Radio Sources in Southern Globular Clusters from the Australia Telescope Compact Array'. *Monthly Notices of the Royal Astronomical Society* **513**:3818–3835.

P. J. Turk & D. R. Lorimer (2013). 'An Empirical Bayesian Analysis Applied to the Globular Cluster Pulsar Population'. \mnras **436**(4):3720–3726.

R. Urquhart, et al. (2020). 'The MAVERIC Survey: New Compact Binaries Revealed by Deep Radio Continuum Observations of the Galactic Globular Cluster Terzan 5'. *arXiv e-prints* **2009**:arXiv:2009.07286.

A. Vahdat Motlagh, et al. (2019). 'Investigating State Transition Luminosities of Galactic Black Hole Transients in the Outburst Decay'. *Monthly Notices of the Royal Astronomical Society* **485**:2744–2758.

M. van den Berg, et al. (1999). 'Optical Spectroscopy of X-ray Sources in the Old Open Cluster M 67'. *Astronomy and Astrophysics* **347**:866–875.

E. P. J. van den Heuvel (1975). 'Modes of Mass Transfer and Classes of Binary X-ray Sources.'. \apjl **198**:L109–L112.

R. P. van der Marel & J. Anderson (2010). 'New Limits on an Intermediate-Mass Black Hole in Omega Centauri. II. Dynamical Models'. *The Astrophysical Journal* **710**(2):1063–1088.

L. M. van Haaften, et al. (2013). 'Population synthesis of ultracompact X-ray binaries in the Galactic bulge'. *Astronomy and Astrophysics* **552**:A69.

L. M. van Haaften, et al. (2012). 'The evolution of ultracompact X-ray binaries'. *Astronomy and Astrophysics* **537**:A104.

L. A. C. van Son, et al. (2020). 'Polluting the Pair-instability Mass Gap for Binary Black Holes through Super-Eddington Accretion in Isolated Binaries'. *The Astrophysical Journal* **897**(1):100.

F. Verbunt, et al. (1995). 'The ROSAT XRT Sky Survey of X-ray Sources in Globular Clusters.'. *Astronomy and Astrophysics* **300**:732.

F. Verbunt & P. Hut (1987). 'The Globular Cluster Population of X-Ray Binaries' **125**:187.

O. Vilhu & F. M. Walter (1987). 'Chromospheric-Coronal Activity at Saturated Levels'. *The Astrophysical Journal* **321**:958–966.

R. A. Wade & K. Horne (1988). 'The Radial Velocity Curve and Peculiar TiO Distribution of the Red Secondary Star in Z Chamaeleontis'. *The Astrophysical Journal* **324**:411.

P. M. Weilbacher, et al. (2020). 'The Data Processing Pipeline for the MUSE Instrument'. *Astronomy & Astrophysics, Volume 641, id.A28, <NUMPAGES>30</NUMPAGES> pp.* **641**:A28.

R. Wijnands & M. van der Klis (1998). 'A Millisecond Pulsar in an X-ray Binary System'. *Nature* **394**:344–346.

R. J. Wilman, et al. (2008). 'A Semi-Empirical Simulation of the Extragalactic Radio Continuum Sky for next Generation Radio Telescopes'. *Monthly Notices of the Royal Astronomical Society* **388**:1335–1348.

J. Wilms, et al. (2000). 'On the Absorption of X-Rays in the Interstellar Medium'. *The Astrophysical Journal* **542**:914–924.

W. E. Wilson, et al. (2011). 'The Australia Telescope Compact Array Broad-band Backend: Description and First Results'. *Monthly Notices of the Royal Astronomical Society* **416**:832–856.

S. E. Woosley (2017). 'Pulsational Pair-instability Supernovae'. *The Astrophysical Journal* **836**:244.

S. E. Woosley (2019). 'The Evolution of Massive Helium Stars, Including Mass Loss'. *The Astrophysical Journal* **878**:49.

S. E. Woosley, et al. (2007). 'Pulsational Pair Instability as an Explanation for the Most Luminous Supernovae'. *Nature* **450**:390–392.

S. E. Woosley & A. Heger (2021). 'The Pair-instability Mass Gap for Black Holes'. *The Astrophysical Journal Letters* **912**(2):L31.

C. S. Ye, et al. (2019). 'Millisecond Pulsars and Black Holes in Globular Clusters'. *The Astrophysical Journal* **877**(2):122.

C. S. Ye, et al. (2021). 'Compact Object Modeling in the Globular Cluster 47 Tucanae'. *arXiv:2110.05495 [astro-ph]* .

L. R. Yungelson, et al. (2019). 'Wind-Accreting Symbiotic X-ray Binaries'. *\mnras* **485**(1):851–860.

Y. Zhao, et al. (2019). 'Identifications of Faint Chandra Sources in the Globular Cluster M3'. *Monthly Notices of the Royal Astronomical Society* **483**:4560–4577.

Y. Zhao, et al. (2020a). 'A Deep Chandra Survey for Faint X-ray Sources in the Galactic Globular Cluster M30, and Searches for Optical and Radio Counterparts'. *arXiv:2009.07924 [astro-ph]* .

Y. Zhao, et al. (2020b). 'The MAVERIC Survey: A Hidden Pulsar and a Black Hole Candidate in ATCA Radio Imaging of the Globular Cluster NGC 6397'. *arXiv e-prints* **2003**:arXiv:2003.00135.